Characterization and performance evaluation of electrodeposition synthesized cobalt-nickel layered double hydroxide and composites for high-efficiency hybrid capacitor applications

by

GIFT RUTAVI

A thesis submitted in partial fulfilment of the requirements for the degree of

DOCTOR OF PHILOSOPHY (PhD) IN PHYSICS

Faculty of Natural and Agricultural Sciences

University of Pretoria

Hatfield Pretoria

September 2022

Supervisor/promoter: Prof. Ncholu. I. Manyala

DECLARATION

I, **Gift Rutavi** declare that this thesis, entitled *"Characterization and performance evaluation of electrodeposition synthesized cobalt-nickel layered double hydroxide and composites for high-efficiency hybrid capacitor applications "* which I hereby submit for the degree **Doctor of Philosophy (PhD)** in the Department of Physics, University of Pretoria, South Africa has not previously been submitted by me for a degree at any other tertiary institution.

Signature…………………………………   Date …………………….

DEDICATION

To God Almighty, who gave me this opportunity.

To my family for being there for me.

To those who had faith in me.

To myself.

ACKNOWLEDGEMENTS

TABLE OF CONTENTS

LIST OF FIGURES

LIST OF TABLES

LIST OF EQUATIONS

ABSTRACT

The focus of this study is on the synthesis and characterisation of cobalt nickel layered double hydroxide (CoNi-LDH) and its composite for application in supercapacitors. CoNi-LDH was chosen because of its unique layered structure with many exposed redox active sites, tunable anion exchange, and large interlayer separation. However, CoNi-LDH has low electron transport and low cyclic stability due to the restacking of its layers. Careful engineering of cobalt nickel layered double hydroxide-based composites enables the electrodes to have sustainable practical applications. Due to its great electrical conductivity (the measure of how easily a material allows the passage of current), wettability and mechanical strength, sulphur-reduced graphene oxide (RGO-S) can increase electron transport while minimising restacking. Wettability is the ability of the liquid to maintain contact with the solid. It is dependent on the balance of the adhesive and cohesive intermolecular interactions.

Careful engineering of the electrode structure that provides support for the LDH can reduce the restacking thereby increasing the electron transport and cycling stability while increasing the specific capacity of CoNi-LDH. Bimetallic metal oxides such as Hausmannite (MO), manganese cobaltite (MCO) and manganese chromite ($MnCr_2O_4$) can improve the electrochemical performance because of their high redox activity, Jahn-Teller distortion, and wide range of active oxidation states.

RGO-S was produced using modified Hummer's methods while MO, CN, MCO, $MnCr_2O_4$, and MO/RGO-S were synthesized through electrodeposition. Electrodeposition method can yield a variety of materials structure without involving binders. Its robustness leads to greater stability of the electrodes, and it can control the structure of the electrode by varying parameters such as input current, number of electrodeposition cycles and the electrodeposition duration (time). Morphology, elemental mapping/composition, and thickness were characterised using

scanning electron microscope (SEM), transmission electron microscope (TEM), energy-dispersive X-ray spectroscopy (EDS), X-ray powder diffraction (XRD) and Raman spectroscopy.

The first composite MO/RGO-S-50@CN synthesized through a two-step electrodeposition procedure yielded a great specific capacity of 582.1 mAh g^{-1} at a specific current of 0.5 A g^{-1} in 2 M KOH. It was used to fabricate an asymmetric device MO/RGO-S-50@CN//CCBW with activated carbon from cooked chicken bones waste (CCBW) as the negative electrode. The device generated a great specific energy of 56.0 Wh kg^{-1} at a specific current of 0.5 A g^{-1} corresponding to a specific power of 515 W kg^{-1}. The device also produced capacity retention and coulombic efficiency of 85.1 and 99.7 %, respectively at 10, 000 galvanostatic charge-discharge (GCD) cycles at 6 A g^{-1}.

A second composite device was also synthesised through successive electrodeposition of MCO, and CoNi-LDH on NF. The optimised electrode MCO-2.5@CN-LDH produced a competitive specific capacity of 415.9 mAh g^{-1} at 1 A g^{-1}. It was incorporated into an asymmetric capacitor device, MCO-2.5@CN-LDH//CCBW which produced a superb specific energy of 55.8 Wh kg^{-1} corresponding to a specific power of 940.4 W kg^{-1} at a 1 A g^{-1}. A device stability measurement up to 10,000 GCD at 7 A g^{-1} produced great capacity retention of 81.6 % and coulombic efficiency of 99.8 %.

MnCr$_2$O$_4$ as the third composite electrode with CoNi-LDH was synthesised through a repeated electrodeposition process. The optimised electrode, MnCr$_2$O$_4$-1.2 @CoNi-LDH produced a phenomenal specific capacity of 424.7 mAh g^{-1} at a specific current of 1 A g^{-1}. The electrode served as a positive electrode in the device MnCr$_2$O$_4$-1.2@CoNi-LDH//AMH with the activated carbon from Amarula husk (AMH) as the negative electrode. The device yielded an outstanding specific energy of 80.2 Wh kg^{-1} at a specific current of 1 A g^{-1} corresponding to a

specific power of 1117.7 W kg^{-1}. The stability of the device was also phenomenal with a coulombic efficiency of 99.7 and 72.9 % after 15,000 GCD cycles at 9 A g^{-1}. The findings of this study have availed electrodeposition synthesized electrodes of cobalt nickel layered hydroxides composites as candidates for high-performance supercapacitor application.

<h1 style="text-align:center">CHAPTER 1</h1>

1.0 INTRODUCTION

This chapter covers the background of the study and the problem statement. It is followed by the motivation, the objective of the study and finally the scope of the thesis.

1.1 Background of the study

The quest for control of energy is as old as humanity itself. With the discovery, interaction and control of fire about 400,000 years ago, the purpose of energy was to cover primary human needs such as food preparation and warmth [1–3]. With the population explosion coupled with the rapid technological evolution, the need for energy has evolved in complexity with purposes such as transportation, telecommunication, portable electronic devices and space travel [4]. The need for reliable sources of energy is increasing at a rate that the planet cannot cope with. The main source of energy has for centuries come from non-renewables sources such as coal and oil. Despite the concerns about the dangers caused by these non-renewable sources of energy which have been there for ages, non-renewable sources of energy have continued to be the main source of energy even now in the 21st century, making up to 80 % of the global world consumption [5]. There are at least two reasons why cleaner and safer renewable energy sources such as solar, wind, tidal and geothermal energy have failed to completely replace fossil fuels. It was proved by scientists and economists that the energy output from renewable sources is often less than the energy expended in the extraction and delivery to the consumers [6]. On the other hand, the availability of these sources of energy is dependent on many factors and conditions such as time of the day, season of the year, geographical location, weather conditions, and climate dynamics [7]. The ways to alleviate the meagre energy output and the intermittent nature of the renewable sources of energy include the development of energy

storage devices [8]. Among the most prominent energy storage devices are batteries and supercapacitors (SC). Batteries which are popular because of high specific energy come in different forms, but lithium ion batteries (LIBs) have become popular due to their improved specific energy [9,10]. One of the commonly used battery devices are the Lithium ion batteries (LIBs), due to the rising use of portable electric device where they are commonly used [11]. LIBs are popular in areas such as electronic devices because of have higher specific energy, faster charging capability, higher voltage output, less discharge, higher specific power and lasts longer than rechargeable batteries[12] . LIBs consist of metal oxide positive electrode which serves as the source of lithium and the negative electrode which acts as the sink of these ions [13]. The storage of the ions occurs through intercalation in the bulk or at the surface of the electrode. The electrolyte inside the LIBs facilitates ion transport. However, the main drawback of LIBs is their low specific power [14]. The implication is that for them to meet the peak power requirements of applications such as in portable electronic devices, hybrid vehicles and backup energy systems which are characterised with rapid power delivery, LIBs would have to be designed in large sizes which will limit their portability. Toxicity, sluggish charge-discharge, and poor cycling stability are additional demerits of LIBs.

Supercapacitors (SCs) which are also known as electrochemical capacitors (ECs) or ultracapacitors (UCs), are storage devices which have generated a lot of interest among researchers because of their higher specific power, better cycling stability and environmental friendliness compared to LIBs [15]. However, the specific energy of supercapacitors is significantly lower than that of LIBs. The specific energy (E_S) of storage devices is directly proportional to product of the specific capacitance (C_S) and the square of the voltage (V), ($E_S \propto C_S V^2$). Therefore, to improve the specific energy of SCs, it is essential to investigate the electrode material with the intention to improve the charge storage ability (capacity/capacitance) and to source compatible electrolytes and attempt to widen their

potential window [16]. The electrochemical attributes of SCs such as electrochemical stability also depend on the synthesis method [17].

1.2 Problem statement

SCs can be classified into two categories, depending on their energy storage mechanism: Electric double layers capacitors (EDLCs) and pseudocapacitors (PS) [18]. EDLCs store energy through the accumulation and separation of charges at the electrode-electrolyte interface. EDLC electrode materials are mainly carbon-based materials such as graphene, activated carbons and carbon nanotubes. These are characterised by large specific surface areas, wider operation voltages and larger intrinsic electric conductivity, electric conductivity where the concentration of impurities is negligible [19]. PS store energy chemically mainly through fast and reversible Faradaic reaction where electron transfer cause reduction or oxidation to occur. This chemical energy storage mechanism endows PS with higher specific capacitance than EDLCs. Pseudocapacitors comprise conducting polymers and transitional metal oxides (TMOs) and hydroxides (TMOHs) which have been investigated because of their variable oxidation states and great electrochemical stability [20]. The most attractive TMOs which have been investigated include ruthenium oxide (RuO_2) and iridium oxide (IrO_2). Due to their abundant oxidation states and great intrinsic electrical conductivity, fully reversible Faradaic reaction and high chemical stability TMOs possess great promising energy storage potential [21]. However, their high cost and toxicity make them unsustainable for incorporated into energy storage devices [22]. TMOs consisting of cheaper, less toxic metals such as cobalt (Co), Nickel (Ni), manganese (Mn) and chrome (Cr) have been experimented with as electrode material for supercapacitors as they have the potential to possess comparable electrochemical performance to RuO_2 and IrO_2 if their electrical conductivity can be improved. Layered double hydroxides (LDH) which are also known as anionic clays are materials which have generated

a lot of interest to their unique layered structure, high anion exchange capacity and tuneable composition [23]. They also possess larger theoretical specific capacity than single metal hydroxides such as $Ni(OH)_2$ and $Co(OH)_2$ due to the presence of multiple redox active sites responsible for great ion exchange and intercalation and flexible ion interchangeability. Cobalt nickel layered double hydroxide (CoNi-LDH) has presented great potential for use as a positive electrode for a supercapacitor. This is because of the synergetic effects of the hydroxides of Ni and Co, providing more electroactive sites [24]. CoNi-LDHs however, suffer from poor electrical conductivity, poor rate capability and poor cyclic stability due to restacking [25]. These short-comings can be reduced through the synthesis of LDH composites with materials that have better electrical conductivity.

1.3 Motivation for the study

This thesis will focus on the synthesis of CoNi-LDH materials for supercapacitor applications. As detailed in the problem statement, the challenges of this material can be reduced by forming composites with conductive material, and nanostructure material consist of redox species. Graphene which is a one-atom thick sp^2 hexagonal array of carbon atoms is one of the most suitable materials to improve the electrochemical performance of CoNi-LDH. This is due to the many several favourable properties that graphene has. These include excellent electrical conductivity [26], which helps to compensate for the low electrical conductivity of CoNi-LDH. It also has an extreme tensile strength of 130 GPa which helps in providing support to reduce the restacking of the layers of CoNi-LDH [27]. This goes a long way toward improving the mechanical and electrochemical stability of CoNi-LDH. The method commonly used to produce it in considerable amounts results in the formation of graphene oxide (GO) with

a lot of functional groups. This process results in the alteration of the structural composition of graphene. This can be corrected by reduced graphene oxide (RGO) which leads to a reduction of the oxygen functional groups on the surface of graphene [28]. Optimisation of these functional groups helps to improve the rate capabilities of the electrode materials [29]. The inclusion of sulphur into the RGO to form sulphur-reduced graphene oxide (RGO-S) helps to alter the chemical and physical properties due to the proximity of the electronegativity of sulphur to that of the carbon in graphene. This helps to reduce the charge transfer resistance while increasing the wettability [30].

The electrochemical properties of CoNi-LDH can also be enhanced by the construction of a stable heterostructure system with highly redox-active materials. Manganese-based spinels are suitable materials for this purpose. Spinel is mixed metal oxide material usually with a chemical structure AB_2O_4, where A and B are divalent and trivalent metals, respectively [31]. The synergetic effect of two metals A and B in their spinel increases the multivalent charge transport and the number of redox-active sites. The presence of the Mn^{3+} ions bestows it with an excellent Jahn-Teller effect which facilitates ion diffusion and enables the possibility of reversible phase transformation. The reversible phase transformation occurs when the distinct and homogeneous state of a medium can be altered to another state and still returns to the initial state, The Jahn-Teller effect is a geometric distortion of a non-linear molecular system that reduces its symmetry and energy, this effect is affected by the electronic state of the system [32]. Manganese which is in the middle of the periodic table has the highest number of oxidation states (+2,+3,+4,+6 and +7), also it is the only element which possesses the highest oxidation state of +7 in the whole periodic table due to the presence of 5 unpaired electrons [33]. These properties when combined with the layered structure of the LDHs result in an electrochemically stable and high pseudocapacitive electrode material.

Manganese oxide spinel (Mn_3O_4) also known as Hausmannite has a high theoretical specific capacitance of 1370 F g^{-1}. Mn_3O_4 provide prospects for being included in composite electrodes with CoNi-LDH to improve the electrochemical performance. This is because of the presence of a wide range of active oxidation states which greatly enhances the charge exchangeability. However, the electrical conductivity of Mn_3O_4 is low and the incorporation of RGO-S into the composite of Mn_3O_4 helps alleviate this problem. For example, Tarimo et al. reported the incorporation of MnO_2 into RGO-S to produce a high-performance electrode material with great stability for supercapacitor application [34].

Manganese cobaltite (MCO) is another spinel which is an interesting candidate for improving the electrical performance of CoNi LDH. It has a very high theoretical specific capacitance of 3620F g^{-1}, whereby the presence of Co ions increases the electrochemical performance of the composite [35].

Metal chromites have found use in hydrogen production, electrocatalytic activities, semiconductor material, and purification activities [36]. However, there have not been a lot of instances where metal chromites have been incorporated into electrode materials for electrochemical energy storage. Manganese chromite ($MnCr_2O_4$) has interesting prospects for high electrochemical properties due to remarkable electrical conductivity [37].

Besides the investigation of improving the components of a supercapacitor's electrode such as electrode material, electrolyte and current collector, the synthesis method plays an important role in the performance of the electrode. Binder-free synthesis has the merits of eliminating the electrical resistance introduced by polymeric binders which would need to be compensated by the addition of conducting additives [38]. Electrodeposition is a facile and cost-effective route to synthesise electrodes directly on current conductors. It uses an electric current to permanently deposit electrode materials on the substrate. This method ensures efficient

utilisation of materials while at the same time ensuring an intact adherence of the electrode material to the current collector. Unlike other binder-free syntheses such as chemical vapour deposition (CVD), the process can be carried out using safe and cost-effective conditions such as room temperature and pressure, low current and neutral solutions. This method makes it possible to control the properties of the materials such as the thickness, grain size, electrical conductivity and texture by varying the applied voltage or current, the composition of solutes in the solution, and the pH [39].

The present thesis intendeds on using the electrodeposition method to synthesize fuse CoNi-LDH with RGO-S, and composites of manganese-based spinel to construct positive electrode materials for supercapacitors. Very few researchers have utilised electrodeposition for the synthesis of electrode materials for supercapacitors [40–43]. However, the combination of multiple materials which are distinct LDH, a spinel and carbon material to form a high-performance electrochemical material using a successive electrodeposition route has not received much attention in the field of energy storage research. The evaluation of the produced electrode materials will be analysed to recommend a binder-free, high stable and best-performed electrode material.

1.4 Objectives of the study

The major aim of the study is to create composites of manganese-based spinel combined with CoNi-LDH, and RGO-S for the general improvement of the electrochemical performance of the resulting electrode materials and their supercapacitors devices. The specific objectives are as follows:

i. Synthesis of cobalt nickel layered double hydroxide (CoNi-LDH) using the electrodeposition method.

ii. Synthesis of Hausmannite sulphur reduced graphene oxide/cobalt nickel layered double hydroxide (Mn_3O_4/RGO-S@CoNi-LDH) using the hummers method followed by the electrodeposition synthesis.

iii. Synthesis of manganese cobaltite/cobalt nickel layered double hydroxide ($Mn_{2-x}Co_{1+x}$@CoNi-LDH) composite using electrodeposition followed by annealing.

iv. Synthesis of manganese chromite/cobalt nickel layered double hydroxide ($MnCr_2O_4$@CoNi-LDH) composite using electrodeposition followed by annealing.

v. Evaluations of thickness, elemental composition, morphological and structure analysis using energy-dispersive X-ray spectroscopy (EDS), scanning electron microscopy (SEM), transmission electron microscopy (TEM) and Raman spectroscopy.

vi. Evaluation of the electrochemical performance utilizing potential window, resistivity and charge storage mechanism of the electrode using half-cell set-up via cyclic voltammetry (CV), galvanostatic charge discharge (GCD), electrochemical impedance spectroscopy (EIS) and stability measurement.

vii. Assembly of supercapacitor devices using the above-specified materials above as positive electrodes and activated carbon from cooked chicken bone wastes as negative electrode in 2 M KOH with the intention to assess the practical application of the material for the determination of the specific power and energy yielded.

1.5 Scope of the thesis

This thesis is apportioned into five chapters summarises as follows:

Chapter 1

Introduction: This chapter gives a thorough discussion of the background, problem statement, motivation, objectives of the study and scope of the thesis.

Chapter 2

Literature review: This chapter covers the theory of electrochemical energy storage focusing on the evaluation of the performance, classification, energy storage mechanism, and electrode materials for supercapacitors followed by electrolytes and electrode fabrication, testing and performance evaluation of the electrode materials.

Chapter 3

Experimental details characterisation techniques: The scope of this chapter is on the experimental procedures used during the synthesis of the materials together with the linked characterisation techniques applied in the analysis of the performance of the materials.

Chapter 4

Results and discussion: This chapter discusses the results obtained after the synthesis, characterisation and evaluation of cobalt nickel layered double hydroxide composite materials.

Chapter 5

Conclusion and suggestions for further studies: This chapter covers the overall conclusion drawn from this study and suggestions for possible future work.

References

[1]   J.A.J. Gowlett, The discovery of fire by humans: A long and convoluted process, Philos. Trans. R. Soc. B Biol. Sci. 371 (2016). https://doi.org/10.1098/rstb.2015.0164.

[2]   M. Chazan, Toward a long prehistory of fire, Curr. Anthropol. 58 (2017) S351–S359. https://doi.org/10.1086/691988.

[3]   W. Roebroeks, P. Vill, On the earliest evidence for habitual use of fire in Europe, Proc. Natl. Acad. Sci. U. S. A. 108 (2011) 5209–5214. https://doi.org/10.1073/pnas.1018116108.

[4]   P.S. Aithal, S. Aithal, OPPORTUNITIES & CHALLENGES FOR GREEN TECHNOLOGIES IN 21 st CENTURY, Int. J. Curr. Res. Mod. Educ. ISSN. I (2016) 2455–5428. www.rdmodernresearch.com.

[5]   C. Magazzino, M. Mele, G. Morelli, The relationship between renewable energy and economic growth in a time of COVID-19: A machine learning experiment on the Brazilian economy, Sustain. 13 (2021) 1–24. https://doi.org/10.3390/su13031285.

[6]   R.L. Rana, M. Lombardi, P. Giungato, C. Tricase, Trends in scientific literature on energy return ratio of renewable energy sources for supporting policymakers, Adm. Sci. 10 (2020). https://doi.org/10.3390/admsci10020021.

[7]   W. Uchman, A. Skorek-Osikowska, M. Jurczyk, D. Węcel, The analysis of dynamic operation of power-to-SNG system with hydrogen generator powered with renewable energy, hydrogen storage and methanation unit, Energy. 213 (2020). https://doi.org/10.1016/j.energy.2020.118802.

[8]   C. Senthil, C.W. Lee, Biomass-derived biochar materials as sustainable energy sources for electrochemical energy storage devices, Renew. Sustain. Energy Rev. 137 (2021) 110464. https://doi.org/10.1016/j.rser.2020.110464.

[9]   Y. Morita, Y. Saito, T. Yoshioka, T. Shiratori, Estimation of recoverable resources used in lithium-ion batteries from portable electronic devices in Japan, Resour. Conserv. Recycl. 175 (2021) 105884. https://doi.org/10.1016/j.resconrec.2021.105884.

[10]   T. Yu, B. Ke, H. Li, S. Guo, H. Zhou, Recent advances in sulfide electrolytes toward high specific energy solid-state lithium batteries, Mater. Chem. Front. 5 (2021) 4892–4911. https://doi.org/10.1039/d1qm00474c.

[11]   M. Assefi, S. Maroufi, Y. Yamauchi, V. Sahajwalla, Pyrometallurgical recycling of Li-ion, Ni–Cd and Ni–MH batteries: A minireview, Curr. Opin. Green Sustain. Chem. 24 (2020) 26–31. https://doi.org/10.1016/j.cogsc.2020.01.005.

[12]   Z. Cui, L. Wang, Q. Li, K. Wang, A comprehensive review on the state of charge estimation for lithium-ion battery based on neural network, Int. J. Energy Res. 46 (2022) 5423–5440. https://doi.org/10.1002/er.7545.

[13]   G.N. Newton, L.R. Johnson, D.A. Walsh, B.J. Hwang, H. Han, Sustainability of Battery Technologies: Today and Tomorrow, ACS Sustain. Chem. Eng. 9 (2021) 6507–6509. https://doi.org/10.1021/acssuschemeng.1c02909.

[14]   L. Jin, C. Shen, A. Shellikeri, Q. Wu, J. Zheng, P. Andrei, J.G. Zhang, J.P. Zheng, Progress and perspectives on pre-lithiation technologies for lithium ion capacitors, Energy Environ. Sci. 13 (2020) 2341–2362. https://doi.org/10.1039/d0ee00807a.

[15]   H. Chen, H. Hu, F. Han, J. Liu, Y. Zhang, Y. Zheng, CoMoO4/bamboo charcoal hybrid material for high-energy-density and high cycling stability supercapacitors, Dalt. Trans. 49 (2020) 10799–10807. https://doi.org/10.1039/d0dt00147c.

[16]   B. Yang, D. Zhang, W. She, J. Wang, S. Gao, Y. Wang, K. Wang, Remarkably improving the specific energy of supercapacitor based on a biomass-derived interconnected hierarchical porous carbon by using a newly-developed mixed alkaline aqueous electrolyte with widened operation voltage, J. Power Sources. 492 (2021) 229666. https://doi.org/10.1016/j.jpowsour.2021.229666.

[17]   S. Yadav, A. Sharma, Importance and challenges of hydrothermal technique for synthesis of transition metal oxides and composites as supercapacitor electrode materials, J. Energy Storage. 44 (2021) 103295. https://doi.org/10.1016/j.est.2021.103295.

[18]   R. Pothu, R. Bolagam, Q.H. Wang, W. Ni, J.F. Cai, X.X. Peng, Y.Z. Feng, J.M. Ma, Nickel sulfide-based energy storage materials for high-performance electrochemical capacitors, Rare Met. 40 (2021) 353–373. https://doi.org/10.1007/s12598-020-01470-w.

[19]   H. Shao, Y.C. Wu, Z. Lin, P.L. Taberna, P. Simon, Nanoporous carbon for electrochemical capacitive energy storage, Chem. Soc. Rev. 49 (2020) 3005–3039. https://doi.org/10.1039/d0cs00059k.

[20]   P. Veerakumar, A. Sangili, S. Manavalan, P. Thanasekaran, K.C. Lin, Research Progress on Porous Carbon Supported Metal/Metal Oxide Nanomaterials for Supercapacitor Electrode Applications, Ind. Eng. Chem. Res. 59 (2020) 6347–6374. https://doi.org/10.1021/acs.iecr.9b06010.

[21]   J. Wang, T. Ye, Y. Shao, Z. Lu, Y. Lin, H. Wu, G. Li, K. Chen, D. Tang, Flower-Like Nanostructured ZnCo 2 O 4 /RuO 2 Electrode Materials for High Performance Asymmetric Supercapacitors , J. Electrochem. Soc. 168 (2021) 120553. https://doi.org/10.1149/1945-7111/ac42a4.

[22]   Y.C. Chung, A. Julistian, L. Saravanan, P.R. Chen, B.C. Xu, P.J. Xie, A.Y. Lo, Hydrothermal synthesis of cuo/ruo2/mwcnt nanocomposites with morphological variants for high efficient supercapacitors, Catalysts. 12 (2022) 1–12. https://doi.org/10.3390/catal12010023.

[23]   M. Sajid, S.M. Sajid Jillani, N. Baig, K. Alhooshani, Layered double hydroxide-modified membranes for water treatment: Recent advances and prospects, Chemosphere. 287 (2022) 132140. https://doi.org/10.1016/j.chemosphere.2021.132140.

[24]   F. Chen, C. Chen, Q. Hu, B. Xiang, T. Song, X. Zou, W. Li, B. Xiong, M. Deng, Synthesis of CuO@CoNi LDH on Cu foam for high-performance supercapacitors, Chem. Eng. J. 401 (2020) 126145. https://doi.org/10.1016/j.cej.2020.126145.

[25]   G.M. Tomboc, J. Kim, Y. Wang, Y. Son, J. Li, J.Y. Kim, K. Lee, Hybrid layered double hydroxides as multifunctional nanomaterials for overall water splitting and supercapacitor applications, J. Mater. Chem. A. 9 (2021) 4528–4557. https://doi.org/10.1039/d0ta11606h.

[26]   C. Fang, J. Zhang, X. Chen, G.J. Weng, Calculating the electrical conductivity of graphene nanoplatelet polymer composites by a monte carlo method, Nanomaterials. 10 (2020) 1–15. https://doi.org/10.3390/nano10061129.

[27]   K. Cao, S. Feng, Y. Han, L. Gao, T. Hue Ly, Z. Xu, Y. Lu, Elastic straining of free-standing monolayer graphene, Nat. Commun. 11 (2020) 1–7. https://doi.org/10.1038/s41467-019-14130-0.

[28]   Y. Jin, Y. Zheng, S.G. Podkolzin, W. Lee, Band gap of reduced graphene oxide tuned by controlling functional groups, J. Mater. Chem. C. 8 (2020) 4885–4894. https://doi.org/10.1039/c9tc07063j.

[29]   X.R. Li, Y.H. Jiang, P.Z. Wang, Y. Mo, W. De Lai, Z.J. Li, R.J. Yu, Y.T. Du, X.R. Zhang, Y. Chen, Effect of the oxygen functional groups of activated carbon on its electrochemical performance for supercapacitors, Xinxing Tan Cailiao/New Carbon Mater. 35 (2020) 232–243. https://doi.org/10.1016/S1872-5805(20)60487-5.

[30]   D.J. Tarimo, K.O. Oyedotun, A.A. Mirghni, N. Manyala, Sulphur-reduced graphene oxide composite with improved electrochemical performance for supercapacitor applications, Int. J. Hydrogen Energy. 45 (2020) 13189–13201. https://doi.org/10.1016/j.ijhydene.2020.03.059.

[31]   B. Sriram, J.N. Baby, S.F. Wang, M. George, X.B. Joseph, J.T. Tsai, Surface Engineering of Three-Dimensional-like Hybrid AB2O4(AB = Zn, Co, and Mn) Wrapped on Sulfur-Doped Reduced Graphene Oxide: Investigation of the Role of an Electrocatalyst for Clioquinol Detection, ACS Appl. Electron. Mater. 3 (2021) 362–372. https://doi.org/10.1021/acsaelm.0c00906.

[32]   I.A. Kühne, A. Barker, F. Zhang, Modulation of Jahn – Teller distortion and electromechanical response in a Mn 3 + spin crossover complex, (2020).

[33]   M. Abu-Samak, S. Kumar, R.N. Aljawfi, M.A. Swillam, Electronic structure and energy gaps evaluation of perovskite manganite single crystals using XES and XAS spectroscopy, J. Electron Spectros. Relat. Phenomena. 250 (2021) 147084. https://doi.org/10.1016/j.elspec.2021.147084.

[34]   D.J. Tarimo, K.O. Oyedotun, A.A. Mirghni, N.F. Sylla, N. Manyala, High energy and excellent stability asymmetric supercapacitor derived from sulphur-reduced graphene oxide/manganese dioxide composite and activated carbon from peanut shell, Electrochim. Acta. 353 (2020) 136498. https://doi.org/10.1016/j.electacta.2020.136498.

[35]   F. Liao, X. Han, Y. Zhang, X. Han, C. Xu, H. Chen, Hydrothermal synthesis of mesoporous MnCo 2 O 4 /CoCo 2 O 4 ellipsoid-like microstructures for high-performance electrochemical supercapacitors, Ceram. Int. 45 (2019) 7244–7252. https://doi.org/10.1016/j.ceramint.2019.01.005.

[36]   R. Shafique, M. Rani, A. Mahmood, S. Khan, N.K. Janjua, M. Sattar, K. Batool, T. Yaqoob, Copper chromite/graphene oxide nanocomposite for capacitive energy storage and electrochemical applications, Int. J. Environ. Sci. Technol. 19 (2021) 7517–7526. https://doi.org/10.1007/s13762-021-03616-4.

[37]   F.F. Alharbi, S. Aman, N. Ahmad, S.R. Ejaz, S. Manzoor, R.Y. Khosa, M.U. Nisa, M.A. Iqbal, S. Abbas, M. Awais, Design and fabrication of novel MnCr2O4 nanostructure: electrochemically deposited on stainless steel strip with enhanced efficiency towards supercapacitor applications, J. Mater. Sci. Mater. Electron. 33 (2022) 7256–7265. https://doi.org/10.1007/s10854-022-07909-3.

[38]   S. Poorahong, D.J. Harding, S. Keawmorakot, M. Siaj, Free standing bimetallic nickel cobalt selenide nanosheets as three-dimensional electrocatalyst for water splitting, J. Electroanal. Chem. 897 (2021) 115568. https://doi.org/10.1016/j.jelechem.2021.115568.

[39]   Y. Xiao, X. Chen, T. Li, Y. Mao, C. Liu, Y. Chen, W. Wang, Mo-doped cobalt hydroxide nanosheets coupled with cobalt phosphide nanoarrays as bifunctional catalyst for efficient and high-stability overall water splitting, Int. J. Hydrogen Energy. 47 (2022) 9915–9924. https://doi.org/10.1016/j.ijhydene.2022.01.071.

[40]   N. Zhao, H. Fan, M. Zhang, C. Wang, X. Ren, H. Peng, H. Li, X. Jiang, X. Cao, Preparation of partially-cladding NiCo-LDH/Mn3O4 composite by electrodeposition route and its excellent supercapacitor performance, J. Alloys Compd. 796 (2019) 111–119. https://doi.org/10.1016/j.jallcom.2019.05.023.

[41]   M. Zhang, Y. Chen, D. Yang, J. Li, High performance MnO2 supercapacitor material prepared by modified electrodeposition method with different electrodeposition voltages, J. Energy Storage. 29 (2020). https://doi.org/10.1016/j.est.2020.101363.

[42]   S. Yu, X. Xiong, J. Ma, H. Qian, One-step preparation of cobalt nickel oxide hydroxide@cobalt sulfide heterostructure film on Ni foam through hydrothermal electrodeposition for supercapacitors, Surf. Coatings Technol. 426 (2021) 127791. https://doi.org/10.1016/j.surfcoat.2021.127791.

[43]   X. Dai, M. Zhang, J. Li, D. Yang, Effects of electrodeposition time on a manganese dioxide supercapacitor, RSC Adv. 10 (2020) 15860–15869. https://doi.org/10.1039/d0ra01681k.

CHAPTER 2

2.0.   LITERATURE REVIEW

The scope of this chapter is on the theory and classifications of electrochemical energy storage. It focuses on the classification of energy storage devices while emphasising the supercapacitor. The chapter also focuses on the electrolytes, electrodes, and their synthesis, and finally the electrochemical analysis and testing of the supercapacitor electrodes and devices.

2.1. Theory of electrochemical energy storage (EES)

The history of electrochemical energy storage can be traced back to as early as the year 200 BCE. A fuel cell was discovered in present-day Iraqi. It was believed to have been assembled during the reign of the Parthian empire. This fuel cell was in the form of a clay pot containing copper and iron electrodes in an acidic electrolyte possibly produced by the fermentation of grapefruit juice or vinegar. However, the output of this archaic device could not exceed 2 V [44]. In 1745 von Kleist and van Musschenbroek invented a Leyden jar which was the most ancient form of a capacitor. It comprised metal electrodes inside the glass jar which was coated with conducting foils. Benjamin Franklin joined Leyden jars together to improve their output [45]. It was Michael Faraday who invented the first practical fixed capacitor, a variable capacitor. He used oil barrels to assemble the first capacitor which could be used. He also came up with the concept of the dielectric constant after discovering that spheres with insulators between them always stored more charge, this helped in reducing the size of the capacitor [46,47]. His experimental work led him to device a way to measure capacitance [48]. It was not until the year 1800 that the first battery was invented by Alessandro Volta, this consisted of silver and zinc electrodes in salt solution electrolytes [49]. The battery evolved a lot in the late 20th century culminating in the first commercial Lithium-Ion Battery (LIB) in 1991 by SONY [50]. In 1853 Hermann von

Helmholtz described the electric double layer (EDL) model which involved a pair of separated oppositely charged layers at the electrolyte-electrode interface. This led Howard I. Becker to invent the first low-voltage capacitor which became the first energy storage device consisting of EDLs. This was shortly followed by the development of the first supercapacitor (SC) by the Standard Oil of Ohio (SOHIO) in 1966. This led to a lot of research into the improvement of supercapacitor devices and their commercialization [51].

 A capacitor is a passive device that stores energy electrostatically in an electric field [52]. The simplest form of a capacitor is the parallel plate capacitor, consisting of two electrodes/plates separated by a dielectric material. When a potential difference is applied across the electrodes, a stationary electric field is set between them, and charges flood the dielectric material. For a fixed potential difference, the energy stored is linearly dependant on the charge stored. The applied potential is limited by the dielectric material as the dielectric materials breakdown at a certain potential difference, therefore the operating potential difference of a capacitor can be increased by improving the strength of the dielectric material [53]. This in turn increases the charges that can be stored translating to more energy being stored.

Among the most prominent energy storage devices are batteries and supercapacitors (SC). Batteries come in different forms, but lithium-ion batteries (LIBs) have become popular because of the rising use of portable electric devices where they are commonly used [9]. LIBs consist of metal oxide positive electrodes which serve as the source of lithium and the negative which act as the sink of these ions [13]. The storage of the ions occurs through intercalation in the bulk or at the surface of the electrode. The electrolyte inside the LIBs facilitates ion transport. The specific energy stored by the LIBs can reach as high as (120-200 Wh kg^{-1}) [54], however, the main draw-back is the meagre specific power which is lower than 1 kW kg^{-1} and very limited number of charge-discharge cycles. Both of these are caused by the polarisation which takes place during cycling [55,56].

On the other hand, supercapacitors possess low intrinsic specific energies (~ 50 Wh kg^{-1}) [57]. However, the main benefits of supercapacitors are the high power density (~14 kW kg^{-1}) [58]. Other favourable attributes of supercapacitors include longer cycle life, faster charge-discharge and, handling and more environmental safety compared to LIBs [59].

A Ragone plot in figure 2.1 displays the comparison between different energy storage devices in terms of specific energy and power [60]. LIBs have more energy than conventional capacitors and supercapacitors but their rate of dissipation of this energy (power) is superior. The slow Faradaic intercalations in the positive electrodes in LIBs lower their specific power [61]. The lower specific energy of conventional capacitors is due to the electrostatic charge storage. Supercapacitors can be able to bridge the gap between conventional capacitors and LIBs by combining some of their attributes and increasing the specific energy without compromising the specific power. This can be attained by engineering the electrode materials and optimizing the electrolytes which will enhance the cell potential.
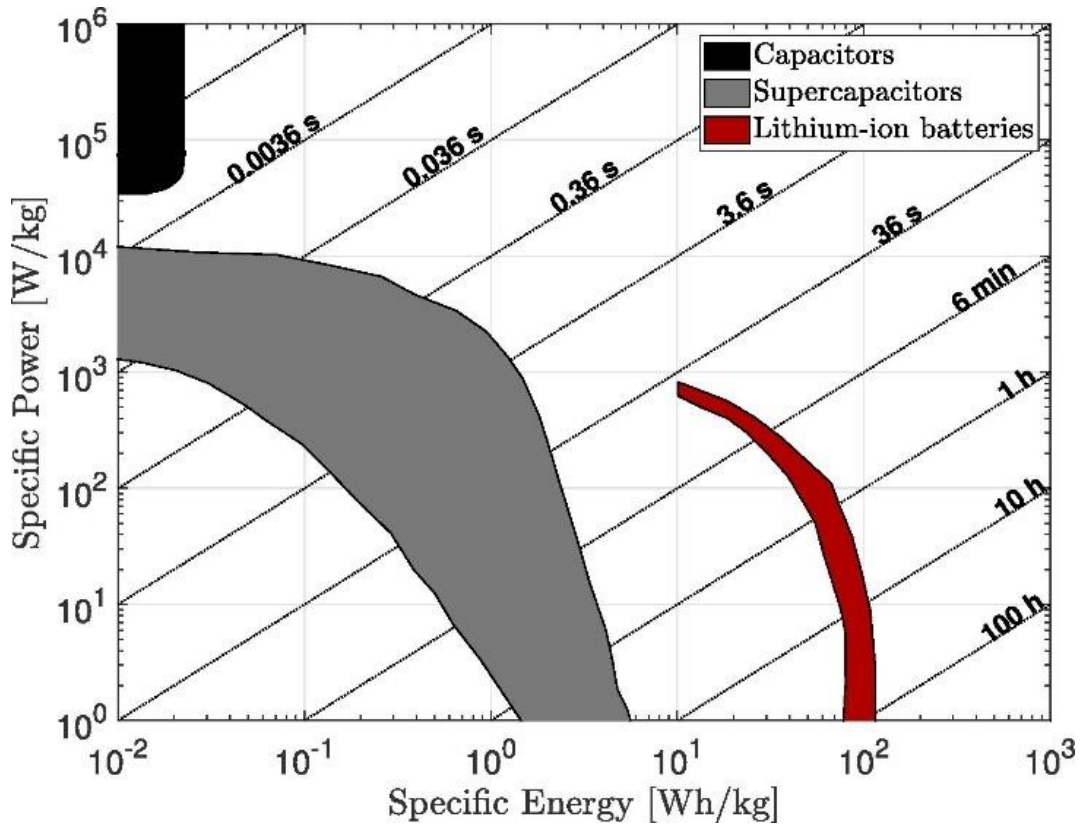
Figure 2. 1: *Ragone plot showing specific power as a function of specific energy for various energy storage devices [18].*

Supercapacitor technology has been applied in a diversity of areas such as in military applications, in energy recovery storage such as the windmills where they are used as the source of power for the motors, in portable electrical gadgets, and in medicine where SCs have been incorporated into pacemakers. In transport, it is applied in vehicles such as trams, racing cars and forklifts which helped significantly decrease fuel consumption [62].

2.2. Evaluating the performance of supercapacitors

The goal in synthesizing a supercapacitor device is to come up with a high specific energy and specific power. Specific energy (E_S) also known as gravimetric energy density, is best measured

in Wh kg^{-1}. The specific power is the rate of energy delivery with the unit of W kg^{-1}. The maximum power that can be delivered by the device is obtained from the maximum power transfer theory which states the maximum power is delivered when the load resistance matches the internal resistance of the power source [63]. It depends on the cell potential and equivalent series resistance (ESR). These relationships are shown in equations (2.1) to (2.3).

$$E_S \, [Wh \, kg^{-1}] = \frac{1}{7.2} C_S V^2 \tag{2.1}$$

$$P_S \, [W \, kg^{-1}] = \frac{3600 \times E_S}{\Delta t} \tag{2.2}$$

$$P_{max} \, [W \, kg^{-1}] = \frac{V^2}{4mR_s} \tag{2.3}$$

where C_S is the specific capacitance in (F g^{-1}), V is the cell potential and R_S is the ESR, Δt is the discharge time (s). From these equations, it is evident that to improve the specific energy of a supercapacitor without reducing the power delivery, the specific capacitance and cell potentials should be increased while the ESR is minimized.

2.3. Classification of supercapacitors

Supercapacitors can be categorised into three groups (figure. 2.2) depending on the charge storage mechanism.

- The electric double layer capacitors, (EDLCs) store energy through the accumulation and separation of charge at the electrode/electrolyte interface [64]. These do not involve chemical reactions.

- Pseudocapacitors/Faradaic capacitors store charge chemically through rapid and reversible redox reactions [65].

- Hybrid capacitors involve the EDLC and the pseudocapacitive energy storage mechanisms [66]. These are further classified into different types such as asymmetric capacitors and battery-type capacitors.

Factors which determine the performance of an SC include the electrode material, the electrolyte, the device assembly, and the energy storage mechanisms.
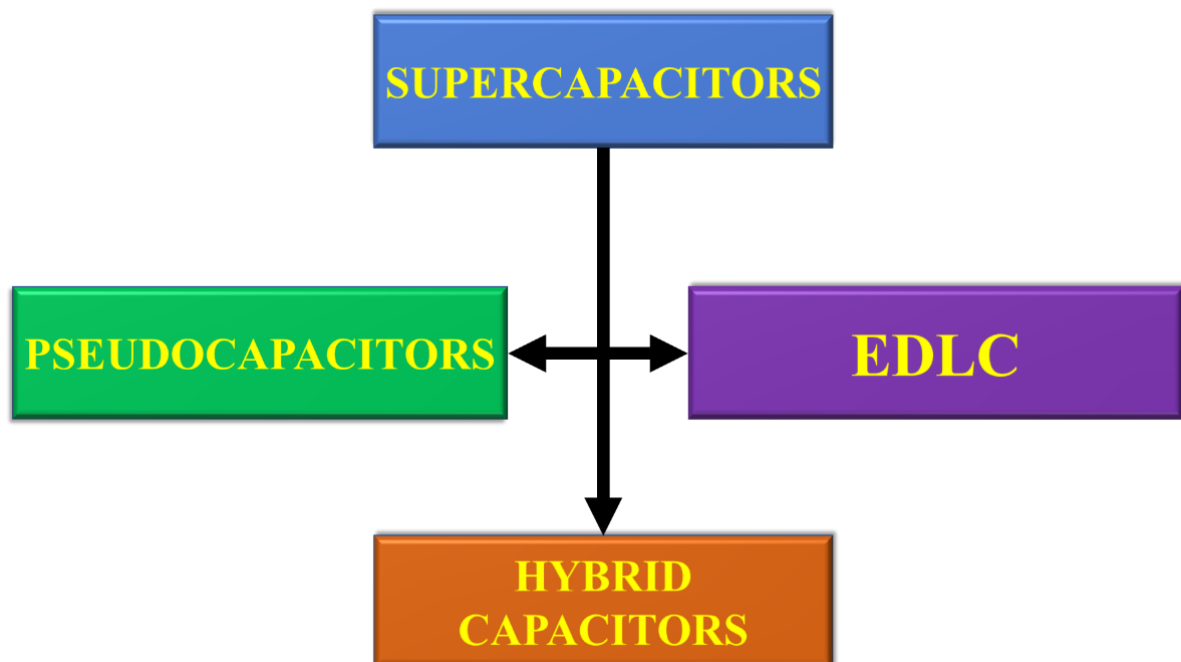
Figure 2. 2: *Classification of supercapacitors and their combination to form hybrid capacitors.*

2.4 Energy storage mechanism of a supercapacitor

2.4.1. Electric double-layer capacitance (EDLC)

In EDLC, the storage of energy occurs electrostatically at the electrode-electrolyte interface through the formation of a pair of layers consisting of oppositely charged ions when a voltage is applied [67]. This pair of layers are separated by a layer of solvent molecules which attaches to the electrode as shown in figure 2.3 (a). This ensures that the separation of the charge's layers remains unchanged. This double layer whose thickness is about 1-2 nm serves to block Faradaic charge transfer [68]. This model was first proposed by Helmholtz in 1853 [69]. When the applied voltage is less than the decomposition voltage, it has a linear dependence on the charge storage. Since the charge storage in EDLC is electrostatic, the capacitance is proportional to the dielectric constant such that the capacitance can be estimated using the relationship in equation (2.4) [70].

$$C_{EDLC} \ [F] \approx \frac{\varepsilon A}{d} \qquad\qquad (2.\ 4)$$

where C_{EDLC} is the capacitance (F), ε is the permittivity of the dielectric material (F m^{-1}), A is the surface area of the electrodes (m^2), and d is the separation distance of the double layer (m).

Louis Georges Gouy and David Lenard Chapman, modified this model to include the diffusion layer to incorporate ion mobility due to thermal motion to form a continuous distribution of ions which can be modelled using the Maxwell-Boltzmann statistics [71]. In this Gouy-Chapman model, the potential dropped exponentially from the electrode surface to the bulk of the electrolyte as shown in figure 2.3 (b). The model excludes the permittivity at the electrode/electrolyte interface and doesn't take into consideration the large accumulation of charges in the diffusive layer. One of the weaknesses of this model was that it overestimated the

capacitance [72]. It was Otto Stern who solved this problem in 1924 by combining both the Helmholtz and the Gouy-Chapman models. The Gouy-Chapman-Stern model separated the regions into two: The outer Gouy-Chapman diffusion layer (OHP) and the inner region, the inner compact Stern layer (IHP) as illustrated by figure 2.3 (c). From this model, the total capacitance is a result of the capacitance of these two regions in series as shown in equation (2.5) [73]:

$$\frac{1}{C_T} = \frac{1}{C_H} + \frac{1}{C_{diff}}$$

(2. 5)

where C_T, C_H, and C_{diff} represent the total capacitance, the Helmholtz capacitance, and the Gouy-Chapman capacitance respectively. In the Gouy-Chapman-Stern model, the finite size of the ions is accounted for and there are no interactions among ions from the electrodes and ions from the bulk of the liquid. This help to maintain the concentration of the electrolyte during the charge-discharge processes [74].
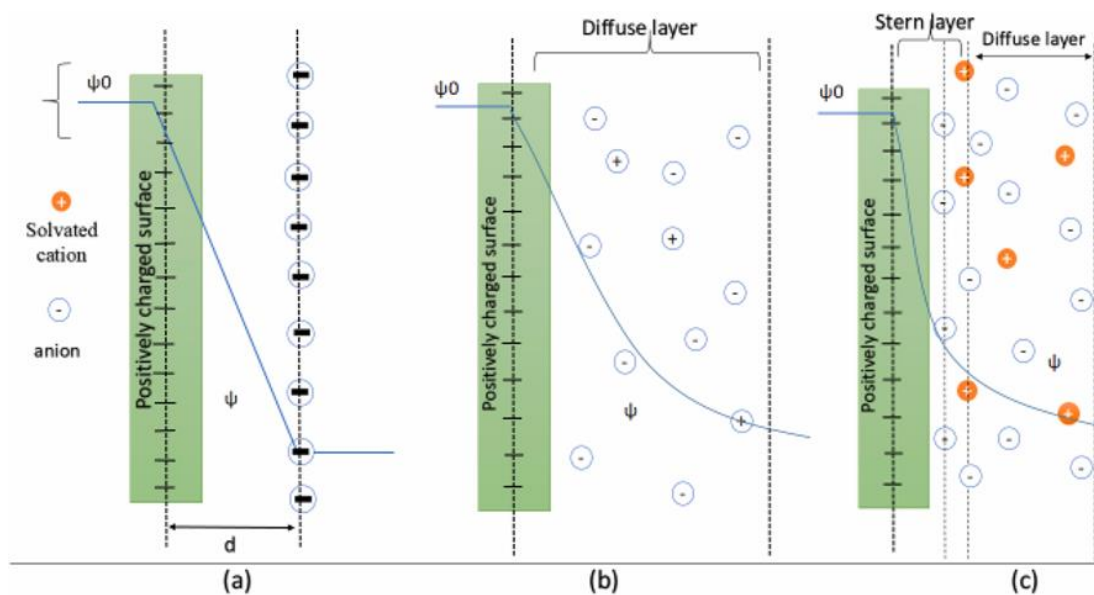
Figure 2. 3: Double-layer model showing the (a) Helmholtz model, (b) Gouy-Chapman model and (c) Stern layer [32].

21

For an EDLC device, the total capacitance is given by equation (2.6)

$$\frac{1}{C_T} = \frac{1}{C_A} + \frac{1}{C_B}$$ (2. 6)

where C_T is the total capacitance, and C_A and C_B are the capacitance of electrodes A and B, respectively.

- For an ideal EDLC device $C_A = C_B$, since the electrodes are identical, $C_T = C_A/2$.
- For hybrid capacitors with a pseudocapacitive electrode, C_B, then $C_A \ll C_B$ so $C_T = C_A$.

EDLC electrode materials are characterised by high specific surface area (SSA) and high chemical stability. These materials are mainly carbon materials such as graphene, carbon nanotubes (CNT), carbon aerogels and activated carbons. The power and energy density of EDLC can be enhanced by improving the specific capacitance of the device. These can be achieved using electrodes with high electrical conductance and electrolyte with high operation potential difference [75].

2.4.2. Pseudocapacitors

Pseudocapacitors store energy through electronic charge transfer between the electrolyte and the electrode. This occurs through a chain of fast and reversible redox reactions, intercalation or underpotential deposition. Redox reactions involve electronic charge transfer between the electrolyte and the electrode. Intercalation is the insertion of ions into the pores, tunnels, or inner layers of the bulk material by Faradaic processes without crystallographic phase transformation. Underpotential deposition refers to the electrodeposition of adsorbed monolayer(s) on the surface

of the electrode from metal ions and protons in the electrolyte [76]. Transitional metal oxides/hydroxides and conducting polymers are some of the materials which exhibit pseudocapacitive behaviour. The occurrence of multiple oxidation states (OS) in most of the transitional metal oxides endows them with capacities and energy which are at least ten times two more than those of EDLC [77]. Different types of reversible redox mechanisms in Faradaic capacitors are shown in figure 2.4.
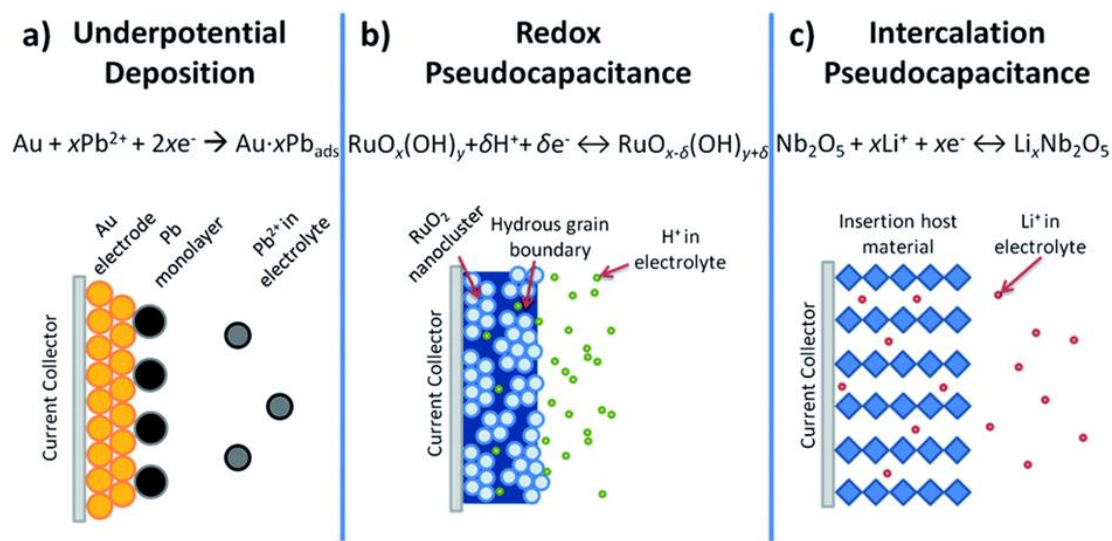
Figure 2. 4: *Different types of reversible redox mechanisms in Faradaic capacitors [36].*

2.4.3   Hybrid capacitors

Hybrid capacitors combine both pseudocapacitors and EDLC to produce energy storage devices with high electrochemical performances. Here, the EDLC behaviour contributes high electrical conductivity and wider operating potentials leading to high specific power whereas pseudocapacitive behaviour endows the device with high specific capacity leading to high specific energy. Hybrid capacitors have received a lot of attention in research because they take advantage of the synergistic effect of different energy storage to enhance specific energy while

the specific power remains uncompromised. The most common type of hybrid capacitors is the asymmetric capacitor where one electrode has a pseudocapacitive behaviour while the other has EDLC behaviour. It can also be fabricated through the synthesis of the composite electrode which combines EDLC, usually carbon materials with pseudocapacitive electrode materials such as transitional metal oxides or conducting polymers [78]. Furthermore, it can be produced from battery-type materials. Here, carbon-based electrode material and metal oxide operate in one cell [79]. The classification of material used in hybrid capacitors is illustrated in figure 2.5.
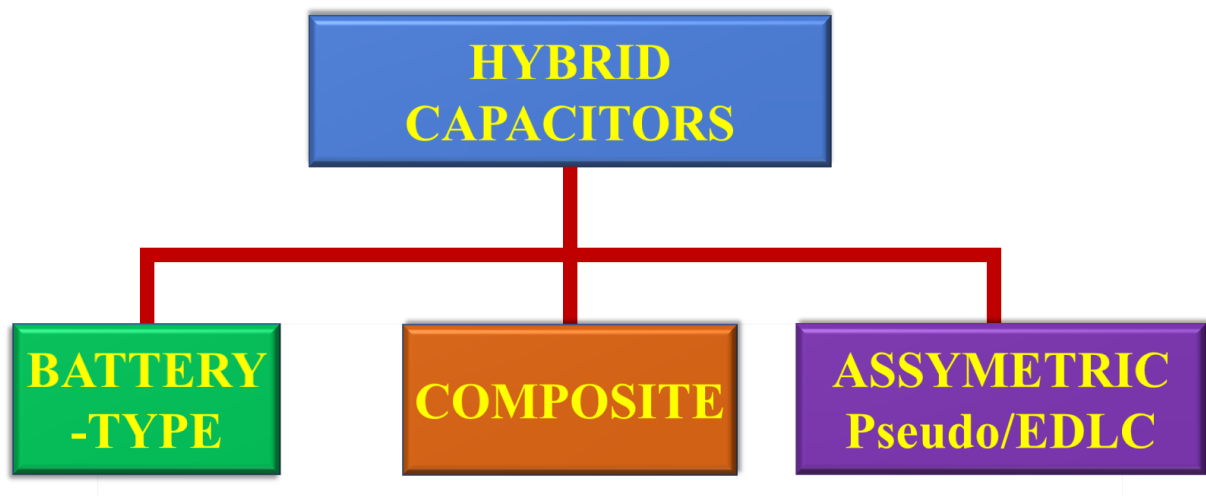
Figure 2. 5: The classification of hybrid capacitors according to the material.

2.5 Electrode materials for supercapacitors

The main components of a supercapacitor include electrode material, electrolyte and a separator [80]. To enhance the electrochemical performance of a supercapacitor device, the electrode material plays a very important role and the selection of the electrode is very crucial [81]. For a device to provide high specific energy and power, the electrode materials need to have a large specific surface area, minimal internal and ohmic resistance, short diffusion lengths and small pore volume [82]. Other important properties to be considered for the choice of electrode material include low cost, easy availability/extraction, environment benignity and low weight

24

and volume [83–85]. There are four main types of electrode materials for a supercapacitor: Carbon-based, transitional metal oxides/hydroxides, conducting polymers and composites (hybrid electrodes) [86].

2.5.1 Carbon electrode materials

Carbon materials are the most utilized class of electrodes for supercapacitors [87]. Carbon-based materials are materials which have different properties due to the local bonding of their carbon atoms. This is because of some favourable properties such as easy availability, non-toxicity, large specific surface areas in the range of 1000-3500 m^2 g^{-1}, high electrical conductivity, high chemical stability, and wide operating potential window and temperature [88–90]. Carbon materials are also versatile as they appear in various forms such as powder, monoliths, mats, fibres, felts and foils [91]. The energy storage in carbon material electrodes occurs through the formation of an electric double layer at the electrolyte/electrode interface. There are ways which can be employed to improve the specific capacitance of the carbon electrodes. These include increasing the porosity of the electrode, increasing the specific surface area of the carbon material and introduction of the functional groups on the surface of the electrode [92,93]. Since energy storage occurs at the surface of the electrode, increasing the specific surface area improves the accumulation of charges. This helps to improve the specific capacitance of carbon materials which is significantly lower than that of transitional metal oxides. The presence of functional groups on the surface of carbon materials stimulates the Faradaic redox reaction causing the capacitance to improve [94]. The hydrophilicity and wettability of the carbon surfaces are improved through the introduction of oxygen functional groups. The carbon materials which has become very popular in the fabrication of supercapacitor electrodes are graphene and activated carbon [95].

Graphene is a 2-D allotrope of carbon whose lattice structure consists of sp^2 carbon atoms at the vertices of the hexagonal lattice structure [96]. Synthesis approaches for graphene include, chemical vapour deposition (CVD), exfoliation, Hummer's method and micro-wave assisted synthesis. The CVD method is where thin films are grown on the substrate through a chemical reaction where the precursors of the film are in the gaseous compounds. The Hummers' method is a chemical process that can be used to generate graphite oxide through the addition of potassium permanganate to a solution of graphite, sodium nitrate, and sulfuric acid. Microwave-assisted synthesis works based on aligning dipoles of the material in an external field via the excitation produced by microwave electromagnetic radiations. Some of the attributes of graphene include good thermal and cyclic stability, large specific surface area and large electrical conductivity [97]. These attributes are due to low diffusion lengths, the existence of functional groups, good pore size distribution, great mechanical strength, the existence of functional groups and a wide potential in different types of electrolytes. However, the theoretical specific surface area ($2630 \, m^{-2} \, g^{-1}$) is greatly reduced by restacking and agglomeration [98]. The electrochemical performance can be greatly enhanced by making composites with pseudocapacitive materials such as TMOs or doping with a heteroatom such as boron, nitrogen, sulphur, or phosphorus. Among the heteroatom dopants, sulphur is one of the most favourite as it improves wettability, reduces charge transfer resistance (CTR) and improves electrical conductivity due to its low electronegativity [99]. Mane et al. used a binder-free successive ionic layer adsorption and reaction (SILAR) route to synthesize silver-doped manganese oxide/graphene oxide composite films (Mn-Ag$_3$/GO). Mn-Ag$_3$/GO yielded a high specific capacitance of 877 F g^{-1} at a scan rate of 5 mV s^{-1} which was significantly higher than 786 F g^{-1} for the Mn-Ag$_3$ electrode without graphene oxide [100]. Javed et al. combined the binder -free hydrothermal reaction and phosphorization to synthesize nickel-cobalt phosphide nano-horns wrapped with phosphorous-reduced graphene oxide (NCP@P-rGO) with an excellent specific capacity of 264.9 mAh g^{-1} at

1 A g^{-1} [101]. This shows the compatibility of heteroatom-doped metal oxide with graphene for the improvement of the electrochemical performance of electrodes.

Activated carbon (AC) is a type of carbon material which has been processed using gas-absorbent activation agents such as potassium hydroxide (KOH), The successive activation steps used in the processing of the carbon materials cause a significant decrease in nitrogen, oxygen and hydrogen gases leaving behind a nanoporous network with tunable pore volume, porosity, and specific surface area tunable for various purposes [102]. Decreasing the pore size while increasing the specific surface help to increase specific capacitance of ACs [103]. It has also received a lot of attention in the research for supercapacitor electrode. This is due to many merits such as easy availability, environmental safety, and natural abundance. Very high SSA, wide potential window and electrical conductivity endow AC with favourable electrochemical attributes. Vinayagam et al. used physical activation of Syzygium cumini fruit shells (SCFS) for the fabrication of a symmetric supercapacitor with a high specific energy of 27.22 Wh kg^{-1} at a specific power of 200 W kg^{-1} [104]. Ouyang et al. designed composite materials of the nickel sulphide nanoparticles and activated carbon nanotubes (NiS/ACNTs) through a hydrothermal route and annealing, the NiS/ACNTs hybrid electrode delivered a high specific capacitance of 1266 F g^{-1} at a current density of 1.0 A g^{-1} [105]. These results exhibit the compatibility of AC for synthesizing composite electrodes and its contribution to the overall supercapacitor devices due to its merits.

2.5.2. Transitional metal oxides/hydroxides (TMOs/TMOHs)

Transitional metal oxides/hydroxides have received a lot of attention as electrode materials for supercapacitors. This is attributed to their very high theoretical capacities which leads to high specific energy in the devices [106–108]. It has been proved by theoretical calculations that the electronic structure of TMOs/Ohs can be tuned by co-doping thereby improving the electron

transport and electrical conductivity [109]. For improved electrochemical performance, TMOs/TMOHs need to be electrically conductive and be capable of existing in at least two oxidation states (OS) without phase change and their lattice should allow protons to intercalate and detach freely during redox processes. TMOs/TMOHs also have better electrochemical stabilities compared to conducting polymers [110]. RuO_2 is one of the TMOs with very promising pseudocapacitive behaviour due to high electrical conductivity, high stability, large specific capacitance and reversibility, however, scarcity and environmental toxicity have limited its application in electrochemical energy storage devices [111–113].

Spinels with mixed bimetallic oxides possessing a chemical structure of AB_2O_4 have attracted a lot of interest in the investigation of positive electrode materials for pseudocapacitors. This is because spinels, besides their natural abundance, have higher electrical conductivities, more abundant redox reactions, higher electrochemical activity and higher theoretical capacities than oxides of monometallic A and B [114]. Recently, manganese-based spinels have generated a lot of enthusiasm for energy storage devices. This is credited to the ability of manganese to exist in multiple oxidation states and also the Jahn-Teller distortion increases ion diffusion and facilitates more phase transformation [115].

TMOHs such as $Ni(OH)_2$ and $Co(OH)_2$ are often used as electrodes for battery-type capacitors due to their natural abundance and affordability, however, they have limited diffusion pathways and low intrinsic conductivities ($\approx 10^{-5}$ to 10^{-8} S.cm^{-1}) [116]. This leads to experimental-specific capacities which are much less than the theoretical capacities. To alleviate the challenge hybrid hydroxides can be used instead since they benefit from the synergetic effect of multiple components.

One form of these hybrid hydroxides is the layered double hydroxides (LDHs). LDHs also known as hydrotalcite-like anionic clays have a general formula $[M_{1-x}^{2+} M_x^{3+}(OH)_2]^{x+}(A^{n-})_{\frac{x}{n}}.mH_2O$, where M^{2+} and M^{3+} are divalent and trivalent metals

respectively, x $=M^{3+}/(M^{2+}+M^{3+})$ is the proportion of the divalent metal M^{3+} and also the layer charge density, A^{n-} is the interlaminar organic or inorganic anion to balance the charges [117]. They benefit from a unique 2-D layered structure, more redox active and more electrical conductivity compared to monometallic hydroxides. Cobalt-nickel layered hydroxide (CoNi-LDH) has generated a lot of attention due to its high theoretical specific capacity, high SSA, large interconnected networks, high redox reversibility, tunable chemical composition, abundant electrochemical active sites, phenomenal ion exchange as well as synergistic effects between bimetallic ions [118–120].

CoNi-LDH however suffers from low electrical conductivity and aggregation of materials which impedes ion transport resulting in a lower experimental capacitance [121]. These challenges can be alleviated by the synthesis of composites of CoNi-LDH with conductive materials such as graphene and/or engineering the design of the electrode material through the inclusion of other redox active metal oxides such that the aggregation of CoNi-LDH is prevented, and the ion and electron transport is improved. Yang et al. used a solvothermal technique to grow NiCo-LDH nanostructure anchored onto KCu_7O_4 nanowires and applied this structure as an electrode material for supercapacitors. KCu_7S_4 nanowires act as a dependable "skeleton" for supporting the NiCo-LDH nanosheets, thus preventing the aggregation of NiCo-LDHs and improving their conductivity. The KCu_7S_4@NiCo-LDH yielded a high specific capacity of 122.7 mAh g^{-1} at a specific current of 2 A g^{-1} [122]. Liang et al. fabricated a hierarchical $NiCo_2O_4$@NiCo-LDH core-shell structure on carbon cloth through a hydrothermal strategy and an electrodeposition step. The core-shell structure facilitated electron and ion transport. This gave the composite electrode a great areal capacitance of 6092 mF cm^{-2} which was significantly larger than the areal capacitance of $NiCo_2O_4$ and NiCo-LDH which were 870 and 3408 mF cm^{-2}, respectively [123]. Zou et al. used the microwave synthesis to prepare a honeycomb-like Ni-Co LDH nanosheets on

graphene (Ni-Co LDH/G) composite. The presence of graphene helped alleviate the low intrinsic conductivity of Ni-Co LDH and achieve phenomenal capacity retention of 87.1% which was significantly higher than that of Ni-Co LDH which was only 50.5 % [124]. The performance of CoNi-LDH can be improved by creating multidimensional hierarchical electrode materials with metal oxides [125]. A comparison of other reports from the literature on CoNi-LDH materials tested in a three-electrode (half-cell) configuration is provided in table 2.1.

Furthermore, the integration of carbon material into the layered double hydroxide has proved to enhance the electrochemical performance of a supercapacitor device. For example, Chang et al. designed a reduced graphene oxide@cobalt nickel sulfide@nickel cobalt layered double hydroxide composite (rGO@CoNi$_2$S$_4$@NiCo LDH) with a p-n junction structure. The Faradic activities of both components were enhanced due to the charge redistribution across the p-n junction enabling the composite electrode to a huge specific capacity of 364 mAh g^{-1} at 1 A g^{-1} while maintaining a large capacity retention of 77 % [126]. Wang et al. used the hydrothermal reaction and phosphorization treatment to grow a hybrid material with FeNiP and CoNi-LDH nanosheets. The 3D interconnected nanosheet array architecture hierarchical pore structure, and abundant active sites with multiple valances, provide rapid electron and mass transfer channels within its conducive network. This enabled the binder-free electrode to possess a large specific capacity of 285.1 mAh g^{-1} at 1 A g^{-1} maintaining a large capacity retention of 70.4 % after 5, 000 galvanostatic charge-discharge (GCD) cycles [127]. Archarya et al. prepared a 3D porous and hierarchical zinc−nickel−cobalt (ZNCO)@Co−Ni-LDH (LDH-1 and LDH-2) core−shell nanostructured arrays on Ni foam as a pseudocapacitive electrode by using a facile hydrothermal and metal−organic framework (MOF) assisted co-precipitation method. Due to the fast and efficient transmission/transfer of both electrolyte ions and electrons, due to the higher electroactive surface areas and enhanced electrical conductivity, the ZNCO@Co−Ni-LDH-2 electrode material delivered an excellent electrochemical performance with a higher specific

capacity of 398.1 mAh g^{-1} at 1 A g^{-1} with an ultrahigh capacity retention of 68.35% at a higher current density of 10 A g^{-1} [128].

From table 2.1 and the examples cited above, LDH materials consisting of Ni and Co improve their electrochemical performance significantly when attention is given to the design of its composite with material that enhances ion and electron transport prevents aggregation, and provide more abundant redox active sites. Therefore, CoNi-LDH has opted for this research as the main material and its composite materials incorporated mainly spinels containing Mn, Co, and Cr. To improve the electrical conduction of CoNi-LDH, reduced graphene oxide enhanced by sulphur heteroatom dopant (sulphur reduced oxide (RGO-S)) was selected. The positive electrode materials for this research were Hausmannite sulphur reduced graphene oxide cobalt nickel layered double hydroxide (MO/RGO-S-50@CN), manganese cobaltite cobalt nickel layered double hydroxide composite (MCO-2.5@CN-LDH) and manganese chromite cobalt nickel layered double hydroxide (MnCr$_2$O$_4$@CoNi-LDH).

Table 2.1: Electrochemical performance of different CoNi-LDH based materials in a three electrode configuration.

CoNi-LDH based material	Electrolyte	Specific current (A g^{-1})	Specific capacity (mAhg^{-1})	Number of cycles	Capacitance retention (%)	Ref.
NCO@Ni-Co-LDH	2M KOH	1	362.1	5,000	89.0	[129]
Co$_1$Ni$_4$LDHs/SCNTF	3M KOH	1	165.3	5,000	81.0	[119]
CNT/Co$_3$S$_4$@NiCoLDH	6 M KOH	1	206.7	7,000	90.0	[130]
P@NiCo LDHs	6 M KOH	1	148.9	5,000	55.9	[131]
CoNi LDH-6	2M KOH	1	216.6	3,000	87.2	[132]
MnO$_2$@Co-Ni LDH	1M KOH	1	199.4	10,000	96.1	[125]
ZNCO@Co−Ni-LDH-2	2M KOH	1	398.1	8,000	68.4	[128]
Co$_{0.2}$Ni$_{0.8}$(OH)$_2$	3M KOH	1	221.1	2,000	79.9	[133]
rGO@CoNi$_2$S$_4$@NiCoLDH	2M KOH	1	363.4	5,000	77.0	[126]
Co$_3$O$_4$@CoNi LDH	2M KOH	0.5	371.8	10,000	67.7	[134]
FeNiP@CoNi-LDH	2M KOH	1	285.1	5,000	70.4	[127]
CoNi-LDH4	6 M KOH	1	182.5	5,000	99.9	[135]
(NiCo-LDH)$_{SHH}$	6 M KOH	1	196.1	5,000	86.0	[136]
CoNi-LDH@PCPs	1M KOH	1	397.3	10,000	94.2	[137]
CC/NiCoP@NiCo-LDH	PVA/KOH	0.9	271.0	5,000	81.1	[120]
Co$_3$O$_4$/NiCo-LDH	6 M KOH	1	296.4	10,000	88.4	[138]
MnCo$_2$O$_4$@NiCoLDH/NF	6 M KOH	1	569.4	5,000	78.7	[139]
CN-LDH@NCS NSs	6 M KOH	1	384.9	6,000	75.2	[140]
Co$_3$O$_4$@Ni–Co LDH/NF	KOH/PVA	1	296.9	5,000	67.9	[141]

2.5.3. Conducting polymers (CPs)

Due to their high electrical conductivity in a doped state, high voltage window porosity, low ESR, large pseudocapacitance, high intrinsic flexibility, light-weight, low cost and reversibility, conducting polymers have been utilized as electrode material for supercapacitor devices [142,143]. Polyaniline (PANI), polypyrrole (PPY), poly(3,4 ethylene dioxythiophene) (PEDOT) and polythiophene (PT) are some of the CPs commonly used in energy storage [144]. Methods for the synthesis of polymers include polymerization and electropolymerisation of their monomers [145]. The high content of the functional group is the source of the redox reactions that leads to their energy storage. The ions drift from the electrolyte along the conjugated backbone of the polymer during the process of oxidation, and they move in the reverse direction during reduction [146]. CPs have high SSA and short pathways for mass/charge transfer [147]. The main draw-back for CPs is the swelling and shrinking which occurs during the processes of charge-discharge which reduces the electrochemical performance of the electrodes [148,149].

2.5.4. Composites

EDLC materials have the potential to possess high specific power and long cycling stabilities due to a combination of high SSA, high operating voltages and electric conductivity [150]. However, the electrostatic charge storage mechanism limits their charge storage which limits their specific energy and their low electrode density result in low volumetric capacitance [151]. On the other hand, pseudocapacitors (PS) are capable of high specific energy due to the Faradaic reactions. The low electric conductivities however limit their electron transport property [152]. The combination of PS and EDLC synthesized into composite material benefits from the favourable attributes of different materials [153]. In this thesis, the incorporation of an EDLC material such as graphene into TMOs and TMOHs such as Mn_3O_4 and CoNi-LDH helps to

improve the electrical conductivity and the SSA of the resulting composite. The PS also help to reduce graphene's restacking and improve charge storage.

2.6. Electrolytes

The electrolyte is one of the most important components of a supercapacitor device [154]. In a full-cell configuration, the electrolyte is between the electrodes so that the ions pass through a separator, while in a half-cell set-up, the counter electrode, reference electrode and working electrodes are immersed in the electrolyte. There are several parameters to be considered for the optimal performance of an electrolyte. These are high ionic conduction, high electrochemical stability, wide operating voltages, low toxicity, low volatility, high purity, low ionic radius, low cost, and high ionic concentration [155]. For high power transfer of supercapacitor, the operating voltage should be high, and the equivalent series resistance (ESR) should be low as shown in equation (2.3). The high ionic conductivity of an electrolyte leads to low ESR enabling the device to have high power output. The ionic conduction is in turn influenced by ionic concentration and mobility inside the electrolyte [156]. These two parameters depend on the ability of the salts to dissolve into the solvents and how much they can dissociate in their dissolved form. There are three types of conventional liquid-state electrolytes. These are:

1. Aqueous electrolytes (AE)
2. Ionic electrolytes (IE)
3. Organic electrolytes (OE)

2.6.1. Aqueous electrolytes (AEs)

Due to their facile preparation method, low cost and environment friendliness, aqueous electrolytes are the most utilized in supercapacitors [157]. AEs are classified as neutral

electrolytes such KNO$_3$, basic electrolytes such as KOH, and acidic electrolytes such as H$_2$SO$_4$. Additional properties which make AEs more suitable in supercapacitors include non-flammability, low volatility, and high ionic conductivity due to low ionic radius and excellent concentration [158]. Some drawbacks of AEs arise due to the limitation of the working potential to a theoretical value of 1.23 V due to oxygen evolution reactions [159,160]. This makes the specific energies of AEs to be inferior to ionic and organic electrolytes. However, the maximum working potential can be increased due to the synergetic effect of the AEs with the electrode material [161]. For example, Pappu et al. used the direct current (DC) and the pulsed electrodeposition (PED) modes of electrodeposition of MnO$_2$. An optimized concentration of 0.1 M KI in electrolyte yielded a specific capacitance of 134 F g^{-1} at 3 A g^{-1} with an active voltage window of 2.2 V and excellent capacity retention of 83.3% for 10,000 continuous GCD cycles [162]. The devices in this thesis benefitted from the synergistic effect of the electrode materials and the optimized 2M KOH aqueous electrolyte to achieve enhanced properties for supercapacitor application.

2.6.2. Ionic liquid electrolytes (ILEs)

Ionic liquids are molten salts which consist of organic cations and counter anions. One of their main advantages which makes them favourable for high-energy supercapacitor devices is their wide operating potential (2-6 V) [163]. Typical examples of ILEs are cyclic amines such as imidazolium and quaternary ammonium salts such as [R$_4$N]$^+$. ILEs benefit from low volatility, non-flammability and low vapour pressure [164]. However, the use of ILEs is limited by their higher costs compared to AEs, the high viscosity at low temperatures which retards ion mobility and penetration into the pores of the electrodes which leads to the reduction in the specific capacitance of the SC devices [165]. ILEs also suffer from low electrical conductivity which

contributes to high ESR, this in turn reduces the power delivery of the devices. Solvents such as acetonitrile can be added to decrease the viscosity and improve their electrical conductivity [166]. Another factor which leads to the limitation of the use of ILEs in SC devices is their low chemical stabilities.

2.6.3. Organic electrolytes (OEs)

Another type of electrolyte is the organic electrolyte, which consists of conducting salts such as hexafluorophosphate (PF_6^-) anions dissolved in organic solvents such as carbonate (PC) tetramethylammonium (Et_4N^+) [167]. Some of the most familiar OEs are acetonitrile (ACN), tetramethylammonium borate (TEA BF4), propylene carbonate and their mixtures [168]. OEs have superior operating potential (≈ 3.5 V) compared to AEs [169]. This attribute, combined with low viscosity leads to an improvement in the specific energy and power. The use of OEs in SC devices is however hampered by specific capacitance which is much lower than those of AEs. Their high flammability, toxicity, volatility and environmental unfriendliness restrict their applications only to controlled environments [170].

2.7 Electrode fabrication, testing and performance evaluation of the electrode materials

2.7.1. Electrode fabrication

The method used for the fabrication of an electrode depends on the nature of the current collector (CC) and/or the state of the electrode and the fabrication method of the electrode. If the electrode is not synthesized directly onto the CC, there is a need to use polymeric binders to enable the active material (AM) to stick to the substrate of the CC. However, the addition of the binders decreases the electrical conductivity of the AM and the loss in conductivity has to be

compensated by the addition of conductive additives [171]. The most common binders for electrode material which are in powder form are polytetrafluoroethylene (PTFE) and polyvinylidene fluoride (PVDF) [172]. Carbon acetylene black (CAB) often serves as the conducting additive. The AM, binder and conducting additive are mixed in a ratio of 8:1:1. However, a slight deviation from this ratio may help to optimise the performance in different scenarios. The mass loading of the active material also plays an important role in the performance of the active materials, the larger mass of uniformly distributed nanomaterials affects the operating current leading to great electrochemical performance [173]. To turn the mixture into a homogenous slurry which can be pasted on the substrate, a few drops of N-methyl-2-pyrrolidone (NMP) solvent are added. Nickel foam (NF), copper foam, aluminium foil, carbon paper and carbon fabric (CF) are some of the CCs which are often used [174]. Metallic CC such as NF cannot be used in acidic electrolytes such as HCl because they become unstable due to corrosion. In that case, acid-resistant CC like carbon paper can be used instead [175]. When the electrode material is deposited directly onto the substrate during synthesis using methods such as successive ionic layer adsorption and reaction (SILAR method) and electrodeposition, binders and conductive additive is not needed. In this work binder-free electrodeposition was used to deposit the electrode materials on the NF substrate. This helped to eliminate the resistance of polymeric binders.

2.7.2. Electrochemical configurations and evaluation for SC electrode materials

2.7.2.1. Three-electrode configuration

The electrochemical performance of an electrode is first evaluated using a half-cell configuration also known as a three-electrode set-up. The primary goal of this configuration is to determine the properties of the electrode material such as the charge storage mechanism, appropriate

electrolyte to use, operating potential range, ESR and cycling stability [176,177]. The half-cell set-up comprises the working electrode (WE), the counter electrode (CE), the reference electrode (RE), and a suitable electrolyte, as shown in figure 2.6.

The WE consist of the AM on the CC; this is the electrode under study. The RE serves to enable the measurement of potential differences while blocking the flow of current. The RE is usually made from silver/silver chloride (Ag/AgCl), mercury/mercury oxide or saturated calomel which have standard known electrode potentials. The CE balances the circuit by varying the potential to adjust the current produced by the WE [178]. Platinum (Pt), graphite rods and glass carbon are normally used as CE because of their chemical uncreativeness [179].
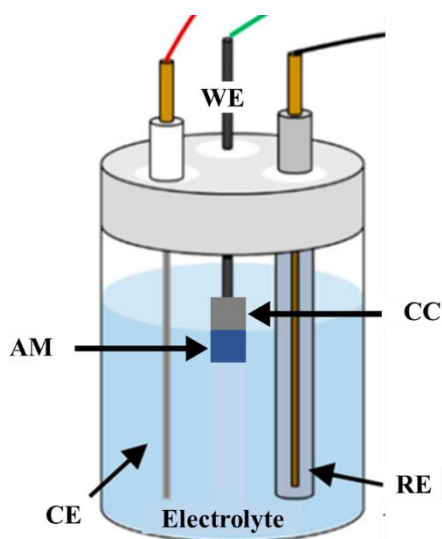
Figure 2. 6: *Schematic diagram of three electrode set-up [127].*

2.7.2.2 Two-electrode configuration

The two-electrode configuration which is also known as the full cell set-up consists of a pair of positive and negative WEs inside an electrolyte electrically insulated from each other by a separator. In symmetric devices, the WEs are similar whereas, in an asymmetric device, these WEs are different [180]. The full cell can be assembled in form of a T-Cell, Swagelok or a coin

cell which is shown in figure 2.7 [181]. Specific power, specific energy, and cyclic stability can be evaluated in the two-electrode configuration.
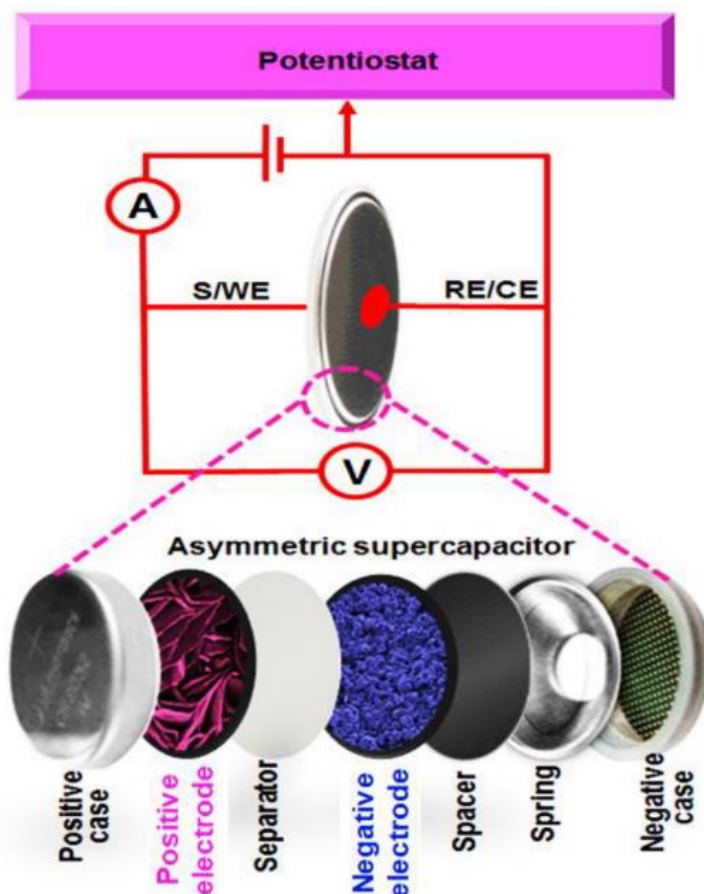
Figure 2. 7: Schematic diagram of two electrode set-up.

2.7.3. Electrochemical performance evaluation

To evaluate the electrochemical performance of the electrode in both two and three-electrode configurations, there are important tools that should be employed. These are cyclic voltammetry (CV), galvanostatic charge-discharge (GCD), electrochemical impedance spectroscopy (EIS) and some stability evaluations [182].

2.7.3.1 Cyclic voltammetry (CV)

Cyclic voltammetry is one of the most important tools for evaluating supercapacitor electrodes and devices in both two and three-electrode set-ups. The CV is useful in determining the charge storage mechanism that occurs at the surface of the electrode, the level of reversibility of the reactions and the reaction kinetics at the WE [183]. These are displayed as cyclic voltammograms which are plots of WE current as a function of applied voltage as shown in figure 2.8. For pure EDLC behaviour, the voltammogram is rectangular whereas the shape deforms into a parallelogram when the electrode is resistive [184–186]. Pseudocapacitance behaviour introduces highly reversible and broadened peaks in the quasi-rectangular voltammograms. Battery-type capacitors are synonymous with well-defined peaks. These peaks reflect the accumulation of charges due to Faradaic redox reactions [187]. The CV provides a way to determine the operating potential for a particular electrode.
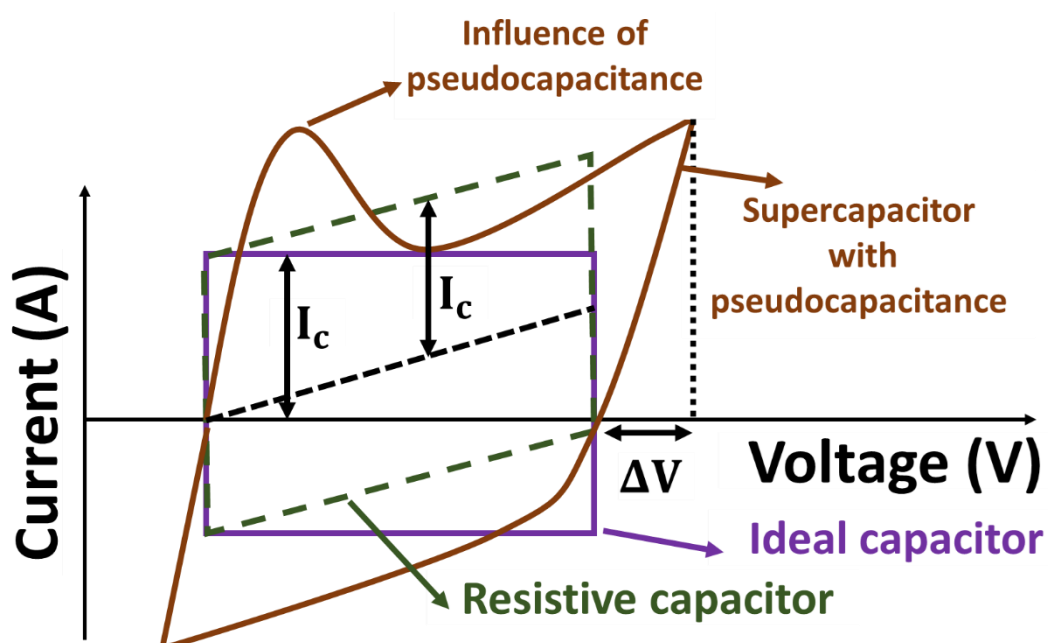
Figure 2. 8: CV curves showing the different between ideal capacitor (EDLC), resistive

For reactions characterised by redox reactions, the shape of the curve and the peak current is due to the Randles- Sevcik equation displayed in equation (2.7).

$$i_p \, [A] = 0.4463nFAC \frac{\sqrt{nFvD}}{RT}$$

(2.7)

where i_p is the peak current (A), n is the number of electrons transferred in the redox event (usually 1), A is the electrode area in cm^2, F is the Faraday Constant in (C mol^{-1}) D is the diffusion coefficient (cm^2/s), C is the concentration (mol/cm^3), v is the scan rate (V/s), R is Gas constant (J K^{-1} mol^{-1}), T is the temperature in K.

Specific capacitance (C$_S$) and specific capacity (Q$_S$) can be determined using CVs in both two and three-electrode set-ups. In general, for a three-electrode set-up, C$_S$ is obtained using equations (2.8) [188]:

$$C_S \, [F\,g^{-1}] = \frac{q_S}{\Delta V} = \frac{1}{v \Delta V} \int I_S(V) dV$$

(2.8)

Here q_S is the total charge stored per unit mass (C g^{-1}), ΔV is the maximum potential (V), v is the scan rate (V s^{-1}), I$_S$ (V) is the specific current (A g^{-1}) which is a function of applied potential (V). It can be shown, for ideal EDLC behaviour with a perfect rectangular voltammogram, the specific capacitance is the ratio of the specific current to the scan rate as shown by equation (2.9):

$$C_S \, [F\,g^{-1}] = \frac{I_S}{v}$$

(2.9)

41

For a device, in a two-electrode configuration, the specific capacitance of the cell is obtained using equation (2.10) [189].

$$C_S(\text{cell}) \ [\mathbf{F \ g^{-1}}] = \frac{q_S}{V} = \frac{1}{2vV} \int_0^V I_S(V)dV \qquad (2.10)$$

CV can also be used to calculate the specific energy (E_S) and specific power (P_S) using equations (2.11) and (2.12).

$$E_S \ [\mathbf{W \ h \ kg^{-1}}] = \frac{V}{3.6 \ v} \int_0^V I_S(V)dV \qquad (2.11)$$

$$P_S \ [\mathbf{W \ kg^{-1}}] = 1000 \ V \int_0^V I_S(V)dV = \frac{E_S}{3600v} \qquad (2.12)$$

2.7.3.2 Galvanostatic charge-discharge (GCD)

Galvanostatic charge-discharge which is also referred to as chronopotentiometry displays a plot of potential as a function of times when constant charging and discharge currents are applied. It accurately replicates the charging and discharging processes. GCD is considered one of the most reliable ways to determine the maximum operating potential for a device or electrode in a particular electrolyte [190]. The interpretation of the discharge curve can be employed to determine the reaction mechanisms taking place in a half or full-cell set-up as shown in figure 2.9:
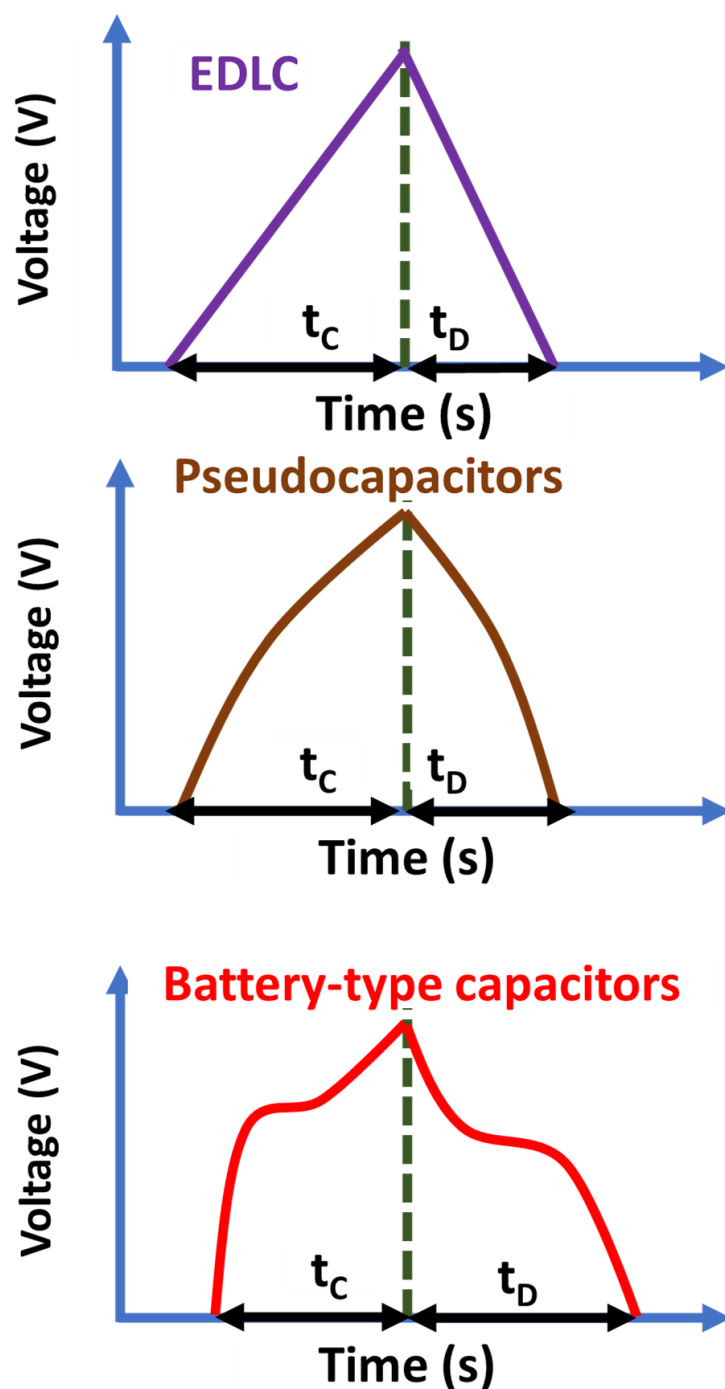
Figure 2. 9: *GCD discharge curves for a typical EDLC, pseudocapacitance and GCD profile for battery materials.*

For EDLC materials, the discharge follows a straight line [191], and it can be deduced that the capacitance is independent of the potential. The discharge exhibit non-linear behaviour in battery-type materials such as Ni(OH)$_2$ [192]. Prominent plateaux are signifying that the

capacitance varies with potential reaching maxima at the plateaux denoting the accumulation of charge during Faradaic redox reactions [193].

The specific capacity (Q_S) can be determined from the discharge segment of the GCD as shown in equation (2.13) for any charge storage mechanism. However, for ideal EDLC behaviour the specific capacitance C_S instead, is determined using equation (2.14).

$$Q_S \, [\mathbf{mAh \, g^{-1}}] = \frac{1}{3.6} \times I_S t_D \tag{2.13}$$

$$C_S \, [\mathbf{F \, g^{-1}}] = \frac{1}{V} \times I_S t_D \tag{2.14}$$

where V is the peak voltage (V). Before assembling a device, it is essential to ensure that the charge on both electrodes balances each other, $Q_+ = Q_-$ to achieve high electrochemical performance [194]. This is achieved by adjusting the ratio of the electrode masses as shown in equations 2.14-2.16. These equations (2.15-2.17) can be used for any type of device, symmetric EDLC device, and asymmetric device with linear and non-linear GCD in the negative and positive electrodes, respectively [195–197].

$$\frac{m_-}{m_+} = \frac{Q_{S+}}{Q_{S-}} \tag{2.15}$$

$$\frac{m_-}{m_+} = \frac{C_{S+}\Delta V_+}{C_{S-}\Delta V_-} \tag{2.16}$$

$$\frac{m_-}{m_+} = \frac{3.6\, Q_{S+}}{C_{S-}\Delta V_-} \tag{2.17}$$

The specific energy and power can be determined very accurately from the GCD curve using equations (2.18) and (2.19).

$$E_S\, [Wh\, kg^{-1}] = \frac{I_s}{3.6}\int_0^V V(t)\, dt \tag{2.18}$$

$$P_S\, [W\, kg^{-1}] = 1000 \times \frac{I_s}{t_D}\int_0^V V(t)\, dt = 3600 \times \frac{E_S}{t_D} \tag{2.19}$$

For ideal EDLC charge/discharge, the energy determination can be obtained using equation (2.20):

$$E_S\, [Wh\, kg^{-1}] = \frac{I_s}{3.6} \times \frac{1}{2}Vt_D = \frac{1}{7.2} \times C_S V^2 \tag{2.20}$$

2.7.3.3 Electrochemical Impedance spectroscopy (EIS)

Electrochemical impedance spectroscopy is a powerful tool to extract information on the reactions occurring on the WE. Unlike other electrochemical techniques, EIS distinguishes between capacitance (C) and resistance (R), enabling the distinguishing of diffusion-controlled processes from other processes. This is made possible by the fact that capacitance is inversely proportional to frequency while resistance is independent of frequency [198]. EIS enables the determination of the bulk and surface properties of the system through the evaluation of the

impedance of the WE as a function of the frequency (f) of the applied alternating voltage. To carry out potentiostat EIS measurements, a low amplitude (5-10 mV), sinusoidal potential, centred around a potential set-point is applied at a wide range of frequencies, typically 10 mHz to 100 kHz. The corresponding sinusoidal current is measured over the frequency spectrum. Fourier transform of the data converts the data from the time domain to the frequency domain [199]. As the frequency is varied, there is a phase shift, ϕ between the E(t) and I (t). The sinusoidal potential, current and frequency-dependant impedance which is a measure of the electrode's opposition to current are expressed by equations (2.21-2.23):

$$\mathbf{E(t) = E_{app} + |E_o| \sin \omega t} \tag{2.21}$$

$$\mathbf{I(t) = |I_o| \sin(\omega t + \phi)} \tag{2.22}$$

$$\mathbf{Z(\omega) = \frac{E(t)}{I(t)}} \tag{2.23}$$

where I (t) is the resulting current (A) due to the application of E(t), E(t) is the alternating voltage (V), and $\omega = 2\pi f$ is the angular frequency (rad s^{-1}), ϕ is the phase shift of the current concerning the potential, and $Z(\omega)$ is the impedance (Ω). The most frequent representation of the EIS data is the Nyquist plot, also known as the Argand diagram [198]. Figure 2.15 is a plot of real and imaginary impedance as a function of frequency.

The Nyquist plot can be divided into two regions as shown in figure 2.10. The kinetic control region at high-frequency values and the Warburg region at low-frequency values [200].

Alternating current (AC) circuit elements can be employed to represent the physical process taking place in the electrochemical reaction. A resistor and capacitor are the most frequently encountered circuit elements. In the kinetically controlled region, the effect of the opposition to the flow of current in the electrolyte manifests. This is the solution resistance (R_S) depicted as the intercept of the plot with the real impedance axes at high frequency. This is also referred to as the equivalent series resistance (ESR) [201].
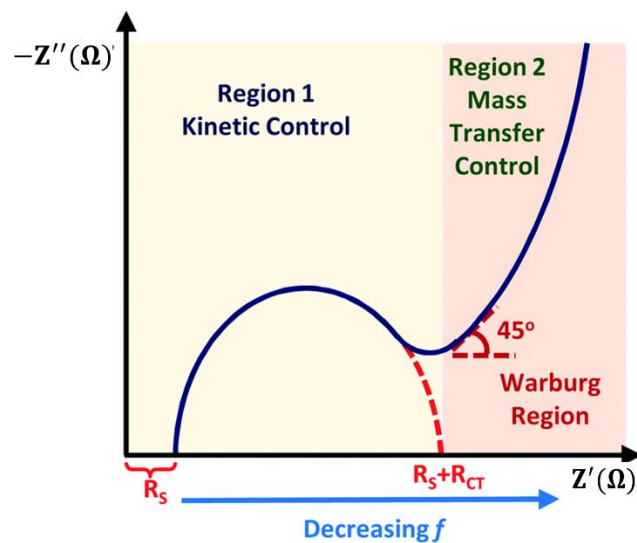
Figure 2. 10: Schematic illustration of imaginary impedance (Z'') versus real impedance (Z') [146].

The charge transfer resistance, R_{CT} is formed by a single kinetically controlled electrochemical reaction [202]. This is indicated by the diameter of the semi-circle [203]. In the mass transfer region (low-frequency zone), the double layer capacitance, C_{dl}, denotes the capacitance at the electrode-electrolyte interface due to the non-Faradaic charge storage at the surface of the electrode [204]. Diffusion or mass transfer can be modelled using the Warburg impedance element (Z_W) [205]. Non-uniformity at the double-layer interface gives rise to a non-ideal capacitor. This can be modelled by replacing the C_{dl} with the constant phase element (CPE) represented by Q [206].

47

The Bode plot is another useful representation of EIS processes. It is a plot of the phase shift (ϕ) and the magnitude of the impedance $|Z(\omega)|$ as a function of frequency, f.

The real and imaginary capacitances can be obtained from equations (2.24-2.26) [207]:

$$C'(\omega) = -\frac{Z''(\omega)}{|Z(\omega)|^2} \tag{2.24}$$

$$C''(\omega) = -\frac{Z'(\omega)}{|Z(\omega)|^2} \tag{2.25}$$

$$C(\omega) = C'(\omega) + jC''(\omega) \tag{2.26}$$

where $C'(\omega)$ and $C''(\omega)$ are the real and imaginary capacitances (F), respectively and $|Z(\omega)|$ is the magnitude of the impedance (Ω). $C'(\omega)$ corresponds to the capacitance obtained during the steady current discharge, whereas $C''(\omega)$ denotes energy dissipation of the electrode through a potential drop and an irreversible Faradaic charge transfer mechanism.

2.7.4. Stability test

2.7.4.1. Charge - discharge cycling

One of the most important electrochemical attributes of all electrochemical storage devices is the cycle life. GCD is often utilized to evaluate the cycle life of WEs and devices [208]. The GCD is run for thousands of charge-discharge cycles by setting the working potential (V_{MAX}), and the

specific current I_S. The purpose of this measurement is to determine quantitatively how much of the electrochemical performance is retained after a given number of cycles. This is achieved through calculating capacity/capacitance retention (CR), coulombic efficiency (ε) and energy efficiency (η) which are expressed in equations (2.27) to (2.29) [209]:

$$\mathbf{CR}\ [\%] = \frac{\mathbf{t_{DN}}}{\mathbf{t_{D1}}} \tag{2.27}$$

$$\boldsymbol{\varepsilon}\ [\%] = \frac{\mathbf{t_D}}{\mathbf{t_C}} \tag{2.28}$$

$$\boldsymbol{\eta}\ [\%] = \frac{\mathbf{E_D}}{\mathbf{E_C}} \tag{2.29}$$

where ε is the coulombic efficiency, η is the energy efficiency, t_D and t_C denote the discharge and charge time (s), respectively. The t_{D1} and t_{DN} are the discharge times (s) after the first and N^{th} cycles, respectively and E_D and E_C are the discharge and charge energies, respectively.

2.7.4.2 Voltage holding (VH)

Voltage holding is one of the methods which is considered by the researcher to be the most rigorous and reliable to test the stability of the device [210]. This is because, unlike charge-discharge cycling, VH reveals more information on the degradation of the material which takes place during the floating test [211]. A certain voltage (maximum voltage of the device) is applied to the device for a certain amount of time after which the device is allowed to undergo a few charge - discharge cycles before being held again at a fixed voltage (maximum voltage) for a

given time. The process is continued until there is a significant depletion in the performance of the device.

2.7.4.3 Self-discharge (SD)

Self-discharge is a stability test technique aimed at determining the spontaneous decrease of the voltage of the device. Initially, a certain fixed voltage is applied to the device for several hours to a maximum voltage then the decrease of the voltage of the device which is not connected to any load (open circuit) is monitored [212]. This test helps to evaluate the loss of energy throughout the test and determine the drop of the capacitance and voltage. Parasitic Faradaic processes, charge redistribution and ohmic leakage of current between the electrodes are some of the mechanisms which cause an increase in SD [213].

References

[1]   E. Danila, Ieei 2010, Ieei 2010. (2015) 1–4. https://doi.org/10.13140/2.1.1564.7040.

[2]   K.S. Gandhi, Storage of electrical energy, Indian Chem. Eng. 52 (2010) 57–75. https://doi.org/10.1080/00194501003759811.

[3]   E. Benthien, Michael faraday, Notes Queries. s5-VI (1876) 190–191. https://doi.org/10.1093/nq/s5-VI.140.190d.

[4]   S.K. Chang, Z. Zainal, K.B. Tan, N.A. Yusof, W.M.D.W. Yusoff, S.R.S. Prabaharan, Recent development in spinel cobaltites for supercapacitor application, Ceram. Int. 41 (2015) 1–14. https://doi.org/10.1016/j.ceramint.2014.07.101.

[5]   B. Brusso, S. Chaparala, The Evolution of Capacitors, IEEE Aerosp. Electron. Syst. Mag. 31 (2016) 17–17. https://doi.org/10.1109/maes.2016.7590294.

[6]   M.Z. Iqbal, M.M. Faisal, S.R. Ali, Integration of supercapacitors and batteries towards high-performance hybrid energy storage devices, Int. J. Energy Res. 45 (2021) 1449–1479. https://doi.org/10.1002/er.5954.

[7]   J.C. Barbosa, R. Gonçalves, C.M. Costa, V. De Zea Bermudez, A. Fidalgo-Marijuan, Q. Zhang, S. Lanceros-Méndez, Metal-organic frameworks and zeolite materials as active fillers for lithium-ion battery solid polymer electrolytes, Mater. Adv. 2 (2021) 3790–3805. https://doi.org/10.1039/d1ma00244a.

[8]   R.B. Choudhary, S. Ansari, B. Purty, Robust electrochemical performance of polypyrrole (PPy) and polyindole (PIn) based hybrid electrode materials for supercapacitor application: A review, J. Energy Storage. 29 (2020) 101302. https://doi.org/10.1016/j.est.2020.101302.

[9]   S.R. Devanhalli, H. Wagh, P.K. Vasani, Study of Auto Cut off Electricity Power Supply on Full Charge of Battery Using Microcontroller, 6 (2020) 46–54.

[10]   Z. Yang, J. Wang, Y. Hu, C. Deng, K. Zhu, J. Qiu, Simultaneously improved dielectric constant and breakdown strength of PVDF/Nd-BaTiO3 fiber composite films via the surface modification and subtle filler content modulation, Compos. Part A Appl. Sci. Manuf. 128 (2020). https://doi.org/10.1016/j.compositesa.2019.105675.

[11]   Y. Morita, Y. Saito, T. Yoshioka, T. Shiratori, Estimation of recoverable resources used in lithium-ion batteries from portable electronic devices in Japan, Resour. Conserv. Recycl. 175 (2021) 105884. https://doi.org/10.1016/j.resconrec.2021.105884.

[12]   G.N. Newton, L.R. Johnson, D.A. Walsh, B.J. Hwang, H. Han, Sustainability of Battery Technologies: Today and Tomorrow, ACS Sustain. Chem. Eng. 9 (2021) 6507–6509. https://doi.org/10.1021/acssuschemeng.1c02909.

[13]   S. Chen, S. Cui, S. Chandrasekaran, C. Ke, Z. Li, P. Chen, C. Zhang, Y. Jiang, Growth of CuCo2O4@MnMoO4 core/shell nanosheet arrays for high energy density asymmetric supercapacitors, Electrochim. Acta. 341 (2020) 135893. https://doi.org/10.1016/j.electacta.2020.135893.

51

[14]   T. Pazhanivel, S. Dhinesh, M. Priyadharshini, R. Gobi, Chapter 6 Aerogels Utilizations in Batteries, 98 (2021) 99–120.

[15]   V. Sharmila, M. Parthibavarman, Lithium manganese phosphate associated with MWCNT: Enhanced positive electrode for lithium hybrid batteries, J. Alloys Compd. 858 (2021) 157715. https://doi.org/10.1016/j.jallcom.2020.157715.

[16]   S.I. Wong, J. Sunarso, B.T. Wong, H. Lin, A. Yu, B. Jia, Towards enhanced energy density of graphene-based supercapacitors: Current status, approaches, and future directions, J. Power Sources. 396 (2018) 182–206. https://doi.org/10.1016/j.jpowsour.2018.06.004.

[17]   M. Karuppaiah, P. Sakthivel, S. Asaithambi, B. Sriram, T. Ahamad, S.M. Alshehri, R. Yuvakkumar, G. Ravi, Heterostructured Ov-Mn2O3@Cu2SnS3@SnS Composite as Battery-Type Cathode Material for Extrinsic Self-Charging Hybrid Supercapacitors, Adv. Mater. Interfaces. (2022). https://doi.org/10.1002/admi.202200104.

[18]   S. Liang, H. Wang, Y. Li, H. Qin, Z. Luo, B. Huang, X. Zhao, C. Zhao, L. Chen, Rare-earth based nanomaterials and their composites as electrode materials for high performance supercapacitors: A review, Sustain. Energy Fuels. 4 (2020) 3825–3847. https://doi.org/10.1039/d0se00669f.

[19]   M.Z. Iqbal, U. Aziz, Supercapattery: Merging of battery-supercapacitor electrodes for hybrid energy storage devices, J. Energy Storage. 46 (2022) 103823. https://doi.org/10.1016/j.est.2021.103823.

[20]   Y. Lian, D. Wang, S. Hou, C. Ban, J. Zhao, H. Zhang, Construction of T-Nb2O5 nanoparticles on/in N-doped carbon hollow tubes for Li-ion hybrid supercapacitors, Electrochim. Acta. 330 (2020) 135204. https://doi.org/10.1016/j.electacta.2019.135204.

[21]   E. Pipitone, G. Vitale, A regenerative braking system for internal combustion engine vehicles using supercapacitors as energy storage elements - Part 1: System analysis and modelling, J. Power Sources. 448 (2020) 227368. https://doi.org/10.1016/j.jpowsour.2019.227368.

[22]   D. Jayananda, N. Kularatna, D.A. Steyn-Ross, Supercapacitor-assisted LED (SCALED) technique for renewable energy systems: A very low frequency design approach with short-term DC-UPS capability eliminating battery banks, IET Renew. Power Gener. 14 (2020) 1559–1570. https://doi.org/10.1049/iet-rpg.2019.1307.

[23]   S.B. Aziz, M.A. Brza, H.M. Hamsan, M.F.Z. Kadir, R.T. Abdulwahid, Electrochemical characteristics of solid state double-layer capacitor constructed from proton conducting chitosan-based polymer blend electrolytes, Polym. Bull. 78 (2021) 3149–3167. https://doi.org/10.1007/s00289-020-03278-1.

[24]   Y. Liu, S.P. Jiang, Z. Shao, Intercalation pseudocapacitance in electrochemical energy storage: recent advances in fundamental understanding and materials development, Mater. Today Adv. 7 (2020) 100072. https://doi.org/10.1016/j.mtadv.2020.100072.

[25]   M. Aadil, S. Zulfiqar, H. Sabeeh, M.F. Warsi, M. Shahid, I.A. Alsafari, I. Shakir, Enhanced electrochemical energy storage properties of carbon coated Co3O4 nanoparticles-reduced graphene oxide ternary nano-hybrids, Ceram. Int. 46 (2020) 17836–17845. https://doi.org/10.1016/j.ceramint.2020.04.090.

[26]   F. Soavi, C. Santoro, Supercapacitive operational mode in microbial fuel cell, Curr. Opin. Electrochem. 22 (2020) 1–8. https://doi.org/10.1016/j.coelec.2020.03.009.

[27]   L.M. Da Silva, R. Cesar, C.M.R. Moreira, J.H.M. Santos, L.G. De Souza, B.M. Pires, R. Vicentini, W. Nunes, H. Zanin, Reviewing the fundamentals of supercapacitors and the difficulties involving the analysis of the electrochemical findings obtained for porous electrode materials, Energy Storage Mater. 27 (2020) 555–590. https://doi.org/10.1016/j.ensm.2019.12.015.

[28]   F. Nasir, M.A. Mohammad, Investigation of Device Dimensions on Electric Double Layer Microsupercapacitor Performance and Operating Mechanism, IEEE Access. 8 (2020) 28367–28374. https://doi.org/10.1109/ACCESS.2020.2972080.

[29]   V.T. Le, H. Ryu, S.A. Han, H. Van Bui, V.H. Nguyen, N. Van Hieu, J.H. Lee, S.W. Kim, Y.H. Lee, Simultaneous enhancement of specific capacitance and potential window of graphene-based electric double-layer capacitors using ferroelectric polymers, J. Power Sources. 507 (2021) 230268. https://doi.org/10.1016/j.jpowsour.2021.230268.

[30]   S. Balasubramaniam, A. Mohanty, S.K. Balasingam, S.J. Kim, A. Ramadoss, Comprehensive Insight into the Mechanism, Material Selection and Performance Evaluation of Supercapatteries, Springer Singapore, 2020. https://doi.org/10.1007/s40820-020-0413-7.

[31]   J.J. López-García, J. Horno, C. Grosse, Combined Ionic Size and Electrode Spacing Effects on the Differential Capacitance of Confined Electrolytic Cells, J. Phys. Chem. C. 126 (2022) 9154–9160. https://doi.org/10.1021/acs.jpcc.2c01598.

[32]   S. Xue, B. Garlyyev, A. Auer, J. Kunze-Liebhäuser, A.S. Bandarenka, How the Nature of the Alkali Metal Cations Influences the Double-Layer Capacitance of Cu, Au, and Pt Single-Crystal Electrodes, J. Phys. Chem. C. 124 (2020) 12442–12447. https://doi.org/10.1021/acs.jpcc.0c01715.

[33]   G. Gonella, E.H.G. Backus, Y. Nagata, D.J. Bonthuis, P. Loche, A. Schlaich, R.R. Netz, A. Kühnle, I.T. McCrum, M.T.M. Koper, M. Wolf, B. Winter, G. Meijer, R.K. Campen, M. Bonn, Water at charged interfaces, Nat. Rev. Chem. 5 (2021) 466–485. https://doi.org/10.1038/s41570-021-00293-2.

[34]   A.S.F.M. Asnawi, S.B. Aziz, M.M. Nofal, M.H. Hamsan, M.A. Brza, Y.M. Yusof, R.T. Abdilwahid, S.K. Muzakir, M.F.Z. Kadir, Glycerolized Li+ ion conducting chitosan-based polymer electrolyte for energy storage EDLC device applications with relatively high energy density, Polymers (Basel). 12 (2020) 1–19. https://doi.org/10.3390/polym12061433.

[35]   S.P. Gupta, H.H. Nishad, S.D. Chakane, S.W. Gosavi, D.J. Late, P.S. Walke, Phase transformation in tungsten oxide nanoplates as a function of post-annealing temperature and its electrochemical influence on energy storage, Nanoscale Adv. 2 (2020) 4689–4701. https://doi.org/10.1039/d0na00423e.

[36]   X. Zhang, X. Liu, Y. Zeng, Y. Tong, X. Lu, Oxygen Defects in Promoting the Electrochemical Performance of Metal Oxides for Supercapacitors: Recent Advances and Challenges, Small Methods. 4 (2020) 1–18. https://doi.org/10.1002/smtd.201900823.

[37]   A. Moyseowicz, G. Gryglewicz, High-performance hybrid capacitor based on a porous polypyrrole/reduced graphene oxide composite and a redox-active electrolyte, Electrochim. Acta. 354 (2020). https://doi.org/10.1016/j.electacta.2020.136661.

[38]   H. Liu, X. Liu, S. Wang, H.K. Liu, L. Li, Transition metal based battery-type electrodes in hybrid supercapacitors: A review, Energy Storage Mater. 28 (2020) 122–145. https://doi.org/10.1016/j.ensm.2020.03.003.

[39]   D. Xu, G. Teng, Y. Heng, Z. Chen, D. Hu, Eco-friendly and thermally stable cellulose film prepared by phase inversion as supercapacitor separator, Mater. Chem. Phys. 249 (2020) 122979. https://doi.org/10.1016/j.matchemphys.2020.122979.

[40]   M. Tomy, A. Ambika Rajappan, V. VM, X. Thankappan Suryabai, Emergence of Novel 2D Materials for High-Performance Supercapacitor Electrode Applications: A Brief Review, Energy and Fuels. 35 (2021) 19881–19900. https://doi.org/10.1021/acs.energyfuels.1c02743.

[41]   N. Talreja, S.H. Jung, L.T.H. Yen, T.Y. Kim, Phenol-formaldehyde-resin-based activated carbons with controlled pore size distribution for high-performance supercapacitors, Chem. Eng. J. 379 (2020) 122332. https://doi.org/10.1016/j.cej.2019.122332.

[42]   L. Sun, Y. Zhang, H. Si, Y. Shi, C. Sun, Y. Zhang, Porous Mo-C coverage on ZnO rods for enhanced supercapacitive performance, Dalt. Trans. 49 (2020) 5134–5142. https://doi.org/10.1039/d0dt00704h.

[43]   B.K. Roy, I. Tahmid, T.U. Rashid, Chitosan-based materials for supercapacitor applications: A review, J. Mater. Chem. A. 9 (2021) 17592–17642. https://doi.org/10.1039/d1ta02997e.

[44]   S.A. Delbari, L.S. Ghadimi, R. Hadi, S. Farhoudian, M. Nedaei, A. Babapoor, A. Sabahi Namini, Q. Van Le, M. Shokouhimehr, M. Shahedi Asl, M. Mohammadi, Transition metal oxide-based electrode materials for flexible supercapacitors: A review, J. Alloys Compd. 857 (2021) 158281. https://doi.org/10.1016/j.jallcom.2020.158281.

[45]   S. Arunachalam, B. Kirubasankar, D. Pan, H. Liu, C. Yan, Z. Guo, S. Angaiah, Research progress in rare earths and their composites based electrode materials for supercapacitors, Green Energy Environ. 5 (2020) 259–273. https://doi.org/10.1016/j.gee.2020.07.021.

[46]   Y. Wen, L. Chi, K. Wenelska, X. Wen, X. Chen, E. Mijowska, Eucalyptus derived heteroatom-doped hierarchical porous carbons as electrode materials in supercapacitors, Sci. Rep. 10 (2020) 1–12. https://doi.org/10.1038/s41598-020-71649-9.

[47]   M. Karnan, K.H. Prakash, S. Badhulika, Revealing the super capacitive performance of N-doped hierarchical porous activated carbon in aqueous , ionic liquid , and redox additive electrolytes, J. Energy Storage. 53 (2022) 105189. https://doi.org/10.1016/j.est.2022.105189.

[48]   K. Manickavasakam, S. Suresh Balaji, S. Kaipannan, A.G. Karthick Raj, S. Veeman, S. Marappan, Electrochemical Performance of Thespesia Populnea Seeds Derived Activated Carbon - Supercapacitor and Its Improved Specific Energy in Redox Additive Electrolytes, J. Energy Storage. 32 (2020) 101939. https://doi.org/10.1016/j.est.2020.101939.

[49]   G. Liu, L. Qiu, H. Deng, J. Wang, L. Yao, L. Deng, Ultrahigh surface area carbon nanosheets derived from lotus leaf with super capacities for capacitive deionization and dye adsorption, Appl. Surf. Sci. 524 (2020) 146485. https://doi.org/10.1016/j.apsusc.2020.146485.

[50]   N.A. Rashidi, S. Yusup, Recent methodological trends in nitrogen–functionalized activated carbon production towards the gravimetric capacitance: A mini review, J. Energy Storage. 32 (2020) 101757. https://doi.org/10.1016/j.est.2020.101757.

[51]   Q. Abbas, M. Mirzaeian, A.A. Ogwu, M. Mazur, D. Gibson, Effect of physical activation/surface functional groups on wettability and electrochemical performance of carbon/activated carbon aerogels based electrode materials for electrochemical capacitors, Int. J. Hydrogen Energy. 45 (2020) 13586–13595. https://doi.org/10.1016/j.ijhydene.2018.04.099.

[52]   C. Shao, S. Qiu, G. Wu, B. Cui, H. Chu, Y. Zou, C. Xiang, F. Xu, L. Sun, Rambutan-like hierarchically porous carbon microsphere as electrode material for high-performance supercapacitors, Carbon Energy. 3 (2021) 361–374. https://doi.org/10.1002/cey2.81.

[53]   S.C. Abbas, C. Lin, Z. Hua, Q. Deng, H. Huang, Y. Ni, S. Cao, X. Ma, Bamboo-derived carbon material inherently doped with SiC and nitrogen for flexible supercapacitors, Chem. Eng. J. 433 (2022) 133738. https://doi.org/10.1016/j.cej.2021.133738.

[54]   A.R. Selvaraj, A. Muthusamy, Inho-Cho, H.J. Kim, K. Senthil, K. Prabakar, Ultrahigh surface area biomass derived 3D hierarchical porous carbon nanosheet electrodes for high energy density supercapacitors, Carbon N. Y. 174 (2021) 463–474. https://doi.org/10.1016/j.carbon.2020.12.052.

[55]   H.P. Veeravenkata, A. Jain, Density functional theory driven phononic thermal conductivity prediction of biphenylene: A comparison with graphene, Carbon N. Y. 183 (2021) 893–898. https://doi.org/10.1016/j.carbon.2021.07.078.

[56]   Y.B. Pottathara, H.R. Tiyyagura, Z. Ahmad, K.K. Sadasivuni, Graphene Based Aerogels: Fundamentals and Applications as Supercapacitors, J. Energy Storage. 30 (2020) 101549. https://doi.org/10.1016/j.est.2020.101549.

[57]   H. Zhang, D. Yang, A. Lau, T. Ma, H. Lin, B. Jia, Hybridized Graphene for Supercapacitors: Beyond the Limitation of Pure Graphene, Small. 17 (2021) 1–22. https://doi.org/10.1002/smll.202007311.

[58]   G. Ma, G. Ning, Q. Wei, S-doped carbon materials: Synthesis, properties and applications, Carbon N. Y. 195 (2022) 328–340. https://doi.org/10.1016/j.carbon.2022.03.043.

[59]   V.J. Mane, S.B. Kale, S.B. Ubale, V.C. Lokhande, C.D. Lokhande, Enhanced specific energy of silver-doped MnO2/graphene oxide electrodes as facile fabrication symmetric supercapacitor device, Mater. Today Chem. 20 (2021) 100473. https://doi.org/10.1016/j.mtchem.2021.100473.

[60]   U. Javed, G. Dhakal, A.M. Rabie, S. Iqbal, Y.R. Lee, J. Lee, J.J. Shim, Heteroatom-doped reduced graphene oxide integrated with nickel-cobalt phosphide for high-performance

asymmetric hybrid supercapacitors, Mater. Today Nano. 18 (2022) 100195. https://doi.org/10.1016/j.mtnano.2022.100195.

[61]   J. Romanos, M. Beckner, T. Rash, L. Firlej, B. Kuchta, P. Yu, G. Suppes, C. Wexler, P. Pfeifer, Nanospace engineering of KOH activated carbon, Nanotechnology. 23 (2012). https://doi.org/10.1088/0957-4484/23/1/015401.

[62]   Y. Zhai, Y. Dou, D. Zhao, P.F. Fulvio, R.T. Mayes, S. Dai, Carbon Materials for Chemical Capacitive Energy Storage, Adv. Mater. 23 (2011) 4828–4850. https://doi.org/10.1002/adma.201100984.

[63]   M. Vinayagam, R. Suresh Babu, A. Sivasamy, A.L. Ferreira de Barros, Biomass-derived porous activated carbon from Syzygium cumini fruit shells and Chrysopogon zizanioides roots for high-energy density symmetric supercapacitors, Biomass and Bioenergy. 143 (2020) 105838. https://doi.org/10.1016/j.biombioe.2020.105838.

[64]   Y. Ouyang, Y. Chen, J. Peng, J. Yang, C. Wu, B. Chang, X. Guo, G. Chen, Z. Luo, X. Wang, Nickel sulfide/activated carbon nanotubes nanocomposites as advanced electrode of high-performance aqueous asymmetric supercapacitors, J. Alloys Compd. 885 (2021) 160979. https://doi.org/10.1016/j.jallcom.2021.160979.

[65]   J.M. Gonçalves, M.I. da Silva, H.E. Toma, L. Angnes, P.R. Martins, K. Araki, Trimetallic oxides/hydroxides as hybrid supercapacitor electrode materials: a review, J. Mater. Chem. A. 8 (2020) 10534–10570. https://doi.org/10.1039/d0ta02939d.

[66]   M. Guan, Q. Wang, X. Zhang, J. Bao, X. Gong, Y. Liu, Two-Dimensional Transition Metal Oxide and Hydroxide-Based Hierarchical Architectures for Advanced Supercapacitor Materials, Front. Chem. 8 (2020) 1–14. https://doi.org/10.3389/fchem.2020.00390.

[67]   M. Cui, X. Meng, Overview of transition metal-based composite materials for supercapacitor electrodes, Nanoscale Adv. 2 (2020) 5516–5528. https://doi.org/10.1039/d0na00573h.

[68]   W. Liu, Z. Zhang, Y. Zhang, Y. Zheng, N. Liu, J. Su, Y. Gao, Interior and Exterior Decoration of Transition Metal Oxide Through Cu0/Cu+ Co-Doping Strategy for High-Performance Supercapacitor, Nano-Micro Lett. 13 (2021) 1–14. https://doi.org/10.1007/s40820-021-00590-x.

[69]   R.B. Choudhary, S. Ansari, M. Majumder, Recent advances on redox active composites of metal-organic framework and conducting polymers as pseudocapacitor electrode material, Renew. Sustain. Energy Rev. 145 (2021) 110854. https://doi.org/10.1016/j.rser.2021.110854.

[70]   H. Wang, J. Li, K. Li, Y. Lin, J. Chen, L. Gao, V. Nicolosi, X. Xiao, J.M. Lee, Transition metal nitrides for electrochemical energy applications, Chem. Soc. Rev. 50 (2021) 1354–1390. https://doi.org/10.1039/d0cs00415d.

[71]   H. Sun, J.M. Yang, J.G. Li, Z. Li, X. Ao, Y.Z. Liu, Y. Zhang, Y. Li, C. Wang, J. Tang, Synergistic coupling of NiTe nanoarrays with RuO2 and NiFe-LDH layers for high-efficiency electrochemical-/photovoltage-driven overall water splitting, Appl. Catal. B Environ. 272 (2020). https://doi.org/10.1016/j.apcatb.2020.118988.

[72]   S. Pavithra, V.K. Jothi, A. Rajaram, S. Ingavale, A. Natarajan, A Facile Synthesis of a Fusiform-Shaped Three-Dimensional Co/Mn@CNDs-MOF Nanocomposite as an Efficient Electrocatalyst for Oxygen Evolution Reaction in Alkaline Medium, Energy & Fuels. (2022). https://doi.org/10.1021/acs.energyfuels.2c00780.

[73]   X. Zhao, L. Mao, Q. Cheng, J. Li, F. Liao, G. Yang, L. Xie, C. Zhao, L. Chen, Two-dimensional Spinel Structured Co-based Materials for High Performance Supercapacitors: A Critical Review, Chem. Eng. J. 387 (2020) 124081. https://doi.org/10.1016/j.cej.2020.124081.

[74]   P.F. Wang, T. Jin, J. Zhang, Q.C. Wang, X. Ji, C. Cui, N. Piao, S. Liu, J. Xu, X.Q. Yang, C. Wang, Elucidation of the Jahn-Teller effect in a pair of sodium isomer, Nano Energy. 77 (2020) 105167. https://doi.org/10.1016/j.nanoen.2020.105167.

[75]   S. Wang, P. Yang, X. Sun, L. Feng, C. Jin, M. Ren, H. Xing, J. Shi, Fabrication of the flower-like NiCo2O4 @ Ni(OH)2/NiOOH composites supported on nickel foam by the green solvent dimethyl sulfoxide with high performance in supercapacitor and hydrogen evolution reaction, J. Phys. Chem. Solids. 159 (2021) 110257. https://doi.org/10.1016/j.jpcs.2021.110257.

[76]   G. Rutavi, D.J. Tarimo, V.M. Maphiri, N. Manyala, Two-step electrodeposition of Hausmannite sulphur reduced graphene oxide and cobalt-nickel layered double hydroxide heterostructure for high-performance supercapacitor, Int. J. Energy Res. (2022) 1–14. https://doi.org/10.1002/er.7922.

[77]   J. Acharya, M. Park, T.H. Ko, B.S. Kim, Leaf-like integrated hierarchical NiCo2O4 nanorods@Ni-Co-LDH nanosheets electrodes for high-rate asymmetric supercapacitors, J. Alloys Compd. 884 (2021). https://doi.org/10.1016/j.jallcom.2021.161165.

[78]   A.R. Akbar, H. Hu, M.B. Qadir, M. Tahir, Z. Khaliq, Z. Liu, C. Xiong, Q. Yang, Optimized structure and electrochemical properties of sulfonated carbon nanotubes/Co–Ni bimetallic layered hydroxide composites for high-performance supercapacitors, Ceram. Int. 47 (2021) 4648–4658. https://doi.org/10.1016/j.ceramint.2020.10.032.

[79]   X. Gao, Y. Zhao, K. Dai, J. Wang, B. Zhang, X. Shen, NiCoP nanowire@NiCo-layered double hydroxides nanosheet heterostructure for flexible asymmetric supercapacitors, Chem. Eng. J. 384 (2020). https://doi.org/10.1016/j.cej.2019.123373.

[80]   D. Han, Y. Zhao, Y. Shen, Y. Wei, L. Mao, G. Zeng, Co3O4 nanowire@ultrathin Ni-Co layered double hydroxide core-shell arrays with vertical transfer channel for high-performance supercapacitor, J. Electroanal. Chem. 859 (2020). https://doi.org/10.1016/j.jelechem.2020.113887.

[81]   P. Yang, C. Jing, J.C. Liu, K. Chen, Y.X. Zhang, Controllable crystal growth of a NiCo-LDH nanostructure anchored onto KCu7S4 nanowires: Via a facile solvothermal method for supercapacitor application, CrystEngComm. 22 (2020) 1602–1609. https://doi.org/10.1039/c9ce01261c.

[82]   S. Li, Y. Luo, C. Wang, M. Wu, Y. Xue, J. Yang, L. Li, A novel hierarchical core-shell structure of NiCo2O4@NiCo-LDH nanoarrays for higher-performance flexible all-

solid-state supercapacitor electrode materials, J. Alloys Compd. 920 (2022) 165986. https://doi.org/10.1016/j.jallcom.2022.165986.

[83]　J. Zou, D. Xie, J. Xu, X. Song, X. Zeng, H. Wang, F. Zhao, Rational design of honeycomb Ni-Co LDH/graphene composite for remarkable supercapacitor via ultrafast microwave synthesis, Appl. Surf. Sci. 571 (2022) 151322. https://doi.org/10.1016/j.apsusc.2021.151322.

[84]　H. Luo, B. Wang, T. Liu, F. Jin, R. Liu, C. Xu, C. Wang, K. Ji, Y. Zhou, D. Wang, S. Dou, Hierarchical design of hollow Co-Ni LDH nanocages strung by MnO2 nanowire with enhanced pseudocapacitive properties, Energy Storage Mater. 19 (2019) 370–378. https://doi.org/10.1016/j.ensm.2018.10.016.

[85]　J. Chang, S. Zang, W. Liang, D. Wu, Z. Lian, F. Xu, K. Jiang, Z. Gao, Enhanced faradic activity by construction of p-n junction within reduced graphene oxide@cobalt nickel sulfide@nickle cobalt layered double hydroxide composite electrode for charge storage in hybrid supercapacitor, J. Colloid Interface Sci. 590 (2021) 114–124. https://doi.org/10.1016/j.jcis.2021.01.035.

[86]　L. Wan, D. Chen, J. Liu, Y. Zhang, J. Chen, M. Xie, C. Du, Construction of FeNiP@CoNi-layered double hydroxide hybrid nanosheets on carbon cloth for high energy asymmetric supercapacitors, J. Power Sources. 465 (2020). https://doi.org/10.1016/j.jpowsour.2020.228293.

[87]　J. Acharya, T.H. Ko, M.K. Seo, M.S. Khil, H.Y. Kim, B.S. Kim, Engineering the Hierarchical Heterostructures of Zn-Ni-Co Nanoneedles Arrays@Co-Ni-LDH Nanosheets Core-Sheath Electrodes for a Hybrid Asymmetric Supercapacitor with High Energy Density and Excellent Cyclic Stability, ACS Appl. Energy Mater. 3 (2020) 7383–7396. https://doi.org/10.1021/acsaem.0c00781.

[88]　J. Acharya, M. Park, T.H. Ko, B. Kim, Leaf-like integrated hierarchical NiCo2O4 nanorods@Ni-Co-LDH nanosheets electrodes for high-rate asymmetric supercapacitors, J. Alloys Compd. 884 (2021) 161165. https://doi.org/10.1016/j.jallcom.2021.161165.

[89]　D. Wei, Y. Zhang, X. Zhu, M. Fan, Y. Wang, CNT/Co3S4@NiCo LDH ternary nanocomposites as battery-type electrode materials for hybrid supercapacitors, J. Alloys Compd. 824 (2020). https://doi.org/10.1016/j.jallcom.2020.153937.

[90]　G. Wang, Y. Li, T. Zhao, Z. Jin, Phosphatized mild-prepared-NiCo LDHs cabbage-like spheres exhibit excellent performance as a supercapacitor electrode, New J. Chem. 45 (2021) 251–261. https://doi.org/10.1039/d0nj03070h.

[91]　H. Chu, Y. Zhu, T. Fang, J. Hua, S. Qiu, H. Liu, L. Qin, Q. Wei, Y. Zou, C. Xiang, F. Xu, L. Sun, Solvothermal synthesis of cobalt nickel layered double hydroxides with a three-dimensional nano-petal structure for high-performance supercapacitors, Sustain. Energy Fuels. 4 (2019) 337–346. https://doi.org/10.1039/c9se00712a.

[92]　J. Cao, Q. Mei, R. Wu, W. Wang, Flower-like nickel–cobalt layered hydroxide nanostructures for super long-life asymmetrical supercapacitors, Electrochim. Acta. 321 (2019). https://doi.org/10.1016/j.electacta.2019.134711.

[93]   J.J. Zhou, Q. Li, C. Chen, Y.L. Li, K. Tao, L. Han, Co3O4@CoNi-LDH core/shell nanosheet arrays for high-performance battery-type supercapacitors, Chem. Eng. J. 350 (2018) 551–558. https://doi.org/10.1016/j.cej.2018.06.023.

[94]   M.U. Tahir, H. Arshad, H. Zhang, Z. Hou, J. Wang, C. Yang, X. Su, Room temperature and aqueous synthesis of bimetallic ZIF derived CoNi layered double hydroxides and their applications in asymmetric supercapacitors, J. Colloid Interface Sci. 579 (2020) 195–204. https://doi.org/10.1016/j.jcis.2020.06.050.

[95]   M.U. Tahir, H. Arshad, W. Xie, X. Wang, M. Nawaz, C. Yang, X. Su, Synthesis of morphology controlled NiCo-LDH microflowers derived from ZIF-67 using binary additives and their excellent asymmetric supercapacitor properties, Appl. Surf. Sci. 529 (2020). https://doi.org/10.1016/j.apsusc.2020.147073.

[96]   W. Wang, Y. Lu, M. Zhao, R. Luo, Y. Yang, T. Peng, H. Yan, X. Liu, Y. Luo, Controllable tuning of cobalt nickel-layered double hydroxide arrays as multifunctional electrodes for flexible supercapattery device and oxygen evolution reaction, ACS Nano. 13 (2019) 12206–12218. https://doi.org/10.1021/acsnano.9b06910.

[97]   Y. Zhu, S. An, J. Cui, H. Qiu, X. Sun, Y. Zhang, W. He, Three-dimensional network-like amorphous NiCo-LDH nanofilms coupled with Co3O4 nanowires for high-performance supercapacitor, Ceram. Int. 45 (2019) 22095–22103. https://doi.org/10.1016/j.ceramint.2019.07.226.

[98]   Y. Wang, Z. Wang, X. Zheng, X. Teng, L. Xu, Y. Yuan, X. Liu, A. Fu, Y. Li, H. Li, Core-sheath heterostructure of MnCo2O4 nanowires wrapped by NiCo-layered double hydroxide as cathode material for high-performance quasi-solid-state asymmetric supercapacitors, J. Alloys Compd. 904 (2022) 164047. https://doi.org/10.1016/j.jallcom.2022.164047.

[99]   Y. Zhu, S. An, X. Sun, D. Lan, J. Cui, Y. Zhang, W. He, Core-branched NiCo2S4@CoNi-LDH heterostructure as advanced electrode with superior energy storage performance, Chem. Eng. J. 383 (2020) 123206. https://doi.org/10.1016/j.cej.2019.123206.

[100]   Y. Zhang, Y. Wang, J. Zhu, X. Zhang, W. Cai, Regulating the core/shell electric structure of Co3O4@Ni-Co layered double hydroxide on Ni foam through electrodeposition for a quasi-solid-state supercapacitor, Nanotechnology. 32 (2021). https://doi.org/10.1088/1361-6528/abe074.

[101]   L. Wang, H. Zhang, Y. Li, S. Xiao, F. Bi, L. Zhao, G. Gai, X. Yang, Construction of bundle-like cobalt/nickel hydroxide nanorods from metal organic framework for high-performance supercapacitors, J. Mater. Sci. Mater. Electron. 33 (2022) 10540–10550. https://doi.org/10.1007/s10854-022-08040-z.

[102]   S. Sardana, A. Gupta, K. Singh, A.S. Maan, A. Ohlan, Conducting polymer hydrogel based electrode materials for supercapacitor applications, J. Energy Storage. 45 (2022) 103510. https://doi.org/10.1016/j.est.2021.103510.

[103]   M.G. Sumdani, M.R. Islam, A.N.A. Yahaya, S.I. Safie, Recent advancements in synthesis, properties, and applications of conductive polymers for electrochemical energy

storage devices: A review, Polym. Eng. Sci. 62 (2022) 269–303. https://doi.org/10.1002/pen.25859.

[104]   Z. Chen, E. Villani, S. Inagi, Recent progress in bipolar electropolymerization methods toward one-dimensional conducting polymer structures, Curr. Opin. Electrochem. 28 (2021) 100702. https://doi.org/10.1016/j.coelec.2021.100702.

[105]   M.A.A. Mohd Abdah, N.H.N. Azman, S. Kulandaivalu, Y. Sulaiman, Review of the use of transition-metal-oxide and conducting polymer-based fibres for high-performance supercapacitors, Mater. Des. 186 (2020) 108199. https://doi.org/10.1016/j.matdes.2019.108199.

[106]   Q. Yang, J. Huang, J. Tu, K. Wu, H. Huang, D. Wang, J. Yao, L. Li, A micropore-dominant N,P,S-codoped porous carbon originating from hydrogel for high-performance supercapacitors mediated by phytic acid, Microporous Mesoporous Mater. 316 (2021) 110951. https://doi.org/10.1016/j.micromeso.2021.110951.

[107]   A.A. Vannathan, S. Maity, T. Kella, D. Shee, P.P. Das, S.S. Mal, In situ vanadophosphomolybdate impregnated into conducting polypyrrole for supercapacitor, Electrochim. Acta. 364 (2020) 137286. https://doi.org/10.1016/j.electacta.2020.137286.

[108]   S. Suriyakumar, P. Bhardwaj, A.N. Grace, A.M. Stephan, Role of Polymers in Enhancing the Performance of Electrochemical Supercapacitors: A Review, Batter. Supercaps. 4 (2021) 571–584. https://doi.org/10.1002/batt.202000272.

[109]   Z. Yue, H. Dunya, M. Ashuri, K. Kucuk, S. Aryal, S. Antonov, B. Alabbad, C.U. Segre, B.K. Mandal, Synthesis of a very high specific surface area active carbon and its electrical double-layer capacitor properties in organic electrolytes, ChemEngineering. 4 (2020) 1–15. https://doi.org/10.3390/chemengineering4030043.

[110]   Q. Zhu, J. Li, P. Simon, B. Xu, Two-dimensional MXenes for electrochemical capacitor applications: Progress, challenges and perspectives, Energy Storage Mater. 35 (2021) 630–660. https://doi.org/10.1016/j.ensm.2020.11.035.

[111]   S. Kumar, G. Saeed, L. Zhu, K.N. Hui, N.H. Kim, J.H. Lee, 0D to 3D carbon-based networks combined with pseudocapacitive electrode material for high energy density supercapacitor: A review, Chem. Eng. J. 403 (2021) 126352. https://doi.org/10.1016/j.cej.2020.126352.

[112]   S.S. Siwal, Q. Zhang, N. Devi, V.K. Thakur, Carbon-based polymer nanocomposite for high-performance energy storage applications, Polymers (Basel). 12 (2020) 1–30. https://doi.org/10.3390/polym12030505.

[113]   R. Shakil, M.N. Shaikh, S.S. Shah, A.H. Reaz, C.K. Roy, A.N. Chowdhury, M.A. Aziz, Development of a Novel Bio-based Redox Electrolyte using Pivalic Acid and Ascorbic Acid for the Activated Carbon-based Supercapacitor Fabrication, Asian J. Org. Chem. 10 (2021) 2220–2230. https://doi.org/10.1002/ajoc.202100314.

[114]   S. Alipoori, S. Mazinani, S.H. Aboutalebi, F. Sharif, Review of PVA-based gel polymer electrolytes in flexible solid-state supercapacitors: Opportunities and challenges, J. Energy Storage. 27 (2020) 101072. https://doi.org/10.1016/j.est.2019.101072.

[115]   Y.S. Hu, Y. Lu, The Mystery of Electrolyte Concentration: From Superhigh to Ultralow, ACS Energy Lett. 5 (2020) 3633–3636. https://doi.org/10.1021/acsenergylett.0c02234.

[116]   M. Wang, H. Wang, H. Zhang, X. Li, Aqueous K-ion battery incorporating environment-friendly organic compound and Berlin green, J. Energy Chem. 48 (2020) 14–20. https://doi.org/10.1016/j.jechem.2019.12.019.

[117]   R. Verma, P.N. Didwal, J.Y. Hwang, C.J. Park, Recent Progress in Electrolyte Development and Design Strategies for Next-Generation Potassium-Ion Batteries, Batter. Supercaps. 4 (2021) 1428–1450. https://doi.org/10.1002/batt.202100029.

[118]   F. Wan, J. Zhu, S. Huang, Z. Niu, High-Voltage Electrolytes for Aqueous Energy Storage Devices, Batter. Supercaps. 3 (2020) 323–330. https://doi.org/10.1002/batt.201900229.

[119]   D. Zhang, B. Yang, W. She, S. Gao, J. Wang, Y. Wang, K. Wang, H. Li, L. Han, Simultaneously achieving high energy and power density for ultrafast-charging supercapacitor built by a semi-graphitic hierarchical porous carbon nanosheet and a high-voltage alkaline aqueous electrolyte, J. Power Sources. 506 (2021) 230103. https://doi.org/10.1016/j.jpowsour.2021.230103.

[120]   D. Shi, M. Yang, B. Zhang, Z. Ai, H. Hu, Y. Shao, J. Shen, Y. Wu, X. Hao, BCN-Assisted Built-In Electric Field in Heterostructure: An Innovative Path for Broadening the Voltage Window of Aqueous Supercapacitor, Adv. Funct. Mater. 32 (2022) 1–10. https://doi.org/10.1002/adfm.202108843.

[121]   S. Pappu, T.N. Rao, S.K. Martha, S. V. Bulusu, Electrodeposited Manganese Oxide based Redox Mediator Driven 2.2 V High Energy Density Aqueous Supercapacitor, Energy. 243 (2022) 122751. https://doi.org/10.1016/j.energy.2021.122751.

[122]   V.D. Nithya, A review on holey graphene electrode for supercapacitor, J. Energy Storage. 44 (2021) 103380. https://doi.org/10.1016/j.est.2021.103380.

[123]   A. Ray, B. Saruhan, Application of ionic liquids for batteries and supercapacitors, Materials (Basel). 14 (2021). https://doi.org/10.3390/ma14112942.

[124]   F.I. Chowdhury, M.H. Buraidah, A.K. Arof, B.E. Mellander, I.M. Noor, Impact of tetrabutylammonium, iodide and triiodide ions conductivity in polyacrylonitrile based electrolyte on DSSC performance, Sol. Energy. 196 (2020) 379–388. https://doi.org/10.1016/j.solener.2019.12.033.

[125]   S.I. Wong, H. Lin, J. Sunarso, B.T. Wong, B. Jia, Optimization of ionic-liquid based electrolyte concentration for high-energy density graphene supercapacitors, Appl. Mater. Today. 18 (2020) 100522. https://doi.org/10.1016/j.apmt.2019.100522.

[126]   M. Okoshi, Y. Yamada, A. Yamada, H. Nakai, Theoretical Analysis on De-Solvation of Lithium, Sodium, and Magnesium Cations to Organic Electrolyte Solvents, J. Electrochem. Soc. 160 (2013) A2160–A2165. https://doi.org/10.1149/2.074311jes.

[127]   C. Zhong, Y. Deng, W. Hu, J. Qiao, L. Zhang, J. Zhang, A review of electrolyte materials and compositions for electrochemical supercapacitors, Chem. Soc. Rev. 44 (2015) 7484–7539. https://doi.org/10.1039/c5cs00303b.

[128]   D. Gandla, X. Wu, F. Zhang, C. Wu, D.Q. Tan, High-Performance and High-Voltage Supercapacitors Based on N-Doped Mesoporous Activated Carbon Derived from Dragon Fruit Peels, ACS Omega. 6 (2021) 7615–7625. https://doi.org/10.1021/acsomega.0c06171.

[129]   K. Karuppasamy, J. Theerthagiri, D. Vikraman, C.J. Yim, S. Hussain, R. Sharma, T. Maiyalagan, J. Qin, H.S. Kim, Ionic liquid-based electrolytes for energy storage devices: A brief review on their limits and applications, Polymers (Basel). 12 (2020) 1–37. https://doi.org/10.3390/POLYM12040918.

[130]   A.Y.S. Eng, Y. Wang, D.T. Nguyen, S.Y. Tee, C.Y.J. Lim, X.Y. Tan, M.F. Ng, J. Xu, Z.W. Seh, Tunable Nitrogen-Doping of Sulfur Host Nanostructures for Stable and Shuttle-Free Room-Temperature Sodium-Sulfur Batteries, Nano Lett. 21 (2021) 5401–5408. https://doi.org/10.1021/acs.nanolett.1c01763.

[131]   S. Son, B. Koo, H. Chai, H.V.H. Tran, S. Pandit, S.P. Jung, Comparison of hydrogen production and system performance in a microbial electrolysis cell containing cathodes made of non-platinum catalysts and binders, J. Water Process Eng. 40 (2021) 101844. https://doi.org/10.1016/j.jwpe.2020.101844.

[132]   P. Angelopoulou, G. Avgouropoulos, Effect of electrode loading on the electrochemical performance of LiAl0.1Mn1.9O4 cathode for lithium-ion batteries, Mater. Res. Bull. 119 (2019). https://doi.org/10.1016/j.materresbull.2019.110562.

[133]   P. Zhu, D. Gastol, J. Marshall, R. Sommerville, V. Goodship, E. Kendrick, A review of current collectors for lithium-ion batteries, J. Power Sources. 485 (2021) 229321. https://doi.org/10.1016/j.jpowsour.2020.229321.

[134]   A. Pullanchiyodan, L. Manjakkal, S. Dervin, D. Shakthivel, R. Dahiya, Metal Coated Conductive Fabrics with Graphite Electrodes and Biocompatible Gel Electrolyte for Wearable Supercapacitors, Adv. Mater. Technol. 5 (2020). https://doi.org/10.1002/admt.201901107.

[135]   R. Nölle, K. Beltrop, F. Holtstiege, J. Kasnatscheew, T. Placke, M. Winter, A reality check and tutorial on electrochemical characterization of battery cell materials: How to choose the appropriate cell setup, Mater. Today. 32 (2020) 131–146. https://doi.org/10.1016/j.mattod.2019.07.002.

[136]   Y. Xiao, R. Xu, C. Yan, J.Q. Huang, Q. Zhang, M. Ouyang, A Toolbox of Reference Electrodes for Lithium Batteries, Adv. Funct. Mater. 32 (2022) 1–19. https://doi.org/10.1002/adfm.202108449.

[137]   R. Ahmad, N.O. Laschuk, I.I. Ebralidze, O. V. Zenkina, E.B. Easton, Probing the Influence of Counter Electrode Structure on Electrochromic-Device Operating Potentials and Performance Using Electrochemical Impedance Spectroscopy, ChemElectroChem. 8 (2021) 2193–2204. https://doi.org/10.1002/celc.202100195.

[138]   E. Gottlieb, M. Kopeć, M. Banerjee, J. Mohin, D. Yaron, K. Matyjaszewski, T. Kowalewski, In-Situ Platinum Deposition on Nitrogen-Doped Carbon Films as a Source of

Catalytic Activity in a Hydrogen Evolution Reaction, ACS Appl. Mater. Interfaces. 8 (2016) 21531–21538. https://doi.org/10.1021/acsami.6b03924.

[139]   D.-H. Xia, S. Song, Y. Behnamian, W. Hu, Y.F. Cheng, J.-L. Luo, F. Huet, Review—Electrochemical Noise Applied in Corrosion Science: Theoretical and Mathematical Models towards Quantitative Analysis, J. Electrochem. Soc. 167 (2020) 081507. https://doi.org/10.1149/1945-7111/ab8de3.

[140]   S. Oswald, F. Riewald, H.A. Gasteiger, Novel Method for Monitoring the Electrochemical Capacitance by In Situ Impedance Spectroscopy as Indicator for Particle Cracking of Nickel-Rich NCMs: Part III. Development of a Simplified Measurement Setup, J. Electrochem. Soc. 169 (2022) 040552. https://doi.org/10.1149/1945-7111/ac67b3.

[141]   J.C. Martins, J.C. José, R.R. Passos, L.A. Pocrifka, Electrochemical behavior of polyaniline: A study by electrochemical impedance spectroscopy (EIS) in low-frequency, Solid State Ionics. 346 (2020) 115198. https://doi.org/10.1016/j.ssi.2019.115198.

[142]   S. Aderyani, P. Flouda, S.A. Shah, M.J. Green, J.L. Lutkenhaus, H. Ardebili, Simulation of cyclic voltammetry in structural supercapacitors with pseudocapacitance behavior, Electrochim. Acta. 390 (2021) 138822. https://doi.org/10.1016/j.electacta.2021.138822.

[143]   I.M. Badawy, A.M. Elbanna, M. Ramadan, N.K. Allam, Propping the electrochemical impedance spectra at different voltages reveals the untapped supercapacitive performance of materials, Electrochim. Acta. 408 (2022) 139932. https://doi.org/10.1016/j.electacta.2022.139932.

[144]   S. Breitenbach, J. Duchoslav, A.I. Mardare, C. Unterweger, D. Stifter, A.W. Hassel, C. Fürst, Comparative Behavior of Viscose-Based Supercapacitor Electrodes Activated by KOH, H2O, and CO2, Nanomaterials. 12 (2022) 1–10. https://doi.org/10.3390/nano12040677.

[145]   W. Tuichai, A. Karaphun, C. Ruttanapun, Ag nanomaterials deposited reduced graphene oxide nanocomposite as an advanced hybrid electrode material for Asymmetric Supercapacitor device, J. Alloys Compd. 849 (2020) 156516. https://doi.org/10.1016/j.jallcom.2020.156516.

[146]   S. Park, N.M. Shinde, P. V. Shinde, D. Lee, J.M. Yun, K.H. Kim, Chemically grown bismuth-oxy-iodide (BiOI/Bi9I2) nanostructure for high performance battery-type supercapacitor electrodes, Dalt. Trans. 49 (2020) 774–780. https://doi.org/10.1039/c9dt04365a.

[147]   L. Wei, W. Deng, S. Li, Z. Wu, J. Cai, J. Luo, Sandwich-like chitosan porous carbon Spheres/MXene composite with high specific capacitance and rate performance for supercapacitors, J. Bioresour. Bioprod. 7 (2022) 63–72. https://doi.org/10.1016/j.jobab.2021.10.001.

[148]   Y. Wang, D. Gu, J. Guo, M. Xu, H. Sun, J. Li, L. Wang, L. Shen, Maximized Energy Density of RuO2//RuO2 Supercapacitors through Potential Dependence of Specific Capacitance, ChemElectroChem. 7 (2020) 928–936. https://doi.org/10.1002/celc.201901898.

[149] H. Gupta, S. Chakrabarti, S. Mothkuri, B. Padya, T.N. Rao, P.K. Jain, High performance supercapacitor based on 2D-MoS2 nanostructures, Mater. Today Proc. 26 (2018) 20–24. https://doi.org/10.1016/j.matpr.2019.04.198.

[150] A. Zulkifli, M.A. Saadiah, N.F. Mazuki, A.S. Samsudin, Characterization of an amorphous materials hybrid polymer electrolyte based on a LiNO3-doped, CMC-PVA blend for application in an electrical double layer capacitor, Mater. Chem. Phys. 253 (2020) 123312. https://doi.org/10.1016/j.matchemphys.2020.123312.

[151] G.Z. Chen, Linear and non-linear pseudocapacitances with or without diffusion control, Prog. Nat. Sci. Mater. Int. 31 (2021) 792–800. https://doi.org/10.1016/j.pnsc.2021.10.011.

[152] O. Okhay, A. Tkach, Graphene/reduced graphene oxide-carbon nanotubes composite electrodes: From capacitive to battery-type behaviour, Nanomaterials. 11 (2021). https://doi.org/10.3390/nano11051240.

[153] S. Verma, A. Khosla, S. Arya, Performance of Electrochemically Synthesized Nickel-Zinc and Nickel-Iron (Ni–Zn//Ni–Fe) Nanowires as Battery Type Supercapacitor, J. Electrochem. Soc. 167 (2020) 120527. https://doi.org/10.1149/1945-7111/abaf72.

[154] D.J. Tarimo, A.A. Mirghni, K.O. Oyedotun, G. Rutavi, V.N. Kitenge, N. Manyala, Recycling of biomass wastes from amarula husk by a modified facile economical water salt method for high energy density ultracapacitor application, J. Energy Storage. 53 (2022) 105166. https://doi.org/10.1016/j.est.2022.105166.

[155] A.A. Mirghni, K.O. Oyedotun, B.A. Mahmoud, O. Fasakin, D.J. Tarimo, N. Manyala, A study of Co-Mn phosphate supported with graphene foam as promising electrode materials for future electrochemical capacitors, Int. J. Energy Res. 46 (2022) 3080–3094. https://doi.org/10.1002/er.7365.

[156] A.A. Mirghni, K.O. Oyedotun, O. Fasakin, B.A. Mahmoud, D.J. Tarimo, N. Manyala, High-performance bimetallic Ni-Mn phosphate hybridized with 3-D graphene foam for novel hybrid supercapacitors, J. Energy Storage. 31 (2020) 101584. https://doi.org/10.1016/j.est.2020.101584.

[157] N.O. Laschuk, E.B. Easton, O. V. Zenkina, Reducing the resistance for the use of electrochemical impedance spectroscopy analysis in materials chemistry, RSC Adv. 11 (2021) 27925–27936. https://doi.org/10.1039/d1ra03785d.

[158] C. Yun, S. Hwang, Analysis of the Charging Current in Cyclic Voltammetry and Supercapacitor's Galvanostatic Charging Profile Based on a Constant-Phase Element, ACS Omega. 6 (2021) 367–373. https://doi.org/10.1021/acsomega.0c04702.

[159] S. Li, Y. Cui, R. Kang, B. Zou, D.H.L. Ng, S.A. El-Khodary, X. Liu, J. Qiu, J. Lian, H. Li, Oxygen vacancies boosted the electrochemical kinetics of Nb2O5-xfor superior lithium storage, Chem. Commun. 57 (2021) 8182–8185. https://doi.org/10.1039/d1cc02299g.

[160] H. Zhang, Q. Huang, H. Wang, X. Shi, Efficient method to investigate the equivalent series resistance of a capacitor in low frequency range, IET Sci. Meas. Technol. 14 (2020) 494–498. https://doi.org/10.1049/iet-smt.2019.0131.

[161]   R. Rossi, B.E. Logan, Impact of external resistance acclimation on charge transfer and diffusion resistance in bench-scale microbial fuel cells, Bioresour. Technol. 318 (2020) 123921. https://doi.org/10.1016/j.biortech.2020.123921.

[162]   I. Vincent, E.C. Lee, H.M. Kim, Comprehensive impedance investigation of low-cost anion exchange membrane electrolysis for large-scale hydrogen production, Sci. Rep. 11 (2021) 1–12. https://doi.org/10.1038/s41598-020-80683-6.

[163]   N.E. Tolouei, S. Ghamari, M. Shavezipur, Development of circuit models for electrochemical impedance spectroscopy (EIS) responses of interdigitated MEMS biochemical sensors, J. Electroanal. Chem. 878 (2020) 114598. https://doi.org/10.1016/j.jelechem.2020.114598.

[164]   D.P. Burduhos-Nergis, P. Vizureanu, A.V. Sandu, C. Bejinariu, Evaluation of the corrosion resistance of phosphate coatings deposited on the surface of the carbon steel used for carabiners manufacturing, Appl. Sci. 10 (2020). https://doi.org/10.3390/APP10082753.

[165]   M.L. Sartorelli, A.M. Cutrim Gomes, M. de Pauli, C.P. da Silva Reis, R.B. Serpa, F. Toledo Reis, E.F. Jasinski, L.N. Chavero, R.L. Cavalcante, D. Galvão, Z. Ocubo Raulino, Y. Zhou, Y. Feng, T. von Windheim, M. Vasquez Sanchez, E. Ngaboyamahina, J.J. Amsden, C.B. Parker, J.T. Glass, Model-free capacitance analysis of electrodes with a 2D+1D dispersion of time constants, Electrochim. Acta. 390 (2021) 138796. https://doi.org/10.1016/j.electacta.2021.138796.

[166]   M.N. Rantho, M.J. Madito, F.O. Ochai-Ejeh, N. Manyala, Asymmetric supercapacitor based on vanadium disulfide nanosheets as a cathode and carbonized iron cations adsorbed onto polyaniline as an anode, Electrochim. Acta. 260 (2018) 11–23. https://doi.org/10.1016/j.electacta.2017.11.074.

[167]   S. Krishnan, A.K. Gupta, M.K. Singh, N. Guha, D.K. Rai, Nitrogen-rich Cu-MOF decorated on reduced graphene oxide nanosheets for hybrid supercapacitor applications with enhanced cycling stability, Chem. Eng. J. 435 (2022) 135042. https://doi.org/10.1016/j.cej.2022.135042.

[168]   S. Sarkar, R. Akshaya, S. Ghosh, Nitrogen doped graphene/CuCr2O4 nanocomposites for supercapacitors application: Effect of nitrogen doping on coulombic efficiency, Electrochim. Acta. 332 (2020) 135368. https://doi.org/10.1016/j.electacta.2019.135368.

[169]   N. Hillier, S. Yong, A. Cruden, S. Beeby, Acetonitrile-Free Organic Electrolyte for Textile Supercapacitor Applications, J. Electrochem. Soc. 168 (2021) 080520. https://doi.org/10.1149/1945-7111/ac1a58.

[170]   M. Kigozi, R. Kali, A. Bello, B. Padya, G.M. Kalu-Uka, J. Wasswa, P.K. Jain, P.A. Onwualu, N.Y. Dzade, Modified activation process for supercapacitor electrode materials from african maize cob, Materials (Basel). 13 (2020) 1–20. https://doi.org/10.3390/ma13235412.

[171]   M. Haque, Q. Li, C. Rigato, A. Rajaras, A.D. Smith, P. Lundgren, P. Enoksson, Identification of self-discharge mechanisms of ionic liquid electrolyte based supercapacitor under high-temperature operation, J. Power Sources. 485 (2021). https://doi.org/10.1016/j.jpowsour.2020.229328.

[172]   M. Haque, Q. Li, A.D. Smith, V. Kuzmenko, P. Rudquist, P. Lundgren, P. Enoksson, Self-discharge and leakage current mitigation of neutral aqueous-based supercapacitor by means of liquid crystal additive, J. Power Sources. 453 (2020). https://doi.org/10.1016/j.jpowsour.2020.227897.

CHAPTER 3

3.0. EXPERIMENTAL DETAILS AND CHARACTERISATION TECHNIQUES

The scope of this chapter is divided into two categories. The first part focuses on the synthesis of the materials, giving attention to different synthesis procedures and the instruments and devices employed in the synthesis process. The second part focuses on the devices used for the characterization of the synthesized materials and electrodes.

3.1. Experimental details

3.1.1. Preparation methods for electrode materials

3.1.1.1. Electrodeposition synthesis

Electrodeposition is one of the most favoured techniques which has evolved throughout two millennia for the synthesis of nanomaterials and films on various substrates. Factors contributing to the popularity of this method include its simplicity, easiness of reaction control, cost-effectiveness, environment friendliness and flexibility [214–216]. The method involves the application of an electric current or a potential between plates (electrodes) immersed in solution (electrolyte) where the precursors for the synthesized materials are dissolved. In a three-electrode configuration, the conducting working electrode (WE) is the substrate where the electrodeposition occurs. It comes in a variety of forms such as metal foils, metal foams, conductive glass, paper, and fabrics. The electrodeposition process can grow various textures, thicknesses, stoichiometry, and morphology [217]. The microstructure can vary from zero to three dimensions by varying parameters such as the proportions of precursors, concentration, pH, and viscosity of solution. The electrical current density and potential difference is applied

to grow materials which can be used in batteries, supercapacitors, electrocatalysis and photoelectrodes. Unlike deposition methods such as chemical vapour deposition (CVD) and e-beam deposition, it can be carried out at room temperature and pressure using non-sophisticated equipment. The process is scalable to industrial production. In this research theses cobalt nickel layered double hydroxide, Hausmannite sulphur reduced graphene oxide composite, manganese cobaltite and manganese chromite were synthesized using the electrodeposition process [218].

3.1.1.2. Annealing

Annealing is a process where materials are subjected to temperatures which are above their recrystallization temperature for a specific amount of time before being allowed to cool at a prescribed cooling rate [219]. The process of annealing can be carried out in a furnace under air or with different gases flowing. Atoms migrate in the crystal lattice during annealing, which leads to a reduction in dislocations causing a change in the hardness and ductility of materials [220]. During the cooling process, recrystallization takes place. The phase composition and the grain size depend on the heating temperature and cooling rate. This affects the properties of the materials such as electrical conductivity, ductility and magnetic properties [221].

3.1.2. Synthesis of electrode materials

3.1.2.1. Preparation of nickel foam substrates (NF)

NF (1 cm x 2 cm) pieces were carefully treated by dipping in 4M HCl, and acetone, followed by absolute ethanol and lastly deionized water (DW), for 20 minutes each. The cleaned pieces were left to dry in a normal oven at 60° C for 12 hours. This treatment was done to eliminate

the inert oxide or hydroxide layer on nickel metal surface which occurs in a humid environment [222].

3.1.2.2. Preparation of cobalt nickel layered double hydroxide (CN-LDH) on nickel foam (NF)

A 0.01 M of each cobalt nitrate hexahydrate Co $(NO_3)_2.6H_2O$ and nickel nitrate hexahydrate Ni $(NO_3)_2.6H_2O$ were dipped in 50 mL of DW and stirred thoroughly for 30 minutes to form the solution. Electrodeposition of cobalt nickel layered double hydroxide (CN) on NF was performed through the 3-electrode set-up using the Bio Logic VMP 300 workstation. The working electrode (WE) was chemically cleaned NF while platinum wire and Ag/AgCl worked as the counter electrode (CE) and reference electrode (RE), respectively. Cyclic voltammetry (CV) was done at a scan rate of 5 mV s^{-1} for 3 cycles in a potential range of -1.2 up to 0.5 V to deposit CN. The sample was then cleaned in DW and left to dry at 60 $^{\circ}$C for 12 hours. The process was repeated for 6 and 9 CV cycles. The samples were branded as CN-3, CN-6, and CN-9 where the number refers to the number of CV scan cycles. The schematic illustration of the synthesis CN electrode is shown in figure 3.1. The process commences with the reduction of nitrate anions at the cathode. This produces hydroxyl anions for the oxidation of cobalt cation to form CN as shown in equations 3.1 and 3.2 below:

$$NO_3^- + H_2O + 2e^- \rightarrow NO_2^- + 2OH^- \qquad \textbf{(3.1)}$$

.

69

$$Ni^{2+} + 2\,Co^{2+} + 6\,OH^- \rightarrow NiCo_2(OH)_6 \qquad\qquad \textbf{(3.2)}$$
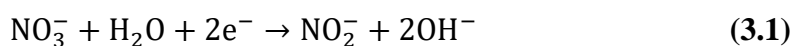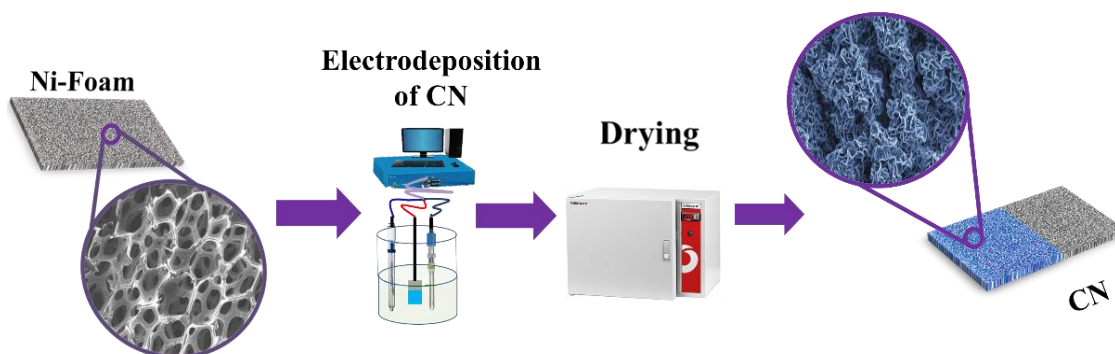
Figure 3.1: *Schematic illustration of the synthesis CoNi-LDH electrode.*

3.1.2.3. Preparation of reduced graphene oxide (RGO)

The synthesis of RGO in detail was explained in our previous work [30]. Graphene oxide (GO) was synthesized using the modified Hummer's method from graphite powder. Briefly, 5 g of graphite powder was slowly added to 100 mL of sulphuric acid (H_2SO_4). After that, 2.5 g of potassium hydrogen sulphate ($KHSO_4$) and calcium chloride ($CaCl_2$) were added subsequently while stirring. The resulting mixture was stirred at 400 rpm for 40 min at 60 ^{o}C, followed by the addition of 10 g of potassium permanganate ($KMnO_4$) and 50 mL of H_2SO_4. The solution was further stirred (250 rpm) for 2 hours at 60 ^{o}C for uniformity. The mixture was then left to cool down naturally to room temperature. Subsequently, 20 mL of hydrogen peroxide (H_2O_2 - 30 %) and 120 mL of deionized water DW were added. The resulting mixture called graphene oxide (GO) was allowed to cool down to room temperature, and subsequently re-dispersed into 100 mL of DW water and sonicated for 2 hours. The mixture was left to settle down for 12 hours, washed several times with DW water and then centrifuged and freeze-dried for 12 hours. The sample was labelled as reduced graphene oxide (RGO).

3.1.2.4. Preparation of sulphur-reduced graphene oxide (RGO-S)

RGO-S was synthesized by following the procedure explained in our previous work [30]. Briefly, 3g of sodium sulphide (Na_2S), and 3 g sulphur (S) were mixed in 100 ml of DW and then sonicated to form a uniform solution branded as A.50 mg of L-ascorbic acid was dissolved into 12 g of DW followed by the addition of 12 mL of hydrochloric (HCl). This solution was labelled B. 3 g of as-prepared RGO-S and sample B were then mixed and added into sample A. This was followed by the sonication of the mixture for 2 h and then stirring for 1 h at a temperature of 40 °C. The mixture was then left to settle on its own for 12 h. It was then rinsed with DW before undergoing centrifugation three times at 10, 000 rpm for 10 min and later freeze-drying for 24 h. The produced was labelled RGOS.

3.1.2.5. Preparation of Hausmannite/sulphur reduced graphene oxide (MO/RGO-S) composite on nickel foam (NF)

A 25 mg mass of RGO-S was then sonicated in DW for 12 hours. Electrodeposition of MO/RGO-S (where MO is Hausmannite) on NF was performed through a 3-electrode set-up using the Bio-Logic VMP-300 at room temperature. A solution was prepared by dissolving 0.16 M of manganese acetate tetrahydrate [$(CH_3COO_2)_2Mn. 4H_2O$] and 0.16 M of sodium sulphate (Na_2SO_4) into 200 mL of DW containing 25 mg RGO-S then stirring for 45 minutes. Na_2SO_4 served as a morphology-directing agent and assisted in reducing particle aggregation [223]. The RE and CE were as reported in section 3.1.2.2. The MO/RGO-S was grown using the galvanostatic electrodeposition method at 5 mA cm^{-2} for 30 minutes. MO/RGO-S on NF was then washed in DW and dried up at 80 °C for 5 hours. The deposition process was repeated by varying the mass of RGO-S in the solution. The samples were labelled MO and MO/RGO-S-25, MO/RGO-S-50, and MO/RGO-S- 75 depending on the mass of RGO-S in the solution and the mass loading of the material on NF was 0.9, 1.1, 1.0, and 1.2 mg, respectively. The

RGO-S nanorods are absorbed within the MO matrix. The steps for this electrodeposition synthesis are illustrated in the schematic in figure 3.2.
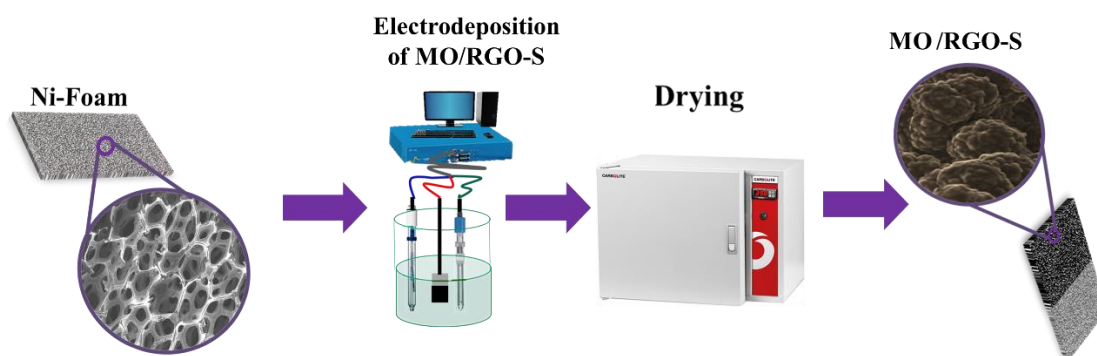
Figure 3.2: *Schematic illustration of the synthesis MO/RGO-S electrode.*

The process is summarized by equations 3.3 to 3.5:

$$NCH_3COO^- + H_2O \rightarrow CH_3COOH + OH^- \tag{3.3}$$

$$Mn^{2+} + 2OH^- \rightarrow Mn(OH)_2 \tag{3.4}$$

$$6\,Mn(OH)_2 + O_2 \rightarrow 2Mn_3O_4 + 6\,H_2O \tag{3.5}$$
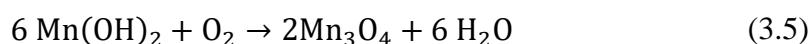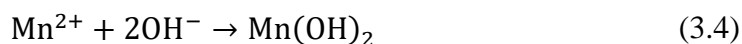
3.1.2.6. Preparation of CoNi-LDH on Mn₃O₄/RGO-S

The electrodeposition process followed the same steps as in section 3.1.2.2. but with MO as the WE in place of NF and 6 CV cycles were used because CN-6 yielded the best electrochemical results for 6 cycles. The process was also repeated with the samples produced in section **3.1.2.3.** with MO/RGO-S-25, MO/RGO-S-50, and MO/RGO-S-75 as the WE. The samples were labelled MO@CN, MO/RGO-S-25@CN, MO/RGO-S-50@CN, and MO/RGO-

S-75@CN with the total mass loading of the electrode's materials on NF as 1.0, 1.9, 2.1, 2.0, and 2.1 mg, respectively. The synthesis procedures are shown in figure 3.3.
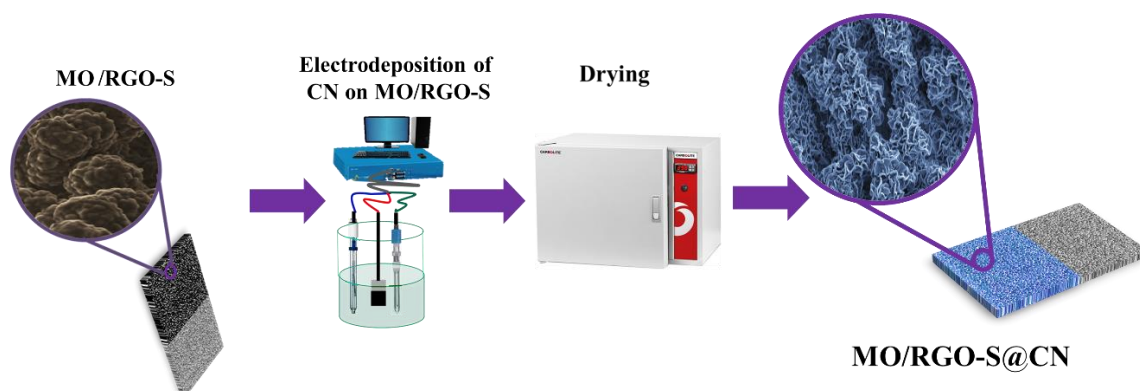
Figure 3.3: Schematic illustration of the synthesis of MO/RGO-S@CoNi-LDH electrode.

3.1.2.7. Preparation of activated carbon from cooked chicken bone waste (CCBW)

The cooked chicken bone waste activated carbon was synthesised following the procedure reported in our previous work [224]. In summary, the CCBW were treated with ethanol then left to dry at 60 $^{\circ}$C in the oven for 24 hours. The bones were pre-carbonized at 400 $^{\circ}$C for 4 hours using argon gas. Later, the pre-carbonized material was mixed with potassium hydroxide before the addition of a few drops of DW and dried up at 100 $^{\circ}$C for 12 hours. Thereafter, the mixture was carbonized at 700 $^{\circ}$C for 2 hours in an argon environment. The resulting sample was treated with 3 M HCl and washed with DW until neutrality was achieved in the pH scale. The product was dried in an oven for 24 hours at 60 $^{\circ}$C.

3.1.2.8. Preparation of manganese cobaltite (MCO) on NF electrode

Manganese acetate tetrahydrate [Mn $(CH_3COOH)_2 \cdot H_2O$] (0.006 mol) and cobalt nitrate hexahydrate [$Co(NO_3)_2 \cdot 6H_2O$] (0.012 mol) were mixed in 250 ml deionized water (DW) and agitated for 1 hour to produce a uniform solution. Sodium sulphate (Na_2SO_4) (0.01) was added

to the solution to serve as a morphology-directing agent and to avoid particle agglomeration. This solution was identified as S. The electrodeposition was carried out using Bio-Logic VMP-300 workstation operating on the EC-lab V11-30 (Edmonton, AB, Canada) at room temperature. The CE, RE and WE were as used in section 3.1.1.2 in a 3-electrode set-up. The electrodeposition was carried out using cyclic voltammetry (CV) at 1.25 mV s^{-1} for 6 cycles in a potential range of -1.2 to 0.5 V vs Ag/AgCl. The electrode which consisted of Co and Mn mixed oxides were then washed in DW and dried at 80°C in a normal oven for 5 hours then annealed in air at 200°C for 1 hour. Annealing helps to transform the phase structure from layered double hydroxides to the spinel phase [225]. The procedure was repeated at scan rates of 2.5 and 5 mV s^{-1}. The samples were identified as MCO-1.25, MCO-2.5 and MCO-5 depending on the scan rates used for synthesis. The mass loading of the deposited materials on NF were 1.4, 1.1 and 0.8 mg for MCO-1.25, MCO-2.5 and MCO-5, respectively.

3.1.2.9. Preparation of cobalt nickel layered double hydroxide on manganese cobaltite (MCO-LDH)

The synthesis of CN-LDH on NF substrate was like the one reported in section 3.1.2.2. To deposit CoNi-LDH on MCO-2.5, the procedure in section 3.1.2.2 was followed but with MCO-2.5 on NF as the WE. The CV was done at a scan rate of 2.5 mV s^{-1}. The electrodes were branded as MCO-2.5@CN-LDH. The steps are shown in figure 3.4.
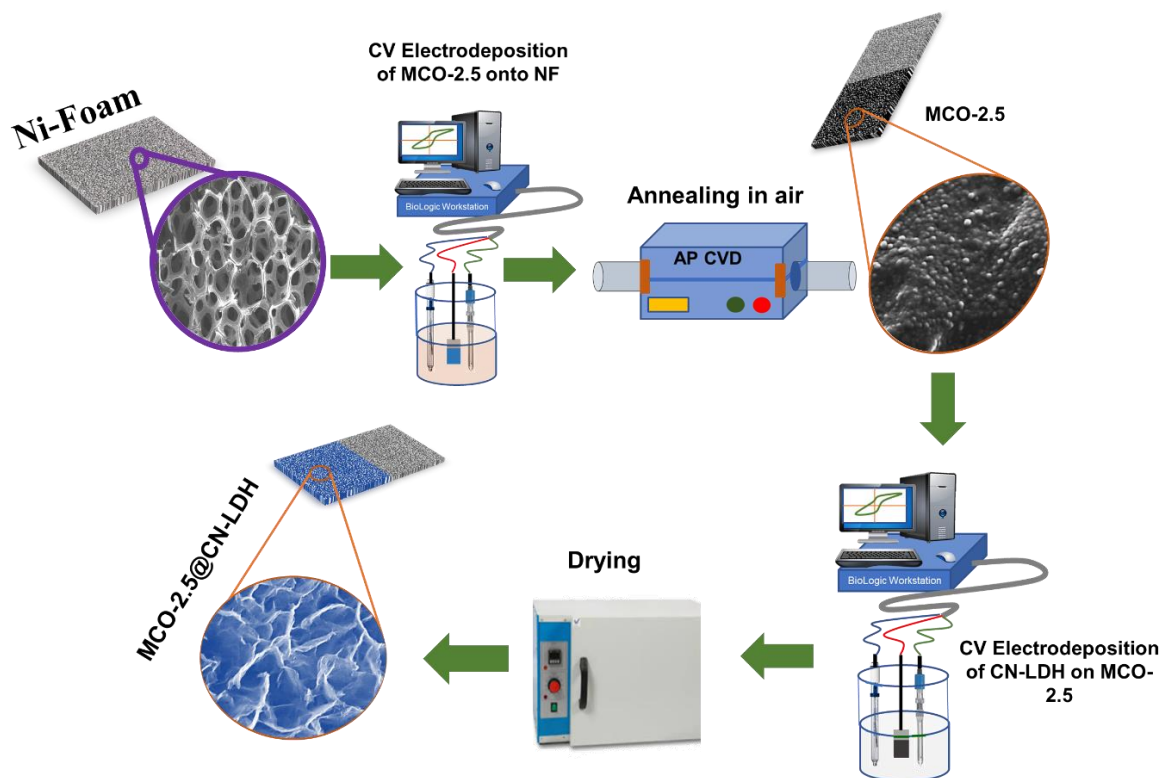
Figure 3.4: Schematic illustration of the synthesis of MCO-2.5@CN-LDH electrode.

3.1.2.10. Preparation of manganese chromite (MnCr$_2$O$_4$) on nickel foam (NF).

0.01M each of Chromium(III) potassium sulphate dodecahydrate [KCr$_2$(SO$_4$).12H$_2$O] and manganese acetate hexahydrate [Mn(CH$_3$CO$_2$)$_2$.4H$_2$O] were added to 500 ml DW and stirred for 30 minutes. 0.01 M sodium sulphate (Na$_2$SO$_4$) was then added to prevent aggregation and the stirring continued for a further 45 minutes. This solution was labelled S. To perform the electrodeposition, the Bio-Logic workstation was used, with the CE, RE and WE as described in the section, (3.1.2.2.), these were all dipped in S. Cycling voltammetry (CV) at 2.5 mV s^{-1} was used in a voltage range of -1.2 to 0.5 V vs Ag/AgCl. The voltage was repeated for voltage ranges -1.0 to 0.5 V vs Ag/AgCl and -1.4 to 0.5 V vs Ag/AgCl. The electrode was then washed in DW and dried in an oven at 90°C for 8 hours. The electrode was labelled as MnCr$_2$O$_4$-1.0, MnCr$_2$O$_4$-1.2, and MnCr$_2$O$_4$-1.4 according to their lower potential value.   Varying the voltage

range is an alternative way of altering the electrodeposition time which has effects on the thickness of the deposited film.

3.1.2.11 Preparation of manganese chromite cobalt nickel layered double hydroxide (MnCr$_2$O$_4$@CoNi-LDH)

The electrodeposition synthesis of MnCr$_2$O$_4$@CoNi-LDH was like the procedure in section 3.1.2.2 with the only exceptions being that MnCr$_2$O$_4$-1.2 V on NF was used as the WE instead of NF alone and the scan rate of 2.5 mV s^{-1} was utilised. After rinsing in DW, the electrode was dried at 60° C for 5 hours. The synthesis procedure is illustrated in figure 3.5.
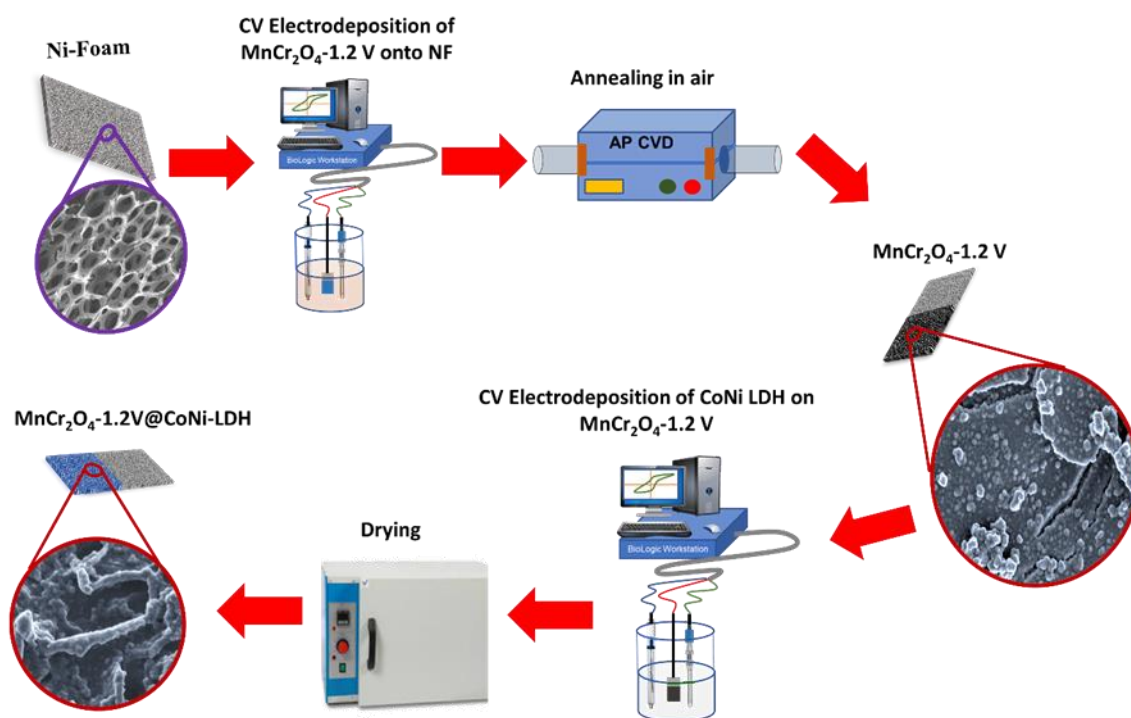
Figure 3.5: Schematic illustration of the synthesis of MnCr2 O4-1.2V@CoNi-LDH electrode.

3.1.2.12. Preparation of activated carbon biomass wastes from amarula seed husk (AMH)

The activated carbon nanostructure from the Amarula seed husk used in this thesis was prepared as reported in our previous work [195]. Briefly, the Amarula seed husks (AMH) were collected and washed thoroughly with DW followed by ethanol to remove impurities and then dried at 80 °C for 12 h. 1 g each of calcium chloride ($CaCl_2$) and phosphoric acid (H_3PO_4) together were dissolved into 70 ml of DW and stirred for 20 min followed by soaking 10 g of AMH into the mixture. The mixture was transferred into an autoclave and boiled at 150 °C for 12 h to let the raw material interact well with the mixture. The products were left to cool to room temperature, rinsed until getting a neutral pH then dried for 12 h at 80 °C. The dried products were mixed with potassium hydroxide (KOH) in a mass ratio of 1:1, followed by the addition of a few drops of DW then carbonized and activated at 700 °C (5 °C/min) for 2 h under argon (300 cm) environment. The products were treated with 3 M hydrochloric acid (HCl) and DW water until pH value showed neutrality, dried at 60 °C for 12 h and named as treated AMH activated carbon.

3.2. Materials characterization techniques

3.2.1. X-ray diffraction (XRD)

X-ray diffraction is a non-destructive analysis method that is used to extract information on the molecular structure, grain size, crystallinity, strain and crystal defects of the materials [226]. X-ray diffraction comprises three main components: the X-ray tube, the sample holder, and the detector [227].

When the filament is heated through the application of electric current, electrons are generated and accelerated towards the cobalt or copper target. When the electrons bombard the metal

target, a spectrum is generated when the electrons possess enough energy to liberate electrons from the inner shells of the atoms. The generated spectrum is then filtered and collimated to produce monochromatic X-ray radiation which is then directed towards the sample. Diffracted rays are produced when the X-rays interact with the sample due to constructive inference when the condition satisfies Bragg's law as shown in equation 3.6 [228].

$$n\lambda = 2d \sin\theta, \qquad n = 1, 2, 3, \dots \qquad (3.6)$$

where n is an integer number, λ is the wavelength (m) of the incident radiation, d is the interplanar spacing (m) and θ is the incident angle (degrees). The experimentally measured diffraction angle is 2θ. The schematic illustration of the X-ray diffraction is shown in Figures 3.5 (a) and (b). In this thesis, the XRD-Bruker BV 2D PHASER Best Benchtop (PANalytical BV, Amsterdam, Netherlands) with a $\theta/2\theta$ configuration utilizing Cu $K_{\alpha 1}$ source (wavelength $\lambda = 0.15406$ nm) at 30 mA and 50 kV using 0.005° step increment was used to analyse the samples. The schematic illustration of the XRD system and the main components are shown in figure 3.6.
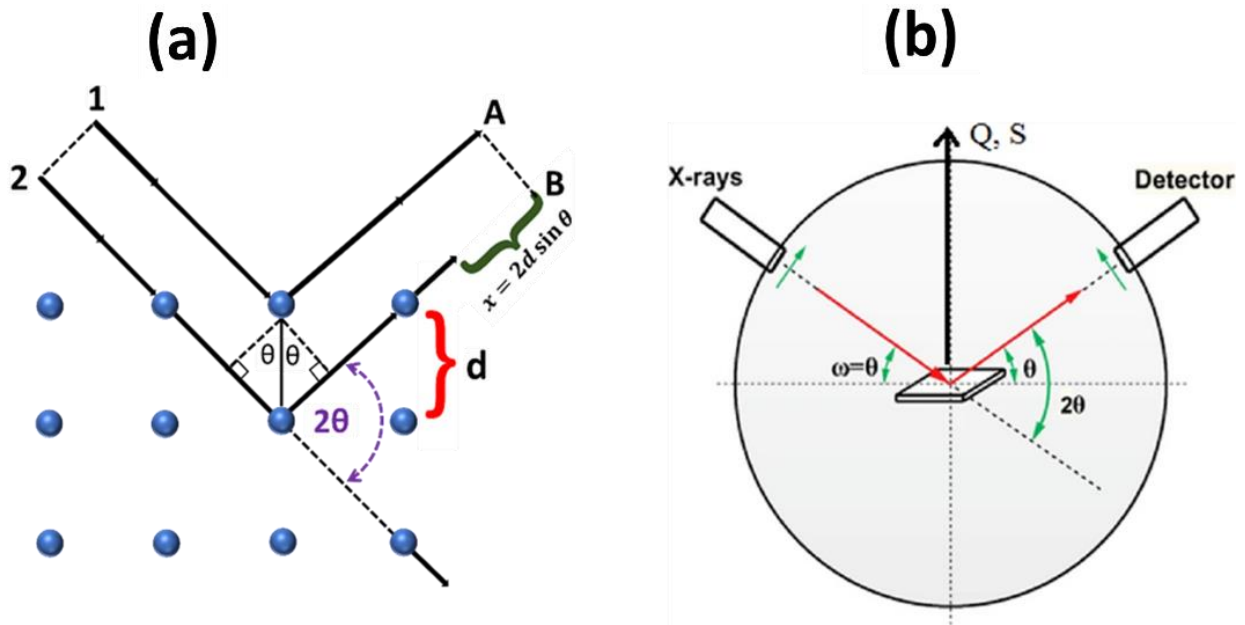
Figure 3.6: Schematic illustration (a) of the diffraction of incident X-rays by atomic planes, and (b) X-ray source sample and detector [18].

For spherical crystallite particles, the average crystallite size can be obtained by employing Scherer's equation [229]:

$$D = \frac{k\lambda}{\beta \cos\theta}$$

(3.7)

where *D* is the average crystalline size (nm), *k* is the Scherer's dimensionless constant, which is 0.89, λ is the wavelength of the X-ray, β is the full width at half maximum (radians), θ is the diffraction angle (radians).

3.2.3. Raman spectroscopy

Raman spectroscopy is a non-destructive technique used to extract information on the phase/chemical structure, molecular interaction, and crystallinity of substances [230]. In Raman spectroscopy, laser sources provide monochromatic incident radiation with

wavelengths in the visible, near-infrared or near-ultraviolet region of the spectrum [231]. The incident photons interact with the chemical bonds to cause the energy of the system to be increased from the ground state to a higher virtual energy. The virtual state is unstable making the system return to the ground state by emitting a photon. The most probable scenario is elastic scattering which occurs when the emitted photon has the same frequency as that of the incident photon, and this phenomenon is called Rayleigh scattering [232]. It is possible that the photon loses some of its energy on interaction with the molecule and disperses from the sample with lower energy, this inelastic process is called Stokes scattering [233]. In very rare cases when the molecule was in an excited state and then returns to the ground after interaction with the photon, then the sample gains energy from the interaction. This process which is less probable than the Stokes scattering at room temperature is called the Anti-Stoke scattering [234]. These interactions are illustrated using the Jablonski energy diagram in figure 3.7.
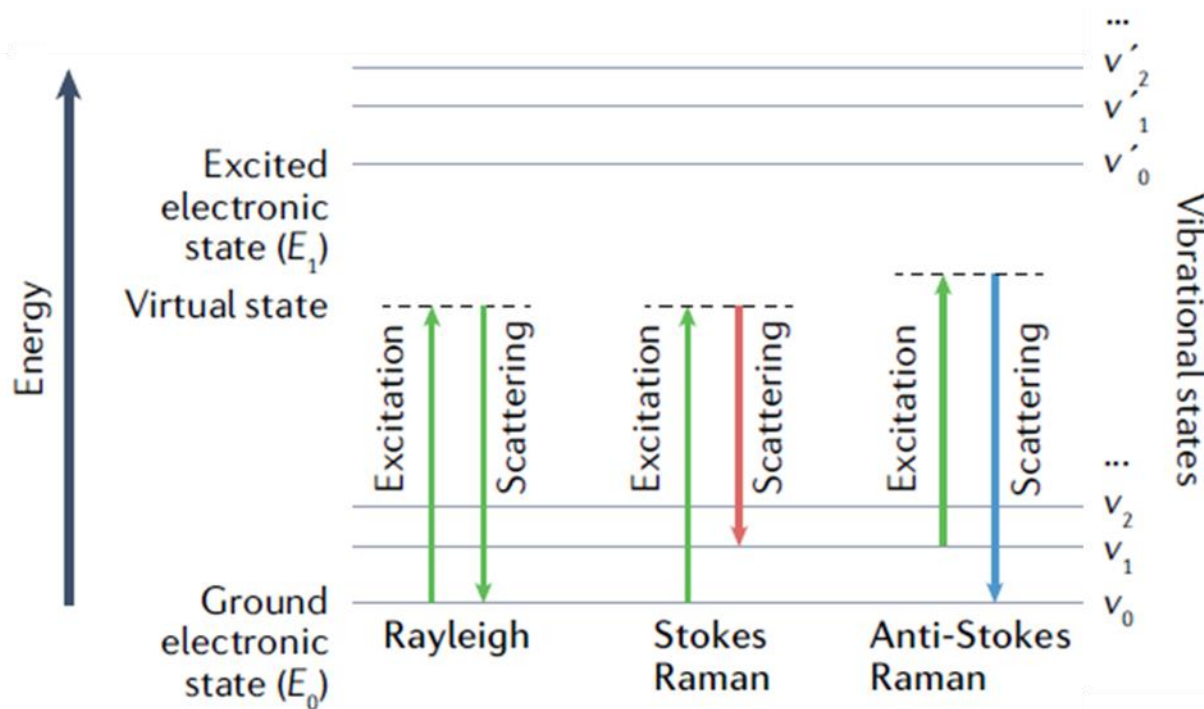
Figure 3.7: Part of the Jablonski energy diagram for the Rayleigh, Raman Stokes and the anti-Stoke transitions [25].

The transitions shown in the Jablonski diagram for Rayleigh, and Raman Stokes transitions can be summarised in equations 3.8 to 3.10 respectively [235]:

$$\hbar\omega_{Sc} = \hbar\omega_{L} \qquad (3.8)$$

$$\hbar\omega_{Sc} = \hbar\omega_{L} - \hbar\omega_{phonon} < 0 \qquad (3.9)$$

$$\hbar\omega_{Sc} = \hbar\omega_{L} + \hbar\omega_{phonon} \qquad (3.10)$$

where $\hbar\omega_{Sc}$ is the energy of the photon, $\hbar\omega_{L}$ is the energy of the incident laser radiation and $\hbar\omega_{phonon}$ is the phonon (vibration) energy. In this thesis, the WITEC Alpha 300 RAS+ Confocal micro-Raman microscope (Ulm, Germany) which is shown in figure 3.8 was used for the analysis of the samples. The laser wavelength of 532 nm was used with the spectral acquisition of 120 s, laser power of 4 mW and 50X objective.
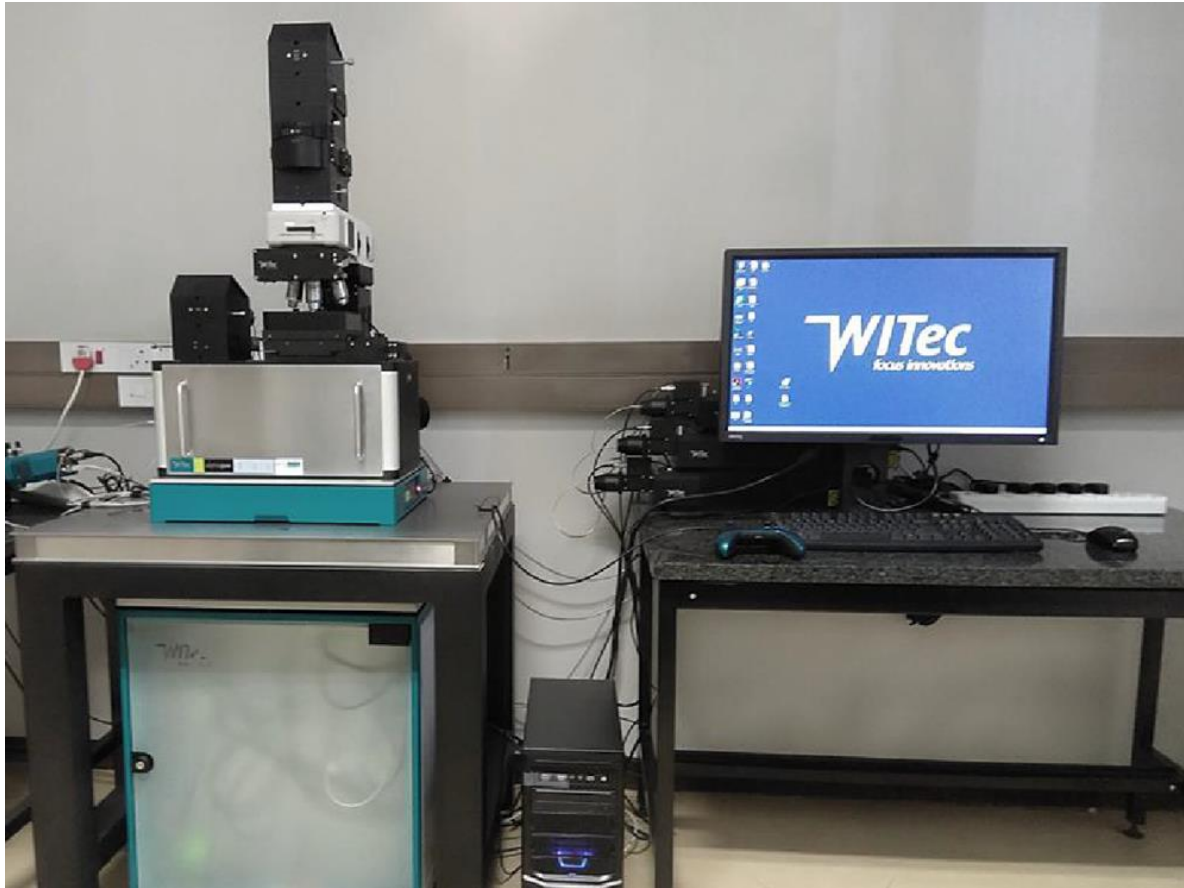
Figure 3.8: *A WITec Confocal Raman Microscope (WITec alpha 300 RAS+, Ulm,*

Germany)used for sample analysis in this work.

3.2.4. Scanning electron microscopy (SEM)

Scanning electron microscopy is an analysis method used on a sample to obtain information

such as topology, morphology, orientation and chemical composition [236]. The microscope's

main components are the source of the electrons, the column for electron passage, the

electromagnetic lenses, the electron detector, the sample chamber and the display. A Schottky

field emission source at the top of the column produces electrons under ultra-high vacuum

conditions. The beam is focused by passing through apertures and magnetic lenses. As the

electrons interact with the specimen, various signals such as secondary electrons (SE),

backscattered electrons, characteristic X-rays, bremsstrahlung X-rays, Auger electrons, transmitted electrons and cathodoluminescence are produced [237].

Energy dispersive X-ray spectroscopy (EDS) is a microanalysis technique used to evaluate the elemental composition in a sample. The EDS setup is usually incorporated into the SEM instrument and the measurements can occur concurrently [238]. A high beam of charged particles incident on the surface of the sample causes the emission of characteristic X-rays by causing the excitation of inner shell electrons.
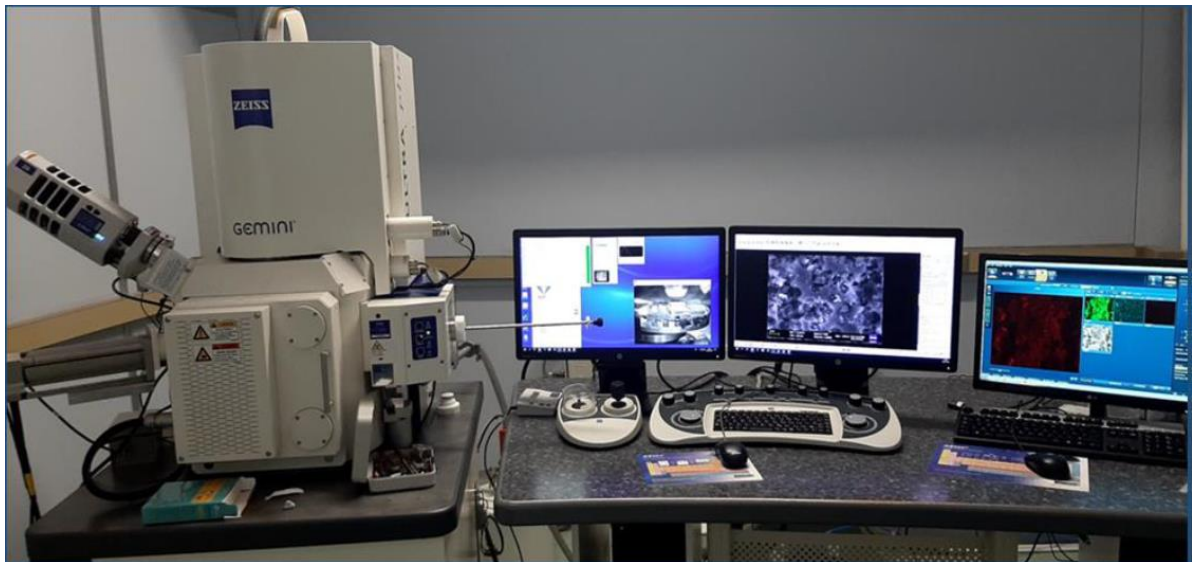
Figure 3.9: *High-resolution Field Emission Scanning Electron Microscope instrument (Zeiss, Ultra Plus 55 FE-SEM).*

The X-rays are then resolved with energy-dispersive detectors and integrated onto the SEM system. In this thesis, the SEM-Zeiss Ultra Plus 55 field emission scanning microscope Akishima-shi Japan) shown in figure 3.9 operating at 2.0 kV incorporating an energy dispersive X-ray spectroscopy (EDS) at 20 kV was used to analyse the morphology of the samples.

3.2.5. Transmission electron microscopy (TEM)

Transmission electron microscopy is a non-destructive imaging technique using transmission electron (TE) to get microstructure information on the specimen such as particle shape, crystal orientation, size, crystallinity and morphology [239]. Electrons under very high vacuum conditions are accelerated using very large potential differences. The beam is then narrowed by the electromagnetic lenses. On interaction with the samples, some of the beams bounce back while others are transmitted to form an image upon reaching the detector in the form of a charge-coupled device (CCD) or a fluorescent screen [240]. Unlike SEM which only images the surface of the samples, TEM is also able to image the interior of the samples with higher resolution enabling the extraction of information such as stress and crystallization. Due to the low de-Broglie wavelength of the accelerated electron, which is less than that of the visible spectrum, transmission electron microscopes are capable of yielding resolution three orders higher than light microscopes [241]. The JEOL JEM 2100-F transmission electron microscope shown in figure 3.10 operating at 200 kV was used to image the samples used in this thesis.

Figure 3.10: *Transmission electron microscope (JEOL JEM-2100F).*

3.3 Electrochemical characterization

The Bio-Logic VMP 300 workstation shown in figure 3.11 operating on the EC-lab V11-33 software was used to perform electrochemical evaluations.
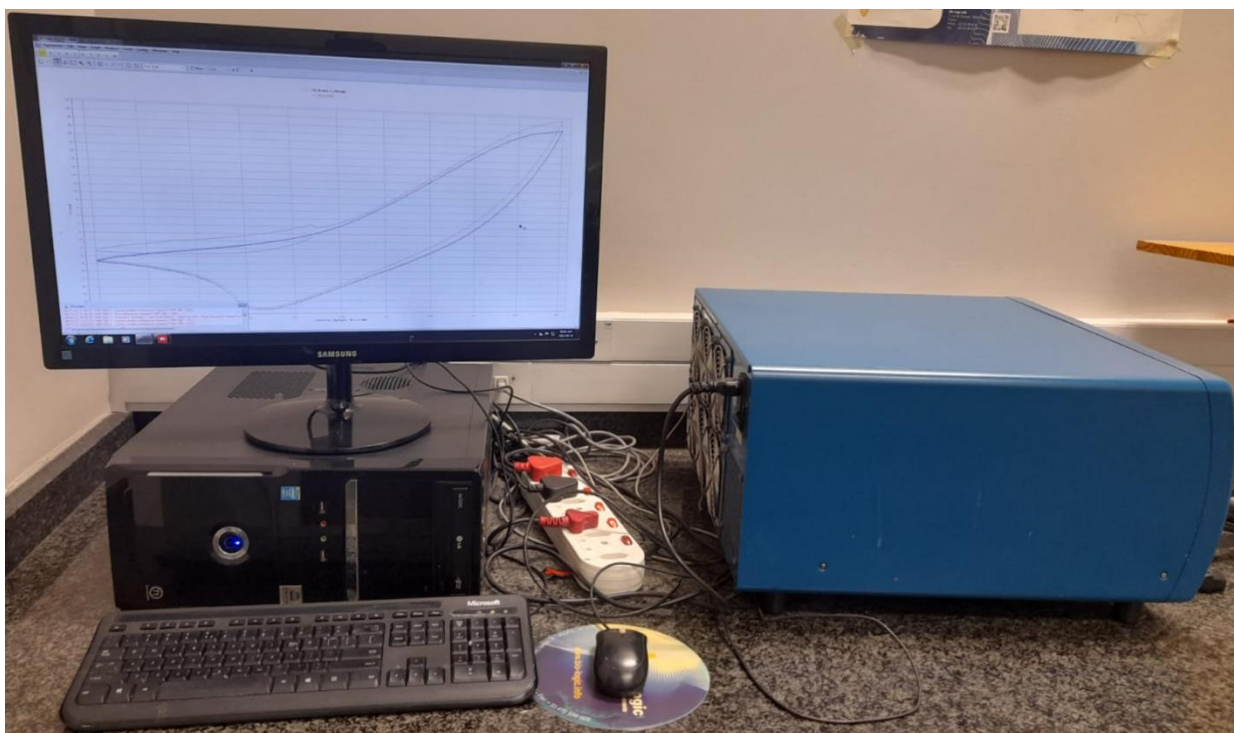
Figure 3.11: *Biologic VMP-300 potentiostat (Knoxville 37930, USA) operated by the EC-Lab V11.33 software.*

The preparation of the electrode used as the WE in the half-cell (three-electrode) configuration and the positive electrode in the device was done using the electrodeposition and annealing methods as described in section 3.1.2. For the positive electrode of the device, the electrode material was deposited on one side of the piece of nickel foam and then reshaped into circular disks. The negative electrode for the device was prepared using the pasting method whereby the AM was mixed with the polyvinylidene fluoride (binder) and the carbon black (conducting additive) using the ratio 8:1:1. A few drops of N-methyl-2-pyrrolidone (NMP) was added to make a homogeneous slurry after mixing. The slurry was then pasted on nickel foam disks then dried for 12 hours at 60° C.

Three and two-electrode set-ups were used to evaluate the electrochemical behaviour of the individual electrodes and the asymmetric devices, respectively. In three electrode set-ups, the

AM on NF, the platinum wire and Ag/AgCl served as the WE, CE and RE respectively. For the device, a separator was inserted between the disk-shaped electrodes in a coin cell. The CV, GCD and EIS were carried out in both configuration

References

[1]   S. Azmi, O.A. Layachi, M.E. Ouardi, E.M. Khoumri, A. Moujib, A.E. Brouzi, M. Nohair, L. Pezzato, M. Dabala, Growth of Cu2ZnSnS4 thin film absorber layer on transparent conductive oxides and molybdenum substrates by electrodeposition for photovoltaic application, Optik (Stuttg). 250 (2022) 168320. https://doi.org/10.1016/j.ijleo.2021.168320.

[2]   J. Pu, Z. Shen, C. Zhong, Q. Zhou, J. Liu, J. Zhu, H. Zhang, Electrodeposition Technologies for Li-Based Batteries: New Frontiers of Energy Storage, Adv. Mater. 32 (2020) 1–28. https://doi.org/10.1002/adma.201903808.

[3]   R. Li, Y. Li, P. Yang, D. Wang, H. Xu, B. Wang, F. Meng, J. Zhang, M. An, Electrodeposition: Synthesis of advanced transition metal-based catalyst for hydrogen production via electrolysis of water, J. Energy Chem. 57 (2021) 547–566. https://doi.org/10.1016/j.jechem.2020.08.040.

[4]   D. Tishkevich, S. Grabchikov, T. Zubar, D. Vasin, S. Trukhanov, A. Vorobjova, D. Yakimchuk, A. Kozlovskiy, M. Zdorovets, S. Giniyatova, D. Shimanovich, D. Lyakhov, D. Michels, M. Dong, S. Gudkova, A. Trukhanov, Early-stage growth mechanism and synthesis conditions-dependent morphology of nanocrystalline bi films electrodeposited from perchlorate electrolyte, Nanomaterials. 10 (2020) 1–17. https://doi.org/10.3390/NANO10061245.

[5]   S.A. Lee, J.W. Yang, S. Choi, H.W. Jang, Nanoscale electrodeposition: Dimension control and 3D conformality, Exploration. 1 (2021) 20210012. https://doi.org/10.1002/exp.20210012.

[6]   H. Pan, X. Shen, D. Li, Y. Liu, J. Cao, Y. Tian, H. Zhan, H. Wang, Z. Wang, Y. Xiao, Effect of annealing process on microstructure, texture, and mechanical properties of a Fe-Si-Cr-Mo-C deep drawing dual-phase steel, Crystals. 10 (2020) 1–16. https://doi.org/10.3390/cryst10090777.

[7]   Z. Tang, F. Jiang:, M. Long, J. Jiang, H. Liu, M. Tong, Effect of annealing temperature on microstructure, mechanical properties and corrosion behavior of Al-Mg-Mn-Sc-Zr alloy, Appl. Surf. Sci. 514 (2020). https://doi.org/10.1016/j.apsusc.2020.146081.

[8]   L. Xiao, M. Li, W. Cheng, H. Fan, X. Chen, Y. Sun, C. Ding, L. Yu, Influence of Annealing Methods on the Magnetic Properties and Flexural Strength of Iron-OER Soft Magnetic Composites, Adv. Mater. Sci. Eng. 2016 (2016). https://doi.org/10.1155/2016/5378276.

[9]   J. Zhang, W. Zhang, L. Xing, H. Su, Q. Xu, Experimental investigation on the effect of mixed acids etched nickel foam electrode on performance of an alkaline direct ethanol fuel cell, E3S Web Conf. 194 (2020). https://doi.org/10.1051/e3sconf/202019402021.

[10]   D.J. Tarimo, K.O. Oyedotun, A.A. Mirghni, N. Manyala, Sulphur-reduced graphene oxide composite with improved electrochemical performance for supercapacitor applications, Int. J. Hydrogen Energy. 45 (2020) 13189–13201. https://doi.org/10.1016/j.ijhydene.2020.03.059.

[11]   G.T. Pan, S. Chong, T.C.K. Yang, C.M. Huang, Electrodeposited porous

mn1.5co1.5o4/ni composite electrodes for high-voltage asymmetric supercapacitors, Materials (Basel). 10 (2017) 1–12. https://doi.org/10.3390/ma10040370.

[12] D.J. Tarimo, K.O. Oyedotun, N.F. Sylla, A.A. Mirghni, N.M. Ndiaye, N. Manyala, Waste chicken bone-derived porous carbon materials as high performance electrode for supercapacitor applications, J. Energy Storage. 51 (2022) 104378. https://doi.org/10.1016/j.est.2022.104378.

[13] H. Insight, E.S. Zhitova, H.C. Greenwell, M.G. Krzhizhanovskaya, D.C. Apperley, I. V Pekov, V.N. Yakovenchuk, Thermal Evolution of Natural Layered Double and Cl-Members of the Hydrotalcite Supergroup, (n.d.).

[14] D.J. Tarimo, A.A. Mirghni, K.O. Oyedotun, G. Rutavi, V.N. Kitenge, N. Manyala, Recycling of biomass wastes from amarula husk by a modified facile economical water salt method for high energy density ultracapacitor application, J. Energy Storage. 53 (2022) 105166. https://doi.org/10.1016/j.est.2022.105166.

[15] A. Ali, Y.W. Chiang, R.M. Santos, X-Ray Diffraction Techniques for Mineral Characterization: A Review for Engineers of the Fundamentals, Applications, and Research Directions, Minerals. 12 (2022). https://doi.org/10.3390/min12020205.

[16] S.R. Falsafi, H. Rostamabadi, S.M. Jafari, X-ray diffraction (XRD) of nanoencapsulated food ingredients, Elsevier Inc., 2020. https://doi.org/10.1016/b978-0-12-815667-4.00009-2.

[17] H. Khan, A.S. Yerramilli, A. D'Oliveira, T.L. Alford, D.C. Boffito, G.S. Patience, Experimental methods in chemical engineering: X-ray diffraction spectroscopy—XRD, Can. J. Chem. Eng. 98 (2020) 1255–1266. https://doi.org/10.1002/cjce.23747.

[18] M. Rabiei, A. Palevicius, A. Monshi, S. Nasiri, A. Vilkauskas, G. Janusas, Comparing methods for calculating nano crystal size of natural hydroxyapatite using X-ray diffraction, Nanomaterials. 10 (2020) 1–21. https://doi.org/10.3390/nano10091627.

[19] M. Panigrahi, B. Avar, Synthesis and Characterization of Binary Reduced Graphene Oxide/Metal Oxide Nanocomposites, Phys. Chem. Solid State. 23 (2022) 101–112. https://doi.org/10.15330/pcss.23.1.101-112.

[20] M.O. Guerrero-Pérez, G.S. Patience, M.A. Bañares, Experimental methods in chemical engineering: Raman spectroscopy, Can. J. Chem. Eng. 99 (2021) 97–107. https://doi.org/10.1002/cjce.23884.

[21] X. Bao, Y. Wang, Recent Advancements in Rayleigh Scattering-Based Distributed Fiber Sensors, Adv. Devices Instrum. 2021 (2021) 1–17. https://doi.org/10.34133/2021/8696571.

[22] F. Tebbenjohanns, M. Frimmer, V. Jain, D. Windey, L. Novotny, Motional Sideband Asymmetry of a Nanoparticle Optically Levitated in Free Space, Phys. Rev. Lett. 124 (2020) 13603. https://doi.org/10.1103/PhysRevLett.124.013603.

[23] N. Gupta, S. Kumar, S.B. Bhardwaj, Stimulated Raman scattering of self focused elliptical q-Gaussian laser beam in plasma with axial temperture ramp: effect of ponderomotive force, J. Electromagn. Waves Appl. 36 (2022) 767–786. https://doi.org/10.1080/09205071.2021.1983877.

[24] T.H. Kauffmann, N. Kokanyan, M.D. Fontana, Use of Stokes and anti-Stokes Raman scattering for new applications, J. Raman Spectrosc. 50 (2019) 418–424.

https://doi.org/10.1002/jrs.5523.

[25] F. Sepúlveda, N. Butto, J.L. Arias, M. Yazdani-Pedram, P.K. Szewczyk, A. Gruszczynski, U. Stachewicz, A. Neira-Carrillo, Effect of Porous and Nonporous Polycaprolactone Fiber Meshes on CaCO3Crystallization through a Gas Diffusion Method, Cryst. Growth Des. 20 (2020) 5610–5625. https://doi.org/10.1021/acs.cgd.0c00803.

[26] T. Walther, Measuring Non-Destructively the Total Indium Content and Its Lateral Distribution in Very Thin Single Layers or Quantum Dots Deposited onto Gallium Arsenide Substrates Using Energy-Dispersive X-ray Spectroscopy in a Scanning Electron Microscope, (2022).

[27] M. Tahirukaj, B. Olluri, A. Surleva, A study of the effect of working parameters and validation of SEM/EDS method for determination of elemental composition of commonly encountered GSR samples in shooting events in Kosovo, J. Forensic Sci. 66 (2021) 2393–2404. https://doi.org/10.1111/1556-4029.14803.

[28] C. Trager-Cowan, A. Alasamari, W. Avis, J. Bruckbauer, P.R. Edwards, G. Ferenczi, B. Hourahine, A. Kotzai, S. Kraeusel, G. Kusch, R.W. Martin, R. McDermott, G. Naresh-Kumar, M. Nouf-Allehiani, E. Pascal, D. Thomson, S. Vespucci, M.D. Smith, P.J. Parbrook, J. Enslin, F. Mehnke, C. Kuhn, T. Wernicke, M. Kneissl, S. Hagedorn, A. Knauer, S. Walde, M. Weyers, P.M. Coulon, P.A. Shields, J. Bai, Y. Gong, L. Jiu, Y. Zhang, R.M. Smith, T. Wang, A. Winkelmann, Structural and luminescence imaging and characterisation of semiconductors in the scanning electron microscope, Semicond. Sci. Technol. 35 (2020). https://doi.org/10.1088/1361-6641/ab75a5.

[29] J. Jeong, N. Cautaerts, G. Dehm, C.H. Liebscher, Automated Crystal Orientation Mapping by Precession Electron Diffraction-Assisted Four-Dimensional Scanning Transmission Electron Microscopy Using a Scintillator-Based CMOS Detector, Microsc. Microanal. 27 (2021) 1102–1112. https://doi.org/10.1017/S1431927621012538.

[30] S. Kretschmer, T. Lehnert, U. Kaiser, A. V. Krasheninnikov, Formation of Defects in Two-Dimensional MoS2 in the Transmission Electron Microscope at Electron Energies below the Knock-on Threshold: The Role of Electronic Excitations, Nano Lett. 20 (2020) 2865–2870. https://doi.org/10.1021/acs.nanolett.0c00670.

CHAPTER 4

4.0. RESULTS AND DISCUSSION

This chapter covers the results obtained after the synthesis and characterisation of all the materials. The source of all the results discussed in this chapter is the original research works of the author. Some of the work has already been published while the last paper is to be submitted to a particular journal for publication.

4.1 Two-step electrodeposition of Hausmannite sulphur reduced graphene oxide and cobalt-nickel layered double hydroxide heterostructure for high-performance supercapacitor

4.1.1. Introduction

Transitional metal oxides (TMO) and hydroxides (TMOH) have been preferred for use as positive electrodes for supercapacitor applications. This is attributed to their specific capacities which are superior to carbon-based materials such as activated carbon (AC) [146]. Bimetallic metal hydroxides such as layered double hydroxides (LDH) which are environmentally friendly and naturally abundant have the potential to yield amazing electrochemical performance because of their unique porous lamellar structure, tuneable composition, and great redox ability due to the presence of abundant exposed redox-active sites [242]. Cobalt Nickel layered double hydroxide (CN) has a potential for excellent electrochemical performance because of the synergies of nickel (Ni) and cobalt (Co) metals which provide a various oxidation state and the large interlayer distance. However, one of the major set-back of CN is the low electrical conductivity which is caused by the restacking of the layers during charge-discharge process [243]. This can be alleviated by a careful fabrication of a hierarchical structure which provides mechanical support of the structure to minimise the restacking and improve the electrical

conductivity. The composite of Hausmannite (Mn_3O_4) and sulphur-reduced graphene oxide (RGO-S) can improve the performance of CoNi-LDH. Naturally abundant and environmentally friendly Mn_3O_4 improves the electrochemical performance of CN due to the Jahn-Teller effect of the Mn^{3+} which improves ion diffusion [244]. The presence of divalent and trivalent ions also improves the electrochemical activity. RGO-S benefits from the high mechanical strength and electrical conductivity to provide the support needed to minimise restacking thereby increasing the stability while improving electron transport. The presence of sulphur in RGO-S also improves wettability [30]. Different mass loading X (X=0, 25, 50 and 75 mg) of RGO-S were added to MO before electrodeposition on NF to form MO/RGO-S-X. The second electrodeposition was performed to form the final electrode: MO/RGO-S-X@CN. SEM, TEM, EDS, XRD and Raman spectroscopy was carried out on the electrodes. For the electrochemical performance of the electrodes in a three-electrode configuration, the best electrode, MO/RGO-S-50@CN used in a 2 M KOH electrolyte.

4.1.2. Results and discussion

The results for the synthesis procedures, characterisation and electrochemical evaluations are detailed in the following attached publication.

RESEARCH ARTICLE

INTERNATIONAL JOURNAL OF
ENERGY RESEARCH   WILEY

Two-step electrodeposition of Hausmannite sulphur reduced graphene oxide and cobalt-nickel layered double hydroxide heterostructure for high-performance supercapacitor

Gift Rutavi | Delvina Japhet Tarimo | Vusani Muswa Maphiri |
Ncholu Manyala [ORCID]

Department of Physics, Institute of
Applied Materials, SARChI in Carbon
Technology and Materials, University of
Pretoria, Pretoria, 0002, South Africa

Correspondence
Ncholu Manyala, Department of Physics,
Institute of Applied Materials, SARChI in
Carbon Technology and Materials,
University of Pretoria, Pretoria 0002,
South Africa.
Email: ncholu.manyala@up.ac.za

Summary

Hausmannite/sulphur reduced graphene oxide (MO/RGO-S) and cobalt-nickel layered double hydroxide (CN) composite was synthesized through a two-step electrodeposition approach. This process began with galvanostatic electrodeposition of MO/RGO-Son a nickel foam, followed by cyclic voltammetry electrodeposition of CN. The inclusion of RGO-S increases the electrical conductivity of the active material (AM) and its wettability while Mn_3O_4 (MO) enhances the pseudocapacitive active sites which help to increase the specific capacity of CN. The materials' electrochemical evaluations were carried out via three- and two-electrode configurations using 2 M KOH electrolyte. An enhanced composite material (MO/RGO-S-50@CN) produced a phenomenal specific capacity of 582.1 mA h g^{-1} in a three-electrode configuration at 0.5 A g^{-1}. The device (MO/RGO-S-50@CN//CCBW) consisting of MO/RGO-S-50@CN and activated carbon from cooked chicken bone waste (CCBW) as positive and negative electrodes, respectively delivered specific energy of 56.0 Wh kg^{-1} with a specific power of 515.0 W kg^{-1} at a specific current of 0.5 A g^{-1}. The device produced capacity retention of 85.1% and coulombic efficiency of 99.7% at 10 000 galvanostatic charge-discharges cycles at 6 A g^{-1}. Because of these excellent results, the fabricated materials demonstrated great potential for application as a high specific energy supercapacitor.

KEYWORDS

energy storage, hybrid capacitor, layered double hydroxide, specific capacity, spinels

1 | INTRODUCTION

There are rising concerns over problems caused by the continued use of fossil fuels as an energy source. This is because of the pressure exerted on the environment and the depletion of fossil fuels. The intermittent nature of renewable sources of energy and the insufficient energy they produce is hampering the transformation from non-renewable to safer renewable energy sources.[1] From this background, it is essential to channel resources in researching on improving storage devices for renewable energy. Supercapacitors have been proven to have a very important contribution to renewable energy storage. This is because they possess some more favourable properties

compared to batteries and fuel cells such as larger specific power, more rapid charge-discharge, longer cyclic life, and they are more environmentally benign.[2,3] Supercapacitors are classified into pseudocapacitors (PS), electric double-layer capacitors (EDLC), and battery-type capacitors.[4] Battery-type capacitors and pseudocapacitors have become very popular in energy-storage, because of their reversible and rapid redox reactions at the electrolyte-electrode interface leading to very high theoretical specific capacities.[5]

Transitional metal hydroxides (TMOH) which include $Co(OH)_2$ and $Ni(OH)_2$ are commonly utilised as battery-type materials owing to their low costs and abundant natural reserves.[6,7] However, these TMOH possess experimental capacities which are much less than their theoretical capacities. This is due to very low intrinsic electrical conductivities ($\approx 10^{-5}$ to 10^{-8} S.cm^{-1}) and limited diffusion pathways.[8] Hybrid hydroxides can alleviate this problem due to the synergistic effect of multiple components of materials consisting of more than one TMOHs such as layered double hydroxides (LDHs).

LDHs are inorganic, brucite-like materials with interlaminar anion between TMOH layers. The structure of LDH is $\left[M_{1-x}^{2+} M_x^{3+}(OH)_2\right]^{x+}(A^{n-})_{\frac{x}{n}}.mH_2O$, where M^{3+} and M^{2+} are trivalent and divalent metals respectively, x = $M^{3+}/(M^{2+}+M^{3+})$ is the proportion of the divalent metal M^{3+} and also the layer charge density, A^{n-} is the interlaminar organic or inorganic anion to balance the charges. This unique structure leads to high anion exchange capacity and tunable chemical composition which makes them suitable for use in supercapacitors.[9-12] LDHs which possess a 2D structure, are better alternatives to TMOHs as they exhibit larger theoretical specific surface area and possess many redox-active sites which enhance ion exchange and intercalation, promote redox reactions, flexible ion interchangeability, and increase the number of structural defects.[13]

Several methods have been utilised to synthesise LDHs, these include, electrodeposition, microwave-assisted synthesis, co-precipitation, and solvothermal synthesis.[14,15] Electrodeposition is a more favourable method for the synthesis of LDHs. This is due to attributes such as low cost and efficient utilisation of active materials, morphology control, the absence of binders, and strong adhesive forces between AM and the current collector (substrate). These properties endow electrodeposited LDHs with a larger specific capacity, higher rate capability, and cyclic stability.[16,17]

LDHs, however, suffer from low electrical conductivity, low cyclic performance, aggregation, poor electrochemical stability, and poor rate capability due to slow reaction kinetics at high specific currents when performing charge-discharge processes.[18,19] This can be alleviated by producing a highly conductive and more stable heterostructure system with spinels configuration.[20] Spinels, which possess chemical structure MM'_2O_4, with M and M' as divalent and trivalent metals respectively benefit from having high electrochemical activity due to reversible adsorption characteristics, multivalent charge transport, elevated chemical stability, and increased redox reactions, these attributes increase the theoretical specific capacity. This is a result of the improvement of electron transport efficiency and ion diffusion ratio.[21,22] The composite will benefit from the synergistic effect of different properties mentioned above and hence deliver a very high specific capacity.

Mn_3O_4 (Hausmannite) is one of the spinels structure that has been researched intensively as an electrode due to several favourable attributes which include large theoretical capacitance (1370 F g^{-1}),[23] a wide range of active oxidation states, environmental safety, stable potential window in aqueous electrolyte and an outstanding Jahn-Teller effect.[24,25] However, it suffers from low electrical conductivity which reduces its performance. This can be improved by making a composite with functionalized carbon materials. Sulphur-reduced graphene oxide (RGO-S) is one of the most favourable among the functionalized carbon materials because of the high electrical conductivity, enhanced redox-active sites, stability, and excellent wettability with electrolyte ions.[26]

The objectives of this study are to utilise a binder-free method to synthesize a composite electrode with three different types of materials, to perform structural and electrochemical characterisation of the composite and to incorporate it into the electrode for supercapacitor device. Only a few studies have reported the combination of cobalt-nickel layered double hydroxide and Hausmannite spinel for supercapacitor applications. In this study, we are reporting for the first time the combination of cobalt-nickel layered double hydroxide, hausmannite spinel, and carbon material through a binder-free and conductive additive-free synthesis route for supercapacitor applications. Also, the method is simple, safe, and cost-effective as it is carried out at room temperature and atmospheric pressure and only very little material is lost during synthesis.

We are hereby reporting a two-step electrodeposition synthesis method to synthesise MO/RGO-S-X@CN heterostructure as a positive supercapacitor electrode where X denotes various masses in mg of RGO-S in the composite. MO/RGO-S-50@CN electrode produced the highest electrochemical attributes with an excellent specific capacity of 582.1 mAh g^{-1} at a specific current of 0.5 A g^{-1} in a three-electrode set up ahead of other

composites. Furthermore, this electrode presented a capacity retention of 86.5% and a coulombic efficiency of 99.9% after 5000 GCD cycles at 6 A g^{-1}. An asymmetric device was constructed by employing MO/RGO-S-50@CN as a positive electrode with CCBW as the negative electrode. This device MO/RGO-S-50@CN//CCBW produced specific energy of 56.0 Wh kg^{-1} at a specific current of 0.5 A g^{-1} with a specific power of 515.0 W kg^{-1}. The device also produced a coulombic efficiency of 99.7% after 10 000 GCD cycles at 6 A g^{-1}. This study presents a novel approach of combining multiple electrode materials with different energy storage mechanisms by utilising just one simple binder-free method to produce excellent performance electrodes which are suitable contenders for high specific energy and power supercapacitor devices.

2 | EXPERIMENTAL SECTION

2.1 | Materials

Only analytic quality chemicals were used in this research and no further processing of the chemicals was involved. These are the chemicals and materials used: nickel foam [NF] purchased from Alantum (Munich, Germany). Ethanol [CH_3CH_2OH], acetone [$(CH_3)_2 CO$], and hydrochloric acid [HCl] were bought from (Sigma Aldrich, Steinheim, Germany). Nickel nitrate hexahydrate [Ni (NO_3)$_2$·6H_2O], cobalt nitrate hexahydrate [Co (NO_3)$_2$·6H_2O], sodium sulphate [Na_2SO_4], manganese acetate hexahydrate [$Mn(CH_3COO)_2$·4H_2O], sulphur, and sodium sulphide [Na_2S] were supplied from Merck (Johannesburg, South Africa). Deionised water (DW) was obtained using a DRAWELL purification machine.

2.2 | Preparation of NF substrates

NF (1 cm × 2 cm) pieces were thoroughly treated by immersing in 4 M HCl, acetone, followed by absolute ethanol and finally deionised water, each for 20 minutes. The treated pieces were left to dry in an oven at 60°C for 12 hours. This procedure was done because nickel metal is susceptible to forming inert oxide or hydroxide layer in a humid environment.

2.3 | Synthesis of CN on NF

A 0.01 M of each Co (NO_3)$_2$·6H_2O and Ni (NO_3)$_2$·6H_2O were immersed in 50 mL of DW and stirred vigorously for 30 minutes to form the solution. Electrodeposition of

CN on NF was performed via the 3-electrode set-up using the Bio Logic VMP 300 workstation (Knoxville, USA) controlled by EC-Lab V11.33 (Edmonton, AB, Canada). The working electrode (WE) was pre-treated NF while platinum wire and Ag/AgCl served as the counter electrode (CE) and reference electrode (RE), respectively. Cyclic voltammetry (CV) was carried out at a scan rate of 5 mV s^{-1} for 3 cycles within a potential range −1.2 up to 0.5 V to deposit CN. The sample was then rinsed in DW and left to dry at 60 °C for 12 hours. The procedure was repeated for 6 and 9 CV cycles. The samples were labelled as CN-3, CN-6, and CN-9 where the number refers to the number of CV scan cycles.

2.4 | Synthesis of MO/RGO-S composite on NF

RGO-S was produced using the procedure conveyed in our previous work.[27] A 25 mg of RGO-S was then sonicated in DI water for 12 hours. Electrodeposition of MO/RGO-S on NF was performed via 3-electrode set-up using the Bio-Logic VMP-300 at room temperature. A solution was prepared by dissolving 0.16 M of Mn (CH_3COO)$_2$·4H_2O and 0.16 M of Na_2SO_4 into 200 mL of DI water containing 25 mg RGO-S then stirring for 45 minutes. Na_2SO_4 served as a morphology directing agent and also helped minimise particle aggregation.[28] The RE and CE were as reported in Section 2.3. The Mn_3O_4/RGO-S was grown using the galvanostatic electrodeposition method at 5 mA cm^{-2} for 30 minutes. Mn_3O_4/RGO-S on NF was then washed in DW and dried up at 80°C for 5 hours. The deposition process was repeated by changing the mass of RGO-S in the solution. The samples were labelled MO (ie, Mn_3O_4 without RGO-S) and MO/RGO-S-25, MO/RGO-S-50, and MO/RGO-S-75 according to the mass of RGO-S in the solution and the mass loading of the material on NF was 0.9, 1.1, 1.0, and 1.2 mg, respectively.

2.5 | Synthesis of CN on MO/RGO-S

The electrodeposition process followed the same procedure in Section 2.3 but with MO as the WE instead of NF and 6 CV cycles were used because CN-6 produced superior electrochemical results. The procedure was also repeated with the samples produced in Section 2.4 as MO/RGO-S-25, MO/RGO-S-50, and MO/RGO-S-75 as the WE. The samples were labelled MO@CN, MO/RGO-S-25@CN, MO/RGO-S-50@CN, and MO/RGO-S-75@CN with the total mass loading of the electrode's materials on NF as 1.0, 1.9, 2.1, 2.0, and 2.1 mg, respectively.

FIGURE 1 Schematic illustration of the synthesis of Mn_3O_4/RGO-S@CN electrode

2.6 | Synthesis of CCBW

The activated carbon from cooked chicken bone waste (CCBW) was synthesized as follows: The CCBW were cleaned with ethanol then left to dry at 60°C in the oven for 24 hours. A 5 g of the bones were pre-carbonized at 400°C for 4 hours using argon gas (200 sccm in a flow rate of 5°C/min) to remove volatile particles and impurities. Subsequently, the pre-carbonized material was mixed with potassium hydroxide (weight ratio of 1:1) as an activating agent in the agitate motor followed by the addition of a few drops of DW to form a compacted block-like structure which was dried up at 100°C for 12 hours. Thereafter, the mixture was carbonized at 700°C for 2 hours in an argon environment (300 sccm at 5°C/min). The attained sample was treated with 3 M HCl and washed with DW until neutrality was attained in the pH scale. The obtained sample was dried up for 24 hours in an oven at 60°C.

2.7 | Material characterisation

The electrodeposition of MO/RGO-S as displayed in Figure 1 began with the reduction of the acetate anions (CH_3COO^-) to acetic acid (CH_3COOH) at the cathode. This introduces hydroxyl anions (OH^-) into the sodium sulphate electrolyte. This leads to the deposition of manganese hydroxide on the nickel foam anode, which is then oxidised to Mn_3O_4 in the air. The GO-S nanorods are absorbed within the Mn_3O_4 matrix. The process is summarised by Equation (1) to (3):

$$CH_3COO^- + H_2O \rightarrow CH_3COOH + OH^-, \quad (1)$$

$$Mn^{2+} + 2OH^- \rightarrow Mn(OH)_2, \quad (2)$$

$$6Mn(OH)_2 + O_2 \rightarrow 2Mn_3O_4 + 6H_2O. \quad (3)$$
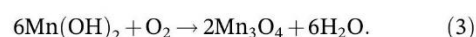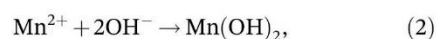
For the electrodeposition of CN on MO/RGO-S, the process commences with the reduction of nitrate anions at the cathode. This produces hydroxyl anions for the oxidation of cobalt cation to form CN as shown in Equations (4) and (5) below:

$$NO_3^- + H_2O + 2e^- \rightarrow NO_2^- + 2OH^-, \quad (4)$$

$$Ni^{2+} + 2Co^{2+} + 6OH^{-1} \rightarrow NiCo_2(OH)_6. \quad (5)$$
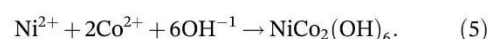
X-ray diffraction (XRD) was employed to evaluate the samples' structure, The instrument incorporates a diffractometer (Brucker 2D PAN analytical BV, Amsterdam, Netherlands), operating with Cu $K_{\alpha1}$ ($\lambda = 0.154061$ nm) at 2θ values 5 to 90° with intervals of 0.05°. Raman spectroscopy measurements were carried out by employing a WITec Confocal Raman microscopy (WITec alpha-300R, Ulm Germany) with a 532 nm laser, spectral acquisition of 120 seconds using a 50X objective. The morphology of CN and MO/RGO-S@CN were acquired using a Zeiss Ultra PLUS FEG-SEM (Ashikima Shi, Japan) at 2000 V incorporating the oxford energy dissipation spectroscopy (EDS) operated at 20 kV. Transmission electron

FIGURE 2 (A) and (B) Low- and high-resolution micrographs respectively of MO, (C) and (D) low- and high-resolution images respectively of CN, (E) and (F) low- and high-resolution images respectively of MO/RGO-S, and (G) and (H) low- and high-resolution images respectively of MO/RGO-S-50@CN
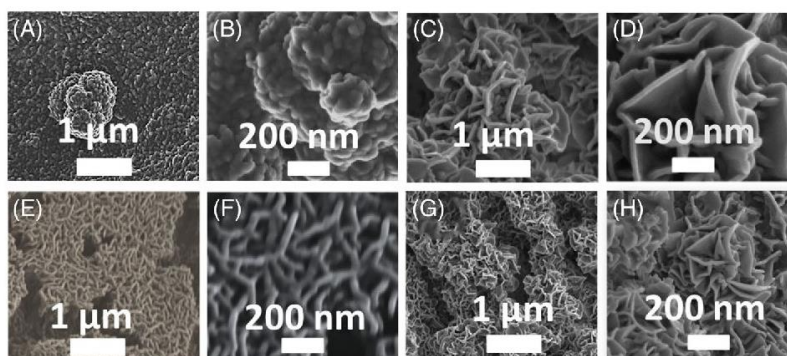
microscopy (TEM) was acquired from JEOL JEM 2100-F operating at 200 kV.

2.8 | Electrochemical characterisation

Electrochemical characterisations were performed using the Biologic potentiostat. CE and RE were similar to those reported in Section 2.3, respectively, CN and MO/RGO-S-X@CN served as the WE in three-electrode configuration. The positive three-electrode measurements of all the samples were performed in 2 M KOH. The CV was executed over scan rates ranging from 5 to 100 mV s^{-1} vs Ag/AgCl, The GCDs were run at a specific current of 0.5-10 A g^{-1}. Electrochemical impedance spectroscopy (EIS) was performed in an open circuit potential at frequencies ranging from 10 mHz to 100 kHz.

3 | RESULTS AND ANALYSIS

3.1 | Microstructural characterisation and analysis

Figure S1(a-c) (Data S1) shows low-resolution SEM images of CN synthesized by varying the number of CV cycles at 5 mV s^{-1}. The nanoflake morphology is maintained even after varying the number of cycles from 3 to 9. Figure S2(a) and (b) reveals the SEM images respectively of CCBW at low and high magnifications. The morphology displays the porous nature of carbon material. Figure 2 shows SEM micrographs at low and high magnifications of the produced samples. Figure 2A, B displays densely packed MO nanospheres while Figure 2C,D presents the morphology of CN nanoflakes of about 300 nm in width vertically grown on NF. Figure 2E,F displays the morphology of MO/RGO-S which confirms the presence of RGO-S nanorods of about 250 nm in length within the samples. Figure 2G,H
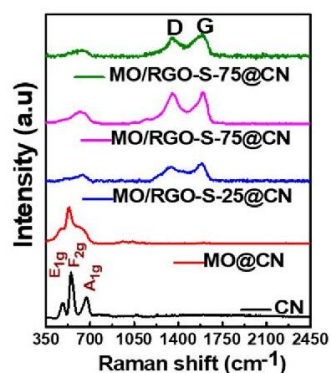
FIGURE 3 Raman spectrum for different samples: CN, MO@CN, MO/RGO-S-25@CN, MO/RGO-S-50@CN, and MO/RGO-S-75@CN

illustrates the images of MO/RGO-S@CN, in which the surface is almost completely covered with nanoflakes from cobalt-nickel layered double hydroxide. Figure S3 indicates the high-resolution TEM image of the MO/RGO-S-50@CN composite sample. The structure consists of a shroud of nanoflakes of CN encompassing the nanorod array of RGO-S. This array facilitates ion penetration and enhances redox reaction through the enlargement of the contact area between the electrode material and electrolyte.

Figure S4(a)–(f) shows the EDS mapping of the MO/RGO-S-50@CN displaying oxygen, manganese, carbon, nickel, sulphur, and cobalt respectively within the material. The images show that the elements are evenly distributed on the sample with Co (5.96%), Ni (11.03%), Mn (25.75%), O (44.78%) S (0.49%), and C (11.98%). From these images, it is evident that the elements are evenly spread in the sample. Figure S4(g) shows the spectrum which displays the percentage composition of these elements.

Figure S5 shows XRD patterns of CN, MO/RGO-S@CN with different RGO-S mass loading and NF. The

diffraction peaks at $2\theta = 9.7°$, $19.4°$, $33.3°$, $38.2°$, $47.7°$, $58.7°$, and $61.9°$, corresponds to the planes (003), (006), (009), (015), (018), (110), and (113) respectively of CN (JCPDS No.14-0191).[29] The peaks 2θ values of $17.9°$, $27.6°$, $28.9°$, $34.5°$, $55.4°$, and $60.3°$, corresponds to the planes (101), (112), (103), (211), (312), and (224), respectively of MO (JCPDS No.24-0734).[29] The 2θ value at $26.5°$ corresponds to the (002) plane showing the presence of graphitic material and evidence of the incorporation of RGO-S. The amorphous nature of AM is evident in the broad and unclear peaks. These peaks are however overshadowed by the sharp peaks from nickel foam.

Figure 3 indicates the Raman spectrum of CN, MO/RGO-S-X@CN where X denotes the various mass loading of RGO-S. CN shows the E_{1g} at 479 cm^{-1} which reveals the presence of O–Ni–O and O–Co–O while F_{2g} and A_{1g} at 546 and 673 cm^{-1} respectively reveal the presence of Ni–OH and Co–OH bonds.[30] The peak at 645 cm^{-1} in MO/RGO-S-X@CN relates to the A_{1g} stretching of the Mn–O bond of the Hausmannite spinel.[31,32] The G and D peaks at 1595 and 1354 cm^{-1}, respectively confirm the successful integration of RGO-S in the composite's material. The D peak is the k-point phonon of A_{1g} symmetry[33] which can be attributed to the structural defects, edges, or the presence of functional groups. The G peak denotes the in-plane stretching of the sp^2 carbon atom.[34] The Raman in Figure S6 shows the spectrum of CN samples synthesized by varying the number of CV cycles during the electrodeposition at 5 mV s^{-1}. The E_{1g} and F_{2g} peaks are present in all the samples while the A_{1g} is also visible for 3 and 9 cycles scan. The A_{1g} peak is most pronounced in the 6 cycle scans presenting the appropriate number of CV cycles scan required for effective deposition of CN samples.

3.2 | Electrochemical performance of the as-synthesized samples

3.2.1 | Three-electrode evaluations

Figure S7 shows the CV traces of MO/RGO-S-50@CN at 50 mV s^{-1} using different electrolytes. It is evident that 2 M KOH displays the highest specific current, hence 2 M KOH was selected for further electrochemical tests. Figure S8(a) exhibits the CV of the CN samples synthesized at a range of number cycles in 2 M KOH electrolytes. The 6 cycles sample presents the superior current peak which is supported by the GCD in Figure S8 (b) where the 6 cycles sample has the longest discharge time. Figure S8(c) shows that the 6-cycle sample has the highest specific capacity compared to 3 and 9 cycles at 0.5 A g^{-1}. The EIS Nyquist plot in Figure S8(d) shows

that the 6-cycles sample has the smallest equivalent series resistance (ESR) and short diffusion length compared to others. The overall electrochemical comparison is shown in Figure S8 reveals an outstanding performance for sample synthesized for 6 cycles, thus, all further electrodeposition of CN on the composites was performed using 6 cycles sample.

Figure 4 presents the 3-electrode measurements of all different samples using 2 M KOH. Figure 4A displays the CV at a 50 mV s^{-1} in a voltage range 0 to 0.5 V vs Ag/AgCl. The traces show reduction peaks demonstrating the presence of Faradaic charge storage structure within the material. The reduction peaks are within (0.1-0.3) V vs Ag/AgCl, while in the entire voltage range the oxidation peak is not visible. The lack of prominence in the redox peaks points to pseudocapacitive charge storage mechanism rather than pure Faradaic battery-type charge storage. The MO/RGO-S-50@CN showed the best current response compared to CN, MO@CN, MO/RGO-S-25@CN, and MO/RGO-S-75@CN samples. This may be credited to the enhanced electrical conductivity due to the optimum content of RGO-S in the MO matrix. The manifestation of the Faradaic nature of the layered double hydroxide and spinel is supported by the GCD in Figure 4B at a specific current of 0.5 A g^{-1}. The slanted plateaux support the redox mechanisms shown in the CVs in Figure 4A and the lengthiest discharge time is observed in MO/RGO-S-50@CN in coherence with the highest current peak in the CV trace. Figure 4C indicates the specific capacity vs specific current at 0.5 A g^{-1} with the MO/RGO-S-50@CN sample showing the highest specific capacities for all specific currents reported. The specific capacity (Q_S) is calculated using equation[6,35]:

$$Q_S\left(\text{mAh g}^{-1}\right) = \frac{1}{3.6} \times I_S \Delta t, \qquad (6)$$

where I_S denotes the specific current (A g^{-1}) and Δt represents the time of discharge (s). All samples show high specific capacities and rate capability which could be due to the synergistic effects of multi-components.[29] The rate capabilities at 10 A g^{-1} are 84%, 51%, 71%, 62%, and 35% for CN, MO@CN, MO/RGO-S-25@CN, MO/RGO-S-50@CN, and MO/RGO-S-75@CN, respectively. The high rate capability is due to the high electrical conductivity of samples.[36] However, the lower rate capability of MO/RGO-S-75@CN can be attributed to the increased contact resistance due to the large mass loading of RGO-S in composite.[37] Figure 4D shows the Nyquist plot to analyse the electrical conductivity and kinetics of charges of all samples. The ESR magnitudes correspond to the intercept of the x-axis, as shown in the insert at high
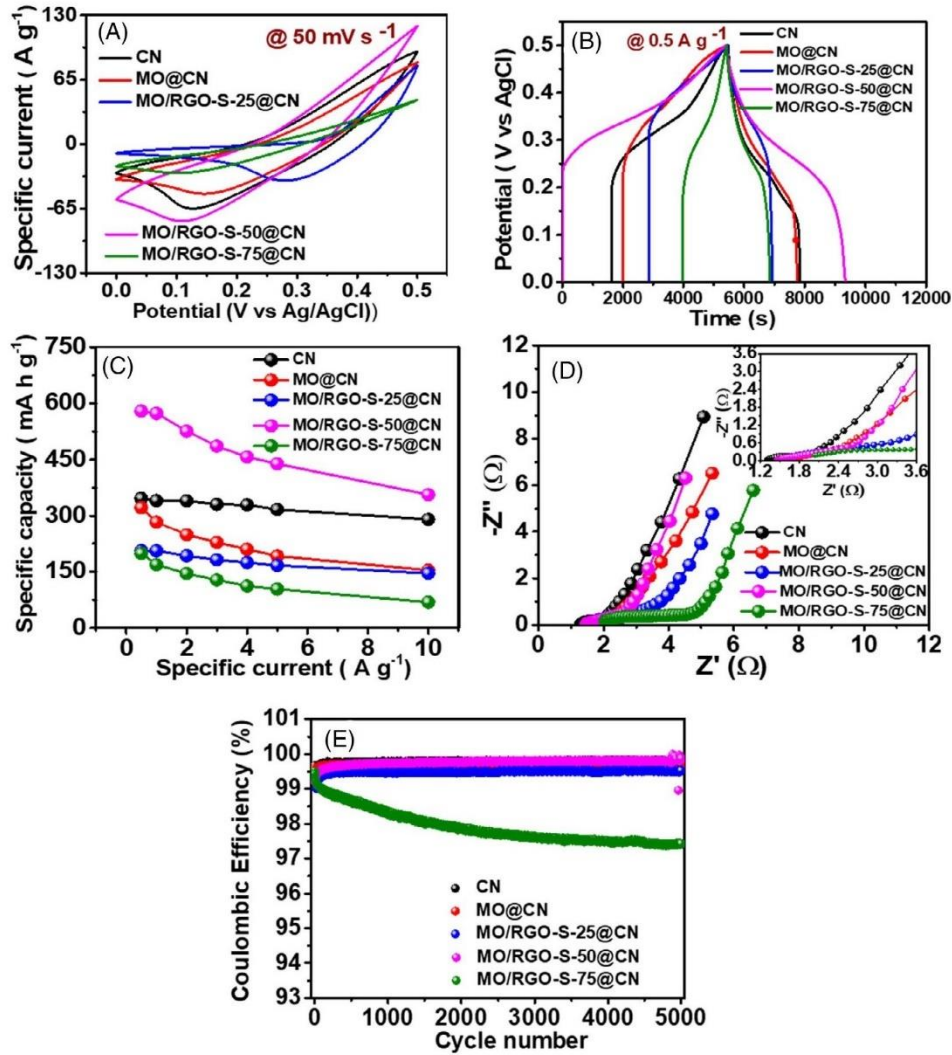
FIGURE 4 (A) The CV traces, (B) The GCD traces, (C) specific capacity vs specific current, (D) EIS Nyquist plot, and (E) Coulombic efficiency of CN, MO@CN, MO/RGO-S-25@CN, MO/RGO-S-50@CN, and MO/RGO-S-75@CN, respectively

frequency in Figure 3D are 1.32, 1.46, 1.58, 1.39, and 2.04 Ω for CN, MO@CN, MO/RGO-S-25@CN, MO/RGO-S-50@CN, and MO/RGO-S-75@CN, respectively. These small values indicate the electrolyte's low ionic resistance, minimal contact resistance of the AM, and current collector with better conductivity of the AM. The small contact resistance of NF with the AM is attributed to the strong adhesive forces of the electrodeposition method. The diameters of the semi-circles which are depressed by the constant phase element (CPE) are very short for all the samples signifying low charge transfer resistance. Figure 4E shows the cyclic stability of up to 5, 000 GCD cycles at 6 A g^{-1}. The coulombic efficiency (η) is calculated using Equation (7):

$$\eta = \frac{t_D}{t_C} \times 100\%, \qquad (7)$$

where t_C and t_D are the times (s) for charge and discharge, respectively. Coulombic efficiency of CN, MO@CN, MO/RGO-S-25@CN, MO/RGO-S-50@CN, and MO/RGO-S-75@CN were 99.8%, 99.7%, 99.5%, 99.9%, and 97.4%, respectively which are almost 100% which was is expected of supercapacitors. All the samples except the MO/RGO-S-75@CN had an excellent coulombic efficiency of at least 99.5%. The decrease of the efficiency of MO/RGO-S-75@CN is due to excess content of RGO-S in the sample causing saturation. The excellent performance presented by other samples shows good redox
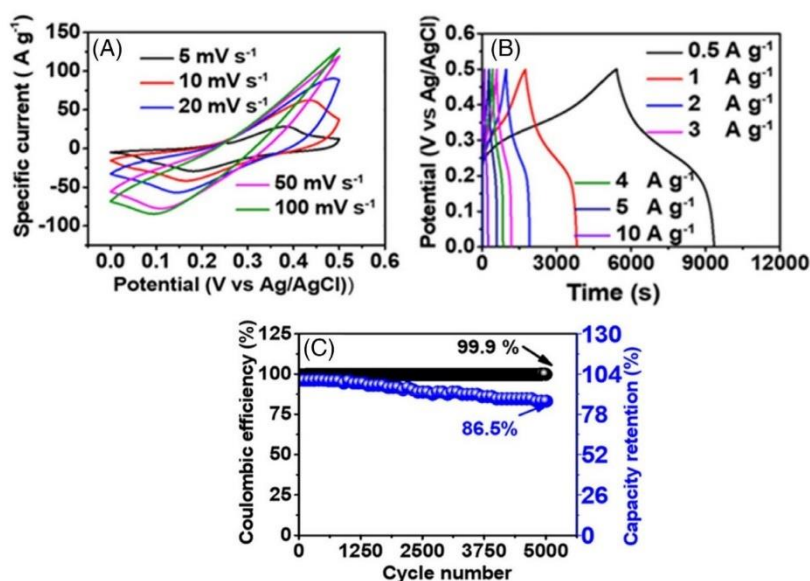
FIGURE 5 (A) CV traces, (B) GCD traces, and (C) capacity retention and coulombic efficiency for MO/RGO-S-50@CN sample

reversibility which is attributed to the high chemical stability of MO and excellent structural design of the electrodeposition synthesis. The increased redox reactivity and high adsorption property of MO enhanced the phenomenal electrochemical attributes of the composite samples. The composites have a dominant Faradaic charge storage mechanism due to the presence of CN and MO and it is more prominent than the EDLC storage mechanism from RGO-S. The synergistic effect of both storage mechanisms helps to considerably enhance the electrochemical performance of the composite material as compared to individual electrode materials. The superior coulombic efficiency of 99.9% for MO/RGO-S-50@CN is due to the structural stability owing to the optimum amount of RGO-S in the sample. From Figure 4 it is evident that the electrochemical execution of MO/RGO-S-50@CN surpasses all the other samples.

Figure 5 summarises the electrochemical functioning of the best (optimal) sample MO/RGO-S-50@CN. Figure 5A indicates the CV curves in a voltage range of 0 to 0.5 V vs Ag/AgCl with scan rates range 5 to 100 mV s^{-1}. There are pairs of reduction and oxidation peaks for all the scan rates. However, at higher scan rates of 50 and 100 mV s^{-1}, the oxidation peaks are merely invisible. This is due to the increase in charge diffusion polarisation in the electrode material with scan rate which leads to the reduction in the reversibility of the redox process. The peaks are due to the following electrochemical reactions:

$$Ni(OH)_2 + OH^- \rightleftharpoons NiOOH + H_2O + e^-, \quad (8)$$

$$Co(OH)_2 + OH^- \rightleftharpoons CoOOH + H_2O + e^-, \quad (9)$$

$$CoOOH + OH^- \rightleftharpoons CoO_2 + H_2O + e^-. \quad (10)$$

Figure 5B presents the GCD at a specific current range from 0.5 to 10 A g^{-1}, the absence of a well-pronounced plateau indicates pseudocapacitive behaviour instead of a pure battery type storage mechanism. Figure 5C displays the capacity retention and coulombic efficiency during 5000 GCD cycles at 6 A g^{-1}. The high-capacity retention of 86.5% and a coulombic efficiency of 99.9% are due to the strong adhesion between the current collector and electrode material. This is also attributed to electrodeposition synthesis and the mechanical stability from the inclusion of RGO-S in the composite material. Therefore, MO/RGO-S-50@CN was preferred for use as the positive electrode for fabrication of the device due to the superior electrochemical performance displayed by this sample compared to the other electrodes.

Table 1 shows a comparison of electrochemical performance of LDH electrode materials synthesized using various methods which were reported beforehand (the units were all converted to mAh g^{-1} for comparison). The electrode in this work produced the highest specific capacity of 582.1 mAh g^{-1} at 0.5 A g^{-1} and excellent capacity retention of 86.5% at 5000 GCD cycles at 6 A g^{-1}. The synthesized electrode revealed higher performance in a three-electrode configuration ahead of other related materials appearing in the recently published studies as displayed in Table 1. From the table, we observe various synthesis methods for cobalt-nickel-based electrodes. We observe slightly higher specific

TABLE 1 Electrochemical performance of recently reported LDHs in a three-electrode system

Material	Synthesis method	Capacity (mAh g^{-1})	Capacity retention (cycles)	References
Ni-Co LDHs	Electrodeposition	287 (1 A g^{-1})	81.8% (3000)	38
Ni-Co LDH	Hydrothermal	217 (6 Ag^{-1})	86% (1000)	39
P@NiCo LDHs	Co-precipitation	149 (1 Ag^{-1})	55.9% (5000)	40
Ni-Co LDH/CFC	Electrodeposition	235 (1 Ag^{-1})	82.9% (5000)	41
FeNiP@CoNi-LDH	Hydrothermal	285 (1 Ag^{-1})	70.4% (5000)	42
CoNi-LDH67	Co-precipitation	183 (1 Ag^{-1})	77.14% (5000)	43
MO/RGO-S-50@CN	Electrodeposition	582.1 (0.5 A g^{-1})	86.5% (5000)	This work

FIGURE 6 (A) CV traces of the negative and positive electrode at 50 mV s^{-1}, (B) CV traces of the device at different scan rates, (C) GCD traces at a range of specific currents, (D) specific capacity vs specific current, (E) cyclic stability and capacity retention vs cycle number with an insert being 5 LED lighted by two asymmetric devices in parallel, and (F) Ragone plot of MO/RGO-S-50@CN//CCBW device, respectively
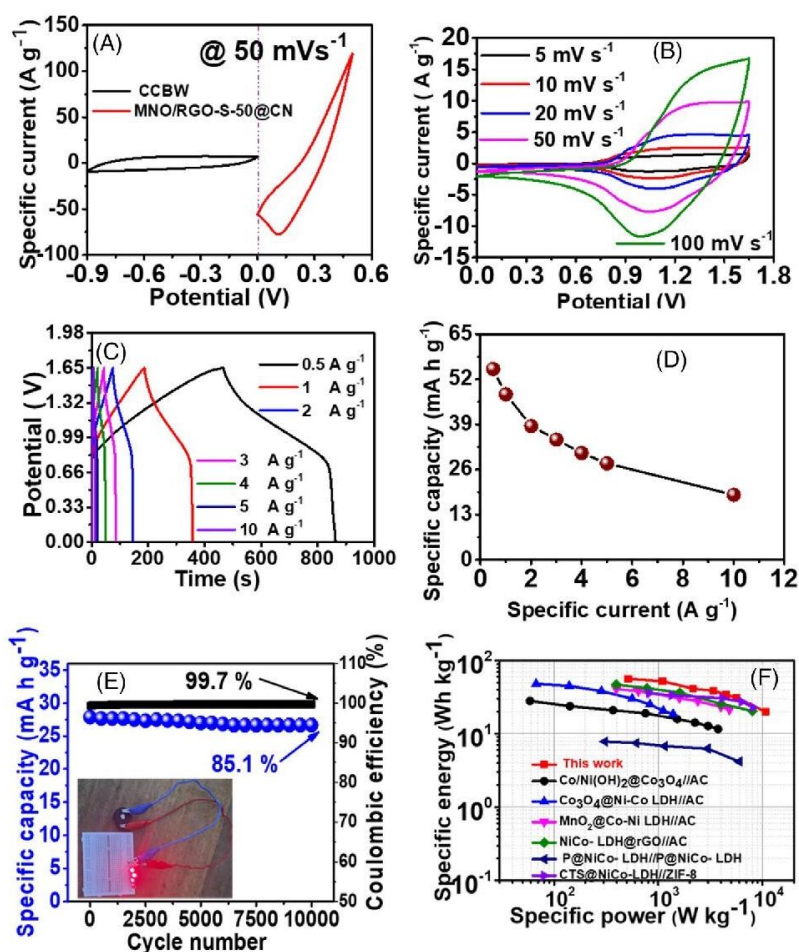
capacities from electrodes synthesized via the electrode-position methods compared to other synthesis methods. The composites of the LDH with other materials lead to better electrochemical performance. The electrode materials in this work are superior and this may be as a result of the presence of a carbon material that is absent in other electrodes reported in the literature.

3.2.2 | Electrochemical properties of the asymmetric supercapacitor

To evaluate the actual performance of the synthesized electrode, an asymmetric device MO/RGO-S-50@CN//CCBW was made using MO/RGO-S-50@CN as a positive electrode and CCBW as a negative electrode with 2 M

KOH electrolyte. To attain charge balance of the electrodes, the mass ratio of the negative and positive electrode materials was obtained using mass balance equation[44]:

$$\frac{m_-}{m_+} = 3.6 \frac{Q_{S+}}{C_{s-} \times V_{S_-}}, \tag{11}$$

here m_- and m_+ denotes the negative and positive electrode masses (mg), Q_{S+} is the positive electrode specific capacity (mAh g^{-1}), C_{S-} is the negative electrode's specific capacitance (F g^{-1}), and V_{S-} is the potential (V) of the negative electrode.

The total mass of AM in the device was 5.0 mg/cm^2 and the calculated ratio m_-/m_+ was 10:1. Figure 6A indicates the CV curves for the negative and positive electrodes at 50 mV s^{-1} in which the CCBW manifests a rectangular-like EDLC behaviour within the potential windows of −0.9 to 0 V vs Ag/AgCl, while MO/RGO-S-50@CN shows a Faradaic behaviour in the positive voltage range of 0-5 V vs Ag/AgCl. Figure 6B displays the CV of the device at 5 to 100 mV s^{-1} scan rate whereby the redox crests are manifested even at a large scan rate of 100 mV s^{-1} proving great rate performance for the device. Figure 6C presents the GCD at specific currents ranging from 0.5 to 10 A g^{-1} with non-linear traces that are coherent with the Faradaic charge storage mechanism.[45] Figure 6D represents specific capacity vs specific current with the largest specific capacity of 55.0 mAh g^{-1} at 0.5 A g^{-1}. Figure 6E demonstrates coulombic efficiency and capacity retention variation with cycle number. The device retains a coulombic efficiency of 99.7% and capacity retention of 85.1% at 10 000 GCD cycles performed at 6 A g^{-1}. This performance is influenced by the absence of polymeric binders in the positive electrode which contributes to these high stability values.[46] The insert in Figure 6E shows 5 light-emitting diodes (LEDs) lighted by two MO/RGO-S-50@CN//CCBW devices connected in parallel after 10 000 cycles of stability test. The specific energy (E_s) is calculated using the following equation[47]:

$$E_s \left(\text{Wh kg}^{-1} \right) = \frac{I_s}{3.6} \int V(t) dt, \tag{12}$$

where $\int V(t) dt$ depicts the integral (V_s) and I_S is the specific current (A g^{-1}) of the GCD curve. The specific power (P_S) is obtained from the following expression[48]:

$$P_s \left(\text{W kg}^{-1} \right) = 3600 \times \frac{Es}{\Delta t}, \tag{13}$$

where Δt is the time of discharge (s).

The device MO/RGO-S-50@CN//CCBW in this work produced specific energy of 56.0 Wh kg^{-1} at a specific current of 0.5 A g^{-1} which corresponds to a specific power of 515.0 W kg^{-1}. Figure 6F displays the Ragone plot associating the specific energy and power of this work to other similar devices on cobalt-nickel layered double hydroxide/spinel composites in the literature. The plot shows that the specific energy and power of the device in this work is mostly better than other reported related work.[18,30,40,49-51] The maximum power is transferred when the resistance of the load is equal to the ESR. The maximum specific power P_{MAX} of the device is obtained by employing equation[52]:

$$P_{MAX} \left(\text{kW kg}^{-1} \right) = \frac{V^2}{4m \times R_S}, \tag{14}$$

where m is the mass (g) of AM in the device, V is the cell potential (V), and R_S (Ω) is the ESR of the device. The device produces a maximum specific power of 139.9 kW kg^{-1}.

Table 2 displays a contrast of the electrochemical characteristics of devices previously reported which are based on CN materials. The device in this work produced huge specific energy of 56 Wh kg^{-1} at a cell potential of 1.65 V.

Figure 7A illustrates the Nyquist plot of the device displaying the experimental results together with the fitting line. The insert shows the equivalent circuit used to fit data. The device presented a meagre value of ESR denoted as R_S of 1.059 Ω which is attributed to minimal contact resistance at the AM/current collector interface and electrolyte ions/electrode materials interface. The equivalent circuit shows the charge transfer resistance (R_{CT}) of 4.31 Ω which demonstrates the occurrence of Faradaic reactions. R_{CT} is parallel to the CPE (Q), which causes the semi-circle to be depressed such that the centre is below the real impedance axes. The resistance due to leakage currents, R_L which has a value of 1.69 Ω, causes the plot curve to bend away from the imaginary impedance axes causing the magnitude of the phase angle to be less than 90°. The Warburg-frequency (Z_w) also causes the slope to deviate from the imaginary impedance axes in the low-frequency section, this impedes ion diffusion to the electrode surface. Figure 7B shows the EIS Nyquist plot before cycling and after 10 000 GCD cycles. The R_S decreases to 0.980 Ω after 10 000 cycles which indicate a decrease in the resistance at electrolyte-electrode plotline and the reduction in AM-current collector contact resistance. However, the slope of the plotline after the stability test indicates a rise in the diffusion resistance on the electrode-electrolyte interface due to the water molecules in the electrolyte

TABLE 2 Electrochemical performance of earlier reported LDHs-based electrode material in a device

Device	Electrolyte	Cell potential (V)	E_S (Wh kg^{-1})	P_S (W kg^{-1})	References
NiCo$_2$O$_4$@NiCo-LDH//NGH	2 M KOH	1.55	50.7	773.5	53
NiCoP/NiCo-OH//PC	6 M KOH	1.6	34	775	54
Ni-Co LDH/CFC//rGO/NF	6 M KOH	1.6	37	800	41
CoNi LDH-6//EWC-2 ASC	2 M KOH	1.7	51.1	1700	55
MnO$_2$@ Co-Ni LDH//AC	1 M KOH	1.6	40.9	400	50
MCS@CN LDH//N-rGO	6 M KOH	1.6	48.8	800	56
MO/RGO-S@CN//CCBW	2 M KOH	1.65	56	515	This work

FIGURE 7 (A) Nyquist plot of the experimental data with the fitting curve and an equivalent circuit, (B) Nyquist plot before and after cycling stability with insert, (C) Bode plot, and (D) imaginary and real capacitance vs frequency
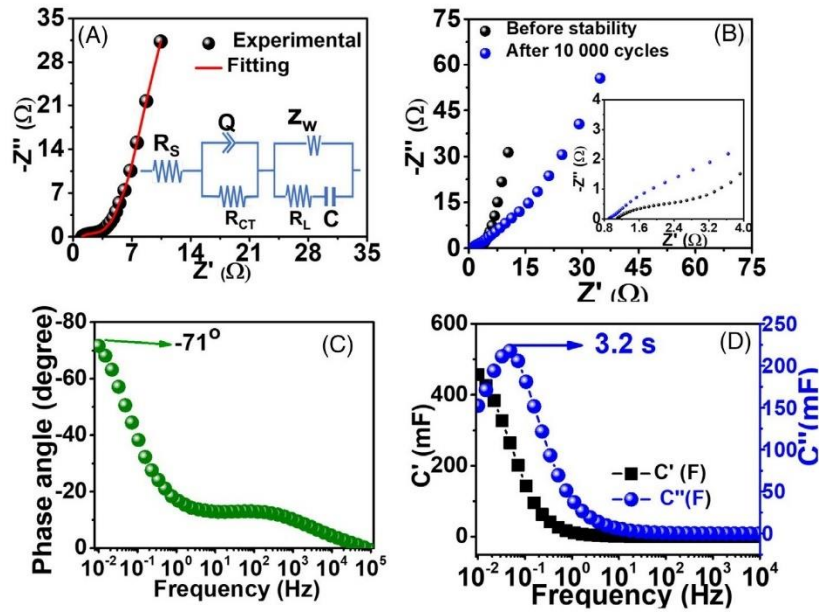
decomposing.[56] Figure 7C is the Bode plot showing the variation of phase angle with frequency in which the phase angle for our device at the low-frequency region is $-71°$. This value which is close to $-90°$ indicates the presence of capacitive behaviour in the device. Figure 7D shows the variation of imaginary and real capacitance ($C''(\omega)$ and $C'(\omega)$) with frequency. The imaginary and real capacitances are calculated from the equation expressed below[57]:

$$Z'(\omega) = 2\pi f C''(\omega)|Z(\omega)|, \qquad (15)$$

$$Z''(\omega) = 2\pi f C'(\omega)|Z(\omega)|, \qquad (16)$$

where ω is the angular frequency (rad s^{-1}) which is given by $\omega = 2\pi f$, f depicts the frequency (Hz), and Z represents the impedance (Ω). The real capacitance $C'(\omega)$ is the capacitance (F) of the device which is accessible and

transferred and it denotes a maximum value of 0.46 F at low frequency as shown in Figure 7D. The imaginary component of the capacitance $C''(\omega)$ correspond to the energy lost by the electrodes through irreversible processes. The $C''(\omega)$ has a peak maximum value of 0.44 F at 0.05 Hz. This corresponds to the relaxation time τ of 3.2 seconds obtained using $2\pi f\tau = 1$. This demonstrates that the MO/RGO-S-50@CN//CCBW device can be fully charged quickly with 3.2 seconds.

4 | CONCLUSION

MO/RGO-S-X@CN was produced through a two-step electrodeposition method. The optimized electrode material (MO/RGO-S-50@CN) produced an outstanding performance with an excellent specific capacity of 582.1 mAh g^{-1} at 0.5 A g^{-1}. The electrode further demonstrated a coulombic efficiency of 99.9% after 5000 GCD

cycles at 6 A g^{-1}. A device was fabricated with activated carbon from cooked chicken bone waste (CCBW) as the negative electrode and the synthesized material (MO/RGO-S-50@CN) as the positive electrode. The MO/RGO-S-50@CN//CCBW device produced specific energy of 56.0 Wh kg^{-1} at 0.5 A g^{-1} with an equivalent specific power of 515.0 W kg^{-1}. The device also presented a coulombic efficiency of 99.7% at 10 000 GCD cycles at 6 A g^{-1} with a capacity retention of 85.1%. This outstanding electrochemical performance of the device enables it to be incorporated in energy storage systems for renewable energy.

DATA AVAILABILITY STATEMENT
Data will be available upon request

ORCID
Ncholu Manyala https://orcid.org/0000-0003-2990-4284

REFERENCES
1. Relva SG, Silva VO, Gimenes ALV, Udaeta MEM, Ashworth P, Peyerl D. Enhancing developing countries' transition to a low-carbon electricity sector. *Energy*. 2021;220:119659.
2. Ji Y, Zou H, Zhang P, et al. Carbon aerogels with mutual support structures constructed by hybrid hydrogels: robust energy storage materials mater. *Today Commun*. 2020;25:101444.
3. Chodankar NR, Selvaraj S, Ji SH, Kwon Y, Kim DH. Interface-engineered nickel cobaltite nanowires through NiO atomic layer deposition and nitrogen plasma for high-energy, Long-cycle-life foldable all-solid-state supercapacitors. *Small*. 2019;15:1-12.
4. Sharma P, Kumar V. Current Technology of Supercapacitors: a review. *J Electron Mater*. 2020;49:3520-3532.
5. Yu F, Huang T, Zhang P, et al. Design and synthesis of electrode materials with both battery-type and capacitive charge storage. *Energy Storage Mater*. 2019;22:235-255.
6. Zou Q, Khalafallah D, Wu Z, Chen J, Zhi M, Hong Z. Supercritical ethanol deposition of Ni(OH)$_2$ nanosheets on carbon cloth for flexible solid-state asymmetric supercapacitor electrode. *J Supercrit Fluids*. 2020;159:104774.
7. Wang D, Li J, Zhao Y, Xu H, Zhao J. Bifunctional Cu$_2$S–Co (OH)$_2$ nanotube array/Cu foam electrocatalyst for overall water splitting. *Electrochim Acta*. 2019;316:8-18.
8. Hu P, Liu Y, Song J, Song X, Wu X. Transition metal oxide@hydroxide assemblies as electrode materials for asymmetric hybrid capacitors with excellent cycling stabilities. *RSC Adv*. 2019;9:32510-32516.
9. Tomboc GM, Kim J, Wang Y, et al. Hybrid layered double hydroxides as multifunctional nanomaterials for overall water splitting and supercapacitor applications. *J Mater Chem A*. 2021;9:4528-4557.
10. Tang Y, Wu F, Fang L, Guan T, Hu J, Zhang SF. A comparative study and optimization of corrosion resistance of ZnAl layered double hydroxides films intercalated with different anions on AZ31 mg alloys. *Surf Coatings Technol*. 2019;358:594-603.
11. Manohara GV, Norris D, Maroto-Valer MM, Garcia S. Acetate intercalated mg-Al layered double hydroxides (LDHs) through modified amide hydrolysis: a new route to synthesize novel mixed metal oxides (MMOs) for CO$_2$ capture. *Dalt Trans*. 2021; 50:7474-7483.
12. Arrabito G, Bonasera A, Prestopino G, et al. Layered double hydroxides: a toolbox for chemistry and biology. *Crystals*. 2019; 9:361.
13. Li C, Zhou Y, Li X, Wang H, Huo P, Wang X. Ni dopping Co2Al ternary layered double hydroxides for improving electrochemical performance of high-performance hybrid supercapacitors. *Appl Surf Sci*. 2021;536:147780.
14. Zhao Z, Kou K, Wu H. 2-Methylimidazole-mediated hierarchical Co$_3$O$_4$/N-doped carbon/short-carbon-fiber composite as high-performance electromagnetic wave absorber. *J Colloid Interface Sci*. 2020;574:1-10.
15. Enhtuwshin E, Mhin S, Kim KM, et al. Ni-Fe-Cu-layered double hydroxides as high-performance electrocatalysts for alkaline water oxidation. *Int J Energy Res*. 2021;45:15312-15322.
16. Yan Z, Liu H, Hao Z, Yu M, Chen X, Chen J. Electrodeposition of (hydro)oxides for an oxygen evolution electrode. *Chem Sci*. 2020;11:10614-10625.
17. Mbugua NS, Kang M, Zhang Y, Ndiithi NJ, V. Bertrand G, Yao L. Electrochemical deposition of Ni, NiCo alloy and NiCo-ceramic composite coatings-a critical review. *Materials (Basel)*. 2020;13:3475.
18. Bao Y, Deng Y, Wang M, et al. A controllable top-down etching and in-situ oxidizing strategy: metal-organic frameworks derived α-Co/Ni(OH)$_2$@Co$_3$O$_4$ hollow nanocages for enhanced supercapacitor performance. *Appl Surf Sci*. 2020;504:144395.
19. Sherryna A, Tahir M. Recent developments in layered double hydroxide structures with their role in promoting photocatalytic hydrogen production: a comprehensive review. *Int. J. Energy Res*. 2021;1–48:2093-2140. doi:10.1002/er.7335
20. Kashale AA, Yi CH, Cheng KY, Guo JS, Pan YH, Chen IWP. Binder-free heterostructured NiFe$_2$O$_4$/NiFe LDH nanosheet composite electrocatalysts for oxygen evolution reactions. *ACS Appl Energy Mater*. 2020;3:10831-10840.
21. Zhao X, Mao L, Cheng Q, et al. Two-dimensional spinel structured Co-based materials for high performance supercapacitors: a critical review. *Chem Eng J*. 2020;387:124081.
22. Wang Z, Su H, Liu F, et al. Establishing highly-efficient surface faradaic reaction in flower-like NiCo$_2$O$_4$ nano−/microstructures for next-generation supercapacitors. *Electrochim Acta*. 2019;307:302-309.
23. Chen J, Hu X, Gao H, Yan S, Chen S, Liu X. Graphene-wrapped MnCO$_3$/Mn$_3$O$_4$ nanocomposite as an advanced anode material for lithium-ion batteries: synergistic effect and electrochemical performances. *J Mater Sci Technol*. 2021;99:9-17.

24. Song B, Cerkez EB, Elzinga EJ, Kim B. Effects of Ni incorporation on the reactivity and stability of hausmannite (Mn3O4): environmental implications for Mn, Ni, and As solubility and cycling. *Chem Geol.* 2020;558:119862.

25. Bhagwan J, Krishna BNV, Yu JS. Template and sol-gel routed CoMn$_2$O$_4$ nanofibers for supercapacitor applications. *Int J Energy Res.* 2021;45:19413-19422.

26. Singh A, Ojha SK, Ojha AK. Facile synthesis of porous nanostructures of NiCo$_2$O$_4$ grown on rGO sheet for high performance supercapacitors. *Synth Met.* 2020;259:116215.

27. Tarimo DJ, Oyedotun KO, Mirghni AA, Manyala N. Sulphur-reduced graphene oxide composite with improved electrochemical performance for supercapacitor applications. *Int J Hydrogen Energy.* 2020;45:13189-13201.

28. Pan GT, Chong S, Yang TCK, Huang CM. Electrodeposited porous mn1.5co1.5o4/ni composite electrodes for high-voltage asymmetric supercapacitors. *Materials (Basel).* 2017;10:1-12.

29. Zhao N, Fan H, Zhang M, et al. Preparation of partially-cladding NiCo-LDH/Mn$_3$O$_4$ composite by electrodeposition route and its excellent supercapacitor performance. *J Alloys Compd.* 2019;796:111-119.

30. Zhu Y, An S, Sun X, et al. Core-branched NiCo$_2$S$_4$@CoNi-LDH heterostructure as advanced electrode with superior energy storage performance. *Chem Eng J.* 2020;383:123206.

31. Li Q, Li Y, Fulari AV, Ghodake GS, Kim DY, Lohar GM. Performance of chemically synthesized Mn$_3$O$_4$/rGO nanocomposite for electrochemical supercapacitor: a cost-effective high-performance electrode. *Nanotechnology.* 2020;31:415403.

32. Sreekanth TVM, Kisoo Y, Kim J. Temperature-dependent synthesis of Mn$_3$O$_4$ nanostructures by microwave irradiation method for high-performance supercapacitors. *Int J Energy Res.* 2022;46:1683-1692.

33. Maphiri VM, Rutavi G, Sylla NF, Adewinbi SA, Fasakin O, Manyala N. Novel thermally reduced graphene oxide micro-supercapacitor fabricated via mask—free axidraw direct writing. *Nanomaterials.* 2021;11:1909.

34. Hiremath V, Lim AC, Seo JG. Highly porous honeycomb-like activated carbon derived using cellulose pulp for symmetric supercapacitors. *Int J Energy Res.* 2021;45:4385-4395.

35. Kitenge VN, Oyedotun KO, Fasakin O, et al. Enhancing the electrochemical properties of a nickel–cobalt-manganese ternary hydroxide electrode using graphene foam for supercapacitors applications. *Mater Renew Sustain Energy.* 2021;10:1-16.

36. Zhang L, Shi G. Preparation of highly conductive graphene hydrogels for fabricating supercapacitors with high rate capability. *J Phys Chem C.* 2011;115:17206-17212.

37. Han H, Song T, Lee EK, et al. Dominant factors governing the rate capability of a TiO$_2$ nanotube anode for high power lithium ion batteries. *ACS Nano.* 2012;6:8308-8315.

38. Ju A, Xu R, Zhang Y, Feng S, Chen C, Liao J. Electrodeposition of ultrathin Nanosheets of nickel-cobalt double hydroxides with layered structure for improved supercapacitor performance. *Int J Electrochem Sci.* 2021;16:1-15.

39. Pu J, Tong Y, Wang S, Sheng E, Wang Z. Nickel-cobalt hydroxide nanosheets arrays on Ni foam for pseudocapacitor applications. *J Power Sources.* 2014;250:250-256.

40. Wang G, Li Y, Zhao T, Jin Z. Phosphatized mild-prepared-NiCo LDHs cabbage-like spheres exhibit excellent performance as a supercapacitor electrode. *New J Chem.* 2021;45:251-261.

41. Li Y, Shan L, Sui Y, et al. Ultrathin Ni–Co LDH nanosheets grown on carbon fiber cloth via electrodeposition for high-performance supercapacitors. *J Mater Sci Mater Electron.* 2019;30:13360-13371.

42. Wan L, Chen D, Liu J, et al. Construction of FeNiP@CoNi-layered double hydroxide hybrid nanosheets on carbon cloth for high energy asymmetric supercapacitors. *J Power Sources.* 2020;465:228293.

43. Tahir MU, Arshad H, Zhang H, et al. Room temperature and aqueous synthesis of bimetallic ZIF derived CoNi layered double hydroxides and their applications in asymmetric supercapacitors. *J Colloid Interface Sci.* 2020;579:195-204.

44. Mahmoud BA, Mirghni AA, Oyedotun KO, Fasakin O, Manyala N. Nanoplatelets ammonium nickel-cobalt phosphate graphene foam composite as novel electrode material for hybrid supercapacitors. *J Alloys Compd.* 2021;883:160897.

45. Pallavolu MR, Gaddam N, Banerjee AN, Nallapureddy RR, Joo SW. Superior energy-power performance of N-doped carbon nano-onions-based asymmetric and symmetric super-capacitor devices. *Int J Energy Res.* 2021;1234–1249:1234-1249. doi:10.1002/er.7242

46. Sun C, Li X, Cai Z, Ge F. Carbonized cotton fabric in-situ electrodeposition polypyrrole as high-performance flexible electrode for wearable supercapacitor. *Electrochim Acta.* 2019;296:617-626.

47. Tarimo DJ, Oyedotun KO, Mirghni AA, et al. Enhanced electrochemical performance of supercapattery derived from Sulphur-reduced graphene oxide/cobalt oxide composite and activated carbon from peanut shells. *Int J Hydrogen Energy.* 2020;45:33059-33075.

48. Mirghni AA, Oyedotun KO, Fasakin O, Mahmoud BA, Tarimo DJ, Manyala N. High-performance bimetallic Ni-Mn phosphate hybridized with 3-D graphene foam for novel hybrid supercapacitors. *J Energy Storage.* 2020;31:101584.

49. Han D, Zhao Y, Shen Y, Wei Y, Mao L, Zeng G. Co$_3$O$_4$ nanowire@ultrathin Ni-Co layered double hydroxide core-shell arrays with vertical transfer channel for high-performance supercapacitor. *J Electroanal Chem.* 2020;859:113887.

50. Luo H, Wang B, Liu T, et al. Hierarchical design of hollow Co-Ni LDH nanocages strung by MnO$_2$ nanowire with enhanced pseudocapacitive properties. *Energy Storage Mater.* 2019;19:370-378.

51. Long D, Liu H, Yuan Y, Li J, Li Z, Zhu J. A facile and large-scale synthesis of NiCo-LDHs@rGO composite for high performance asymmetric supercapacitors. *J Alloys Compd.* 2019;805:1096-1105.

52. Iqbal MZ, Faisal MM, Ali SR. Integration of supercapacitors and batteries towards high-performance hybrid energy storage devices. *Int J Energy Res.* 2021;45:1449-1479.

53. Acharya J, Park M, Ko TH, Kim B. Leaf-like integrated hierarchical NiCo$_2$O$_4$ nanorods@Ni-Co-LDH nanosheets electrodes for high-rate asymmetric supercapacitors. *J Alloys Compd.* 2021;884:161165.

54. Li X, Wu H, Elshawy AM, et al. Cactus-like NiCoP/NiCo-OH 3D architecture with tunable composition for high-

SO

performance electrochemical capacitors. *Adv Funct Mater.* 2018;28:1-10.

55. Chu H, Zhu Y, Fang T, et al. Solvothermal synthesis of cobalt nickel layered double hydroxides with a three-dimensional nano-petal structure for high-performance supercapacitors. *Sustain Energy Fuels.* 2019;4:337-346.

56. Liang H, Lin T, Wang S, et al. A free-standing manganese cobalt sulfide@cobalt nickel layered double hydroxide core-shell heterostructure for an asymmetric supercapacitor. *Dalt Trans.* 2019;49:196-202.

57. Rantho MN, Madito MJ, Ochai-Ejeh FO, Manyala N. Asymmetric supercapacitor based on vanadium disulfide nanosheets as a cathode and carbonized iron cations adsorbed onto polyaniline as an anode. *Electrochim Acta.* 2018;260:11-23.

SUPPORTING INFORMATION

Additional supporting information may be found in the online version of the article at the publisher's website.

SUPPORTING INFORMATION

Two-step electrodeposition synthesis of Hausmannite sulphur reduced graphene oxide cobalt-nickel layered double hydroxide heterostructure for high-performance supercapacitor

Gift Rutavi, Delvina Japhet Tarimo, Vusani Muswa Maphiri, Ncholu Manyala*

Department of Physics, Institute of Applied Materials, SARChI in Carbon Technology and Materials, University of Pretoria 0028, South Africa

*Corresponding author's email: ncholu.manyala@up.ac.za, Tel.: + (27)12 420 3549.

SUPPLEMENTARY INFORMATION
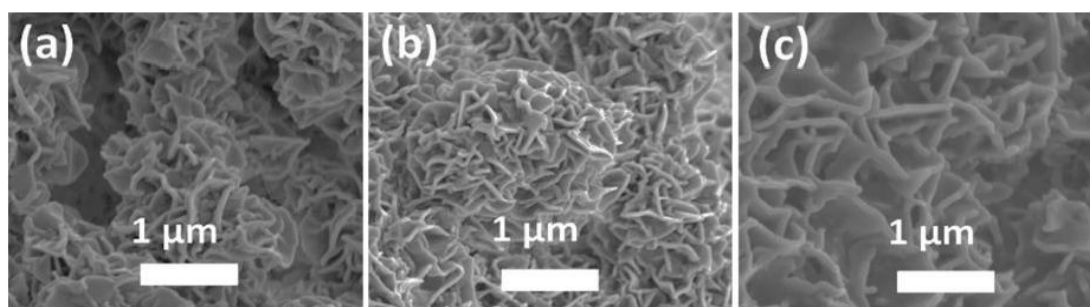
Fig. S1: Low-resolution SEM micrographs of CN samples synthesized using different number of CV cycles at a scan rate of 5 mV s^{-1}: **(a)** CN-3, **(b)** CN-6 and **(c)** CN-9.
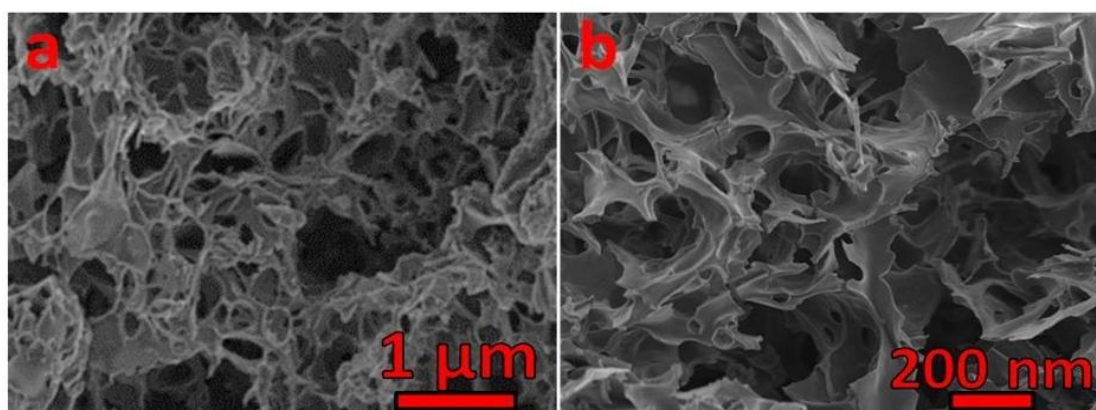
Fig. S2: SEM images of CCBW at: **(a)** low resolution **and (b)** high resolution.

1
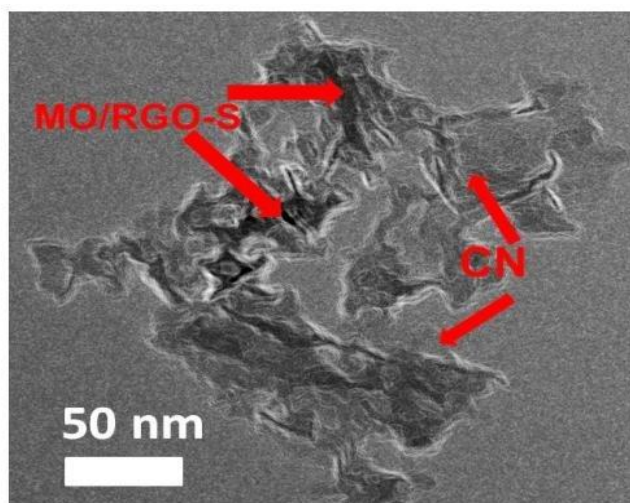
Fig S3: TEM image of MO/RGO-S-50@CN.
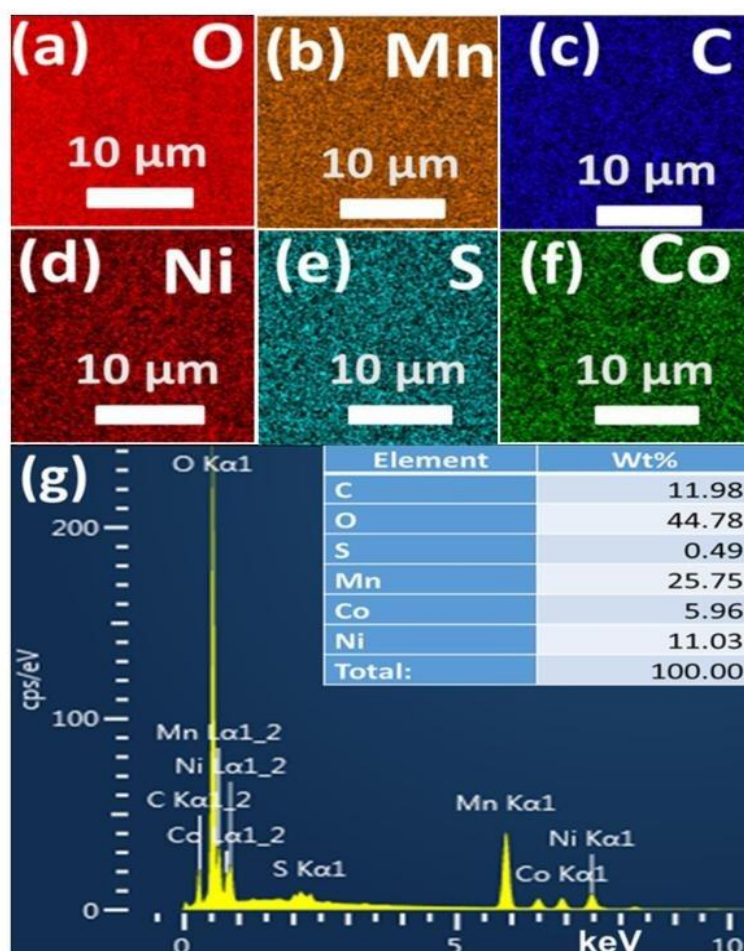
Fig S4: (a)-(f) shows the elemental mapping of MO/RGO-S-50@CN displaying the distribution of oxygen, manganese, carbon, nickel, sulphur, and cobalt, respectively and **(g)** shows the percentage composition of the elements within the material.

2
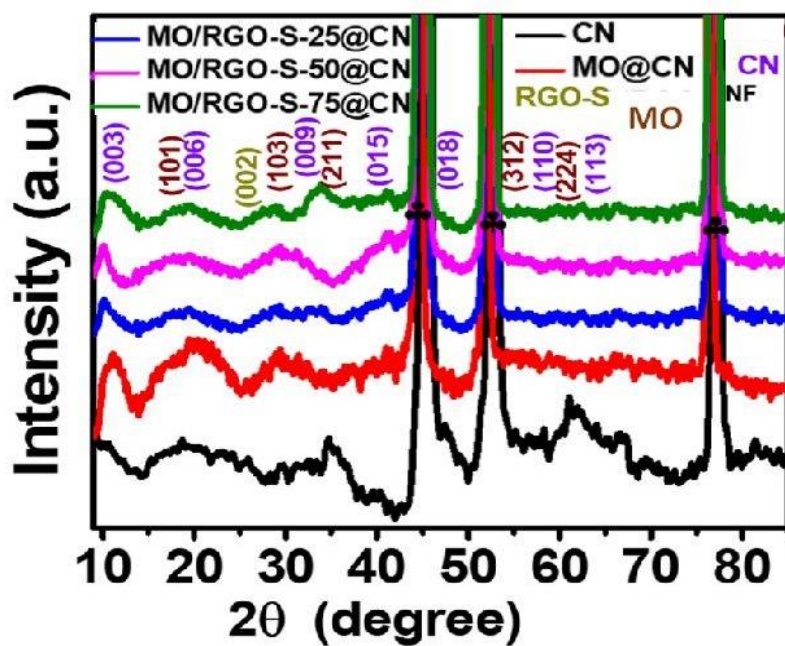
Fig. S5: The XRD patterns of samples with various RGO-S mass loading.
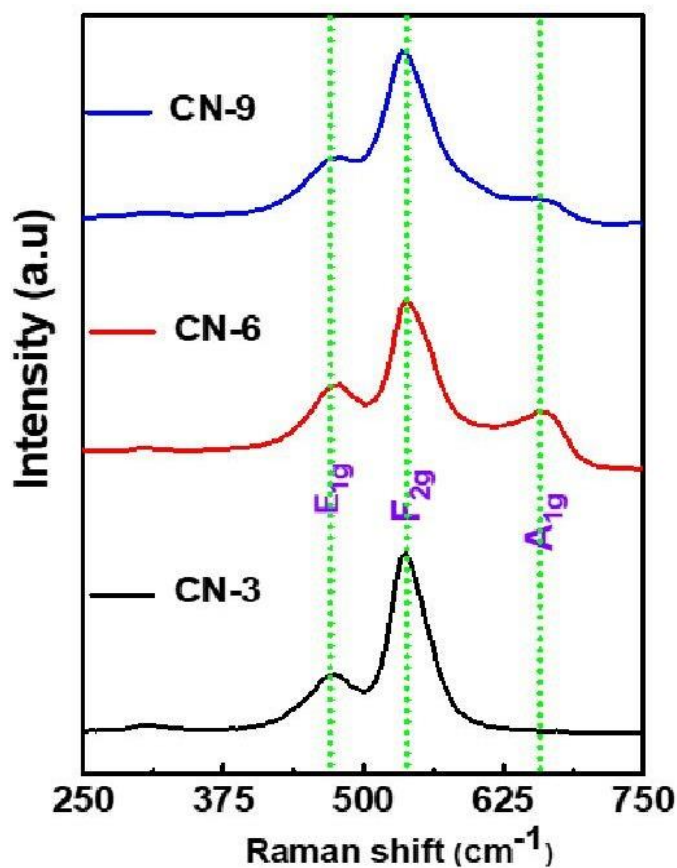
Fig. S6: Raman images of CN samples synthesized using different number of CV cycles.
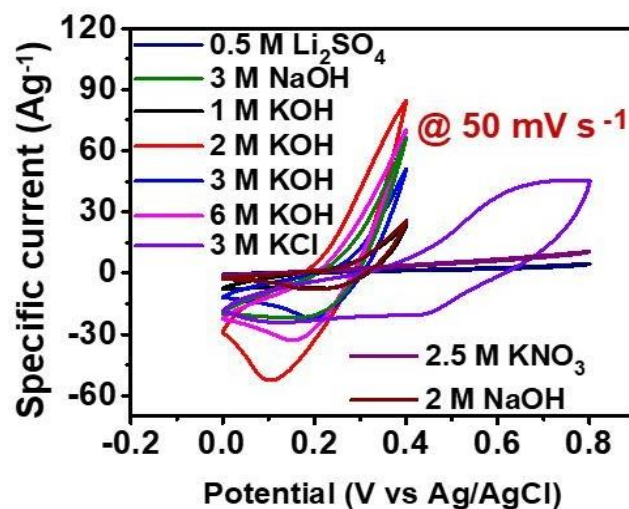
Fig. S7: (a) CV for MO/RGO-S-50@CN at 50 mV s^{-1} using different electrolytes.
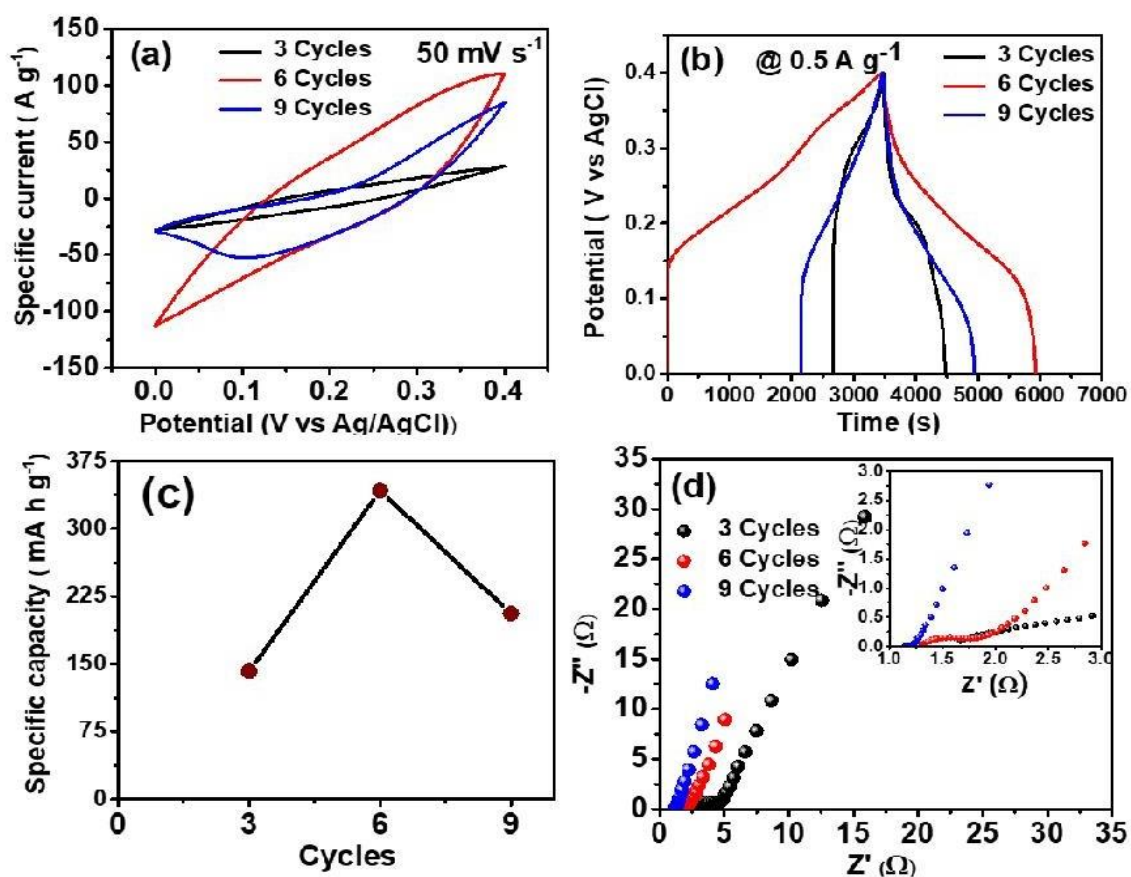
Fig. S8: (a) CV, **(b)** GCD, **(c)** specific capacity vs number of CV cycles and **(d)** Nyquist plot (insert is high frequency magnification indicating ESR values) of CN samples synthesized using different number of CV cycles as indicated in the figure:

4.1.3. Concluding remarks

Hausmannite sulphur reduced graphene oxide nickel cobalt layered double hydroxide (MO/RGO-S-X@CN) was successfully synthesized through a two-step electrodeposition step on nickel foam. The presence of nanospheres, nanorods and nanosheets proved the presence of Hausmannite (MO), sulphur-reduced graphene oxide (RGO-S) and cobalt nickel layered double oxide (CN). MO/RGO-S-50@CN yielded the highest specific capacity of 582.1 mAh g^{-1} at a specific current of 0.5 A g^{-1} in 2 M KOH, in a three electrode set-up. The right mass loading of MO/RGO-S helped to improve the electrical stability and redox activity of CN leading to a phenomenal specific capacity. This electrode was incorporated into a symmetric device (MO/RGO-S-50@CN//CCBW) with CCBW as the negative electrode. The device yielded superb electrochemical results with a specific energy of 56.0 Wh kg^{-1} at 0.5 A g^{-1} corresponding to a specific power of 515 W kg^{-1}. The device also showed great electrochemical stability by displaying a capacity retention of 85.1 % at 10,000 GCD cycles at 6 A g^{-1}. The synergetic effect of three different materials coupled with the robustness of the synthesis method which is based on electrodeposition contributed to these great results. This also provides the synthesized electrode and device as a candidate which can contribute significantly to energy storage and in the long term play a role in the transition from fossil fuel to cleaner renewable sources of energy.

4.2. Exploration of metal-layered double hydroxide composite material for hybrid capacitor produced by facile and efficient electrodeposition process

4.2.1. Introduction

The restacking and low electron transport in cobalt nickel layered double hydroxide (CN-LDH) can be improved by incorporating highly redox active materials in a set-up that reduces the restacking without incorporating carbon materials. Manganese cobaltite (MCO) is a low cost and safe spinel material with a very high theoretical capacity of 3620 F g^{-1} [245,246]. It also benefits from high electrical conductivity, many oxidation states, reversibility and the Jahn-Teller effect [247]. These traits work together to improve the ion diffusion and electron transport. MCO was grown directly on nickel foam (NF) using the process of electrodeposition and annealing. A further electrodeposition of CN-LDH was performed on the best sample, MCO-2.5 where 2.5 is the scan rate (mV s^{-1}) used for electrodeposition of MCO on NF. SEM, EDS, TEM, XRD and Raman spectroscopy was used to characterise the electrodes. The electrochemical analysis of the electrodes was performed in 2 M KOH in three and two electrode set-ups.

4.2.2. Results and discussion

The detailed results obtained from the experimental synthesis, characterisation and electrochemical evaluations are presented in the following manuscript:
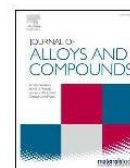
Research Article

Exploration of metal-layered double hydroxide composite material for hybrid capacitor produced by facile and efficient electrodeposition process

Gift Rutavi, Delvina Japhet Tarimo, Vusani Muswa Maphiri, Vianney Ngoyi Kitenge, Ncholu Manyala*

Department of Physics, Institute of Applied Materials, SARChI in Carbon Technology and Materials, University of Pretoria 0028, South Africa

ABSTRACT

Manganese cobaltite (MCO) with an empirical formula $Mn_{2-x} Co_{1+x} O_4$ and cobalt-nickel layered double hydroxide (CN-LDH) composite were synthesized through a dual-step electrodeposition approach. This process commenced with cyclic voltammetry (CV) electrodeposition of manganese cobaltite (MCO) on nickel foam (NF) followed by annealing in air. The next step was the CV electrodeposition of CN-LDH on MCO. The enhanced composite material MCO-2.5 @CN-LDH yielded a remarkable specific capacity of 415.9 mAh g^{-1} at a specific current of 1 A g^{-1} in a three-electrode configuration using 2 M KOH electrolyte. The electrodeposition method is credited for producing these competitive results, since the method excludes polymeric binders which would make it necessary to include conductive additives to compensate for the increased resistivity in the electrode materials. This positive electrode and the activated carbon from cooked chicken bone waste (CCBW) as the negative electrode were assembled into hybrid supercapacitor device (MCO-2.5 @CN-LDH//CCBW) using the same electrolyte. The device generated a specific energy of 55.8 Wh kg^{-1} corresponding to a specific power of 940.4 W kg^{-1} at 1 A g^{-1}. A device stability measurement at 10,000 galvanostatic charge-discharges (GCD) at 7 A g^{-1} produced a capacity retention of 81.6% and coulombic efficiency of 99.8%. Owing to these promising results, the fabricated materials proved to be capable to be employed as high specific energy supercapacitor.

1. Introduction

The use of non-renewable resources is always exerting a lot of pressure on the enviroment. Looking at the tremendous rate of the destruction, the shift from non-renewable to renewable sources of energy that are more environmentally friendly is long overdue. The intermittent nature of renewable energy sources is hindering this transfer and this is worsened by their availability in inadequate quantities [1–4].

These challenges can be alleviated by focusing resources on sourcing, examining, and improving storage devices for renewable energy. Among existing energy storage devices, supercapacitors have generated a lot of interest. They are endowed with some beneficial attributes compared to their counterparts such as batteries and fuel cells. These include long cycle life, greater specific power, and quicker charge-discharge. Above all these, they are more environmentally friendly compared to other storage devices. [5–8].

There are at least three classes of supercapacitors, the most common are electric double-layer capacitors (EDLC), pseudocapacitors (PC), and battery-type capacitors (BT). EDLC electrode materials, which store energy through charge separation at the electrolyte-electrode interface profit from possessing very large specific surface areas (SSA), wide operating potential windows and great electrical conductivities. These properties lead to huge specific power and faster charge discharge. PC and BT benefit from high theoretical specific capacities and specific energies due to rapid redox reactions at their electrolyte/electrode interface [9–11].

Layered double hydroxide (LDH) nanocomposites are promising functional materials because they incorporate the properties and features of the polymer and inorganic phases. The intercalation with functional nanomaterials possesses desirable electronic, magnetic, optical and piezoelectric properties for various universal applications such as medicine, functional coatings, microelectronics, energy storage and harvesting. CN-LDH is an essential bimetallic compound

which has generated a lot of interest in energy storage research due to high specific capacity which is attributed to an abundant reactions sites and unique layered structure [12–15]. However, the two-dimensional structure of CN-LDH leads to aggregation of materials and severe reduction in electrical conductivity leading to a rise in electric resistance during the GCD processes [16–18]. It is recommended to assemble composite electrodes by complementing LDHs with materials with much better electrical conductivities.

Metal cobaltites have been thoroughly investigated for use in supercapacitors as positive electrode because they possess some advantageous features which include very high electrical conductivity and reversibility. With a very large theoretical specific capacitance of 3620 F g^{-1}, MCO is a suitable candidate for synthesizing a high performance composite electrode with CN-LDH. This is because the manganese (Mn) ions enhance the electrical conductivity. The Mn^{3+} also benefit from the Jahn-Teller effect which improves ions diffusion and avails more reversible phase transformation [19]. The cobalt (Co) ions increase the electrochemical activity of the composite [20]. However, low cyclic stability limit their practical application. This can be alleviated through synthesis of a hybrid electrode consisting of a metal cobaltite and an LDH. For instance, Wang et al. hydrothermally synthesized glass-like NiCo$_2$O$_4$ @NiCo-LDH on a carbon cloth which yielded a phenomenal areal capacitance of 5810 mF cm^{-2} at a surface current density of 1 mA cm^{-2} [21].

Synthesis methods also play a very crucial role in the performance of electrode. Binder-free synthesis approaches are favoured because binders which are usually polymeric materials introduce significant resistance to to the electrode materials. To compensate for this, conductive additives have to be added to the electrode materials. Electrodeposition is a very important binder-free synthesis method as it possesses many advantages over other binder-free approaches such as the the successive ionic layer adsorption and reaction (SILAR) methods. These advantages include a very strong adhession between the active material (AM) and the current collector. This method is also very simple, efficient, cost effective and it provides a facile way of controlling the thickness of the films by varying parameters such as electrodeposition duration time, scan rate and number of electrodeposition cycles. There is a great electron transfer between the substrate and the material since the materials is grown directly on the substrate [22–25].

In this study we report the synthesis MCO-2.5, CN-LDH, and MCO-2.5 @CN-LDH as positive electrodes (positrodes) through the process of electrodeposition. The composite electrode: MCO-2.5 @CN-LDH displayed the best electrochemical performances with a specific capacity of 415.9 mAh g^{-1} in 2 M KOH at a specific current of 1 A g^{-1} in a half cell set-up. The electrode further displayed a superb electrochemical stability with a coulomb efficiency of 99.8% after 5000 GCD at 7 A g^{-1}. Due to this amazing performance, the composite electrode was incorporated as the positive electrode for hybrid supercapacitor device (MCO-2.5 @CN-LDH//CCBW), where CCBW served as the negative electrode. The device yielded a huge specific energy of 55.8 Wh kg^{-1} corresponding to a specific power of 940.4 W kg^{-1}. The hybrid device also showed great stability by producing a capacity retention of 81.6% and coulombic efficiency of 99.8% after 10,000 cycles at a gravimetric current of 1 A g^{-1}. Due to these promising results, the fabricated material has a potential for use as high performance renewable energy storage devices.

2. Experimental section

2.1. Materials

All the chemicals were used without further refining. The following chemicals and materials were used in this study: Deionised water (DW), which was extracted using a DRAWELL water purification device. Nickel foam [NF] was bought from Alantum (Munich,

Germany). Ethanol [CH$_3$ CH$_2$OH], Acetone [(CH$_3$)$_2$ CO], and hydrochloric acid [HCl] were acquired from (Sigma Aldrich, Steinheim, Germany). Nickel nitrate hexahydrate [Ni (NO$_3$)$_2$•6 H$_2$O], manganese acetate hexahydrate [Mn(CH$_3$COO)$_2$•4 H$_2$O], cobalt nitrate hexahydrate [Co(NO$_3$)$_2$•6 H$_2$O], sodium sulphate [Na$_2$SO$_4$], sulphur, and sodium sulphide [Na$_2$S] were all purchased from Merck (Johannesburg, South Africa).

2.2. Preparation of NF substrates

The preparation of NF was done as reported in our previous work [26]. Briefly, NF was shaped into (1 cm × 2 cm) rectangular pieces. The pieces were comprehensively cured by first dipping in 3 M HCl, acetone, followed by absolute ethanol (purity > 99%), and lastly in DW, each for 20 min. These pieces were dried for 12 h in an oven at 60° C. The purpose of this rigorous cleansing process was to eliminate the inert hydroxide and oxide layers which form on NF under humid conditions.

2.3. Preparation of MCO on NF electrode

Mn (CH$_3$COOH)$_2$.H$_2$O (0.006 mol) and Co(NO$_3$)$_2$.6 H$_2$O (0.012 mol) were mixed in 250 ml DW and stirred for 1 h to make a homogeneous solution. Na$_2$SO$_4$ (0.01 mol) was added to the solution to serve as a morphology directing agent and to prevent the agglomoration of particles. This solution was labelled S1. The electrodeposition was carried out using BioLogic VMP-300 workstation (Knoxville, TN,37,930 USA) operating on the EC-lab V11–30 software (Edmonton, AB, Canada) at room temperature. NF, platinum rod, and Ag/AgCl served as the working electrode (WE), counter electrode (CE), and reference electrode (RE), respectively in a 3-electrode set-up. The electrodeposition was carried out using cyclic voltammetry (CV) at 1.25 mV s^{-1} for 6 cycles in a potential range of − 1.2–0.5 V vs Ag/AgCl. The electrode which consisted of Co and Mn mixed oxides was then washed in DW and dried at 80° C in an oven for 5 h then annealed in air at 200° C for 1 h. The purpose of annealing was to transform the phase structure from LDH to the spinel phase [27]. The procedure was repeated at scan rates of 2.5 and 5 mV s^{-1}. The samples were labelled as MCO-1.25, MCO-2.5 and MCO-5 according to the scan rates used for synthesis. The mass loading of the deposited materials on NF were 1.4, 1.1 and 0.8 mg for MCO-1.25, MCO-2.5 and MCO-5 respectively.

2.4. Synthesis of CN-LDH, MCO@CN-LDH and CCBW

The synthesis of CN-LDH was similar to the one reported in our previous work [28]. In brief, 0.01 M each of Ni (NO$_3$)$_2$•6 H$_2$O and Co (NO$_3$)$_2$•6 H$_2$O were dissolved in 50 ml of DW and stirred vigorously for 30 min to form the homogeneous solution labeled S2. The electrodeposition procedure was identical to that in Section 2.3 except that the abovementioned solution (S2) served as the electrolyte. The electrode was labelled as CN-LDH. The procedure was then repeated, this time with MCO-2.5 as the working electrode, this composite electrode was labelled as MCO-2.5 @CN-LDH. CCBW which was used as the negative electrode was produced as detailed in our previous work [29]. The synthesis procedures are illustrated in the schematic in Fig. 1.

2.5. Material characterization

The Zeiss Ultra PLUS FEG-SEM (Ashikima Shi, Japan) which operated at 2.0 kV and incorporating the Oxford energy dissipation spectroscopy X-ray (EDS) was used to evaluate the morphology, electrode thickness and elemental composition of MCO, CN-LDH and MCO-2.5 @CN-LDH materials. Transmission electron microscopy (TEM) images were obtained from the JEOL JEM 2100-F which
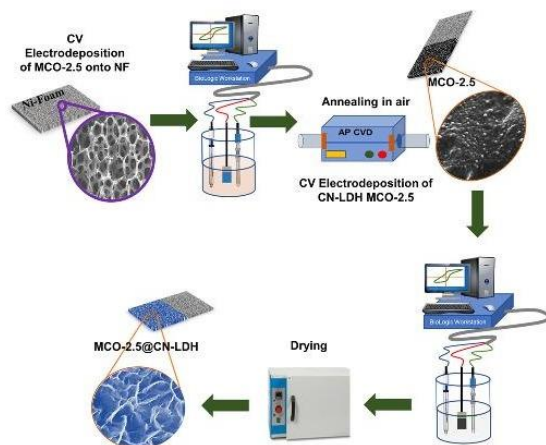
Fig. 1. Schematic illustration of the synthesis of MCO-2.5 @CN-LDH electrode.

operated at 1.0 kV. The X-Ray Diffraction (XRD) was used to analyse the structure of the samples. This makes use of a diffractometer (Brucker 2D PAN analytical BV, Amsterdam, Netherlands), which incorporates Cu $K_{\alpha 1}$ ($\lambda = 0.154061$ nm) at 2θ range from 5 to 90°. Raman spectroscopy measurements were performed using a WITec alpha-300 RAS+ Confocal micro-Raman microscope (Focus Innovations, Ulm Germany) with a 532 nm laser, spectral acquisition of 300 s using a 20X objective with a laser power of 4.5 mW.

2.6. Electrochemical characterization

To evaluate the electrochemical performance of the samples, the Bio-Logic workstation potentiostat was used. In three-electrode arrangement, the CE and RE were similar to those reported in Section 2.3. The WE were CN-LDH, MCO and MCO-2.5 @CN-LDH. CV, GCD and electrochemical impedance spectroscopy (EIS) were carried out in 2 M KOH for both 3-electrode and 2-electrode set-up (for hybrid supercapacitor device), respectively.

3. Results and analysis

3.1. Microstructural characterization and analysis

Fig. 2 displays high magnification SEM micrograms of MCO-1.25, MCO-2.5, and MCO-5. The morphology in Fig. 2(a) shows a mixture of fine and granular nanospheres for the MCO-1.25 sample. The morphology in Fig. 2(b) shows an increase in coarseness in MCO-2.5, revealing a nanosphere morphology with diameters close to 100 nm. This surface structure is endowed with channels which may facilitate ion transport. The nanospheres in Fig. 2(c) belong to MCO-5, these are also coarse but fused together thereby reducing pathways available for ion transport. Fig. 2(d)-(i) reveals low- and high-resolution SEM images of the synthesized MCO-2.5 CN-LDH, and MCO-2.5 @CN-LDH samples, respectively. Fig. 2(d, e) displays nanoflakes morphology of CN-LDH with widths of around 300 nm vertically grown on NF. Fig. 2(f, g) presents the granular MCO-2.5 nanospheres. Fig. 2(h, i) reveal thin sheets of CN-LDH completely covering the MCO-2.5 nanospheres. Fig S1(a) displays the SEM cross section of MCO-2.5 @CN-LDH, where the MCO-2.5 film which has an average thickness of 12 µm is sandwiched by a 8 µm thick CN-LDH film and the NF substrate. Fig S1(b) shows the HRTEM image of MCO-2.5 @CN-LDH composite sample. The morphology reveals a cloud of CN-LDH nanoflakes wrapped around the dense MCO-2.5
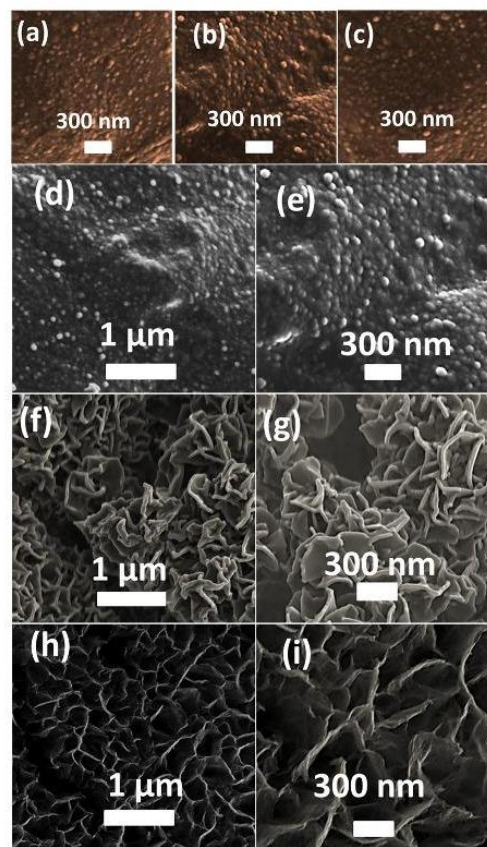
Fig. 2. High resolution SEM micrographs of MCO samples: (a) MCO-1.25, (b) MCO-2.5, and (c) MCO-5, (d, e), (f, g) and (h, i) present low- and high-resolution micrographs of MCO-2.5 CN-LDH, and MCO-2.5 @CN-LDH, respectively.

microstructure. This structure avails more surface area on the electrode essential for ion penetration leading to an increase in redox reactions which contributes to high specific capacity.

Fig. S2 (a)-(d) display the EDS mapping of the MCO-2.5 @CN-LDH composite sample. The maps show the composition of oxygen, manganese, cobalt and nickel, respectively within the material. The uniform distribution of O (21.41%), Mn (1.81%), Co (38.33%) and Ni (38.45%) elements were observed. The percentage composition of these elements are shown in Fig. S2(e).

Fig. 3(a) displays the Raman spectrum of MCO-1.25, MCO-2.5 and MCO-5. The A_{1g} and E_g peaks corresponds to Raman shifts at 685 and 492 cm^{-1}, respectively revealing the octahedral nature of the cobaltite. The F_{2g} peak at 512 cm^{-1} is due to the tetrahedral nature of manganese cobaltite. Both phases are present in MCO-2.5 [30]. There is no significant difference in peak intensity implying that the scan rate range of 1.25–5 mV s^{-1} is sufficient for the formation of the manganese cobaltite phase in a potential range of − 1.2–0.5 V vs Ag/ AgCl. However, the MCO-2.5 sample appears to have a slightly higher intensity compared to the rest. Fig. 3(b) shows the Raman spectrum of MCO-2.5 CN-LDH, and MCO-2.5 @CN-LDH samples. In CN-LDH shows the E_{1g} at 479 cm^{-1} which reveals the presence of O-Ni-O and O-Co-O while F_{2g} and A_{1g} at 546 and 673 cm^{-1}, respectively reveal the presence of Ni-OH and Co-OH bonds [31]. The presence of E_{1g}, F_{2g} and A_{1g} peaks in MCO-2.5 @CN-LDH is evidence of the successful combination of the LDH and the spinel.

3
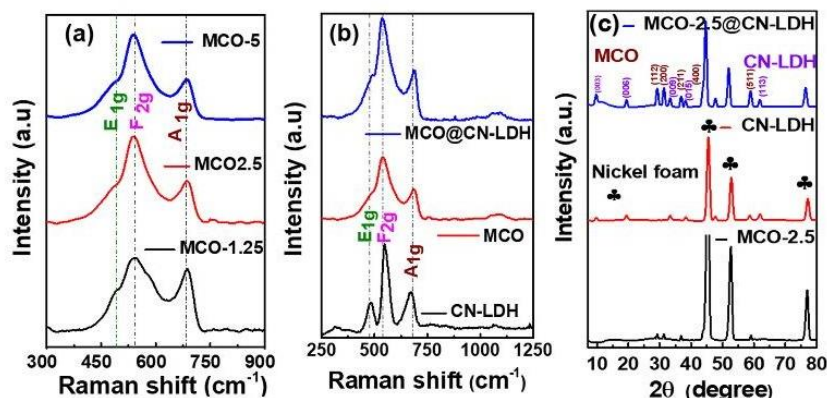
Fig. 3. Raman spectrum of (a) MCO-1.25, MCO-2.5, and MCO-5 and (b) MCO-2.5 CN-LDH, and MCO-2.5 @CN-LDH and (c) XRD of MCO-2.5 CN-LDH, and MCO-2.5 @CN-LDH.

Fig. 3(c) indicates the XRD of MCO-2.5 CN-LDH, and MCO-2.5 @CN-LDH samples. The planes correspond to (003), (006), (009), (015), (018), (110) and (113) occur at diffraction peaks 2θ = 9.7, 19.4, 33.3, 38.2, 47.7, 58.7 and 61.9°, respectively of CN-LDH (JCPDS No.14–0191) [32]. The peaks 2θ values of 29.2, 31.3, and 36.8° correspond to the planes (112), (200), and (211), respectively of the tetragonal $CoMn_2O_4$ in MCO-2.5 (JCPDS No.77–0471) [33]. The (400) and (511) planes at 43.7 and 59.1°, respectively are due to the cubic $MnCo_2O_4$ spinel achieved after annealing in air (JCPDS No.23–1237) [33]. From these observations of $Mn_{1+x}Co_{2-x}O_4$, the tetragonal and cubic phases co-exist for $0.3 < x < 0.9$.

3.2. Electrochemical performance of the as-synthesized samples

3.2.1. Three-electrode evaluations

Fig. S3(a) displays the GCD of MCO-1.25, MCO-2.5, and MCO-5 at 1 A g^{-1}. The samples show a slanted plateau, reflecting the presence of Faradaic reaction with MCO-2.5 demonstrating longest discharge time. The largest discharge time correspond to the highest specific capacity of MCO-2.5 as illustrated in Fig. S3 (b). Eq. (1) was utilised to obtain the specific capacity [34]:

$$Q_S = \frac{1}{3.6} \times I_S \Delta t \qquad (1)$$

where, Q_S is the specific capacity (mAh g^{-1}), I_S indicates the specific current (A g^{-1}), and Δt denotes the discharge time (s). The specific capacities for MCO-1.25, MCO-2.5, MCO-5 are 132.9, 238.1 and 97.8 mAh g^{-1}, respectively. Fig. S3 (c) displays the coulombic efficiency of the samples for 5000 GCD cycles at 7 A g^{-1}. Eq. (2) was used to obtain the columbic efficiency [35]:

$$\eta = \frac{t_D}{t_C} \times 100 \quad \% \qquad (2)$$

where η is the coulombic efficiency (%), t_D and t_C are the times (s) taken to fully discharge and charge, respectively. The coulombic efficiencies are 99.0%, 99.7%, and 99.8% for MCO-2.5, CN-LDH, and MCO-2.5 @CN-LDH, respectively, which are quasi-perfect which is a characteristic of supercapacitors. The robustness of the electrodeposition synthesis resulted in the superior coulombic efficiency. The general electrochemical comparison shown in Fig. S3 shows a superior performance for MCO-2.5, therefore, all further electrodepositions of CN-LDH on MCO-2.5 were carried-out using a scan rate of 2.5 mV s^{-1} to form composite MCO-2.5 @CN-LDH.

Fig. 4(a) shows the GCD traces of MCO-2.5 at 1 A g^{-1} using various electrolytes. 2 M KOH displays the longest discharge time corresponding to the largest specific capacity, and therefore 2 M KOH was

selected for further testing of CN-LDH, MCO-2.5 @CN-LDH in three electrode configuration and the hybrid supercapacitor device. Fig. 4(b)-(c) displays the electrochemical characterisation of CN-LDH, MCO-2.5, and MCO-2.5 @CN-LDH in 3-electrode set-up in 2 M KOH. The mass loading for MCO-2.5 CN-LDH, and MCO-2.5 @CN-LDH electrodes were 0.9, 1.1 and 1.2 mg, respectively. Fig. 4(b) displays the CV in a range of 0.0–0.4 V vs Ag/AgCl potential at 20 mV s^{-1} with MCO-2.5 @CN-LDH exhibiting the highest current response. This can be explained by the improved electrochemical conductivity caused by the CN-LDH and MCO-2.5 complementing each other in the composite. The presence of MCO-2.5 reduces the aggregation of CN-LDH and enhances the ion diffusion. The GCD at 1 A g^{-1} in Fig. 4(c) presents a skewed plateau which further supports the exhibition of the Faradaic nature of the samples in Fig. 4(b). MCO-2.5 @CN-LDH took the longest time to fully discharge, supporting the highest current response seen in Fig. 4(b). The specific capacity as a function of specific current is shown in Fig. 4(d), whereby MCO-2.5 @CN-LDH shows the largest specific capacity for all the specific currents recorded (1–10 A g^{-1}).

The rate capabilities at 10 A g^{-1} are 54.3%, 58.6% and 87.8% for MCO-2.5 CN-LDH, and MCO-2.5 @CN-LDH, respectively. The high rate capabilities demonstrated by the sample can be attributed to the high electrical conductivity demonstrated by the high current response of the samples and the collaborative effect of both the spinel and the LDH [32,36–41]. Fig. 4(e) displays the Nyquist plot used to evaluate the charge dynamics and the electrical resistivities of the samples. The insert is the enlargement of the plots at the high frequency region to reveal the equivalent series resistance (ESR). The ESR values which corresponds to the high frequency real impedance intercept, as shown in the insert are 1.7, 1.3, 1.6 and 6.4 Ω for MCO-2.5, CN-LDH, MCO-2.5 @CN-LDH and NF (nickel-foam), respectively. These ESR values, which are small except for NF, demonstrate that the electrolyte had very small ionic resistance and that the contact resistance between the current collector and the active material (AM) is minimal. The inseparable bonding of the AM and the current collector brought about by the binder-free electrodeposition technique is credited for these small contact resistances. The exclusion of binder in this synthesis approach is very important as the polymeric binder increase the resistance of the electrode materials. The semicircle in the NF has the largest diameter is evidence of the presence of charge transfer resistance (CTR) which shows the prominence of Faradaic reactions due to the presence of metallic components within the NF. The diameters in MCO-2.5, CN-LDH and MCO-2.5 @CN-LDH are significant compared to NF indicating lower CTR. Fig. 4(f) shows the coulombic efficiency and capacity retention of MCO-2.5, CN-LDH, and MCO-2.5 @CN-LDH as a function of number
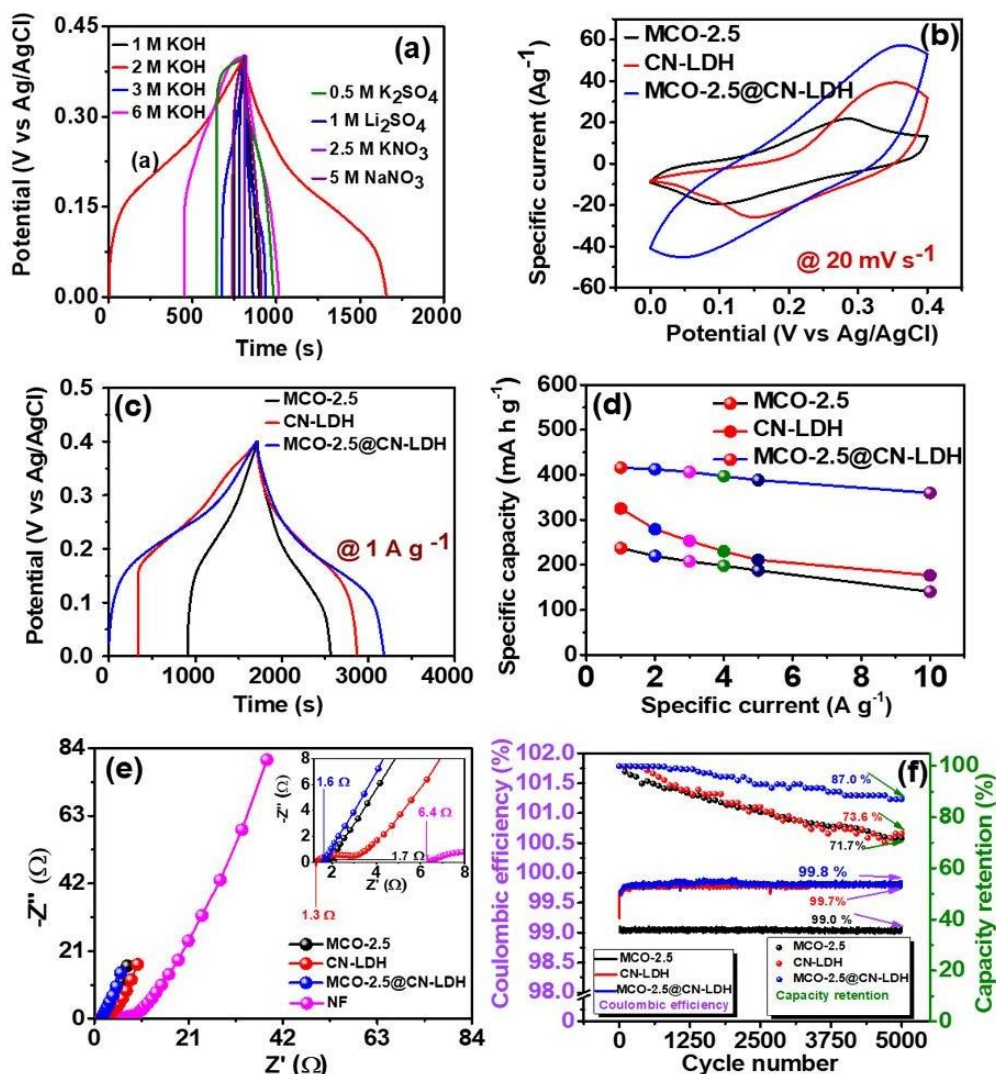
Fig. 4. (a) GCD for MCO-2.5 at 1 A g^{-1} using different electrolytes, Fig (b)- (f) indicated the electrochemical measurements in 2 M KOH electrolyte: (b) the CV traces, (c) GCD traces, (d) specific capacity vs specific current, (e) EIS Nyquist plot with insert, and (f) capacity retention of MCO-2.5, CN-LDH, and MCO-2.5 @CN-LDH, respectively.

of cycles.The coulombic efficiency values are 99.0%, 99.7% and 99.8% for MCO-2.5, CN-LDH, and MCO-2.5 @CN-LDH, respectively. The capacity retentions are 71.7%, 72.6%, and 87.0%, The high strength of the bond created by the electrodeposition method is credited for the high capacity retention values while the synergertic effect of the the LDH and spinel endow the composite with significantly superior capacity retention.

MCO-2.5 and CN-LDH complement each other in the composite to endow MCO-2.5 @CN-LDH with high redox reactivity, high adsorption property and strong chemical stability. MCO-2.5 helps to reduces the the resistivity due to the aggregation of the while CN-LDH provide an abundant active redox sites and also benefit from its unique layered structure. It is evident from Fig. 4 that the electrochemical performance of MCO-2.5 @CN-LDH exceeds those of the from MCO-2.5 and CN-LDH electrodes. This is attributed to the synergistic effect of enhanced ion diffusion due to the Jahn-Teller of

MCO-2.5 and the unique layered structure of CN-LDH resulting in the best electrochemical performance of the individual electrodes.

The electrochemical attributes of the composite MCO-2.5 @CN-LDH are detailed in Fig. 5. The CV traces shown in Fig. 5(a) reveal sets of reduction and oxidation peaks in a potential range of 0.0–0.4 V vs Ag/AgCl for scan rates of 5–100 mV s^{-1}. Nevertheless, the prominence of redox crests diminishes with an increase in scan rate. This is due to the drop in the reversibility of the redox process due to the charge diffusion polarisation in the electrode material. Mn and Co undergo oxidation at the same potential, therefore peaks for Mn and Co are not separated [42]. The reversible reactions in Eqs. (3) - (5) are responsible for the redox crest as indicated below:

$$Mn_{2-x}Co_{1+x}O_4 + H_2O + OH^- \leftrightarrow (2-x)\,MnOOH + (1+x)\,CoOOH + e^- \quad (3)$$

$$MnOOH + OH^- \leftrightarrow MnO_2 + H_2O + e^- \quad (4)$$

5
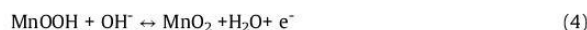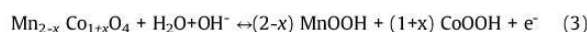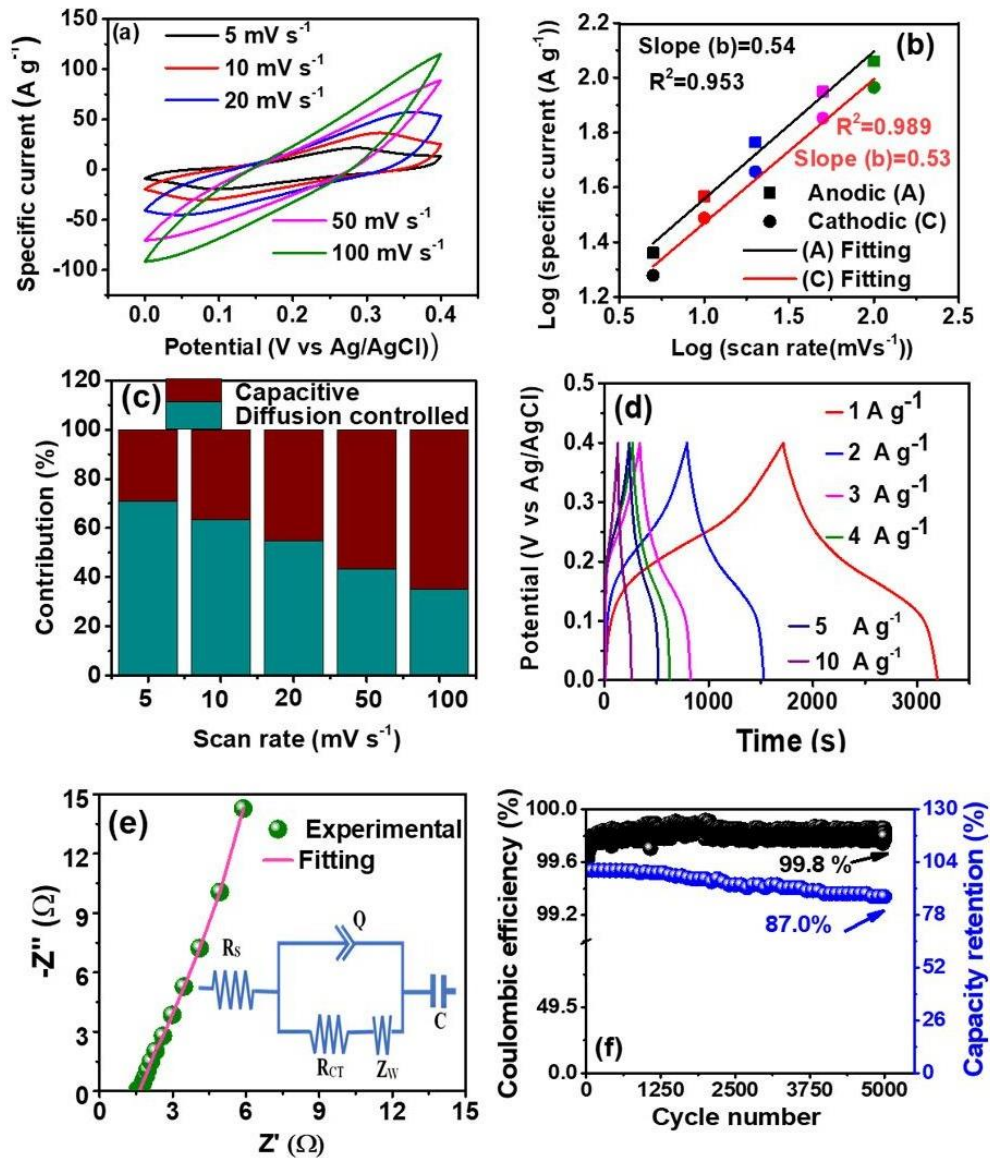
Fig. 5. (a) CV traces, (b) The dependence of log current on log scan rate (power law - anodic and cathodic), (c) Contribution (%) of capacitive and diffusion-controlled charge storage, (d) GCD curves, (e) The Nyquist plot with an inset representing the equivalent circuit, and (f) Coulombic efficiency and capacity retention as a function of cycle number for MCO-2.5@CN-LDH.

$$CoOOH + OH^- \leftrightarrow CoO_2 + H_2O + e^- \tag{5}$$

For a better understanding of the energy storage mechanisms and charge storage contributions, the power laws expressed by Eqs. (6) and (7) were used [43]:

$$I(V) = a \quad \nu^b \tag{6}$$

$$\log I(V) = a + b \quad \log \nu \tag{7}$$

$I(V)$ is the peak current at a given scan rate ν given in mV s^{-1}, a and b are constants. For pure surface-controlled processes, b equals 1 while for pure diffusion-controlled processes b equals 0.5. Fig. 5(b)

indicates a plot of log I vs log ν. From the gradient of the linear plot, b equals 0.54 and 0.53 for anodic and cathodic processes, respectively. Since the values of b are between 0.5 and 1, both processes have a contribution, however, the diffusion-controlled process dominates.

To evaluate the contribution of diffusion-controlled and capacitive processes, Eqs. (8) and (9) were used:

$$I(V) = K_1\nu + K_2\sqrt{\nu} \tag{8}$$

$$\frac{I(V)}{\sqrt{\nu}} = K_1\sqrt{\nu} + K_2 \tag{9}$$

$K_1\nu$ and $K_2\sqrt{\nu}$ signify the capacitive and diffusion-controlled processes, respectively. By plotting $\frac{I(V)}{\sqrt{\nu}}$ vs $\sqrt{\nu}$, the values of the constants,

K_1 and K_2 can be obtained from the gradient and the y-intercept, respectively. Fig. 5(c) shows the capacitive and diffusion controlled contribution for a range of scan rates from 5 to 100 mV s^{-1}. It is evident that the charge storage mechanism involve both capacitive and diffusion-controlled processes. At a scan rate of 5 mV s^{-1}, the diffusion and capacitive contributions are 70.9% and 29.1%, respectively while at a high scan rate of 100 mV s^{-1}, the contributions changes to 35.2% and 64.8%, respectively. This confirms the pseudocapacitive nature of the MCO-2.5 @CN-LDH electrode in 2 M KOH electrolyte. Table S1 compares the capacitive contribution of this work with LDH based electrode materials and composites reported in the literature at 5 mV s^{-1}. The comparison show that the range contribution in this work is within the range of the percentage in the literature.

The GCD of MCO-2.5 @CN-LDH is shown in Fig. 5(d) at a specific currents of 1–10 A g^{-1}. The pseudocapacitive behaviour of the samples is evident in the lack of a flat plateau at the higher specific currents which is the feature of battery-type storage structure. Fig. 5(e) shows the EIS Nyquist plot of MCO-2.5 @CN-LDH whereas the insert shows the equivalent circuit. The equivalent circuit shows the ESR (R$_S$) which corresponds to the real impedance intercept at the high frequency region with a low value of 1.63 Ω and is comparable to the experimental value of 1.60 Ω. The R$_S$ is in series with a branch containing the constant phase element (CPE) Q, the charge transfer resistance (CTR) denoted by the component (R$_{CT}$) and the Warburg component (Z$_W$). R$_{CT}$ proves the presence of Faradaic reactions. The CPE is due to the capacitor behaving non ideally, and Z$_W$ represent the opposition to ion diffusion. The components are in turn in series with the capacitance element (C) corresponding to the slanted line in the low frequency region.

Fig. 5(f) shows the stability results indicating the coulombic efficiency and a capacity retention as a function of number of cycles for MCO-2.5 @CN-LDH composite sample. The coulombic efficiency and capacity retention show large values of 99.8% and 87.0%, respectively. The synergistic effect of chemical stability of MCO-2.5 and great ion exchange capability of CN-LDH coupled with the robust bonding of the electrode material and current collector brought about by the electrodeposition techniques is credited for this huge stability values after 5000 GCD cycles. Due to its exceptional electrochemical attributes, MCO-2.5@CN-LDH was selected for incorporation into hybrid device.

Table 1 compares the electrochemical capabilities of MCO composites based electrodes which were reported from the literature. MCO-2.5 @CN-LDH (this work) generated the highest specific capacity of 415.9 mAh g^{-1} at 1 A g^{-1}. The table also show high stability results for the synthesis method used in this study which involved

Table 1
Electrochemical performance of recently reported manganese cobaltite composites in three-electrode system.

Material	Synthesis method	Capacity (mAh g^{-1})	Capacity retention/ (cycles)	Ref.
Mn$_{1.5}$Co$_{1.5}$O$_4$	Hydrothermal and calcination	618 (0.4 A g^{-1})	90% (300)	[44]
MnCo$_2$O$_{4.5}$ /NiCo$_2$O$_4$	Hydrothermal and calcination	278.4 (1 A g^{-1})	93% (2000)	[45]
MnCo$_2$O$_{4.5}$ /GCD	Hydrothermal and calcination	225.7 (1 A g^{-1})	80% (2000)	[46]
MnCo$_2$O$_{4.5}$/ RGO	Hydrothermal and calcination	129.7 (1 A g^{-1})	95% (5000)	[42]
GW-MCO	Microwave	109.3 (20 mV s^{-1})	92.3% (5000)	[47]
MnX$_2$O$_4$/GNF	Hydrothermal	237.8 (1 A g^{-1})	80% (3500)	[48]
MCO-2.5 @CN-LDH	**Electrodeposition and calcination**	**415.9 (1 A g^{-1})**	**87% (5000)**	**This work**

the electrodeposition (binder free) and annealing process. It was observed that the electrodeposition synthesis route leads to capacity retentions values which are comparable to other synthesis methods. These highly competitive electrochemical values indicate the coherence of the LDH and spinel in a composite synthesized through electrodeposition and calcination procedures.

3.2.2. Electrochemical properties of the hybrid supercapacitor device

A hybrid device MCO-2.5 @CN-LDH//CCBW was assembled with the intention to assess the true performance of the MCO-2.5 @CN-LDH electrode a full-cell system. CCBW from our previous study was used as the negative electrode [29]. The specific capacitance of the CCBW was measured in three-electrode in 2 M KOH from GCD curves. The GCD of CCBW is shown in the supporting information as Fig S4 (a) in a potential range −0.9–0 V vs Ag vs AgCl. The specific capacitance range was 30.4–184.4 F g^{-1} as shown in the specific capacitance vs specific current graph in Fig S4 (b).

The analysis was carried-out in 2 M KOH electrolyte in a two-electrode set-up. To avoid a scenario where one electrode will end up charging the other, the charge in each electrode was balanced. To achieve this, the mass ratio of the electrode materials was determined through the mass balance Eq. (10) [49]:

$$\frac{m_+}{m_-} = \frac{C_{S-} \times V_{S-}}{3.6 Q_{S+}} \qquad (10)$$

Here, the negative and positive electrode masses (mg) are denoted as m$_-$ and m$_+$, the positive electrode specific capacity (mAh g^{-1}) is Q$_{S+}$, while C$_{S-}$ is the negative electrode's specific capacitance (F g^{-1}), and the negative electrode potential (V) is V$_{S-}$. For the hybrid device, the mass of the material negative and on each electrodes was 5.4 mg cm^{-2} and 0.6 mg cm^{-2} respecively, corresponding to the mass ratio of m-/m+ was 9:1.

The CV of an individual CCBW negative and MCO-2.5 @CN-LDH positive electrodes at 20 mV s^{-1} are indicated in Fig. 6(a). CCBW indicates a rectangular EDLC trace CV which displays the capacitive behaviour with a performance at −0.9–0 V vs Ag/AgCl, whereas MCO-2.5 @CN-LDH reveals the Faradaic performance at 0.0–0.4 V vs Ag/AgCl. The CV of the hybrid device at a scan rates of 5–100 mV s^{-1} is shown in Fig. 6(b). The EDLC features manifest at an approximate cell potential range of 0–0.8 V. In the potential range 0.8–1.6 V, the Faradaic behaviour becomes more predominant. This proves that the contribution of negative and positive electrodes in the device occurs at lower and high cell potentials, respectively. However, the disappearance of the redox peaks as the scan rate increases confirms the change from Faradaic to pseudocapacitive nature of the composite material which is credited to the incorporation of the EDLC material within the device. Fig. 6(c) presents the GCD at a specific current from 1 to 10 A g^{-1}. The symmetry in the curves shows the reversibility of the redox reactions. There are no clear horizontal plateaux in the GCD curves showing that the charge storage mechanism is not entirely EDLC or purely Faradaic but rather pseudocapacitive. Fig. 6(d) indicates the variation of specific capacity with specific current from 1 to 10 A g^{-1}. The greatest specific capacity of 59.0 mAh g^{-1} occurs at 1 A g^{-1} corresponding to a rate capability of 52% at 10 A g^{-1}. Fig. 6(e) relates the stability measurements of the device. After 10,000 GCD cycles at 7 A g^{-1}, the device was able to preserve a coulombic efficiency of 99.8% and a capacity retention of 81.6%. The lack of binders in MCO-2.5 @CN-LDH was responsible for such high stability [50]. To obtain the specific energy (E$_s$) and specific power (P$_S$), Eqs. (11) and (12) were used [51], [52]:

$$E_s \ \ (Wh \ \ kg^{-1}) = \frac{I_s}{3.6} \int V(t)dt \qquad (11)$$

$$P_s \ \ (W \ \ kg^{-1}) = 3600 \times \frac{E_s}{\Delta t} \qquad (12)$$

119
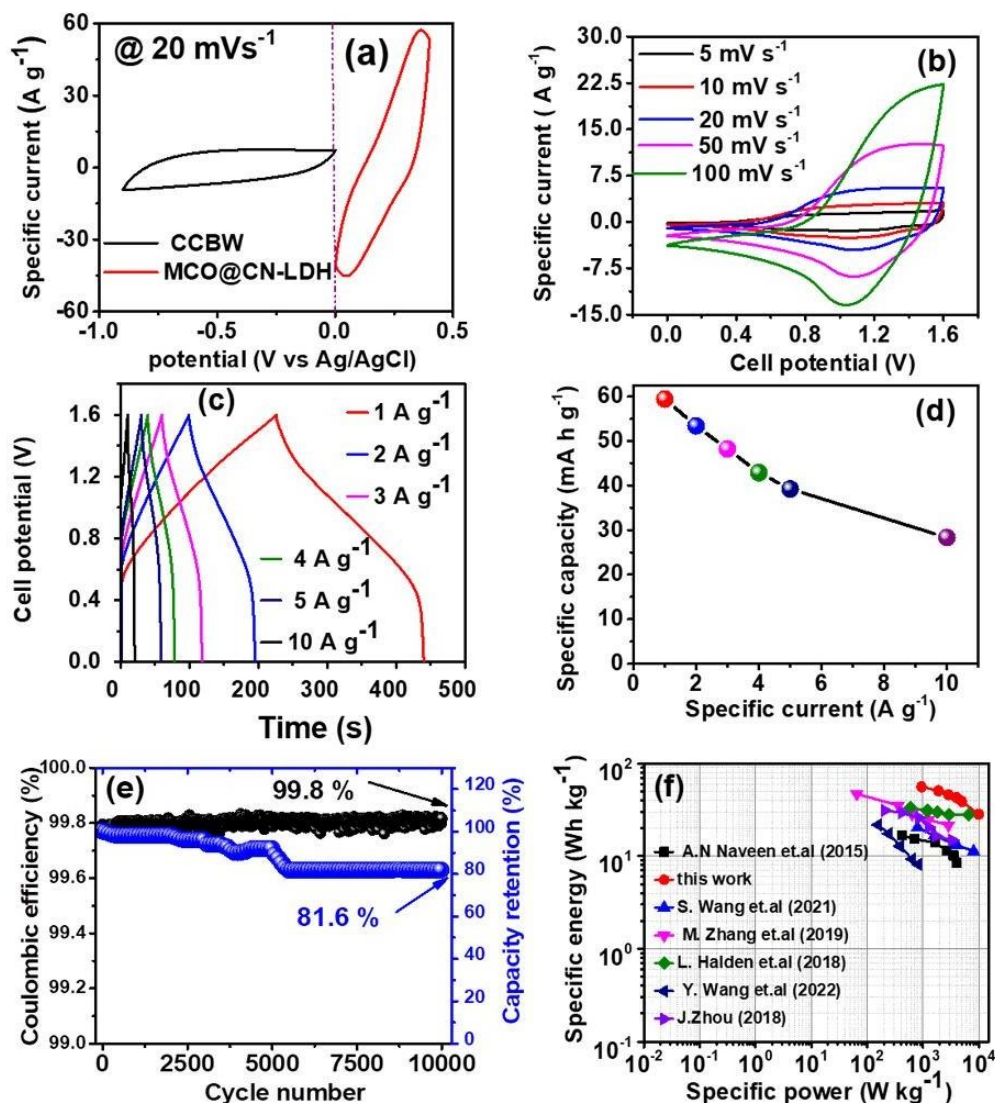
Fig. 6. (a): CV traces of the negative and positive electrodes at 20 mV s⁻¹, Fig (b)-(e) show the electrochemical performance of the MCO-2.5 @CN-LDH//CCBW device. (b) CV traces at various scan rates, (c) GCD traces at a range of specific currents, (d) the specific capacity vs specific current, (e) coulombic efficiency and capacity retention vs cycle number and (f) Ragone plot of MCO-2.5 @CN-LDH//CCBW hybrid device compared to other similar devices in the literature.

where $\int V(t)dt$ denotes the integral (Vs) representing the area under the discharge GCD curve, I_S is the specific current (A g⁻¹) of the GCD curve, and Δt represents the discharge time (s).

This MCO-2.5 @CN-LDH//CCBW hybrid device delivered a great specific energy of 55.8 Wh kg⁻¹ at 1 A g⁻¹ with corresponding specific power of 940 W kg⁻¹. For a comparison of the energy storage and power delivery of this device with those of manganese cobaltite based materials reported in the literature, the Ragone plot in Fig. 6(f) was used for representation. From the plot it is clear that the MCO-2.5 @CN-LDH//CCBW hybrid device outperforms some of the similar devices in the literature in terms of energy storage and rate of energy delivery [20,42,45,46,48,53].

The maximum power (P_MAX) is delivered when the ESR matches the load resistance, in which the P_MAX in this study was calculated from Eq. 13 below [54]:

$$P_{MAX} \quad (kW \quad kg^{-1}) = \frac{V^2}{4m \times R_S} \tag{13}$$

where m is the total mass (g) of the AM in the hybrid device, V is the cell potential (V), and R_S (Ω) is ESR of the assembled device. The value of P_MAX for the device was found to be 106.7 kW kg. ⁻¹.

This phenomenal electrochemical performance of the hybrid device can be credited to the Faradaic and EDLC charge storage in the positive and negative electrodes complementing each other. The high electrical conductivity and wide operating potential of CCBW leads the high specific power and cyclic stability while the large specific capacity of MCO-2.5 @CN-LDH is responsible for the huge specific energy. The electrochemical properties of earlier reported hybrid devices which incorporate manganese cobaltite are displayed in Table 2 for a particular lowest specific current. The MCO-2.5 @CN-

Table 2
Comparison of manganese cobaltite-based hybrid devices reported in the literature in terms of electrochemical performance.

Device	Electrolyte	Cell potential (V)	E_S (Wh kg^{-1})	P_S (W kg^{-1})	Ref.
MnCo$_2$O$_4$ @NiCo-LDH/NF//AC	6 M KOH	1.6	21.3	160	[20]
(MCO/Ni)− 15 min//PAC/Ni	(CMC)-LiNO$_3$ gel	2.0	27.6	1010	[33]
MnCo$_2$O$_{4.5}$/GCD//RGO	1 M LiOH	1.3	46	66	[46]
MnCo$_2$O$_{4.5}$-NiCo$_2$O$_4$ //Fe-rGO	2 M KOH	1.2	34	597	[45]
MnCo$_2$O$_4$ @Co$_3$O$_4$//AC	2 M KOH	1.5	31	208.5	[53]
MnCo$_2$O$_4$//rGO	1 M KOH	1.6	53.7	1600	[55]
MCO-2.5 @CN-LDH//CCBW	**2 M KOH**	**1.6**	**55.8**	**940**	**This work**
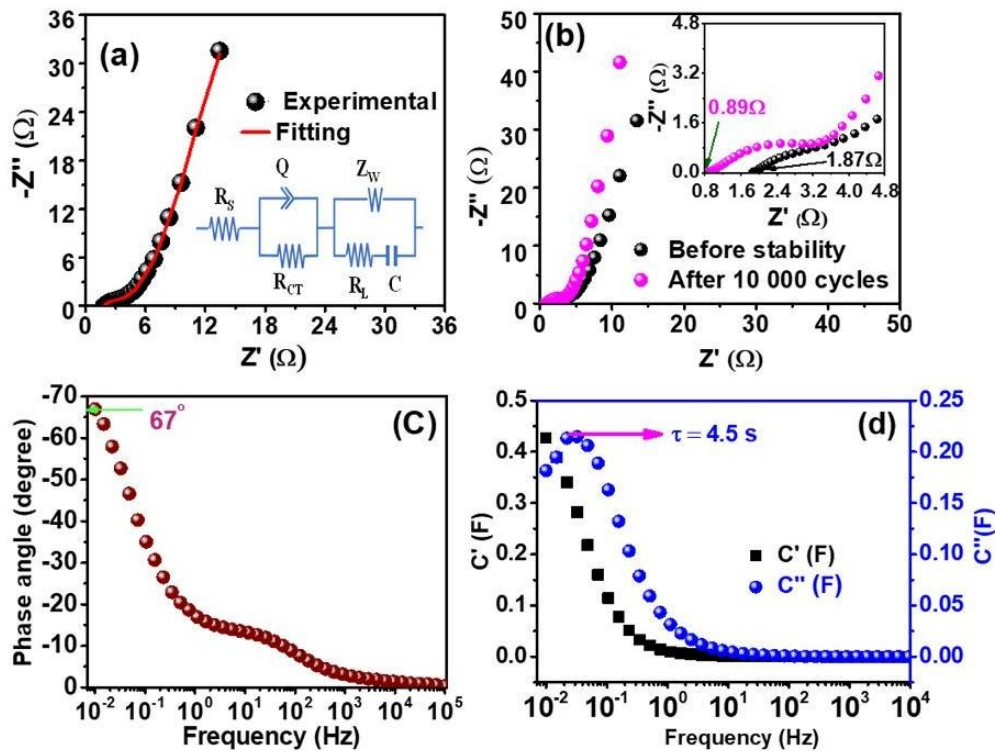
Fig. 7. (a) Nyquist plot of the experimental data with the fitting curve using an equivalent circuit as the inset to the figure, (b) Nyquist plot before and after cycling stability with inset which is magnification in the high frequency region, (c) Bode plot and (d) imaginary and real capacitance vs frequency of the hybrid device.

LDH//CCBW hybrid device yielded a substantial specific energy of 55.8 Wh kg^{-1} corresponding to a specific power of 940 W kg^{-1}.

The Nyquist plot in Fig. 7(a) shows the synthesized device's experimental results alongside the fitting line. The equivalent circuit used to fit is shown in the inset. The small ESR value (R_S) of 1.87 Ω signified the diminished contact resistance between the AM and the current collector. The circuit displays a small R_{CT} of 3.47 Ω. The lowered semicircle is due to the presence of the CPE. The CPE therefore makes R_{CT} appear smaller than its actual value. The resistance due to the leakage currents, R_L is in series with the EDLC capacitance. R_L has a value of 1.73 Ω, and it leads to the curve deflecting further from the imaginary impedance axes decreasing the size of the phase angle from − 90°. The Z_w which is parallel to R_L and C further diverges the slope in the low frequency zone. The EIS Nyquist plots before and after cycling is shown in Fig. 7(b). The reduction of the resistance at the boundary between the electrolyte and the electrode and between AM-current collector cause the R_S to

drop to 0.980 Ω after 10,000 GCD cycles. Nevertheless, the gradient of the trace after 10,000 cycles shows an increase in the diffusion length on the electrolyte-electrode interface caused by the decomposition of the water molecules in the electrolyte [56]. Fig. 7(c) is indicating the Bode plot with the phase angle as a function of frequency. The phase angle at the low frequency region is − 67° which is not very close to − 90° signifying the occurrence of both capacitive and Faradaic characteristics in the device. The variance of real capacitance $C'(\omega)$) and imaginary capacitance ($C''(\omega)$ with frequency (f) is demonstrated in Fig. 7(d). These capacitances are calculated from the equations expressed below [26]:

$$Z'(\omega) = \omega C''(\omega) \mid Z(\omega) \mid \tag{14}$$

$$Z''(\omega) = \omega C'(\omega) \mid Z(\omega) \mid \tag{15}$$

where, $\mid Z(\omega) \mid$, $Z'(\omega)$ and $Z''(\omega)$ are the magnitude of impedance, real and imaginary impedances (Ω), respectively. ω denote the angular

9

frequency (rad s^{-1}) which is given by $\omega = 2\pi f$. The capacitance (F) of the device which can be accessible and transferred is denoted by C' (ω) and it corresponds to a maximum value of 0.44 F at low frequency as shown in Fig. 7(d). C''(ω) depicts the electrode's energy drop caused by non-reversible reactions. The C''(ω) has a crest of 0.24 F at 0.031 Hz. The time τ taken to fully charge the device is 4.5 s obtained from the plot using $2\pi f\tau = 1$. This small value shows that the charging is very fast for this device.

4. Conclusion

A dual electrodeposition approach and calcination was employed to synthesize MCO-2.5, CN-LDH, and MCO-2.5@CN-LDH samples. The best electrochemical performance was achieved in the composite electrode material (MCO-2.5@CN-LDH). It yielded the highest specific capacity of 415.9 mAh g^{-1} at specific current of 1 A g^{-1}. After 5000 GCD cycles performed at 7 A g^{-1}, the electrode produced a coulombic efficiency of 99.8%. The electrode was used to assemble a hybrid device fabricated with activated with CCBW as the negative electrode. This MCO-2.5@CN-LDH//CCBW hybrid device produced a great specific energy of 55.8 Wh kg^{-1} at 1 A g^{-1} corresponding to a specific power of 940.4 W kg^{-1}. Stability tests of the device for 10,000 at a specific current of 7 A g^{-1} yielded a coulombic efficiency of 99.8% and a capacity retention of 81.6%. Due to these satisfactory performances, the hybrid device is a potential candidate for inclusion in high energy performaning devices.

CRediT authorship contribution statement

Gift Rutavi: Conceptualization, Methodology, Investigation, Formal analysis, Writing – original daft, Writing – review & editing. **Delvina J. Tarimo:** Conceptualization, methodology, formal analysis, Writing – review & editing. **Vusani M. Maphiri:** Methodology, Formal analysis, Writing – review & editing. **Vianney N. Kitenge:** Formal analysis, Writing – review & editing. **Ncholu Manyala:** Resources, Supervision, Funding acquisition, Visualization, Formal analysis, Writing – review & editing.

Data Availability

Data will be made available on request.

Declaration of Competing Interest

The authors declare that they have no known competing financial interests or personal relationships that could have appeared to influence the work reported in this paper.

Acknowledgements

Appendix A. Supporting information

Supplementary data associated with this article can be found in the online version at doi:10.1016/j.jallcom.2022.167216.

References

[1] R. Vakulchuk, I. Overland, D. Scholten, Renewable energy and geopolitics: a review, Renew. Sustain. Energy Rev. 122 (2020) 109547, https://doi.org/10.1016/j.rser.2019.109547

[2] S. Ganesan, U. Subramaniam, A.A. Ghodke, R.M. Elavarasan, K. Raju, M.S. Bhaskar, Investigation on sizing of voltage source for a battery energy storage system in microgrid with renewable energy sources, IEEE Access 8 (2020) 188861–188874, https://doi.org/10.1109/ACCESS.2020.3030729

[3] M. Shafiul Alam, F.S. Al-Ismail, A. Salem, M.A. Abido, High-level penetration of renewable energy sources into grid utility: Challenges and solutions, IEEE Access 8 (2020) 190277–190299, https://doi.org/10.1109/ACCESS.2020.3031481

[4] Y. Li, W. Lin, L. Xue, J. Xie, B. Wei, G. Chen, D. Chen, Facile preparation of V2O3/ black fungus-derived carbon composite with hierarchical porosity as a promising electrode for lithium/sodium ion batteries, J. Alloy. Compd. 905 (2022) 164258, https://doi.org/10.1016/j.jallcom.2022.164258

[5] C. Xiong, M. Li, S. Nie, W. Dang, W. Zhao, L. Dai, Y. Ni, Non-carbonized porous lignin-free wood as an effective scaffold to fabricate lignin-free Wood@ Polyaniline supercapacitor material for renewable energy storage application, J. Power Sources 471 (2020) 228448, https://doi.org/10.1016/j.jpowsour.2020.228448

[6] A. Khan, R.A. Senthil, J. Pan, S. Osman, Y. Sun, X. Shu, A new biomass derived rod-like porous carbon from tea-waste as inexpensive and sustainable energy material for advanced supercapacitor application, Electrochim. Acta 335 (2020) 135588, https://doi.org/10.1016/j.electacta.2019.135588

[7] Z. Yang, W. Xu, M. Zhao, W. Yang, J. Xia, Z. Zhou, J. Song, L. Sheng, B. Wei, Ethanol and KOH co-pretreatment towards ultra-high specific surface area carbons for high-rate and high-energy supercapacitors, Chem. Commun. 56 (2020) 15561–15564, https://doi.org/10.1039/d0cc06187e

[8] J. Dong, S. Li, Y. Ding, Anchoring nickel-cobalt sulfide nanoparticles on carbon aerogel derived from waste watermelon rind for high-performance asymmetric supercapacitors, J. Alloy. Compd. 845 (2020) 155701, https://doi.org/10.1016/j.jallcom.2020.155701

[9] F. Yu, C. Zhang, F. Wang, Y. Gu, P. Zhang, E.R. Waclawik, A. Du, K. Ostrikov, H. Wang, A zinc bromine "supercapattery" system combining triple functions of capacitive, pseudocapacitive and battery-type charge storage, Mater. Horizons 7 (2020) 495–503, https://doi.org/10.1039/c9mh01353a

[10] S.J. Patil, N.R. Chodankar, Y.K. Han, D.W. Lee, Carbon alternative pseudocapacitive V2O5 nanobricks and δ-MnO2 nanoflakes @ α-MnO2 nanowires hetero-phase for high-energy pseudocapacitor, J. Power Sources 453 (2020) 227766, https://doi.org/10.1016/j.jpowsour.2020.227766

[11] S. Suriyakumar, P. Bhardwaj, A.N. Grace, A.M. Stephan, Role of polymers in enhancing the performance of electrochemical supercapacitors: a review, Batter. Supercaps 4 (2021) 571–584, https://doi.org/10.1002/batt.202000272

[12] D. Han, Y. Zhao, Y. Shen, Y. Wei, L. Mao, G. Zeng, Co3O4 nanowire@ultrathin Ni-Co layered double hydroxide core-shell arrays with vertical transfer channel for high-performance supercapacitor, J. Electroanal. Chem. 859 (2020) 113887, https://doi.org/10.1016/j.jelechem.2020.113887

[13] Y. Li, L. Wang, Y. Qu, B. Wang, J. Yu, D. Song, C. Duan, Y. Yang, Unique 3D bilayer nanostructure basic cobalt carbonate@NiCo–layered double hydroxide nanosheets on carbon cloth for supercapacitor electrode material, Ionics 26 (2020) 1397–1406, https://doi.org/10.1007/s11581-019-03310-z

[14] G. Zhou, X. Gao, S. Wen, X. Wu, L. Zhang, T. Wang, P. Zhao, J. Yin, W. Zhu, Magnesium-regulated oxygen vacancies of cobalt-nickel layered double hydroxide nanosheets for ultrahigh performance asymmetric supercapacitors, J. Colloid Interface Sci. 612 (2022) 772–781, https://doi.org/10.1016/j.jcis.2021.12.087

[15] L. Xie, S. Chen, Y. Hu, Y. Lan, X. Li, Q. Deng, J. Wang, Z. Zeng, S. Deng, Construction of phosphatized cobalt nickel-LDH nanosheet arrays as binder-free electrode for high-performance battery-like supercapacitor device, J. Alloy. Compd. 858 (2021) 157652, https://doi.org/10.1016/j.jallcom.2020.157652

[16] J.J. Zhou, Q. Li, C. Chen, Y.L. Li, K. Tao, L. Han, Co3O4@CoNi-LDH core/shell nanosheet arrays for high-performance battery-type supercapacitors, Chem. Eng. J. 350 (2018) 551–558, https://doi.org/10.1016/j.cej.2018.06.023

[17] S. Megala, M. Sathish, S. Harish, M. Navaneethan, S. Sohila, B. Liang, R. Ramesh, Enhancement of photocatalytic H2 evolution from water splitting by construction of two dimensional gC3N4/NiAl layered double hydroxides, Appl. Surf. Sci. 509 (2020) 144656, https://doi.org/10.1016/j.apsusc.2019.144656

[18] N.L.W. Septiani, Y.V. Kaneti, Y. Guo, B. Yuliarto, X. Jiang, Y. Ide, N. Nugraha, H.K. Dipojono, A. Yu, Y. Sugahara, D. Golberg, Y. Yamauchi, Holey assembly of two-dimensional iron-doped nickel-cobalt layered double hydroxide nanosheets for energy conversion application, ChemSusChem 13 (2020) 1645–1655, https://doi.org/10.1002/cssc.201901364

[19] P.F. Wang, T. Jin, J. Zhang, Q.C. Wang, X. Ji, C. Cui, N. Piao, S. Liu, J. Xu, X.Q. Yang, C. Wang, Elucidation of the Jahn-Teller effect in a pair of sodium isomer, Nano Energy 77 (2020) 105167, https://doi.org/10.1016/j.nanoen.2020.105167

[20] Y. Wang, Z. Wang, X. Zheng, X. Teng, L. Xu, Y. Yuan, X. Liu, A. Fu, Y. Li, H. Li, Core-sheath heterostructure of MnCo2O4 nanowires wrapped by NiCo-layered double hydroxide as cathode material for high-performance quasi-solid-state asymmetric supercapacitors, J. Alloy. Compd. 904 (2022) 164047, https://doi.org/10.1016/j.jallcom.2022.164047

[21] S. Wang, Y. Zou, F. Xu, C. Xiang, H. Peng, J. Zhang, L. Sun, Morphological control and electrochemical performance of NiCo2O4@NiCo layered double hydroxide as an electrode for supercapacitors, J. Energy Storage 41 (2021) 102862, https://doi.org/10.1016/j.est.2021.102862

[22] K. Ramachandran, C. Jeganathan, S. Karuppuchamy, Electrodeposition of nanostructured bilayer CuI@CuSCN as hole transport material for highly efficient inverted perovskite solar cells, J. Alloy. Compd. 881 (2021) 160530, https://doi.org/10.1016/j.jallcom.2021.160530

[23] X. Li, X. Qian, Y. Xu, F. Duan, Q. Yu, J. Wang, L. Chen, Y. Dan, X. Cheng, Electrodeposited cobalt phosphides with hierarchical nanostructure on biomass carbon for bifunctional water splitting in alkaline solution, J. Alloy. Compd. 829 (2020) 154535, https://doi.org/10.1016/j.jallcom.2020.154535

[24] H. Fan, Y. Ma, W. Chen, Y. Tang, L. Li, J. Wang, Facile one-step electrodeposition of two-dimensional nickel-iron bimetallic sulfides for efficient electrocatalytic oxygen evolution, J. Alloy. Compd. 894 (2022) 162533, https://doi.org/10.1016/j.jallcom.2021.162533

[25] H. Wu, P. Liu, M. Yin, Z. Hou, L. Hu, J. Dang, Surface modification engineering on three-dimensional self-supported NiCoP to construct NiCoOx/NiCoP for highly efficient alkaline hydrogen evolution reaction, J. Alloy. Compd. 835 (2020) 155364, https://doi.org/10.1016/j.jallcom.2020.155364

[26] G. Rutavi, D.J. Tarimo, V.M. Maphiri, N. Manyala, Two-step electrodeposition of Hausmannite sulphur reduced graphene oxide and cobalt-nickel layered double hydroxide heterostructure for high-performance supercapacitor, 2022. https://doi.org/10.1002/er.7922.

[27] H. Insight, E.S. Zhitova, H.C. Greenwell, M.G. Krzhizhanovskaya, D.C. Apperley, I.V. Pekov, V.N. Yakovenchuk, Thermal Evolution of Natural Layered Double and Cl-Members of the Hydrotalcite Supergroup, (n.d.).

[28] G. Rutavi, D.J. Tarimo, V.M. Maphiri, N. Manyala, Two-step electrodeposition of Hausmannite sulphur reduced graphene oxide and cobalt-nickel layered double hydroxide heterostructure for high-performance supercapacitor, Int. J. Energy Res. (2022) 1–14, https://doi.org/10.1002/er.7922

[29] D.J. Tarimo, K.O. Oyedotun, N.F. Sylla, A.A. Mirghni, N.M. Ndiaye, N. Manyala, Waste chicken bone-derived porous carbon materials as high performance electrode for supercapacitor applications, J. Energy Storage 51 (2022) 104378, https://doi.org/10.1016/j.est.2022.104378

[30] R. Hassandoost, A. Kotb, Z. Movafagh, M. Esmat, R. Guegan, S. Endo, W. Jevasuwan, N. Fukata, Y. Sugahara, A. Khataee, Y. Yamauchi, Y. Ide, E. Doustkhah, Nanoarchitecturing bimetallic manganese cobaltite spinels for sonocatalytic degradation of oxytetracycline, Chem. Eng. J. 431 (2022) 133851, https://doi.org/10.1016/j.cej.2021.133851

[31] Y. Zhu, S. An, X. Sun, D. Lan, J. Cui, Y. Zhang, W. He, Core-branched NiCo2S4@CoNi-LDH heterostructure as advanced electrode with superior energy storage performance, Chem. Eng. J. 383 (2020) 123206, https://doi.org/10.1016/j.cej.2019.123206

[32] N. Zhao, H. Fan, M. Zhang, C. Wang, X. Ren, H. Peng, H. Li, X. Jiang, X. Cao, Preparation of partially-cladding NiCo-LDH/Mn3O4 composite by electrodeposition route and its excellent supercapacitor performance, J. Alloy. Compd. 796 (2019) 111–119, https://doi.org/10.1016/j.jallcom.2019.05.023

[33] G.T. Pan, S. Chong, T.C.K. Yang, C.M. Huang, Electrodeposited porous mn1.5co1.5o4/ni composite electrodes for high-voltage asymmetric supercapacitors, Materials 10 (2017) 1–12, https://doi.org/10.3390/ma10040370

[34] V.N. Kitenge, K.O. Oyedotun, O. Fasakin, D.J. Tarimo, N.F. Sylla, X. Van Heerden, N. Manyala, Enhancing the electrochemical properties of a nickel–cobalt–manganese ternary hydroxide electrode using graphene foam for supercapacitors applications, Mater. Renew. Sustain. Energy 10 (2021) 1–16, https://doi.org/10.1007/s40243-021-00192-y

[35] D.T. Bakhoum, K.O. Oyedotun, S. Sarr, N.F. Sylla, V.M. Maphiri, N.M. Ndiaye, B.D. Ngom, N. Manyala, A study of porous carbon structures derived from composite of cross-linked polymers and reduced graphene oxide for supercapacitor applications, J. Energy Storage 51 (2022) 104476, https://doi.org/10.1016/j.est.2022.104476

[36] Y. Wang, C. Shen, L. Niu, Z. Sun, F. Ruan, M. Xu, S. Shan, C. Li, X. Liu, Y. Gong, High rate capability of mesoporous NiWO4–CoWO4 nanocomposite as a positive material for hybrid supercapacitor, Mater. Chem. Phys. 182 (2016) 394–401, https://doi.org/10.1016/j.matchemphys.2016.07.047

[37] L. Zhang, G. Shi, Preparation of highly conductive graphene hydrogels for fabricating supercapacitors with high rate capability, J. Phys. Chem. C 115 (2011) 17206–17212, https://doi.org/10.1021/jp204036a

[38] J. Acharya, M. Park, T.H. Ko, B.S. Kim, Leaf-like integrated hierarchical NiCo2O4 nanorods@Ni-Co-LDH nanosheets electrodes for high-rate asymmetric supercapacitors, J. Alloy. Compd. 884 (2021) 161165, https://doi.org/10.1016/j.jallcom.2021.161165

[39] J. Acharya, T.H. Ko, M.K. Seo, M.S. Khil, H.Y. Kim, B.S. Kim, Engineering the hierarchical heterostructures of Zn-Ni-Co nanoneedles arrays@Co-Ni-LDH

[40] nanosheets core-sheath electrodes for a hybrid asymmetric supercapacitor with high energy density and excellent cyclic stability, ACS Appl. Energy Mater. 3 (2020) 7383–7396, https://doi.org/10.1021/acsaem.0c00781

[40] Y. Ji, F. Chen, S. Tan, F. Ren, Hierarchical coral-like MnCo2O4.5@Co-Ni LDH composites on Ni foam as promising electrodes for high-performance supercapacitor, Nanotechnology 33 (2022) 085402, https://doi.org/10.1088/1361-6528/ac3a3c

[41] S. Jo, N. Jayababu, D. Kim, Rational design of cobalt-iron bimetal layered hydroxide on conductive fabric as a flexible battery-type electrode for enhancing the performance of hybrid supercapacitor, J. Alloy. Compd. 904 (2022) 164082, https://doi.org/10.1016/j.jallcom.2022.164082

[42] A.N. Naveen, S. Selladurai, A 1-D/2-D hybrid nanostructured manganese cobaltite-graphene nanocomposite for electrochemical energy storage, RSC Adv. 5 (2015) 65139–65152, https://doi.org/10.1039/c5ra09288d

[43] A. Elgendy, N.M. El Basiony, F. El-Taib Heakal, A.E. Elkholy, Mesoporous Ni-Zn-Fe layered double hydroxide as an efficient binder-free electrode active material for high-performance supercapacitors, J. Power Sources 466 (2020) 228294, https://doi.org/10.1016/j.jpowsour.2020.228294

[44] J. Li, X. Xiong, X. Li, Y. Qian, Spinel Mn 1.5Co 1.5O 4 core-shell microspheres as Li-ion battery anode materials with a long cycle life and high capacity, J. Mater. Chem. 22 (2012) 23254–23259, https://doi.org/10.1039/c2jm35607d

[45] L. Halder, A. Maitra, A.K. Das, R. Bera, S.K. Karan, S. Paria, A. Bera, S.K. Si, B.B. Khatua, High performance advanced asymmetric supercapacitor based on ultrathin and mesoporous MnCo2O4.5-NiCo2O4 hybrid and iron oxide decorated reduced graphene oxide electrode materials, Electrochim. Acta 283 (2018) 438–447, https://doi.org/10.1016/j.electacta.2018.06.184

[46] M. Zhang, W. Liu, R. Liang, R. Tjandra, A. Yu, Graphene quantum dot induced tunable growth of nanostructured MnCo2O4.5 composites for high-performance supercapacitors, Sustain. Energy Fuels 3 (2019) 2499–2508, https://doi.org/10.1039/c9se00341j

[47] R. Kumar, M.M. Abdel-Galeil, K.Z. Ya, K. Fujita, W.K. Tan, A. Matsuda, Facile and fast microwave-assisted formation of reduced graphene oxide-wrapped manganese cobaltite ternary hybrids as improved supercapacitor electrode material, Appl. Surf. Sci. 481 (2019) 296–306, https://doi.org/10.1016/j.apsusc.2019.03.085

[48] S. Wang, Y. Xu, J. Qin, S. Chen, Y. Du, Y. Xu, J. Xu, W. Zhou, One-pot synthesis of MnX2O4(X = Co, Ni)/graphite nanoflakes composites as high-performance supercapacitor electrodes, Mater. Res. Bull. 141 (2021) 111349, https://doi.org/10.1016/j.materresbull.2021.111349

[49] B.A. Mahmoud, A.A. Mirghni, K.O. Oyedotun, O. Fasakin, N. Manyala, Nanoplatelets ammonium nickel-cobalt phosphate graphene foam composite as novel electrode material for hybrid supercapacitors, J. Alloy. Compd. 883 (2021) 160897, https://doi.org/10.1016/j.jallcom.2021.160897

[50] C. Sun, X. Li, Z. Cai, F. Ge, Carbonized cotton fabric in-situ electrodeposition polypyrrole as high-performance flexible electrode for wearable supercapacitor, Electrochim. Acta 296 (2019) 617–626, https://doi.org/10.1016/j.electacta.2018.11.045

[51] D.J. Tarimo, K.O. Oyedotun, A.A. Mirghni, B. Mutuma, N.F. Sylla, P. Murovhi, N. Manyala, Enhanced electrochemical performance of supercapattery derived from sulphur-reduced graphene oxide/cobalt oxide composite and activated carbon from peanut shells, Int. J. Hydrog. Energy 45 (2020) 33059–33075, https://doi.org/10.1016/j.ijhydene.2020.09.142

[52] A.A. Mirghni, K.O. Oyedotun, O. Fasakin, B.A. Mahmoud, D.J. Tarimo, N. Manyala, High-performance bimetallic Ni-Mn phosphate hybridized with 3-D graphene foam for novel hybrid supercapacitors, J. Energy Storage 31 (2020) 101584, https://doi.org/10.1016/j.est.2020.101584

[53] J.J. Zhou, X. Han, K. Tao, Q. Li, Y.L. Li, C. Chen, L. Han, Shish-kebab type MnCo2O4@Co3O4 nanoneedle arrays derived from MnCo-LDH@ZIF-67 for high-performance supercapacitors and efficient oxygen evolution reaction, Chem. Eng. J. 354 (2018) 875–884, https://doi.org/10.1016/j.cej.2018.08.102

[54] M.Z. Iqbal, M.M. Faisal, S.R. Ali, Integration of supercapacitors and batteries towards high-performance hybrid energy storage devices, Int. J. Energy Res. 45 (2021) 1449–1479, https://doi.org/10.1002/er.5954

[55] J. Xu, Y. Sun, M. Lu, L. Wang, J. Zhang, E. Tao, J. Qian, X. Liu, Fabrication of the porous MnCo2O4 nanorod arrays on Ni foam as an advanced electrode for asymmetric supercapacitors, Acta Mater. 152 (2018) 162–174, https://doi.org/10.1016/j.actamat.2018.04.025

[56] H. Liang, T. Lin, S. Wang, H. Jia, C. Li, J. Cao, J. Feng, W. Fei, J. Qi, A free-standing manganese cobalt sulfide@cobalt nickel layered double hydroxide core-shell heterostructure for an asymmetric supercapacitor, Dalton Trans. 49 (2019) 196–202, https://doi.org/10.1039/c9dt03974k

123

Exploration of metal-layered double hydroxide composite materials for hybrid capacitor produced by facile and efficient electrodeposition process.

Gift Rutavi, Delvina Japhet Tarimo, Vusani Muswa Maphiri, Vianney Ngoyi Kitenge and Ncholu Manyala*

Department of Physics, Institute of Applied Materials, SARChI in Carbon Technology and Materials, University of Pretoria 0028, South Africa
*Corresponding author's email: ncholu.manyala@up.ac.za, Tel.: + (27)12 420 3549.

Supplementary information
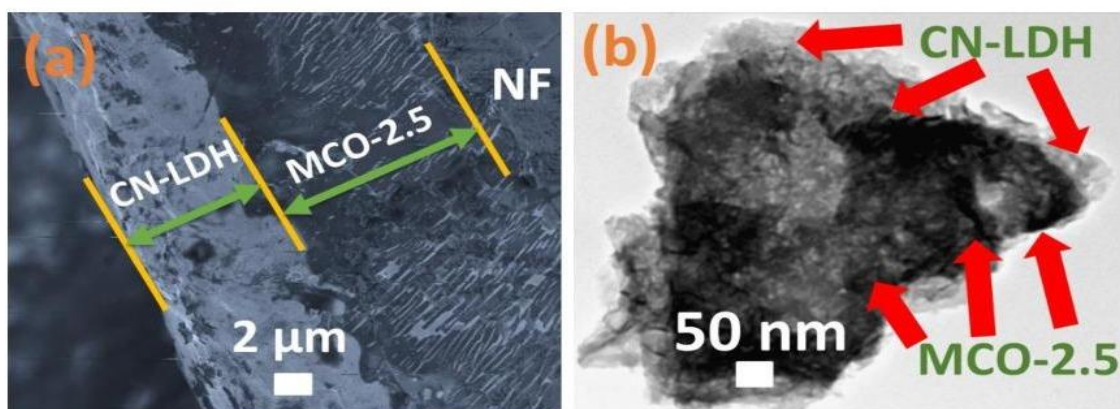
Fig S1: (a) SEM cross section, and **(b)** TEM image of the MCO-2.5@CN-LDH composite sample.

1
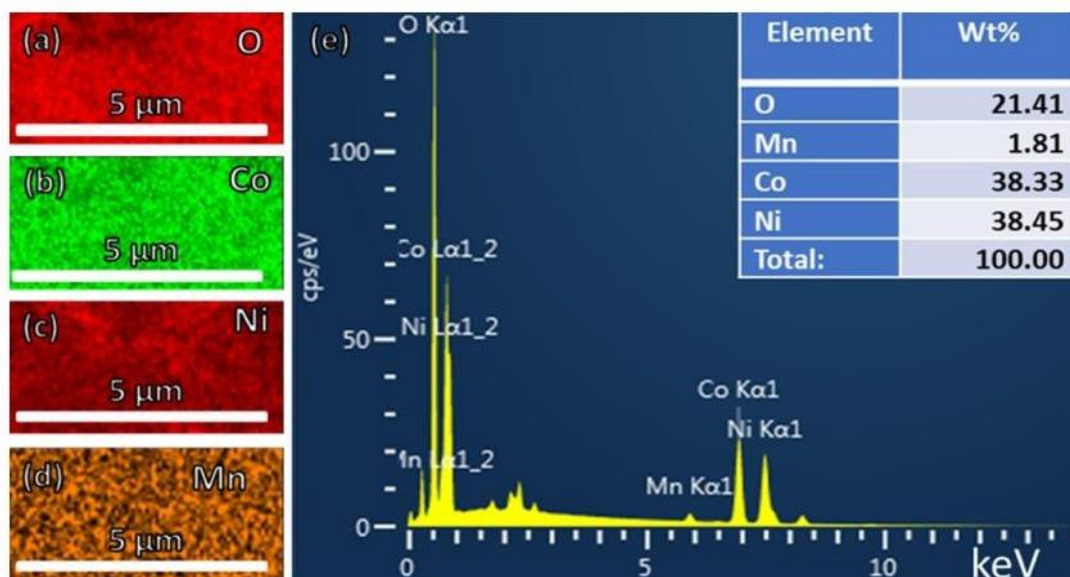
Fig S2: (a) - (d) The elemental mapping of the CMO-2.5@CN-LDH composite sample displaying the distribution of oxygen, cobalt, nickel, and manganese, respectively, and **(e)** the percentage composition of the elements within the composite material.
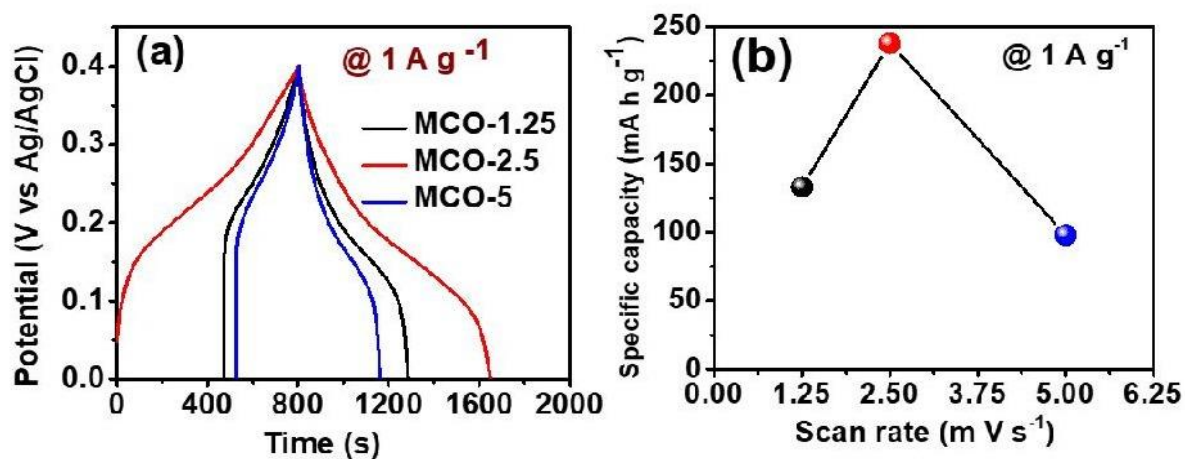
Fig. S3: (a) GCD and **(b)** specific capacity vs CV deposition scan rate of MCO-1.25, MCO-2.5, and MCO-5 samples, respectively in 2 M KOH electrolyte.
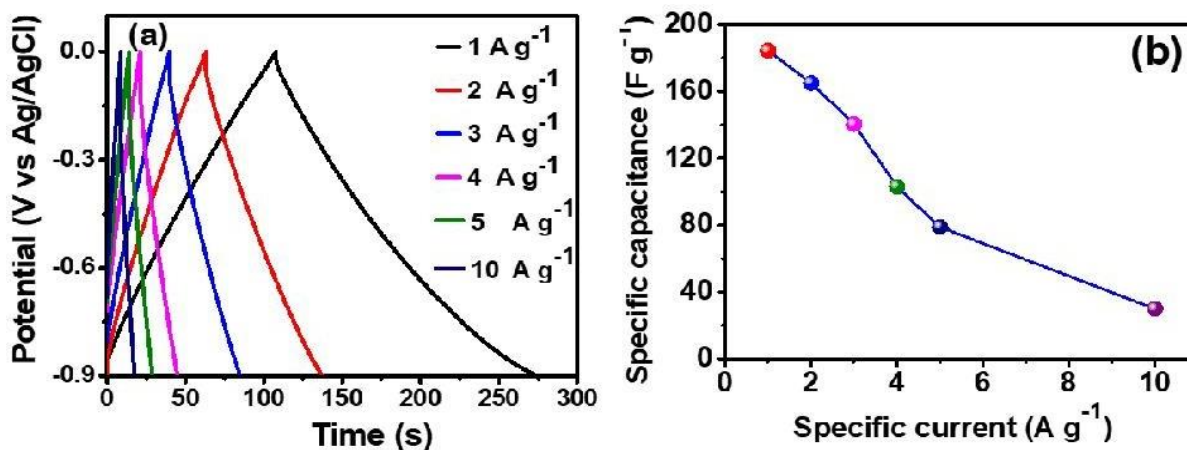
Fig. S4: (a) GCD and **(b)** specific vs specific current of CCBW in 2 M KOH electrolyte.

Table S1: Comparison of the capacitive contribution of LDH based electrodes and devices reported in literature.

Electrode or device	Electrolyte	Voltage (V)	Capacitive Contribution at 5 mVs^{-1} (%)	Ref:
Ni-Zn-Fe LDH	6 M KOH	0.45	7.5	[1]
CoNi-LDH@PCPs	1 M KOH	0.6	83.0	[2]
NiCoAl-LDH/V$_4$C$_3$T$_x$//AC	1 M KOH	1.6	53.8	[3]
C$_{60}$–Ni–Fe-LDH	1 M KOH	0.55	58.7	[4]
NC2S12-15/NF	2 M KOH	0.6	66.1	[5]
Zn$_{0.25}$Ni$_{0.75}$Co-LDH-BA$^-$//AC	2 M KOH	1.6	41	[6]
MCO-2.5@CN-LDH	2 M KOH	0.4	29.1	This work

3

References:

[1]   A. Elgendy, N.M. El Basiony, F. El-Taib Heakal, A.E. Elkholy, Mesoporous Ni-Zn-Fe layered double hydroxide as an efficient binder-free electrode active material for high-performance supercapacitors, J. Power Sources. 466 (2020) 228294. https://doi.org/10.1016/j.jpowsour.2020.228294.

[2]   W. Wang, Y. Lu, M. Zhao, R. Luo, Y. Yang, T. Peng, H. Yan, X. Liu, Y. Luo, Controllable tuning of cobalt nickel-layered double hydroxide arrays as multifunctional electrodes for flexible supercapattery device and oxygen evolution reaction, ACS Nano. 13 (2019) 12206–12218. https://doi.org/10.1021/acsnano.9b06910.

[3]   X. Wang, H. Li, H. Li, S. Lin, J. Bai, J. Dai, C. Liang, X. Zhu, Y. Sun, S. Dou, Heterostructures of Ni-Co-Al layered double hydroxide assembled on V 4 C 3 MXene for high-energy hybrid supercapacitors, J. Mater. Chem. A. 7 (2019) 2291–2300. https://doi.org/10.1039/c8ta11249e.

[4]   Y.H. Kim, X. Jin, S.J. Hwang, Fullerene as an efficient hybridization matrix for exploring high-performance layered-double-hydroxide-based electrodes, J. Mater. Chem. A. 7 (2019) 10971–10979. https://doi.org/10.1039/c9ta01532a.

[5]   Y. Wang, Z. Yin, G. Yan, Z. Wang, X. Li, H. Guo, J. Wang, New insight into the electrodeposition of NiCo layered double hydroxide and its capacitive evaluation, Electrochim. Acta. 336 (2020) 135734. https://doi.org/10.1016/j.electacta.2020.135734.

[6]   Y. Li, B. Huang, X. Zhao, Z. Luo, S. Liang, H. Qin, L. Chen, Zeolitic imidazolate framework-L-assisted synthesis of inorganic and organic anion-intercalated hetero-trimetallic layered double hydroxide sheets as advanced electrode materials for

4

aqueous asymmetric super-capacitor battery, J. Power Sources. 527 (2022) 231149. https://doi.org/10.1016/j.jpowsour.2022.231149.

5

4.2.3. Concluding remarks

The synthesis of MCO, CN-LDH, and MCO-2.5@CN-LDH were successfully carried through electrodeposition. The SEM and TEM micrograms of the composite electrode MCO-2.5@CN-LDH confirm the formation of nanosheets of CN-LDH covering the densely packed MCO-2.5 nanograins. MCO-2.5@CN-LDH produced outstanding electrochemical results with a specific capacity of 415.9 mAh g^{-1} at a specific current of 1 A g^{-1} in 2 M KOH. The electrochemical stability of the MCO-2.5@CN-LDH was great with a capacity retention of 87.0 % and coulombic efficiency of 99.8 % after 5,000 GCD cycles at 7 A g^{-1}. The electrode also served as the positive electrode of the asymmetric supercapacitor device MCO-2.5@CN-LDH//CCBW, where activated carbon from cooked chicken bones (CCBW) was the negative electrode. The performance of the device produced specific energy of 55.8 Wh kg^{-1} and specific power of 940.4 W kg^{-1} at a specific current of 1 A g^{-1}. The device also displayed excellent stability with a capacity retention of 81.6 % and coulombic efficiency of 99.8 % after 10,000 GCD cycles at 8 A g^{-1}. The robustness of the binder-free electrodeposition synthesis and the synergetic effect of the spinel and LDH contributed to the excellent electrochemical performance.

4.3. Assessment of the electrodeposition-synthesized manganese chromite and cobalt-nickel layered double hydroxide composite for high performance supercapacitor applications

4.3.1. Introduction

It is possible to assuage cobalt nickel layered double hydroxide (CoNi-LDH)'s low electrical conductivity and low electrical stability caused by the restacking without incorporating carbon materials such as graphene. This can even be achieved through cheap and environmentally friendly bimetallic metal oxide such as manganese chromite ($MnCr_2O_4$). $MnCr_2O_4$ provides several active oxidation states, great electrical conductivity and high theoretical capacity [37]. The synthesis methods also plays a crucial role in achieving great electrical performance. Electrodeposition is one of the greatest options among binder-free synthesis approaches due to the high strength of the adhesion of the active materials to the current collector [248]. An optimised composite electrode $MnCr_2O_4$-1.2V@CoNi-LDH was synthesized through successive electrodeposition of $MnCr_2O_4$-1.2V (where -1.2 V signify the lower potential used in the CV electrodeposition) and CoNi-LDH on nickel foam. The electrodes were analysed using SEM, EDS, XRD and Raman spectroscopy and the electrochemical analysis was performed in 2 M KOH.

4.3.2. Results and discussion

The results obtained after the synthesis and characterization of the electrodes are displayed in the following manuscript which is about to be submitted for publication.

Assessment of the electrodeposition synthesized manganese chromite and cobalt-nickel layered double hydroxide composite for high-performance supercapacitor applications

Gift Rutavi, Delvina Japhet Tarimo, Vusani Muswa Maphiri, Vianney Ngoyi Kitenge and Ncholu Manyala*

Department of Physics, Institute of Applied Materials, SARChI in Carbon Technology and Materials, University of Pretoria 0028, South Africa

*Corresponding author's email: ncholu.manyala@up.ac.za, Tel.: + (27)12 420 3549.

Abstract

Cyclic voltammetry (CV) electrodeposition synthesis was performed twice to synthesize manganese chromite ($MnCr_2O_4$-ϕ) on NF, where $-1.4 \leq \phi \leq -1.0$ is the lower voltage (V vs Ag/AgCl) set in the CV during electrodeposition, the higher potential being 0.5 V. This was followed by another electrodeposition of cobalt nickel layered double hydroxide (CoNi-LDH) on $MnCr_2O_4$-ϕ. The unique layered structure of CoNi-LDH produce electrodes with excellent electrochemical performance. $MnCr_2O_4$-1.2 V@CoNi-LDH ($\phi = -1.2$ (V vs Ag/AgCl)) yielded the best electrochemical performance in three-electrode set-up in 2 M KOH with the highest specific capacity of 424.7 mAh g^{-1} at a specific current of 1 A g^{-1}. The electrode also exhibited great stability having a capacity retention of 73.6 % after 5,000 galvanostatic charge-discharge (GCD) cycles at a specific current of 9 A g^{-1}. This electrode was incorporated into the hybrid device with activated carbon (AC) from Amarula Husk as the negative electrode (AMH). The device ($MnCr_2O_4$-1.2 V@CoNi-LDH//AMH) produced a superb specific energy of 80.2 Wh kg^{-1} corresponding to a specific power of 1117.7 W kg^{-1} at 1 A g^{-1}. The capacity retention and coulombic efficiency of the device were 72.9 and 99.7 %, respectively after

10,000 GCD cycles at 9 A g^{-1}. Due to the phenomenal performance, the produced materials are suitable candidates for high energy supercapacitor applications.

Keywords: Electrodeposition potential; Manganese chromite; Specific capacity; Supercapacitor; Specific energy.

1.0 Introduction

Supercapacitors have the potential to play a role in facilitating the shift from fossil fuels reliance to cleaner renewable energy sources. This is due to their attractive features such as high specific power, long cycle and life rapid charge-discharge [1–3]. Nevertheless, the specific energy of supercapacitors is still much inferior to that of lithium ion batteries (LIBs). It is essential therefore to source for and investigate affordable and environmentally friendly electrode materials and optimise their synthesis with an intention to improve their specific energy while not compromising their specific power.

Bimetallic metal oxide (BMO) and hydroxide (BMOH) have charge storage mechanisms which are dominated by Faradaic redox reactions produces [4–6]. This gives them superior specific capacity and specific energy when compared to carbon based material whose energy storage mechanism is electrostatic without chemical reactions [7–9].

Besides, natural abundance and environmental friendliness, bimetallic metal oxides (BMO) such as $CoFe_2O_4$, $CuFeS_2$, and $NiCo_2O_4$ have generated a lot of interest recently among researchers for supercapacitor electrodes applications because of various valence of cations and the low activation energy for electron transport among the cations of dual metal compounds. BMO also benefits from possessing more electroactive sites compared to monometallic oxides due to the presence of a pair of distinct metals, this goes a long way in improving the electrical conductivity, and electrochemical stability [10–12]. Manganese

chromite ($MnCr_2O_4$) has found regular use in photocatalysts, ceramic dyes, alkaline batteries and water purification due to its structural, magnetic and electrical properties [13]. However, there are very few reports of $MnCr_2O_4$ used in supercapacitors despite its favourable features such as high theoretical specific capacity, structural stability and high electrical conductivity [14,15].

On the other hand, $MnCr_2O_4$ like most BMO, has lower cycle life compared to carbon based materials [16]. The electrochemical accomplishments of $MnCr_2O_4$ can be greatly enhanced by crafting a composite with layered materials. Two dimensional layered materials allow abundant exposed active sites for more rapid ion diffusion during reduction and oxidation processes [17]. Due to its unique and tunable two dimensional layered structure with large interlayer spaces which results in adjustable chemical composition and high anion exchangeability [18–20], cobalt nickel layered double hydroxide (CoNi-LDH) is capable of yielding an elevated theoretical capacitance of 3000 F g^{-1} [21]. CoNi-LDH however suffer from slow electron transport [22,23]and its electroactive sites are confined. The composite of $MnCr_2O_4$ and CoNi-LDH will benefit from the synergetic effect with $MnCr_2O_4$ compensating CoNi-LDH's low electrical conductivity while CoNi-LDH introduce flexible ion interchangeability [18]. For instance, El-Deen et al. successfully synthesized a 3D hierarchical Ni-Co LDH wrapped around porous Co_3O_4 nanotubes derived from (zeolite imidazolate framework-67) ZIF-67 as a template. The composite electrode nickel cobalt layered double hydroxide cobalt oxide nanocomposite (Ni-Co LDH@Co_3O_4) attained a phenomenal specific capacitance of 1866 F g^{-1} at 2 A g^{-1}. This was significantly superior compared to the specific capacitance of 487 and 1161 F g $^{-1}$ produced by the individual electrodes Co_3O_4 and Ni-Co LDH, respectively [24]. Also, Xu et al. used a facile microwave-assisted hydrothermal method to synthesize a sandwich-like cobalt nickel sulfides@carbon@nickel cobalt double hydroxide ($CoNi_2S_4$@C@NiCo-LDH). The nanostructured composite electrode generated a great

performance with an excellent specific capacity of $1183\,mAh\,g^{-1}$ at $1\,A\,g^{-1}$ and a huge capacity retention of 85.8 % at $20\,A\,g^{-1}$. These are testimonies for the benefits of a composite made from CoNi-LDH with a BMO (spinel) material [25].

Furthermore, the electrical performance and mechanical stability of this material is greatly influenced by the synthesis route [26]. Electrodeposition, which is a cost effective, efficient, facile and safe is one of the most suitable methods for growing materials onto a current collector. As a binder-free route it does not introduce resistivity to the electrode material, and this helps to increase the maximum specific power of the device. Modification of electrodeposition parameters like concentration, precursor solution, pH, current, voltage, number of CV cycles and electrodeposition duration (time) has great effects on the performance of supercapacitor electrode materials [27]. These effects include change in the features of the deposited materials like thickness, surface morphology and conductivity [28–30]. For instance, Zhang et al. were able to improve the specific capacitance of MnO_2 from a general value which is less than $300\,F\,g^{-1}$ at $1\,A\,g^{-1}$ to a great value of $469\,F\,g^{-1}$ at the same specific current by adjusting the electrodeposition potential to 0.6 V vs Ag/AgCl. The electrode also exhibited stability yielding a capacitance retention of 83.9 % after 2,500 cycles [31]. Yavuz et al. explored the influence of cathodic deposition potential on the performance of a cobalt based film [32]. A peak specific capacitance of $1692\,F\,g^{-1}$ with a capacitance retention of 81 % was obtained when the film was deposited at a voltage of -1.7 V vs Ag/AgCl on a graphite electrode. The investigation also showed that the charge storage mechanism evolved with the deposition voltage with surface controlled reaction began to manifest at a deposition voltage of -1.3 V vs Ag/AgCl . These finding shows the important role played by the electrodeposition voltage on the electrochemical performance and stability of supercapacitor electrodes.

In this report, successive electrodeposition was employed. The process started with the CV electrodeposition, of $MnCr_2O_4$-ϕ on nickel foam, where ϕ is the electrodeposition potential

(V), and the values of φ were, -1.0, -1.2 and -1.4 V. The electrode synthesized using -1.2 V ($MnCr_2O_4$-1.2 V) yielded the best electrochemical results and was therefore used to make the composite electrode. The composite electrode ($MnCr_2O_4$-1.2 V@CoNi-LDH) was synthesised through a further CV electrodeposition of CoNi-LDH on $MnCr_2O_4$-1.2 V.

The $MnCr_2O_4$-1.2V@CoNi-LDH electrode produced excellent electrochemical performance in 2 M KOH electrolyte in a three-electrode set-up with a great specific capacity of 424.7 mAh g^{-1} at 1 A g^{-1}. The electrode also exhibited excellent stability yielding a capacity retention of 73.6 % and a coulombic efficiency of 99.9 % after 5,000 cycles at a specific current of 8 A g^{-1}. The electrode was incorporated into an asymmetric device ($MnCr_2O_4$-1.2 V@CoNi-LDH//AMH) with AMH as the negative electrode in 2 M KOH. The device yielded a remarkable specific energy of 80.2 Wh kg^{-1} and a specific power of 1117.7 W kg^{-1} at 1 A g^{-1}. The capacity retention and coulombic efficiency of the device at 10,000 GCD cycles at 9 A g^{-1} were 72.9 and 99.7 %, respectively. The study successfully presents a sustainable way of fusing different materials using one simple, efficient, cost effective route while yielding very competitive electrochemical results. This avails the synthesised material as candidate for high yield supercapacitor devices.

2.0 Experimental section

2.1 Materials

There was no further purification performed on the chemicals used. The following are the chemicals used in this study: Nickel foam [NF] was acquired from Alantum (Munich, Germany). Deionised water [DW] was drawn from the DRAWELL water refining device. Hydrochloric acid [HCl], acetone [$(CH_3)_2CO$], and ethanol [CH_3CH_2OH] were all purchased from (Sigma Aldrich, Steinheim, Germany). Chromium(III) potassium sulphate dodecahydrate

[KCr$_2$(SO$_4$).12 H$_2$O], manganese acetate hexahydrate [Mn(CH$_3$CO$_2$)$_2$.4 H$_2$O], sodium sulphate [Na$_2$SO$_4$], Nickel nitrate hexahydrate [Ni (NO$_3$)$_2$•6H$_2$O], manganese acetate hexahydrate [Mn(CH$_3$COO)$_2$•4H$_2$O], cobalt nitrate hexahydrate [Co(NO$_3$)$_2$•6H$_2$O] were all obtained from Merck (Johannesburg, South Africa).

2.2 Preparation of NF substrates

The treatment of NF was performed according to the procedure described in our prior work [33]. This rigorous chemical treatment served to exclude the inert oxide and hydroxide layers which form on the surface of NF in a moist environment. In summary, NF was reshaped into rectangular pieces with (2 cm x 1 cm) dimensions. These pieces were immersed into 3 M HCl for 20 minutes. The pieces were then dipped in acetone, followed by 99% purity ethanol and finally DW, all for 20 minutes. This process was followed by drying at 60° C in an oven for 12 hours.

2.3 Preparation of MnCr$_2$O$_4$-ϕ on NF electrode

0.01 M each of [KCr$_2$(SO$_4$).12 H$_2$O] and [Mn(CH$_3$CO$_2$)$_2$.4 H$_2$O] were added to 500 ml DW and stirred for 30 minutes. 0.01 M Na$_2$SO$_4$ was then added to prevent aggregation and the stirring continued for a further 45 minutes. This solution was identified as S1. To perform the electrodeposition, the Bio-logic workstation was used, with NF, platinum rod, and Ag/AgCl serving as the working electrode (WE), counter electrode (CE) and reference electrode (RE), respectively, these were all dipped in S1. Cycling voltammetry (CV) at 2.5 mV s^{-1} was used in a voltage range of -1.0 to 0.5 V vs Ag/AgCl. The voltage was repeated for voltage ranges -1.2 to 0.5 V vs Ag/AgCl and -1.4 to 0.5 V vs Ag/AgCl. The electrodes were then washed in deionised water (DW) and dried in an oven at 90° C for 8 hours. To transform the phase of the

electrode materials from LDH to the spinel phase, the electrodes were then annealed in air for 2 hours at 300°C. The electrodes were labelled as $MnCr_2O_4$-1.0 V, $MnCr_2O_4$-1.2 V, and $MnCr_2O_4$-1.4 V, according to their lower electrodeposition voltage value, ($\phi = -1.0, 1.2$ and -1.4 V.

2.4 Synthesis of CoNi-LDH, MnCr₂O₄-1.2 V@CoNi-LDH and AMH

The details of the synthesis of CoNi-LDH was explained in our previous work [33]. Briefly 0.01 M of Co $(NO_3)_2 \cdot 6H_2O$ and Ni $(NO_3)_2 \cdot 6H_2O$ were added into 50 ml of DW. This was followed by thorough stirring for 30 minutes. This uniform solution was branded as S2. The materials were then grown directly onto the NF substrate in accordance with the procedure already described in section 2.3. With the exception that RE, WE and CE were immersed in the solution S2 instead. The resulting electrode was branded as CoNi-LDH. The same process was replicated, but now with $MnCr_2O_4$-1.2 V as the WE. The final electrode was labelled as $MnCr_2O_4$-1.2 V@CoNi-LDH. The schematic illustration in scheme 1 shows the synthesis of $MnCr_2O_4$-1.2 V@CoNi-LDH. The synthesis of the activated carbon from amarula husk (AMH) which served as the negative electrode was discussed in detail in our prior study [34].
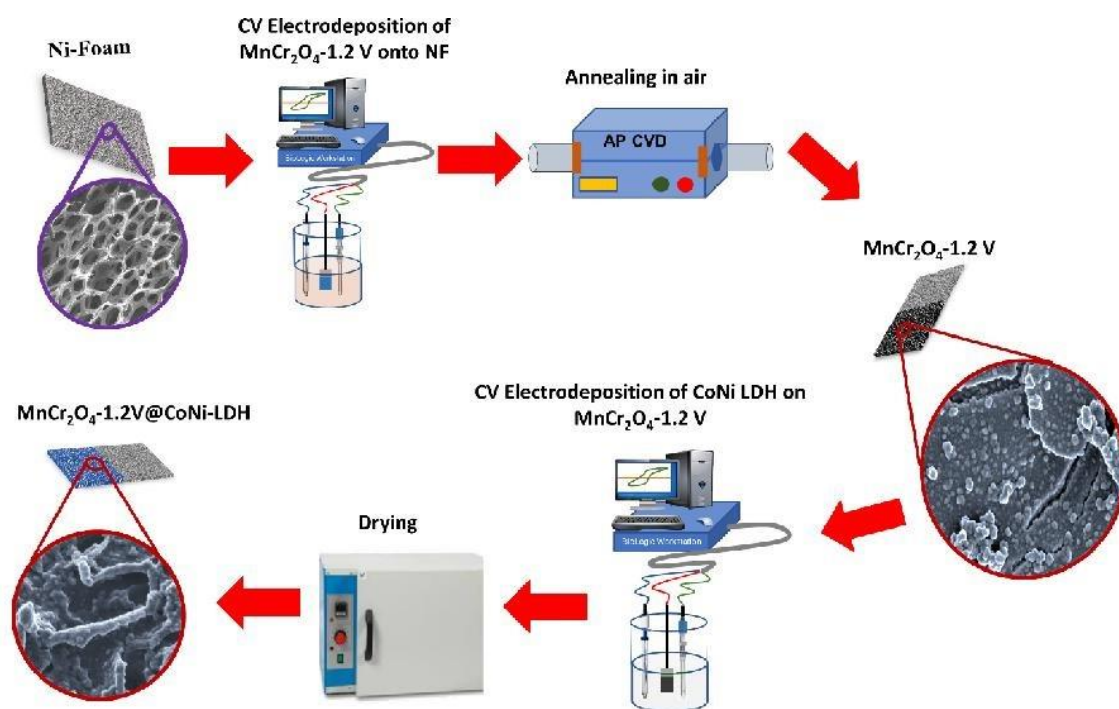
Scheme 1: Schematic illustration of the synthesis of MnCr$_2$O$_4$-1.2 V@CoNi-LDH electrode.

2.5 Material characterisation

To evaluate the scanning electron microscopy (SEM) morphology, elemental composition, and thickness of the MnCr$_2$O$_4$-ϕ, CoNi-LDH and MnCr$_2$O$_4$-1.2 V@CoNi-LDH electrodes, the Zeiss Ultra PLUS FEG-SEM (Ashikima-Shi, Japan) was used. This device also includes the energy dissipation spectroscopy (EDS) worked with an accelerating voltage of 2.0 kV. To obtain the transmission electron microscopy (TEM) micrograms, the JEOL JEM 2100-F device with an accelerating potential of 1.0 kV was used. The structure of the electrodes was evaluated using an X-ray diffraction (XRD) diffractometer (Brucker 2D PAN analytical BV, Amsterdam, Netherlands). This instrument makes use of Cu K$_{\alpha1}$ (1.54061Å) with a range of $5^o \leq 2\theta \leq 90^o$. Raman spectroscopy analysis was carried out by employing the WITec alpha-300 RAS+

Confocal micro-Raman microscope (Focus Innovations, Ulm Germany) with a 532 nm laser at a power of of 4.5 mW, spectral acquisition of 300s using a 20X objective with a laser power.

2.6 Electrochemical characterisation

The assessment of the electrochemical performance of the electrodes was performed using the Bio-Logic workstation potentiostat. In a half cell set-up, the RE and CE operated as stated in section 2.3 while the WE were $MnCr_2O_4$-ϕ, CoNi-LDH, and $MnCr_2O_4$-1.2 V@CoNi-LDH. GCD, CV and electrochemical impedance spectroscopy (EIS) were all performed in 2 M KOH for both the half and full-cell configuration.

3.0 Results and analysis

3.1 Microstructural characterisation and analysis

Fig. 1 shows the SEM images of $MnCr_2O_4$-ϕ. In Fig. 1(a) the nanograins are intact leaving less channels for ion transport in $MnCr_2O_4$-1.0 V. In Fig. 1(b) there is evidence of separation of the nanograin to avail pathways for ion insertion and diffusion in $MnCr_2O_4$-1.2 V. With the increase of the electrodeposition voltage to -1.4 V, as seen in Fig. 1(c) for $MnCr_2O_4$-1.4 V the nanograins gets more separated from each other. The morphology in Fig. 1(b) appears to be the most appropriate for mobility of ions from the electrolyte, therefore, $MnCr_2O_4$-1.2 V was used to make a composite electrode material.
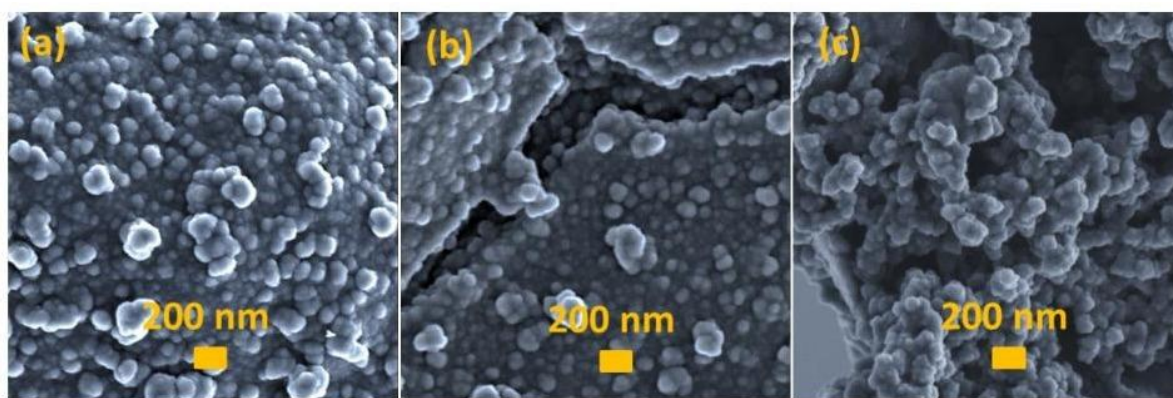
Fig. 1: SEM images of $MnCr_2O_4$-1.0 V, $MnCr_2O_4$-1.2 V and $MnCr_2O_4$-1.4 V.

Fig. 2 shows the SEM micrograms of the $MnCr_2O_4$-1.2 V, CoNi-LDH and $MnCr_2O_4$-1.2 V@CoNi-LDH electrodes. Fig. 2(a) and (b) illustrates the nanograins of $MnCr_2O_4$-1.2 V at low and high resolution, respectively. The nanograins array reveal channels which could be pathways for ion diffusion Fig. 2(c) and (d) shows the nanoflakes of CoNi-LDH at low and high magnification, respectively. The sheet like structure which is synonymous with layered material exposes open structures which could act as the electroactive sites which could lead to improvement of the electrochemical performance. Fig. 2(e) and (f) show the $MnCr_2O_4$-1.2 V@CoNi-LDH nanograins fused into a wide rolled sheet-like structure. This arrangement combines the pathways from the gaps among the nanograins and the sheet-like arrangement provides even more pathways for ion transport.
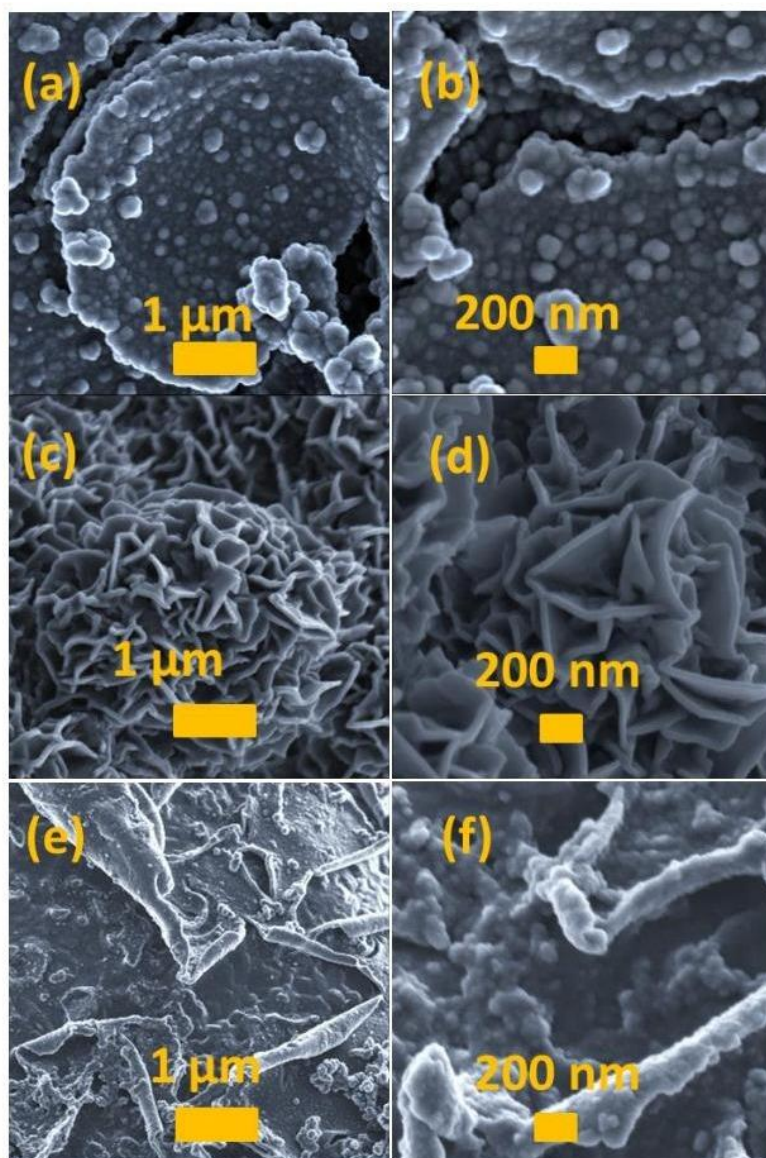
Fig. 2: (a, b), (c, d) and **(e, f)** presents low- and high-resolution micrographs of $MnCr_2O_4$-1.2 V, CoNi-LDH and $MnCr_2O_4$ -1.2 V@CoNi-LDH, respectively.

Fig. 3(a) – (f) reveals the EDS mapping of $MnCr_2O_4$-1.2V@CoNi-LDH composite signifying the homogeneous composition of the elements nickel (Ni), oxygen (O), cobalt (Co), chromium (Cr), and manganese (Mn). Fig. 3(g) indicates the percentage of these elements composition which are 64.4, 11.4, 7.7, 10.4 and 6.2 %, respectively.
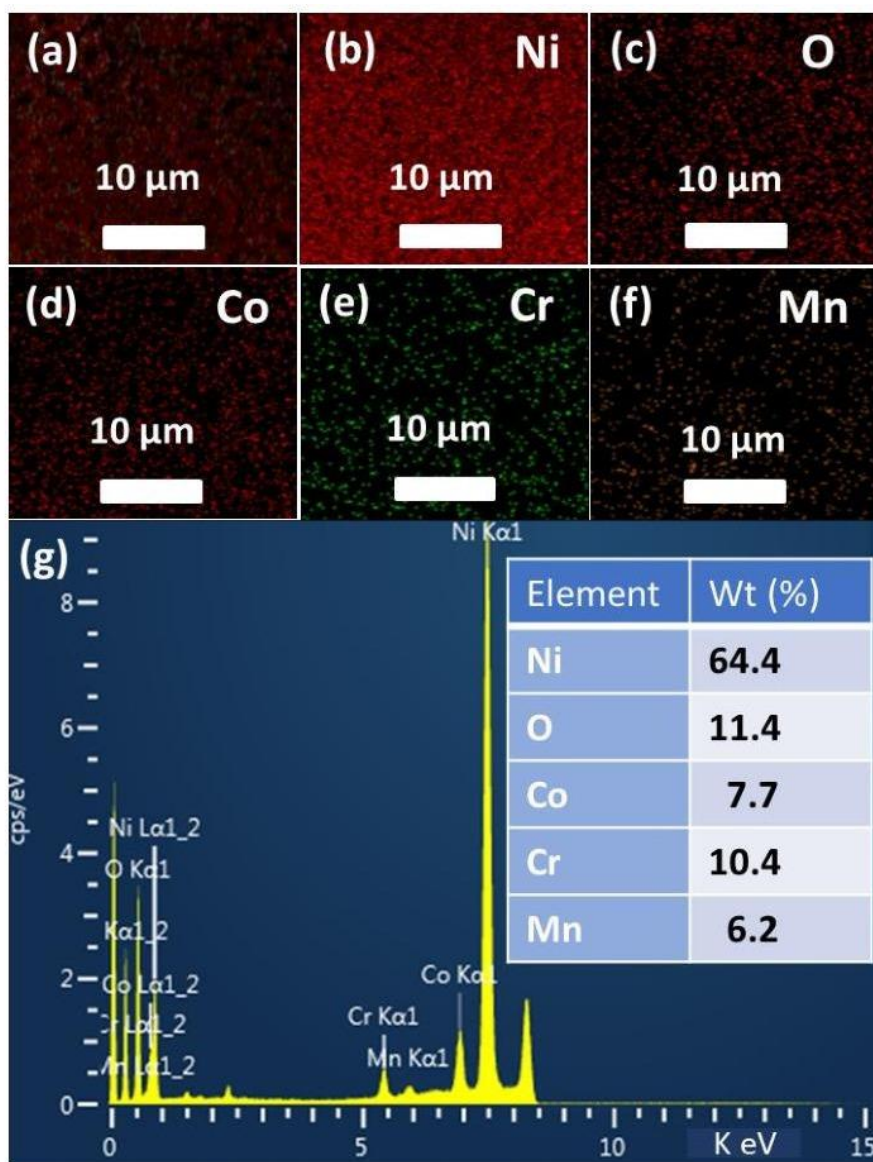
Fig. 3: (a) - (f) presents the elemental mapping of MnCr₂O₄-1.2V@CoNi-LDH composite sample displaying the distribution of nickel, oxygen, cobalt, chromium, and manganese, respectively and **(g)** the percentage composition of the elements within the material.

Fig. 4 (a) shows the Raman spectroscopy of MnCr₂O₄-1.2 V, CoNi-LDH and MnCr₂O₄-1.2 V@CoNi-LDH. For the MnCr₂O₄-1.2 V electrode, the A$_{1g}$ peak at 794 cm⁻¹ signify the presence of CrO₆ whereas the F$_{2g}$ at 562 cm⁻¹ is due to the tetrahedral cations [35]. For CoNi-LDH, the occurrence of the O-Ni-O and O-Co-O bonds is shown by the E$_{1g}$ peak at 480 cm⁻¹

142

while the Co-OH and Ni-OH bonds at 673 and 545 cm^{-1} respectively are due to the A_{1g} and F_{2g} peaks, respectively. The presence of the E_{2g}, F_{2g} and two A_{1g} peaks in the MnCr$_2$O$_4$-1.2 V@CoNi-LDH composite electrode is evidence for the successful combination of the two individual materials to make a composite. The trivial peak shift and increase in broadness for the composite material is due to phonon confinement owing to the change in particle size [36]. Fig. 3(b) shows the XRD of MnCr$_2$O$_4$-1.2 V, CoNi-LDH and MnCr$_2$O$_4$-1.2 V@CoNi-LDH. The peaks at 18.6, 30.3, 35.6, 38.0, 42.5 and 57.0° correspond to the (111), (220), (311), (400), (331) and (440) planes revealing the cubic nature of MnCr$_2$O$_4$ (JCPDS= 01-075-1614) [14]. The diffraction peaks occurring at a $2\theta = 9.7$, 19.4, 33.3, 38.2, 47.7, 58.7 and 61.9°, respectively correspond to the planes (003), (006), (009), (015), (018), (110) and (113) of CoNi-LDH (JCPDS No.14-0191) [37]. The appearance of these planes in MnCr$_2$O$_4$-1.2 V@CoNi-LDH confirms the successful synthesis of the composite from the LDH and BMO.
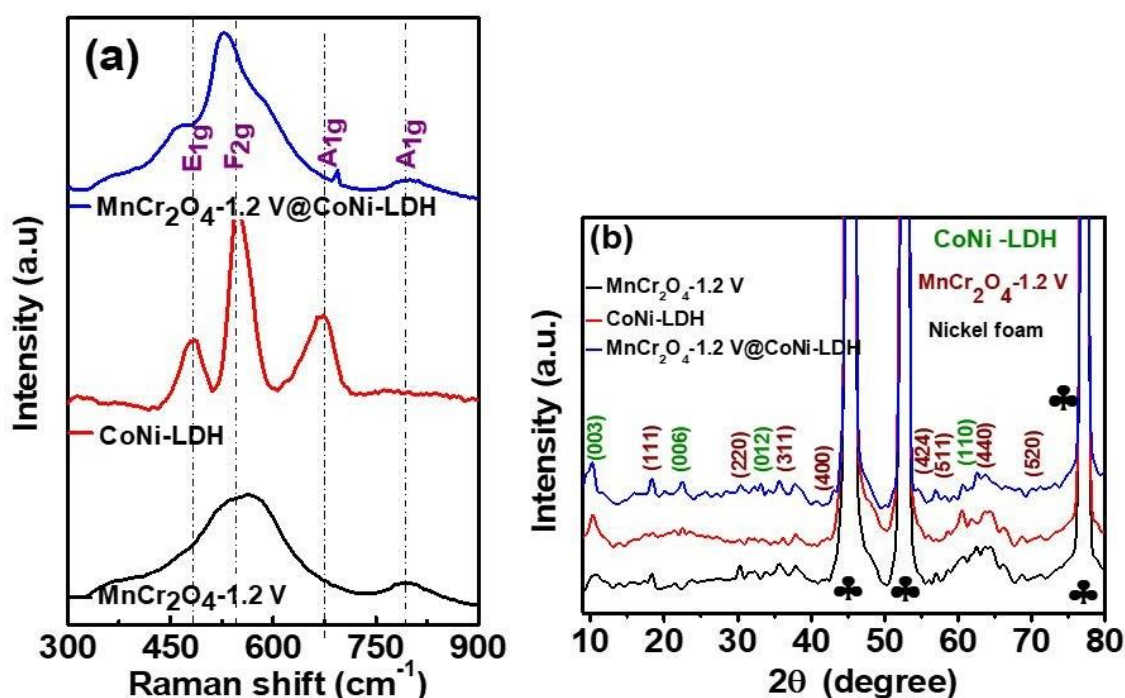
Fig. 4: (a) Raman spectrum and (b) XRD of MnCr$_2$O$_4$-1.2 V, CoNi-LDH and MnCr$_2$O$_4$-1.2 V@CoNi-LDH.

3.2 Electrochemical performance of the as-synthesized samples

3.2.1 Three-electrode evaluations

Fig. 5 (a) displays the GCD of MnCr$_2$O$_4$-1.2V in various electrolytes at 1 A g^{-1}. 2 M KOH gives the largest discharge time compared to other neutral and alkaline electroytes. Fig. 5(b) shows the CV of MnCr$_2$O$_4$-1.0 V, MnCr$_2$O$_4$-1.2V, MnCr$_2$O$_4$-1.4V and Nickel foam in 2 M KOH electrolyte at 20 mV s^{-1}. MnCr$_2$O$_4$-1.2V the greatest current response compared to the other electrodes. The trace for nickel foam is barely visible leading to the conclusion that its contribution to the electrochemical performance of the active materials is negligible. Fig. 5(c) shows the GCD of MnCr$_2$O$_4$-1.0 V, MnCr$_2$O$_4$-1.2 V and MnCr$_2$O$_4$-1.4 V at 1 A g^{-1} in 2 M KOH. All the discharge curves are characterised by nonlinear discharges signifying the accumulation of charges due to Faradaic redox reaction. The MnCr$_2$O$_4$-1.2 V electrode gives the most extended discharge time signifying the highest specific capacity. Fig. 5 (d) shows the specific capacity for these three electrodes. Equation 1 was used to calculate the specific capacity (Q$_S$) [38].

$$Q_S\,[mAh\,g^{-1}] = \frac{1}{3.6} \times I_S\Delta t \qquad (1)$$

where I_S is the specific current (A g^{-1}) and Δt is the discharge time (s). The specific capacities are 50.0, 154.9 and 96.3 mAh g^{-1}. This shows that the electrodeposition voltage of -1.2 V using the scan rate of 2.5 mV s^{-1} yields the best electrochemical performance for the electrodes. For this reason, MnCr$_2$O$_4$-1.2 V was used for the fabrication of the composite electrode for further evaluations.
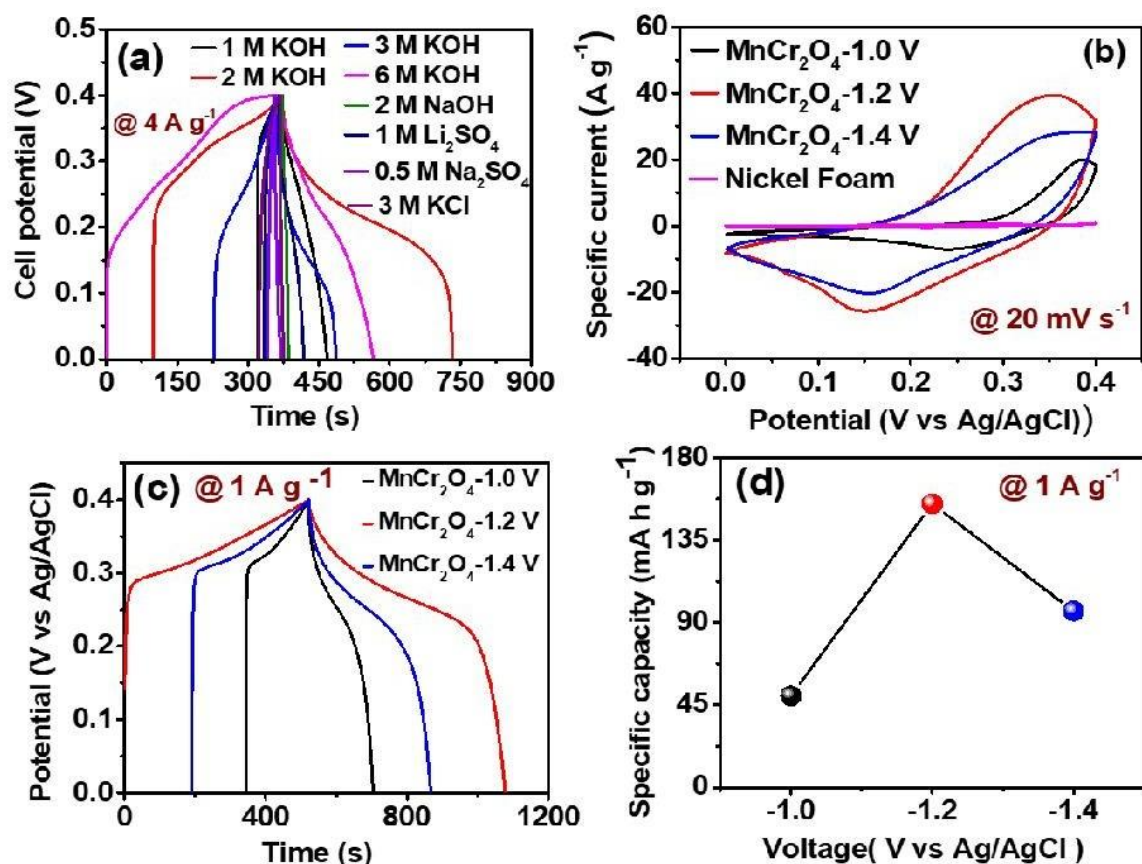
Fig 5: (a) The GCD of $MnCr_2O_4$-1.2V in various electrolytes at 1 A g^{-1}. **(b)** CV of $MnCr_2O_4$-1.0 V, $MnCr_2O_4$-1.2V, $MnCr_2O_4$-1.4V and Nickel foam in 2 M KOH electrolyte at 20 mV s^{-1}. **(c)** The GCD of $MnCr_2O_4$-1.0 V, $MnCr_2O_4$-1.2V, $MnCr_2O_4$-1.4V at 1 A g^{-1} **(d)** Specific capacity vs electrodeposition voltage of $MnCr_2O_4$-1.0 V, $MnCr_2O_4$-1.2V and $MnCr_2O_4$-1.4V in 2 M KOH electrolyte.

Fig. 6 shows the comparison of the electrochemical performance of $MnCr_2O_4$-1.2 V, CoNi-LDH and $MnCr_2O_4$-1.2 V@CoNi-LDH in a half cell set-up in 2 M KOH. Fig. 6(a) shows the CV in a voltage range $0 - 0.4$ V vs Ag/AgCl. All the electrodes show peaks which emanate from Faradaic reactions. The composite electrode, $MnCr_2O_4$-1.2 V@CoNi-LDH has the largest current response in this voltage range. This Faradaic charge storage mechanism is also confirmed by the GCD in Fig. 6(b) with the plateaux signify the accumulation of charges. The longest discharge time in the $MnCr_2O_4$-1.2 V@CoNi-LDH can be explained by the abundant

exposed redox active sites in CoNi-LDH. Fig. 6(c) shows the specific capacity of the electrodes for a range of specific current of 1 - 10 A g^{-1}.

The specific capacities are 154.9, 325.1 and 424.7 mAh g^{-1} for MnCr$_2$O$_4$-1.2 V, CoNi-LDH and MnCr$_2$O$_4$-1.2 V@CoNi-LDH, respectively. MnCr$_2$O$_4$-1.2 V@CoNi-LDH also shows the highest rate capability at 10 A g^{-1}. The rate capabilities values are 42.3, 54.3 and 59.4 %, respectively. Fig. 6(d) shows the EIS Nyquist plot of the electrodes with the inset showing the enlarged high frequency region exposing the equivalent series resistance (ESR) of electrode. The equivalent series resistance (ESR) values as read from the intercept with x-axis are 1.9, 1.3 and 1.6 Ω for MnCr$_2$O$_4$-1.2 V, CoNi-LDH and MnCr$_2$O$_4$-1.2 V@CoNi-LDH respectively. These low ESR values are credited to the intact bonding of the electrode materials and the NF current collector due to the electrodeposition synthesis which also excludes polymeric binder which would otherwise introduce some resistivity. The low magnitude of the imaginary impedance is due to the large value of the specific capacitance of the electrodes [39]. Fig. 6(e) displays the coulombic efficiency of the electrodes which is obtained using equation 2 [40].

$$\eta_C \ [\%] = \frac{t_D}{t_C} \tag{2}$$

where η_C is the coulombic efficiency, t_D and t_C are the discharging and charging times (s). The quasi-perfect coulombic efficiency values are attributed to the robustness of the electrodeposition synthesis.
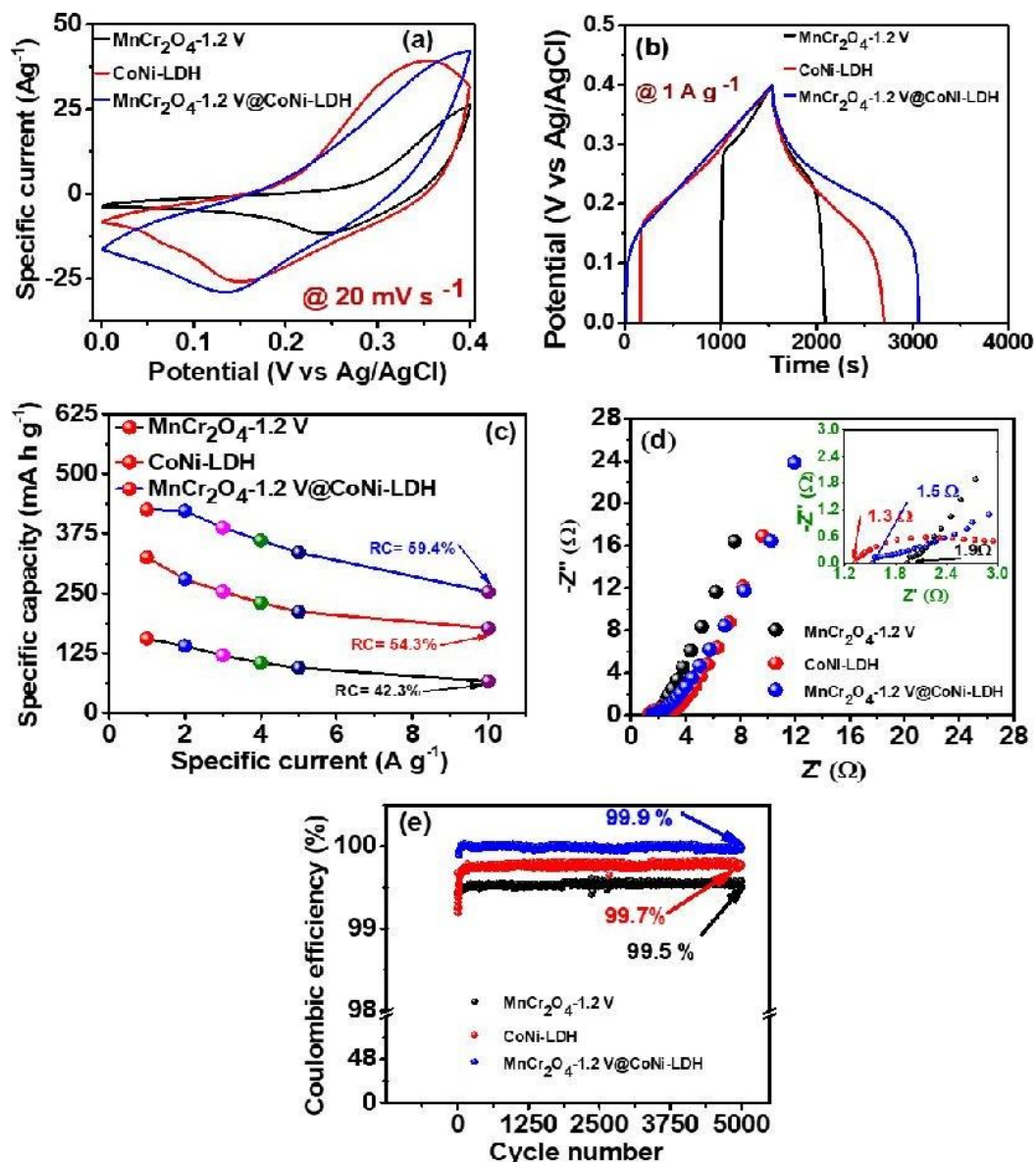
Fig. 6: Electrochemical comparison of MnCr₂O₄-1.2 V, CoNi-LDH and MnCr₂O₄-1.2 V@CoNi-LDH in 2 M KOH; (a) CV curves, (b) GCD curves, (c) specific capacity vs specific current, (d) EIS Nyquist plot and the inset to magnify the high frequency region and (f) coulombic efficiency.

Fig. 6(e) show the coulombic efficiency of the electrodes as a function of number of cycles, the large value of the coulombic efficiency (99.5, 99.7 and 99.9 %, respectively) are partially

credited to the mechanical stability of the synthesis method. The largest value of MnCr$_2$O$_4$-1.2 V@CoNi-LDH shows the stability introduced by the LDH and the BMO.

Due to the superiority shown by MnCr$_2$O$_4$-1.2 V@CoNi-LDH in the electrochemical comparison in Fig. (6), it was opted for further analysis for use as a positive electrode in a device using the same electrolyte (2 M KOH). The electrochemical performance of MnCr$_2$O$_4$-1.2 V@CoNi-LDH in 2 M KOH in a half-cell configuration are shown in Fig. 7. Fig. 7(a) display the CV in a voltage rage from 0 - 0.4 V vs Ag/AgCl. The increase with current due to the Randles-Sevcik equation, which states states that the peak current (i_p) is proprtional to the square-root of the scan-rate, v such that $i_p \propto \sqrt{v}$. oxidation peaks become less pronounced in the voltage range as the scan rate increases. This is because at low scan rate the electrolyte ions and the electrode's active species have ample time to interact with each other increasing the likelihood of redox reactions. As the scan rate increases, the interaction time decrease so the reactions between the electrode species and the ions are suppressed [41]. In the GCD in Fig. 7(b), the plateaux further support the notion of Faradaic reactions. The decrease of charging and discharging time with a rise in specific current is due to the inverse relationship between current and charge/discharge time for a fixed voltage to charge/discharge to a constant charge (I=Q/t). The stability of the composite electrode is shown by the variation of the coulombic efficiency and capacity retention with of cycle number in Fig. 7(c). The high capacity retention value of 73.6 % is caused by a combination of the two materials coupled with the mechanical strength of the electrodeposition synthesis enabling the composite electrode to retain reversibility due to the ability to overcome mechanical stress.
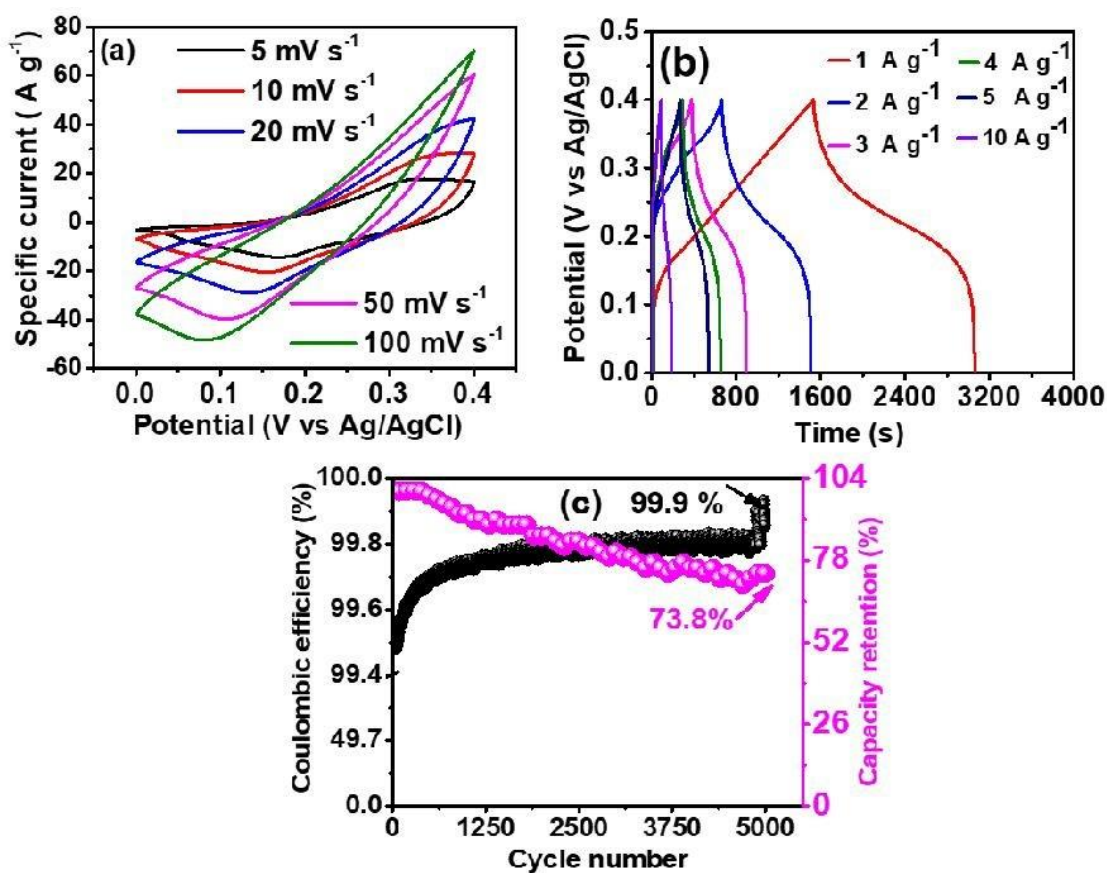
Fig. 7: (a) CV curves, (b) GCD and (c) Capacity retention and coulombic efficiency as a function of the number of cycles of MnCr$_2$O$_4$-1.2 V@CoNi-LDH.

Table 1 contrasts the electrochemical performance of chrome based supercapacitor electrodes. It is transparent from the table that the electrode synthesised in this work using electrodeposition and annealing produced comparable stability and superior specific capacity in three-electrode set-up. This makes it appropriate for participating in supercapacitor devices.

Table 1: Electrochemical performance of newly reported chromium-based composites in three-electrode system.

Electrode	Synthesis method	Capacity retention (%)	Cycle number	Specific capacity (mAh g^{-1})	Specific current (A g^{-1})	Reference:
(NG)/CuCr$_2$O$_4$	Mechanical mixing	98.3	5,000	66.3	0.5	[39]
NG/CuCr$_2$O$_4$/PANI	Mechanical mixing	92	10,000	55.4	1	[42]
CP-CR	Polymerization	77	5,000	73.2	1	[43]
La(CoCrFeMnNiAl$_{0.5}$)$_{1/5}$.5O$_{3-\delta}$	Coprecipitation and calcination	88.6	2,000	49.0	1	[44]
Mn^{II}Cr^{III}$_2$O$_4$/Mn^{II}Mn^{III}$_2$O$_4$/ C	Annealing	75.2	5,000	184	0.5	[45]
MgCr$_2$O$_4$	Sol-gel	84	1,000	5.8	0.25	[46]
MnCr$_2$O$_4$	Electrodeposition	78	1,000	253	0.1	[14]
MIL-101(Cr)	Hydrothermal	86	85	32.7	1	[47]
Cr$_2$O$_3$	Sol-gel	85	85	70.8	0.5	[48]
Ni$_2$Cr$_1$-LDNs	Mechanical mixing	80	10,000	169	2	[49]
FGO-Ap/Cr	Hydrothermal	96.9	5,000	103	1	[50]
MnCr$_2$O$_4$-1.2V @CoNi-LDH	Electrodeposition and annealing	73.6	5,000	424.7	1	**This work**

3.2.2 Electrochemical properties of the hybrid supercapacitor device

To assess the compatibility of $MnCr_2O_4$-1.2 V@CoNi-LDH as a positive electrode in a supercapacitor device, an asymmetric devices $MnCr_2O_4$-1.2 V@CoNi-LDH//AMH, where AMH served as the negative electrode was fabricated. The analysis was performed in a 2-electrode set-up in 2 M KOH electrolyte. To ensure the maximum efficiency of the device, it is essential to perform a mass balance of the electrodes using equation 3 [51,52].

$$\frac{m_+}{m_-} = \frac{C_{s-} \times V_{S_-}}{3.6\, Q_{S+}} \qquad (3)$$

where m_+/m_{--} is the ratio of the masses of the positive to the negative electrode, C_{s-} is the specific capacitance ($F\,g^{-1}$), V_{S-} is the negative electrode potential (V) and Q_{S+} is the specific capacity (mAh g^{-1}). The mass of the negative and positive electrodes used for the devices on each electrode were 5.0 and 0.75 mg cm^{-2}, respectively equivalent to a mass ratio $m_+ : m_{--}$ of 20:3. The total mass of the electrode per unit area was 5.75 mg cm^{-2}.

Fig. 8(a) shows the CV curves of the negative and positive electrodes in three-electrodes configuration. The CV of AMH (negative electrode) in a voltage range of -0.8 - 0 V vs Ag/AgCl shows a quasi-rectangular trace and peaks which is evidence for non-Faradaic energy storage mechanism synonymous with EDLC materials. The curve of $MnCr_2O_4$-1.2 V@CoNi-LDH in a voltage range of 0 - 0.4 V vs Ag/AgCl shows a pair of redox peaks revealing Faradaic redox reaction based energy storage mechanism. Fig. 8(b) illustrates the CV curves of the device in a voltage range of 0 - 1.6 V with scan rates of 5 - 100 mV s^{-1}. In the potential range of 0 - 0.8 V the capacitive behaviour of AMH is dominant without any peaks. From voltage of 0.8 - 1.6 V, there is a sharp increase in current response due to the accumulation of charge due to the manifestation of redox reactions from $MnCr_2O_4$-1.2 V@CoNi-LDH. The GCD in Fig. 8(c)

confirms the presence of both Faradaic and EDLC behaviour where the slanted plateaux are visible from the potential range of 1.6 - 0.8 V and quasi-linear discharge is shown from 0.8 - 0 V. The symmetry of curves for the specific current range of 0.5 - 10 A g^{-1} is due to the reversibility of the charge storage processes [50]. Fig. 8(d) shows the variation of the specific capacity with specific current. The highest specific capacity is 71.6 mAh g^{-1} at a specific current of 1 A g^{-1}, while the specific capacity at 10 A g^{-1} is 40.3 mAh g^{-1} corresponding to a rate capability of 56.3 %. Fig. 8(e) displays the capacity retention and coulombic efficiency as a function of number of cycles. The capacity retention and coulombic efficiency values are 72.9 and 99.7 %, respectively after 15,000 GCD cycles at 9 A g^{-1}. A sharp drop in coulombic efficiency at around the 13000th cycle is due to self discharge is caused by self-discharge [53]. The inherent high stability of AMH and the synergetic effect of CoNi-LDH and MnCr$_2$O$_4$-1.2V contributed to these phenomenal stability values. The specific energy (E_S) and power (P_S) were calculated using equations 4 and 5 [54,55].

$$E_S \ [Wh \ kg^{-1}] = \frac{I_S}{3.6} \times \int V dt \qquad (4)$$

$$P_S \ [W \ kg^{-1}] = \frac{3600}{\Delta t} \times E_S \qquad (5)$$

where I_S is the specific current (A g^{-1}), $\int V dt$ is the area (integral) under the discharge curve (Vs) and Δt is the discharge time (s). E_S for the device was 80.2 Wh kg^{-1} corresponding to P_S of 1117.7 W kg^{-1}. Fig. 8(f) presents the Ragone plot to show the comparison of this hybrid device with related chromium based supercapacitor devices in the literature according to the specific power and specific energy [43,46,56–59]. The insert shows a circuit with 4 diodes connected in parallel lighted by the hybrid device. This plot clearly shows that this work produced a very competitive device with great energy and power output. The circuit demonstrates the practical applicability of the energy delivery.
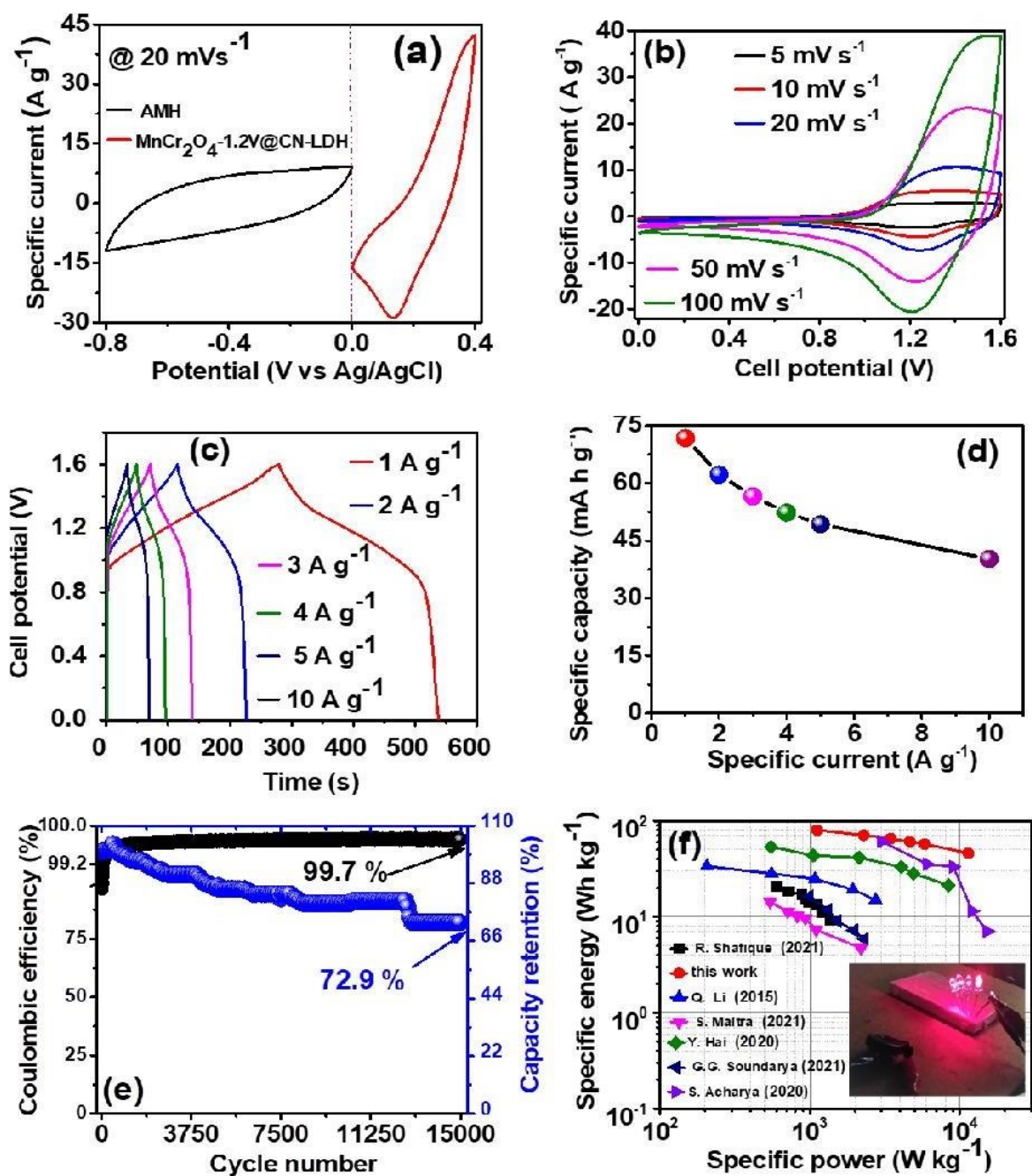
Fig. 8 (a) CV traces of the negative electrode (AMH), and positive electrodes (MnCr$_2$O$_4$-1.2 V@CoNi-LDH) at 20 mV s^{-1}, b) CV curves at different scan rates, (c) GCD curves at various specific currents, (d) the specific capacity as a function of specific current, (e) capacity retention and coulombic efficiency vs cycle number and (f) Ragone plot of MnCr$_2$O$_4$-1.2 V@CoNi-LDH//AMH hybrid device compared to other related devices in the literature, the insert shows 4 diodes in parallel lighted by this hybrid device.

Fig. 9(a) shows the Nyquist plot of the EIS experimental data from the device together with the fitting. The insert shows the equivalent circuit used to perform the fitting. The equivalent series resistance (R_S) in the circuit is linked with to the real impedance intercept of the plot at high frequency. The source of this resistance is the opposition to the flow of charges at the electrode/electrolyte intersection and between the electrode and the current collector [60]. (R_S) is in series with the charge transfer resistance (CTR), the constant phase element (CPE), and the Warburg element (W) represented by circuit elements; R_{CT}, Q and Z_W, respectively. CTR is due to the presence of Faradaic reactions depicted by a small semi-circle in the mid-frequency region [61]. The semi-circle is suppressed due to the presence of the CPE which emanate from non-ideal capacitance due to microscopic roughness caused by scratching at the surface of the electrode [62]. CPE is in series with W. W represents the diffusion through the electrode material [63]. It is responsible for the divergence of the line away from the imaginary impedance axis at the low frequency. These elements are in turn in series with a parallel branch containing the double layer capacitance and the leakage current resistance represented by the circuit elements C_{DL} and R_L, respectively. Ideal C_{DL} behaviour causes the plot to be parallel to the imaginary impedance axes. R_L is the opposition to the movement of ions as they try to reach deep inside fine pores of porous material [64]. Fig. 9(b) indicate the comparison of the Nyquist plot before and after running stability using 15,000 GCD cycles. R_S increases slightly from 1.54 to 1.87 Ω after stability due to the increase in the resistance between the electrode and current collector.

R_S can be used to calculate the maximum power from the device to the load. This maximum power, according to the maximum power transfer theorem is transferred when the resistance of the load and R_S are equal. It is calculated from equation 6 [65].

154

$$P_{MAX}\ [kW\ kg^{-1}] = \frac{V^2}{4mR_S} \tag{6}$$

where V is the cell potential (V), m is the total mass of the electrode material (g) and R_S is the solution resistance (Ω). The P_{MAX} for the device is 111 kW kg^{-1}.

Fig. 9(c) represents the Bode plot indicating the phase angle variation with frequency. The maximum phase angle of -72° which isn't far from the ideal -90° for ideal capacitive behaviour due to the presence of AMH which is an EDLC material. Fig. 9(d) demonstrates the real and imaginary capacitances ($C'\ and\ C''$) respectively as a function of frequency (f). $C'\ and\ C''$ are calculated from equation (5) and (6), respectively [66].

$$C'(\omega)[F] = -\frac{Z''(\omega)}{\omega|Z\,(\omega)|^2} \tag{7}$$

$$C''(\omega)[F] = -\frac{Z'(\omega)}{\omega|Z\,(\omega)|^2} \tag{8}$$

where $Z''(\omega), Z'(\omega)$ and $|Z\,(\omega)|$ are the imaginary impedance, real impedance and magnitude of the impedance (Ω), respectively, and $\omega = 2\pi f$ is the angular frequency (rad s^{-1}).

(C') relates to the useful energy that can be transferred and (C'') is due to the unrecovered energy due to irreversible processes. The peak of the C'' is 221 mF occurring at a frequency of 41 mHz corresponding to a relaxation time (τ) of 3.9 s while the peak of C' is 277 mF. This low τ value signify the ability of the device to be charged quicky. It is obtained from $\omega\tau = 1$ [67].
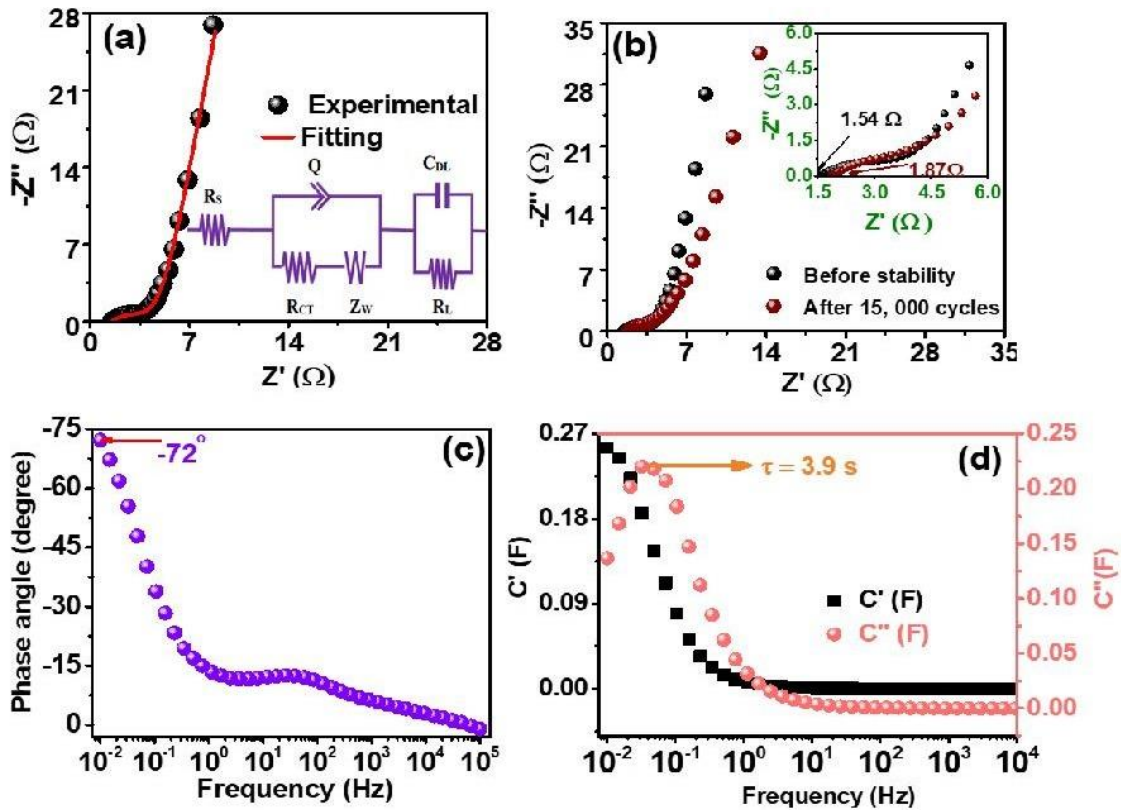
Fig. 9: (a) Nyquist plot for the experimental data and the fitting curve of the equivalent circuit as the inset, (b) Nyquist plot before and after 15, 000 GCD cycles with inset being the enlargement of the higher frequency region, (c) Bode plot and (d) Real and imaginary capacitance vs frequency of the device.

4.0 Conclusion

$MnCr_2O_4 - \phi$, was electrodeposited onto NF. This was done by varying ϕ, the CV electrodeposition potentials (V) to, -1.4, -1.2 and -1.0 V to obtain three electrodes which were then annealed. Of these electrodes, $MnCr_2O_4$-1.2 V electrode produced the best electrochemical results and was selected for the synthesis of the composite electrode $MnCr_2O_4$-1.2V @CoNi-LDH. This was achieved by performing a second electrodeposition of CoNi-LDH on $MnCr_2O_4$-1.2V.

The structural, morphological, and elemental analysis reveals the successively formation of the composite electrode material. The electrode yielded excellent electrochemical performance in 2 M KOH in a three-electrode with a specific capacity of 424.7 mAh g^{-1} at a of 1 A g^{-1}. The electrode was incorporated into an asymmetric supercapacitor device (MnCr$_2$O$_4$-1.2V @CoNi-LDH//AMH) with AMH as the negative electrode. The device also produced exceptional results with a huge specific capacity of 71.6 mAh g^{-1} at 1 A g^{-1}. The specific energy of the device was 80.2 W h kg^{-1} at 1 A g^{-1} relating to a specific power of 1117 W kg. The stability of the device was outstanding with a coulombic efficiency and capacity retention of 99.7 and 72.9 % at 15,000 GCD cycles at 9 A g^{-1}. This phenomenal performance avails the produced hybrid device as a contender for high energy and power applications.

References

[1] C. Yang, L. Hong, P. Chong, Y. Li, M. Wei, Tin-based metal-phosphine complexes nanoparticles as long-cycle life electrodes for high-performance hybrid supercapacitors, J. Colloid Interface Sci. 606 (2022) 148–157. https://doi.org/10.1016/j.jcis.2021.08.012.

[2] Z. Sun, H. Qi, M. Chen, S. Guo, Z. Huang, S. Maganti, V. Murugadoss, M. Huang, Z. Guo, Progress in Cellulose/Carbon Nanotube Composite Flexible Electrodes for Supercapacitors, Eng. Sci. 18 (2022) 59–74. https://doi.org/10.30919/es8d588.

[3] Y. Cao, W. Yang, M. Wang, N. Wu, L. Zhang, Q. Guan, H. Guo, Metal-organic frameworks as highly efficient electrodes for long cycling stability supercapacitors, Int. J. Hydrogen Energy. 46 (2021) 18179–18206. https://doi.org/10.1016/j.ijhydene.2021.03.003.

[4] R. Liu, A. Zhou, X. Zhang, J. Mu, H. Che, Y. Wang, T.T. Wang, Z. Zhang, Z. Kou, Fundamentals, advances and challenges of transition metal compounds-based supercapacitors, Chem. Eng. J. 412 (2021) 128611. https://doi.org/10.1016/j.cej.2021.128611.

[5] S.Y. Hsu, F.H. Hsu, J.L. Chen, Y.S. Cheng, J.M. Chen, K.T. Lu, The supercapacitor electrode properties and energy storage mechanism of binary transition metal sulfide MnCo2S4compared with oxide MnCo2O4studied using: In situ quick X-ray absorption spectroscopy, Mater. Chem. Front. 5 (2021) 4937–4949. https://doi.org/10.1039/d1qm00222h.

[6] R.M. Obodo, N.M. Shinde, U.K. Chime, S. Ezugwu, A.C. Nwanya, I. Ahmad, M.

Maaza, P.M. Ejikeme, F.I. Ezema, Recent advances in metal oxide/hydroxide on three-dimensional nickel foam substrate for high performance pseudocapacitive electrodes, Curr. Opin. Electrochem. 21 (2020) 242–249. https://doi.org/10.1016/j.coelec.2020.02.022.

[7]   S. Malik, I.H. Gul, M.M. Baig, Hierarchical MnNiCo ternary metal oxide/graphene nanoplatelets composites as high rated electrode material for supercapacitors, Ceram. Int. 47 (2021) 17008–17014. https://doi.org/10.1016/j.ceramint.2021.02.272.

[8]   A.M. Baena-Moncada, V. Quispe-Garrido, G. Antonio Cerron-Calle, A. Bazan-Aguilar, J.G. Ruiz-Montoya, E.O. López, Advances in the design and application of transition metal oxide-based supercapacitors, Open Chem. 19 (2021) 709–725. https://doi.org/10.1515/chem-2021-0059.

[9]   Y. Liu, K. Wang, X. Xu, K. Eid, A.M. Abdullah, L. Pan, Y. Yamauchi, Recent Advances in Faradic Electrochemical Deionization: System ArchitecturesversusElectrode Materials, ACS Nano. 15 (2021) 13924–13942. https://doi.org/10.1021/acsnano.1c03417.

[10]   D. Mohanadas, Y. Sulaiman, Recent advances in development of electroactive composite materials for electrochromic and supercapacitor applications, J. Power Sources. 523 (2022) 231029. https://doi.org/10.1016/j.jpowsour.2022.231029.

[11]   X. Zhao, L. Mao, Q. Cheng, J. Li, F. Liao, G. Yang, L. Xie, C. Zhao, L. Chen, Two-dimensional Spinel Structured Co-based Materials for High Performance Supercapacitors: A Critical Review, Chem. Eng. J. 387 (2020) 124081. https://doi.org/10.1016/j.cej.2020.124081.

[12]   J.G. Ruiz-Montoya, Lady V. Quispe-Garrido, J.C. Calderón Gómez, A.M. Baena-Moncada, J.M. Gonçalves, Recent progress in and prospects for supercapacitor

materials based on metal oxide or hydroxide/biomass-derived carbon composites, Sustain. Energy Fuels. 5 (2021) 5332–5365. https://doi.org/10.1039/d1se01170g.

[13] Y. Li, S. Feng, Q. Lv, X. Kan, X. Liu, An investigation of reentrant spin-glass behavior, magnetocaloric effect and critical behavior of MnCr2O4, J. Alloys Compd. 877 (2021) 160224. https://doi.org/10.1016/j.jallcom.2021.160224.

[14] F.F. Alharbi, S. Aman, N. Ahmad, S.R. Ejaz, S. Manzoor, R.Y. Khosa, M.U. Nisa, M.A. Iqbal, S. Abbas, M. Awais, Design and fabrication of novel MnCr2O4 nanostructure: electrochemically deposited on stainless steel strip with enhanced efficiency towards supercapacitor applications, J. Mater. Sci. Mater. Electron. 33 (2022) 7256–7265. https://doi.org/10.1007/s10854-022-07909-3.

[15] M. Gul, Radio frequency abnormal dielectric response of manganese chromite (MnCr2O4) nanoparticles synthesized by coprecipitation method, Mater. Res. Bull. 76 (2016) 431–435. https://doi.org/10.1016/j.materresbull.2016.01.007.

[16] P.R. Kharangarh, N.M. Ravindra, R. Rawal, A. Singh, V. Gupta, Graphene quantum dots decorated on spinel nickel cobaltite nanocomposites for boosting supercapacitor electrode material performance, J. Alloys Compd. 876 (2021) 159990. https://doi.org/10.1016/j.jallcom.2021.159990.

[17] R. Ramachandran, Y. Lan, Z.X. Xu, F. Wang, Construction of NiCo-Layered Double Hydroxide Microspheres from Ni-MOFs for High-Performance Asymmetric Supercapacitors, ACS Appl. Energy Mater. 3 (2020) 6633–6643. https://doi.org/10.1021/acsaem.0c00790.

[18] Y. Zhu, S. An, X. Sun, D. Lan, J. Cui, Y. Zhang, W. He, Core-branched NiCo2S4@CoNi-LDH heterostructure as advanced electrode with superior energy storage performance, Chem. Eng. J. 383 (2020) 123206.

160

https://doi.org/10.1016/j.cej.2019.123206.

[19]   X. Zhang, Q. Lu, E. Guo, J. Feng, M. Wei, J. Ma, NiCo layer double
        hydroxide/biomass-derived interconnected porous carbon for hybrid supercapacitors, J.
        Energy Storage. 38 (2021) 102514. https://doi.org/10.1016/j.est.2021.102514.

[20]   W. Zhou, X. Yan, W. Zhang, Y. Li, Y. Zhu, M. Zhang, W. Zhu, X. Cheng, Tailored
        synthesis of nano-corals nickel-vanadium layered double hydroxide@Co2NiO4 on
        nickel foam for a novel hybrid supercapacitor, J. Energy Storage. 38 (2021) 102584.
        https://doi.org/10.1016/j.est.2021.102584.

[21]   H. Liang, T. Lin, S. Wang, H. Jia, C. Li, J. Cao, J. Feng, W. Fei, J. Qi, A free-standing
        manganese cobalt sulfide@cobalt nickel layered double hydroxide core-shell
        heterostructure for an asymmetric supercapacitor, Dalt. Trans. 49 (2019) 196–202.
        https://doi.org/10.1039/c9dt03974k.

[22]   S. Wang, Y. Zou, F. Xu, C. Xiang, H. Peng, J. Zhang, L. Sun, Morphological control
        and electrochemical performance of NiCo2O4@NiCo layered double hydroxide as an
        electrode for supercapacitors, J. Energy Storage. 41 (2021) 102862.
        https://doi.org/10.1016/j.est.2021.102862.

[23]   X. Xue, J. Zhong, J. Liu, Z. Hou, X. Wu, S. Li, M. Yu, Hydrolysis of metal-organic
        framework towards three-dimensional nickel cobalt-layered double hydroxide for high
        performance supercapacitors, J. Energy Storage. 31 (2020) 101649.
        https://doi.org/10.1016/j.est.2020.101649.

[24]   A.G. El-Deen, M.K. Abdel-Sattar, N.K. Allam, High-performance solid-state
        supercapacitor based on Ni-Co layered double hydroxide@Co3O4 nanocubes and
        spongy graphene electrodes, Appl. Surf. Sci. 587 (2022) 152548.
        https://doi.org/10.1016/j.apsusc.2022.152548.

[25] J. Xu, H. Cao, C. Ni, Y. Wang, J. Cao, Z. Chen, Design and synthesis of sandwich-like CoNi 2 S 4 @C@NiCo-LDH microspheres for supercapacitors, J. Solid State Electrochem. (2019) 1513–1522. https://doi.org/10.1007/s10008-019-04246-0.

[26] R.S. Kate, S.A. Khalate, R.J. Deokate, Overview of nanostructured metal oxides and pure nickel oxide (NiO) electrodes for supercapacitors: A review, J. Alloys Compd. 734 (2018) 89–111. https://doi.org/10.1016/j.jallcom.2017.10.262.

[27] S.S. Haider, M.Z. Iqbal, S. Zakar, A.M. Afzal, K. Yaqoob, S. Aftab, Superior performance of electrodeposited CoMnS as novel electrode material for supercapattery devices, J. Energy Storage. 39 (2021) 102608. https://doi.org/10.1016/j.est.2021.102608.

[28] A.G. Hassan, M.A.M. Yajid, S.N. Saud, T.A.A. Bakar, A. Arshad, N. Mazlan, Effects of varying electrodeposition voltages on surface morphology and corrosion behavior of multi-walled carbon nanotube coated on porous Ti-30 at.%-Ta shape memory alloys, Surf. Coatings Technol. 401 (2020). https://doi.org/10.1016/j.surfcoat.2020.126257.

[29] X. Wang, X. Li, Q. Zhang, Z. Lu, H. Song, Y. Wang, Electrodeposition of ZnO Nanorods with Synergistic Photocatalytic and Self-Cleaning Effects, J. Electron. Mater. 50 (2021) 4954–4961. https://doi.org/10.1007/s11664-021-08958-w.

[30] D. George, A. Garcia, Q. Pham, M.R. Perez, J. Deng, M.T. Nguyen, T. Zhou, S.O. Martinez-Chapa, Y. Won, C. Liu, R.C. Lo, R. Ragan, M. Madou, Fabrication of patterned graphitized carbon wires using low voltage near-field electrospinning, pyrolysis, electrodeposition, and chemical vapor deposition, Microsystems Nanoeng. 6 (2020). https://doi.org/10.1038/s41378-019-0117-7.

[31] M. Zhang, Y. Chen, D. Yang, J. Li, High performance MnO2 supercapacitor material prepared by modified electrodeposition method with different electrodeposition

voltages, J. Energy Storage. 29 (2020). https://doi.org/10.1016/j.est.2020.101363.

[32]   A. Yavuz, P. Yilmaz Erdogan, N. Ozdemir, H. Zengin, G. Zengin, M. Bedir, Effect of cathodic deposition potential on the performance of nanostructured cobalt-based film for asymmetric supercapacitor fabrication, Solid State Sci. 99 (2020) 106074. https://doi.org/10.1016/j.solidstatesciences.2019.106074.

[33]   G. Rutavi, D.J. Tarimo, V.M. Maphiri, N. Manyala, Two-step electrodeposition of Hausmannite sulphur reduced graphene oxide and cobalt-nickel layered double hydroxide heterostructure for high-performance supercapacitor, Int. J. Energy Res. (2022) 1–14. https://doi.org/10.1002/er.7922.

[34]   D.J. Tarimo, A.A. Mirghni, K.O. Oyedotun, G. Rutavi, V.N. Kitenge, N. Manyala, Recycling of biomass wastes from amarula husk by a modified facile economical water salt method for high energy density ultracapacitor application, J. Energy Storage. 53 (2022) 105166. https://doi.org/10.1016/j.est.2022.105166.

[35]   J. Barman, S. Ravi, Effect of Al Substitution in Structural and Magnetic Properties of MnCr2O4, J. Supercond. Nov. Magn. 31 (2018) 99–106. https://doi.org/10.1007/s10948-017-4169-3.

[36]   R.A. Sanguramath, B. Laadan, N. Raz, A. Katalan, D.J. Benarroch, A. Franco, CuO(1−x)ZnOx nanocomposite with broad spectrum antibacterial activity: Application in medical devices and acrylic paints, Nanotechnology. 32 (2021). https://doi.org/10.1088/1361-6528/abe826.

[37]   N. Zhao, H. Fan, M. Zhang, C. Wang, X. Ren, H. Peng, H. Li, X. Jiang, X. Cao, Preparation of partially-cladding NiCo-LDH/Mn3O4 composite by electrodeposition route and its excellent supercapacitor performance, J. Alloys Compd. 796 (2019) 111– 119. https://doi.org/10.1016/j.jallcom.2019.05.023.

[38] Q. Hu, W. Li, B. Xiang, X. Zou, J. Hao, M. Deng, Q. Wu, Y. Wang, Sulfur source-inspired synthesis of β-NiS with high specific capacity and tunable morphologies for hybrid supercapacitor, Electrochim. Acta. 337 (2020) 135826. https://doi.org/10.1016/j.electacta.2020.135826.

[39] S. Sarkar, R. Akshaya, S. Ghosh, Nitrogen doped graphene/CuCr2O4 nanocomposites for supercapacitors application: Effect of nitrogen doping on coulombic efficiency, Electrochim. Acta. 332 (2020) 135368. https://doi.org/10.1016/j.electacta.2019.135368.

[40] P. Mani, V. Vellaikasi, X.T. Suryabai, A.R. Simon, T. Kattaiyan, Cubic like CoMn 2 O 4 nanostructures as advanced high-performance pseudocapacitive electrode, 00 (2022) 1–10.

[41] S. Saini, P. Chand, Effect of aqueous electrolytes on h-WO3 nanorods as an electrode material for supercapacitor application, Chem. Phys. Lett. 802 (2022) 139760. https://doi.org/10.1016/j.cplett.2022.139760.

[42] A. Raghavan, S. Sarkar, S. Ghosh, Dnevelopment of PANI based ternary nanocomposite with enhanced capacity retention for high performance supercapacitor application, Electrochim. Acta. 388 (2021) 138564. https://doi.org/10.1016/j.electacta.2021.138564.

[43] S. Acharya, S. Sahoo, S. Sonal, J.H. Lee, B.K. Mishra, G.C. Nayak, Adsorbed Cr(VI) based activated carbon/polyaniline nanocomposite: A superior electrode material for asymmetric supercapacitor device, Compos. Part B Eng. 193 (2020) 107913. https://doi.org/10.1016/j.compositesb.2020.107913.

[44] M. Guo, Y. Liu, F. Zhang, F. Cheng, C. Cheng, Y. Miao, F. Gao, J. Yu, Inactive Al3+-doped La(CoCrFeMnNiAlx)1/(5+x)O3 high-entropy perovskite oxides as high

performance supercapacitor electrodes, c (2022) 742–753.

[45] Q. Zhou, J. Wang, R. Zheng, Y. Gong, J. Lin, One-step mild synthesis of Mn-based spinel MnIICrIII2O4/MnIIMnIII2O4/C and Co-based spinel CoCr2O4/C nanoparticles as battery-type electrodes for high-performance supercapacitor application, Electrochim. Acta. 283 (2018) 197–211. https://doi.org/10.1016/j.electacta.2018.06.164.

[46] S. Maitra, R. Mitra, T.K. Nath, Sol-gel derived MgCr2O4 nanoparticles for aqueous supercapacitor and alkaline OER and HER bi-functional electrocatalyst applications, J. Alloys Compd. 858 (2021) 157679. https://doi.org/10.1016/j.jallcom.2020.157679.

[47] A. Farisabadi, M. Moradi, S. Borhani, S. Hajati, M.A. Kiani, S.A. Tayebifard, Synthesis and electrochemical properties of Mg-doped chromium-based metal organic framework/reduced graphene oxide composite for supercapacitor application, J. Mater. Sci. Mater. Electron. 29 (2018) 8421–8430. https://doi.org/10.1007/s10854-018-8853-2.

[48] I. Shafi, E. Liang, B. Li, Ultrafine chromium oxide (Cr2O3) nanoparticles as a pseudocapacitive electrode material for supercapacitors, J. Alloys Compd. 851 (2021). https://doi.org/10.1016/j.jallcom.2020.156046.

[49] Z. Chen, H. Deng, M. Zhang, Z. Yang, D. Hu, Y. Wang, K. Yan, One-step facile synthesis of nickel-chromium layered double hydroxide nanoflakes for high-performance supercapacitors, Nanoscale Adv. 2 (2020) 2099–2105. https://doi.org/10.1039/d0na00178c.

[50] M.D. Najafi, E. Kowsari, H.R. Naderi, A. Chinnappan, S. Ramakrishna, A. Ehsani, A. Shokravi, Functionalization of graphene oxide via chromium complexes coordinated on 5-aminopyridine-2-carboxylic acid as a symmetric supercapacitor electrode

materials in energy storage devices, Compos. Sci. Technol. 211 (2021) 108844. https://doi.org/10.1016/j.compscitech.2021.108844.

[51]   A.A. Mirghni, K.O. Oyedotun, B.A. Mahmoud, O. Fasakin, D.J. Tarimo, N. Manyala, A study of Co-Mn phosphate supported with graphene foam as promising electrode materials for future electrochemical capacitors, Int. J. Energy Res. 46 (2022) 3080–3094. https://doi.org/10.1002/er.7365.

[52]   D.J. Tarimo, K.O. Oyedotun, A.A. Mirghni, B. Mutuma, N.F. Sylla, P. Murovhi, N. Manyala, Enhanced electrochemical performance of supercapattery derived from sulphur-reduced graphene oxide/cobalt oxide composite and activated carbon from peanut shells, Int. J. Hydrogen Energy. 45 (2020) 33059–33075. https://doi.org/10.1016/j.ijhydene.2020.09.142.

[53]   Y. Wu, R. Holze, Self-discharge in supercapacitors: Causes, effects and therapies: An overview, Electrochem. Energy Technol. 7 (2021) 1–37.

[54]   A.M. Abuelftooh, N.S. Tantawy, S.S. Mahmouad, M.A. Shoeib, S.G. Mohamed, High specific energy supercapacitor electrode prepared from MnS/Ni3S2composite grown on nickel foam, New J. Chem. 45 (2021) 18641–18650. https://doi.org/10.1039/d1nj03930j.

[55]   S. Sarr, N.F. Sylla, D.T. Bakhoum, K.O. Oyedotun, B.D. Ngom, N. Manyala, Effect of neutral electrolytes on vanadium dioxide microspheres-based electrode materials for asymmetric supercapacitors, J. Energy Storage. 43 (2021) 103294. https://doi.org/10.1016/j.est.2021.103294.

[56]   R. Shafique, M. Rani, A. Mahmood, R.A. Alshgari, K. Batool, T. Yaqoob, N.K. Janjua, S. Khan, S. Khan, G. Murtaza, Investigations of 2D Ti3C2(MXene)-CoCr2O4 nanocomposite as an efficient electrode material for electrochemical supercapacitors,

Int. J. Energy Res. 46 (2022) 6689–6701. https://doi.org/10.1002/er.7605.

[57] Q. Li, J. Zhou, S. Zhao, Y. Li, C. Chen, K. Tao, R. Liu, L. Han, Hollow and Hierarchical Cobalt–Metal Organic Framework@CoCr2O4 Microplate Array as a Battery-Type Electrode for High-Performance Hybrid Supercapacitors, ChemElectroChem. 7 (2020) 437–444. https://doi.org/10.1002/celc.201902015.

[58] Y. Hai, K. Tao, H. Dan, L. Liu, Y. Gong, Cr-doped (Co, Ni)3S4/Co9S8/Ni3S2 nanowires/nanoparticles grown on Ni foam for hybrid supercapacitor, J. Alloys Compd. 835 (2020) 155254. https://doi.org/10.1016/j.jallcom.2020.155254.

[59] G.G. Soundarya, B. Nalini, D. Lakshmi, P. Priyanka, Structural rearrangement by Ni, Cr doping in zinc cobaltite and its influence on supercapacitance, Ceram. Int. 47 (2021) 18635–18645. https://doi.org/10.1016/j.ceramint.2021.03.195.

[60] A. Chowdhury, S. Biswas, T. Singh, A. Chandra, Redox mediator induced electrochemical reactions at the electrode-electrolyte interface: Making sodium-ion supercapacitors a competitive technology, Electrochem. Sci. Adv. 2 (2022) 1–14. https://doi.org/10.1002/elsa.202100030.

[61] Y. He, D. Liu, H. Zhao, J. Wang, Y. Sui, J. Qi, Z. Chen, P. Zhang, C. Chen, D. Zhuang, Carbon-coated NiMn layered double hydroxides/Ni3S2 nanocomposite for high performance supercapacitors, J. Energy Storage. 41 (2021) 103003. https://doi.org/10.1016/j.est.2021.103003.

[62] Y.X. Zhu, G.L. Song, P.P. Wu, D.J. Zheng, Z.M. Wang, A burnished and Al-alloyed magnesium surface with improved mechanical and corrosion properties, Corros. Sci. 184 (2021) 109395. https://doi.org/10.1016/j.corsci.2021.109395.

[63] H. Liu, M. Dai, D. Zhao, X. Wu, B. Wang, Realizing Superior Electrochemical

.

4.3.3 . Concluding remarks

The combination of $MnCr_2O_4$-1.2 V and CoNi-LDH synthesized using the electrodeposition and annealing method achieved exceptional electrochemical performance. The successful fusion of the $MnCr_2O_4$ nanograins and CoNi-LDH nanosheets was seen in the SEM micrograms. The composite electrode $MnCr_2O_4$-1.2 V@CoNi-LDH attained wonderful results in three- an electrode configuration with a specific capacity of 424.7 mA h g^{-1} at 1 A g^{-1} in 2 M KOH with an excellent coulombic efficiency of 99.9 % and capacity retention of 73.6 %. This electrode served as the positive electrode of the $MnCr_2O_4$-1.2 V@CoNi-LDH//AMH with activated carbon from Amarula husk (AMH) as the negative electrode. The asymmetric device achieved outstanding performance with a specific energy and power of 80.2 Wh kg^{-1} and 1117.7 W kg^{-1}, respectively at a specific current of 1 A g^{-1} and a high coulombic efficiency and capacity retention of 99.7 and 72.9 % after 15,000 cycles. This proves the compatibility of electrodeposition-synthesised $MnCr_2O_4$-1.2 V@CoNi-LDH with porous biomass material devices which is a contender for high-performance renewable energy storage devices.

References

[1]   M.A.A. Mohd Abdah, N.H.N. Azman, S. Kulandaivalu, Y. Sulaiman, Review of the use of transition-metal-oxide and conducting polymer-based fibres for high-performance supercapacitors, Mater. Des. 186 (2020) 108199. https://doi.org/10.1016/j.matdes.2019.108199.

[2]   S.J. Patil, N.R. Chodankar, R.B. Pujari, Y.K. Han, D.W. Lee, Core-shell hetero-nanostructured 1D transition metal polyphosphates decorated 2D bimetallic layered double hydroxide for sustainable hybrid supercapacitor, J. Power Sources. 466 (2020) 228286. https://doi.org/10.1016/j.jpowsour.2020.228286.

[3]   N. Song, S. Hong, M. Xiao, Y. Zuo, E. Jiang, C. Li, H. Dong, Fabrication of Co(Ni)-P surface bonding states on core–shell Co(OH)2@P-NiCo-LDH towards electrocatalytic hydrogen evolution reaction, J. Colloid Interface Sci. 582 (2021) 535–542. https://doi.org/10.1016/j.jcis.2020.08.086.

[4]   S.A. Beknalkar, A.M. Teli, T.S. Bhat, K.K. Pawar, S.S. Patil, N.S. Harale, J.C. Shin, P.S. Patil, Mn3O4 based materials for electrochemical supercapacitors: Basic principles, charge storage mechanism, progress, and perspectives, J. Mater. Sci. Technol. 130 (2022) 227–248. https://doi.org/10.1016/j.jmst.2022.03.036.

[5]   D.J. Tarimo, K.O. Oyedotun, A.A. Mirghni, N. Manyala, Sulphur-reduced graphene oxide composite with improved electrochemical performance for supercapacitor applications, Int. J. Hydrogen Energy. 45 (2020) 13189–13201. https://doi.org/10.1016/j.ijhydene.2020.03.059.

[6]   R. Hassandoost, A. Kotb, Z. Movafagh, M. Esmat, R. Guegan, S. Endo, W. Jevasuwan, N. Fukata, Y. Sugahara, A. Khataee, Y. Yamauchi, Y. Ide, E. Doustkhah, Nanoarchitecturing bimetallic manganese cobaltite spinels for sonocatalytic degradation of oxytetracycline, Chem. Eng. J. 431 (2022). https://doi.org/10.1016/j.cej.2021.133851.

[7]   S.G. Krishnan, M.H.A. Rahim, R. Jose, Synthesis and characterization of MnCo2O4cuboidal microcrystals as a high performance psuedocapacitor electrode, J. Alloys Compd. 656 (2016) 707–713. https://doi.org/10.1016/j.jallcom.2015.10.007.

[8]   A.A. Lourenço, V.D. Silva, R.B. da Silva, U.C. Silva, C. Chesman, C. Salvador, T.A. Simões, D.A. Macedo, F.F. da Silva, Metal-organic frameworks as template for synthesis of Mn3+/Mn4+ mixed valence manganese cobaltites electrocatalysts for oxygen evolution reaction, J. Colloid Interface Sci. 582 (2021) 124–136. https://doi.org/10.1016/j.jcis.2020.08.041.

[9]   F.F. Alharbi, S. Aman, N. Ahmad, S.R. Ejaz, S. Manzoor, R.Y. Khosa, M.U. Nisa, M.A. Iqbal, S. Abbas, M. Awais, Design and fabrication of novel MnCr2O4 nanostructure: electrochemically deposited on stainless steel strip with enhanced efficiency towards supercapacitor applications, J. Mater. Sci. Mater. Electron. 33 (2022) 7256–7265. https://doi.org/10.1007/s10854-022-07909-3.

[10]   L. Xiao, P. Yao, T. Xue, F. Li, One-step electrodeposition synthesis of Ni/NiSx@NF catalyst on nickel foam (NF) for hydrogen evolution reaction, Mol. Catal. 511 (2021) 111694. https://doi.org/10.1016/j.mcat.2021.111694.

CHAPTER 5

5.0. GENERAL CONCLUSION AND FUTURE WORK

This chapter is about the overall conclusion of all the results and discussion which emanate from the preceding chapters. The chapter also looks into possible future work.

5.1. General conclusion

Cobalt nickel layered double hydroxide (CoNi-LDH) and its spinel and sulphur-reduced graphene oxide composites were fabricated successfully through processes based on electrodeposition. The micrographs, electrode thickness, chemical composition and structural properties were analysed using the scanning electron microscope (SEM) which also incorporated energy-dispersive X-ray spectroscopy (EDS), Transmission electron microscope (TEM), and Raman spectroscopy. The electrochemical analysis of the electrodes and the devices were all performed using 2 M KOH in three- and two-electrode configurations, respectively.

CN and Hausmannite RGO-S (MO/RGO-S) were produced using cyclic voltammetry (CV) electrodeposition and galvanostatic electrodeposition, respectively, while RGO-S was produced using a modified Hummer's method. CN showed a nanosheet-like morphology, while RGO-S and MO showed a mixture of nanoribbons and nanospheres. The TEM micrograms of the composite (MO/RGO-S@CN) showed the CN wrapped around the nanospheres and nanoribbons. The composite electrode (MO/RGO-S-50@CN) with an RGO-S mass loading of 50 mg yielded an outstanding specific capacity of 582.1 mAh g^{-1} at a specific current of 0.5 A g^{-1}. This was superior to all the other mass loading and the pristine CoNi-LDH proving the synergetic effect of materials with different charge storage mechanisms for

excellent electrochemical results. The fabricated asymmetric device (MO/RGO-S-50@CN//CCBW) showed great electrochemical performances with a specific energy and power of 56.0 Wh kg^{-1} and 515 W kg^{-1} at 0.5 A g^{-1}. It also revealed excellent electrochemical stability with a coulombic efficiency and capacity retention of 99.7 and 85.1 % after 10,000 GCD cycles at 6 A g^{-1}. These excellent results can be credited to the strength of the bond between the nickel foam current collector and the electrode material and the compatibility of the positive electrode with the biomass-activated materials in producing a high-performance supercapacitor device.

To improve the specific capacitance of cobalt nickel layered double hydroxide (CN-LDH) without carbon materials, manganese cobaltite (MCO) was incorporated into a composite electrode (MCO-2.5@CN-LDH) using CV electrodeposition at a scan rate of 2.5 mV s^{-1}. Manganese chromite (MnCr$_2$O$_4$) was produced using CV electrodeposition and annealing. Nanograins morphology was observed for MnCr$_2$O$_4$. This array increases the accessible surface area for ions and increases the specific capacity. This composite electrode yielded a phenomenal specific capacity of 415.9 mAh g^{-1} at a specific current of 1 A g^{-1}. This was superior to the specific capacity of the individual electrodes which were 237.3 and 325.1 mAh g^{-1} for MCO-2.5 and CN-LDH, respectively. This demonstrated the benefit of the two materials for improved specific capacity. The composite also produced great stability with capacity retention and coulombic efficiency of 87.0 and 99.8 %. The presence of the MCO-2.5 nanograins helped to assuage the restacking of CN-LDH to achieve this great stability. The composite electrode served as the positive electrode of a supercapacitor device (MCO-2.5@CN-LDH//CCBW). The device showed a highly competitive performance with specific energy and power of 55.8 Wh kg^{-1} and 940 W kg^{-1} at 1 A g^{-1}, respectively. It reached a high cell potential of 1.6 V. The stability of the device was remarkable with a coulombic efficiency

and capacity retention of 99.8 and 81.6 %. This is an important result proving a cost-effective way of synthesising electrode materials for use in high-performance supercapacitor devices.

To further improve the electrochemical performance of cobalt nickel layered double hydroxide (CoNi-LDH) using a sustainable, cost-effective and safe approach, $MnCr_2O_4$ was used because of high electrical conductivity and multiple oxidation states. The CV electrodeposition and annealing were used to synthesize $MnCr_2O_4 - \phi$ by varying the electrodeposition potential ($\phi = -1.0, -1.2$ and -1.4 V). $MnCr_2O_4 - 1.2$ V yielded the best electrochemical performance and was therefore used to synthesize the composite electrode, $MnCr_2O_4$-1.2 V@CoNi-LDH. The SEM micrograms of the composite showed nanograins from $MnCr_2O_4 - 1.2$ V and nanosheets due to CoNi-LDH. The electrode produced an outstanding performance with a specific capacity of 424.7 mAh g^{-1} at a specific current of 1 A g^{-1}. The electrode also produced great stability with a capacity retention of 73.6 % after 5,000 galvanostatic charge-discharge (GCD) cycles at a specific current of 9 A g^{-1}. The electrode was incorporated into an asymmetric device ($MnCr_2O_4$-1.2 V@CoNi-LDH//AMH) where AMH is the activated carbon from Amarula husk which operated as the negative electrode. The device yielded very competitive results with specific power and energy of 111.7 W kg^{-1} and 80.2 Wh kg^{-1}, respectively at a specific current of 1 A g^{-1}. The coulombic efficiency and capacity retention were 99.7 and 72.9 %, respectively after 10,000 GCD cycles at 9 A g^{-1}.

Among the most important parameters in comparing the electrochemical performance of energy storage devices are specific energy and power. The best visual tool for this comparison is the Ragone plot. The Ragone plot in figure 5.1 compares the specific power and energy of the three asymmetric devices in this thesis. All the tests were carried out in 2 M KOH in a two -electrode set-up. From the figure, CoNi-LDH based devices showed an outstanding specific energy and specific power. These results are a testimony of the contribution of carbon based

materials and bimetallic manganese based metal oxide in improving the conductivity of LDH materials leading to such phenomenal performances.
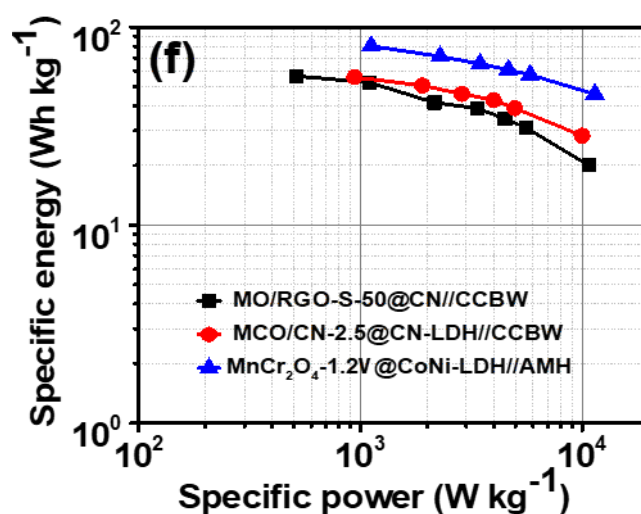
Figure 5.1: Ragone plot of cobalt nickel layered double hydroxide (CoNi-LDH) devices for an asymmetric device.

The electrodeposition synthesis method also played a very crucial role in attaining great results. This is due to the inseparable binding of active material with the substrate coupled with the absence of resistive polymeric binders.

$MnCr_2O_4$-1.2V@CoNi-LDH//AMH had superior specific energy and a competitive specific power compared to the other devices. This is due to the many positive traits of $MnCr_2O_4$ such as more active oxidation states, Jahn-Teller distortion and higher electrical conductivity. These results, therefore, demonstrate the potential of the $MnCr_2O_4$-1.2V@CoNi-LDH synthesised using successive electrodeposition steps and annealing as a candidate electrode for high-performance supercapacitor devices. In summary, the research has managed to provide a novel way to yield very high-performance devices through the utilisation of the successive

electrodeposition route to combine up to three materials which have different charge storage properties.

5.2. Future work

Proposed future work emanating from this study includes attempting to widen the operating voltages through experimenting with ionic liquids and a mixture of ionic and aqueous electrolytes at various mixing ratios while trying to maintain the high specific capacity and stabilities at room temperature.

There are also prospects of using the same electrode material using flexible conducting substrates such as carbon fibres and solid-state electrolytes with a long-term goal of incorporating the supercapacitor device into wearable devices such as heart pacemakers.